EUROPEAN AVIATION SAFETY AGENCY
AGENCE EUROPÉENNE DE LA SÉCURITÉ AÉRIENNE
EUROPÄISCHE AGENTUR FÜR FLUGSICHERHEIT

Research project EASA.2009/4

SAMPLE II - Studying, sAmpling and Measuring of aircraft ParticuLate Emissions II

31 March 2011 – Consolidated version

easa.europa.eu

Disclaimer

This study has been carried out for the European Aviation Safety Agency by an external organization and expresses the opinion of the organization undertaking the study. It is provided for information purposes only and the views expressed in the study have not been adopted, endorsed or in any way approved by the European Aviation Safety Agency. Consequently it should not be relied upon as a statement, as any form of warranty, representation, undertaking, contractual, or other commitment binding in law upon the European Aviation Safety Agency.

CARDIFF UNIVERSITY – SCHOOL OF ENGINEERING

EASA.2009.OP.18

Studying, sampling and measurement of aircraft particulate emissions II (SAMPLE II) – Final Report

31 March 2011

Report Authors:

R Marsh[1], A Crayford[1], A Petzold[2], M Johnson[3], P Williams[4], A Ibrahim[2], P Kay[1], S Morris[1], D Delhaye[5], D Lottin[5], X Vancassel[5], D Raper[6], S Christie[6], M Bennett[6] M Miller[7], Y Sevcenco[1], C Rojo[5], H Coe[4] P Bowen[1]

1 Cardiff University, School of Engineering, CF24 3AA, UK
2 Institute of Atmospheric Physics, DLR Oberpfaffenhofen, 82234 Wessling, Germany
3 Rolls-Royce plc, Derby DE24 8BJ
4 Centre for Atmospheric Science, University of Manchester, M13 NPL, UK
5 ONERA, 92320, Chatillon, France
6 Manchester Metropolitan University, Manchester M1 5GD, UK
7 QinetiQ, Cody Technology Park, Farnborough, Hants GU14 OLX, UK

Table of Contents

Disclaimer

Executive Summary

This report details the methods, results and conclusions of the project entitled “Studying, sampling and measurement of aircraft particulate emissions II” (SAMPLE II) Project. This project was funded via the European Aviation Safety Agency (EASA) under contract number EASA.2009.OP.18. The key objective of this project was to quantify the effects of the sample transport system in particulate measurement experiments during aircraft emissions tests. To achieve this a series of experiments were undertaken, each designed to produce realistic, quantifiable and reproducible conditions that may be used to test the particulate emissions in terms of number, size and mass from gas turbine engine exhausts.

In terms of experimental and measurement activities, this report covers 4 tests undertaken to achieve the objective stated above. These included:

- The use of the combustor – HES facility, located at the Gas Turbine Research Centre (GTRC) at Cardiff University.
- A modern civil gas turbine on a test bed at Rolls-Royce Derby.
- A standard smoke source (CAST burner) at DLR Oberpfaffenhofen.
- LIDAR measurements at Manchester Airport.

These facilities were used to provide a variety of emissions conditions, and stable smoke sources, analogous to real gas turbine engine exhausts.

To complement and enhance this data a total of 4 non-experimental desk-based studies were undertaken. These included:

- A study into the agreement between smoke number and carbon dioxide measurements at some spatial locations in the exhaust of a gas turbine.
- The modelling of sample line effects.
- An investigation of potential methodologies for development of PM mass and number calibration standard.
- A literature review to gain understanding into which PM metrics could be used to replace the existing Annex 16 smoke number.

The systems used to transport the gas sample from the smoke source to the sampling apparatus were developed in such a way as to quantify the effects of sample line conditions, such as particle deposition, agglomeration, evaporation and condensation. This also included quantification of sample dilution at a variety of dilution conditions.

Key Results from this study include:

1. Whilst this study has produced significant results in enhancing the understanding of losses and changes to the nature of PM in sampling systems, there is still work to be done before reliable future measurement standards can be written.
2. More PM engine data is required (particularly measurements made on modern large scale civil gas turbines) in order to comprehensively determine the underlying factors controlling PM loss and transformation in sampling systems.
3. A procedure is required in order to produce a certified instrument standard for the certification of sampling systems. This would also allow for the production of a reliable calibration procedure for sampling systems and instrumentation.

4. Hot tip dilution appears to minimise PM losses in terms of mass and number. Dilution at downstream locations appeared to increase PM losses, but this can't be de-coupled from line residence time.
5. Sample line residence time appears to be a key parameter to PM losses, however it is not possible to de-couple this parameter from other effects such as Reynolds number, pipe diameter and line temperature.
6. There is a measurable difference in terms of PM transmission losses between tip and downstream dilution with tip dilution witnessing lower overall losses. A greater impact is witnessed in terms of PM number compared to mass. However, the effects of residence time could not be de-coupled in this study.
7. Sampling line 'bedding-in' (also known as conditioning) is required but data suggested that stabilisation occurred relatively quickly (during a period of tens of minutes, not hours).
8. VPR efficiency is difficult to analyse and hence a specific lower size PM cut-off may be required to reduce uncertainty.
9. A high dilution ratio (greater than 50:1) is required to limit PM losses. It was witnessed that significantly lower PM losses were witnessed in terms of both number and mass when the dilution ratio introduced at the tip was raised from 10:1 to 50:1 with little further effect if the ratio was further increased to 100:1.
10. There are significant PM losses in undiluted PTFE sample lines, compared to stainless steel. However, these effects are minimised in diluted sample lines.
11. Smoke and gaseous emissions do not necessarily correlate to each other, with Smoke Number variation being greater than the representative CO_2, NO_X and UHC values, although this conclusion came from only one engine test.
12. The RSG miniCAST model 6201 is capable of producing a stable output of combustion particles with respect to black carbon mass and number concentration. The variability is of the order of 10% and 20% for number and mass respectively.
13. During the large-scale engine test, a successful demonstration of an eductor-type PM system in conjunction with a modified Annex16 sampling system (as currently proposed by SAE E31) to measure non-volatile PM number and mass has been undertaken.
14. During the large-scale engine test, in agreement with the HES test campaign, where dilution was added at 7m downstream of the sampling probe, it was observed that a dilution ratio of greater than 10:1 promoted significantly lower number counts (above the expected losses of an additional diluter stage), suggesting that the volatile particles are not fully removed at low dilution ratios.
15. Overall non-volatile PM measurements are not influenced by sample line temperature with almost no difference in the 160/160°C and 160/60°C cases for the Number measurement, and no difference between the 300/160, 160/160 and 160/60°C cases for the Mass measurement.
16. It was observed that there was a 20% – 30% discrepancy in number concentration measured using the 10 nm and 23 nm CPC behind the AVL VPR system. However, this trend was not witnessed when the sample temperature was kept high (>300°C before dilution and 160°C between dilution and VPR) and dilution was high (>100:1). This may indicate that the VPR is not 100% effective at removing the volatile fraction for aero engine exhausts.
17. Single eductor diluter losses witnessed in the large-scale engine tests were of the order of 10% to 15% (for 23nm and 10nm cut-off respectively).
18. In its current commercially-available configuration, the MAAP instrument does not have a fast enough response time to give statistically reliable data during mid to high power

engine testing conditions as potential PM certification measurement windows are less than 4 minutes.

19. Line loss penetration characteristics of the PM measurement system (both the existing Annex 16 hardware and the PM dilution line) are required.

Main recommendations from this study include:

1. More data (particularly engine-derived data) concerning the effects of sampling systems on PM is required to produce a template for future PM measurement procedures.
2. Future PM measurement testing should take account of variability in combustion processes by continuous monitoring using a consistent certified instrument standard in order that sample line effects can truly be evaluated.
3. Better scientific understanding of VPR is required in order to achieve a robust non-volatile PM ARP. Thus further work is required to understand the volatile removal efficiency of commercially available VPR systems for use with modern large-scale civil aero engines.
4. A rigorous investigation of the effect of sample transport residence time on PM losses is required. This would take the form of specifically designed experiments that can decouple the effects of residence time whilst maintaining constant parameters such as Reynolds number and line temperature.
5. Increased understanding of volatile PM, including transportation effects in sampling systems is required.
6. Line loss penetration characteristics of the PM measurement system (both the existing Annex 16 hardware and the PM dilution line) are required.
7. Greater understanding of the use and losses associated with eductor-type diluters is required.

1. Structure of the report

This report draws on a number of experimental tests, reviews and studies, each designed to broaden knowledge in a specific topic area concerned with building a new methodology for the measurement of aircraft Particulate Matter (PM) emissions. Although the report does not provide such a methodology, it is intended that the information contained herein will be used to move EASA and other regulatory bodies towards the development of future practices and procedures for PM measurement.

Key themes in this report are:

- The identification of potential methodologies of calibration sources for PM instrumentation.
- Experimental testing at the combustion – Hot End Simulator (HES) rig at Cardiff University. This work was aimed at measuring some of the physical effects concerned with the transport of PM in sample lines. The effects studied included rig condition, sample line temperature, dilution, flowrate, length, material and diameter.
- Experimental testing on an engine certification rig will be undertaken at Rolls-Royce Derby. This work is aimed at complementing the combustion – HES work using a modern large civilian gas turbine.
- The modelling of the sampling line effects of the combustor – HES and full engine tests. This was undertaken in order to express the behaviour of PM in the sampling systems.
- An intercomparison of the various carbon measurement techniques by burn-off and optical methods.
- PM metrics for engine certification and their relation to smoke number.
- A comparison between carbon dioxide and smoke number concentrations at the exit of a gas turbine on a test bed.
- The feasibility of using a UV Lidar technique for PM measurement at airports.

2. Introduction

The global effects of aircraft PM emissions are a key concern from the point of human health and climate change. Controls on aircraft emissions and maintaining compliance for local air quality standards on European airports is expected to be a prohibitive issue in some cases. Whilst significant effort is being made to identify, quantify, model and predict these effects there is still a sizeable amount of development work required to produce a working specification for the absolute measurement of quantity of PM. Both mass and number concentration will need to be measured in a format that can act as a standardised test under engine certification conditions. Other known problems include the accurate on-site quantification of the ratio of volatile to non-volatile PM emissions, especially aerosol precursors.

The committee on Aviation and Environmental protection (CAEP) within ICAO expects the development of a non volatile PM certification requirement by the end of 2012. EASA and the other Regulatory agencies (FAA, EPA) requested SAE E-31 to provide a final non-volatile PM mass and number ARP by the end of 2011. The SAE E-31 PM sub-committee on aircraft exhaust emissions measurement has been working on improved measurement activities for aircraft PM emissions.
EASA funded a 1 year study (known as the SAMPLE I project), commencing in October 2008, which was one of the first collaborative programmes designed to evaluate the applicability of a number of modern measurement techniques whilst assessing the nature of PM. Conclusions from the SAMPLE I programme (EASA study, Petzold and Marsh, 2009) suggested that calibration of the measurement techniques is critical, the effects of the sampling system on the PM in the sample need to be fully understood, further analysis of volatile species is required and that a subsequent phase of testing should involve a full gas turbine test.

A need therefore exists to reliably quantify the effects the sampling system has on the nature of the PM sample itself. Whilst previous studies during SAMPLE I have quantified the nature of PM, the interaction between this material and the transport process used to convey it from the point of generation to the analyser needs to be understood before a certification requirement for non-volatile PM measurement can be agreed.

3. Objectives of SAMPLE II

The objectives of the SAMPLE II project were:

1. To undertake a review of potential calibration sources for aircraft PM monitoring hardware.
2. To construct and characterise an exhaust sample transport system to systematically capture emissions from gas turbine exhausts. Development also involved consideration of how to minimise the transformation of the sample as it moves through the system.
3. To employ a carefully controlled dilution system, analysing the differences of probe tip vs. downstream dilution and diluent temperature in order to minimise changes in sample dilution due to changes in analyser demands.
4. Development of a procedure to use an existing emissions sampling rake conforming to engine certification procedures to make simultaneous gaseous and particulate measurements from a modern gas turbine exhaust.
5. Make measurements using commercial state-of-the art particulate mass and number instrumentation described in AIR6037 and directly compare to standard ICAO smoke number instrumentation.
6. Improve the methodologies, techniques and understanding of volatile particulate matter in the plume of gas turbine exhausts using commercially available technology.
7. Rig testing, making use of a combustor and turbine simulator, combined with engine testing under certification conditions.

4. Identification of possible calibration sources and of gaps in instrumentation.

4.1 Objective

This task of the EASA SAMPLE II study is focusing on the identification of potential aerosol sources for instrument calibration and testing in terms of quality assurance. So far in the aeronautics sector there is no procedure agreed on how to calibrate instruments for particle number and particle mass measurements. Therefore, instrument calibration approaches for number and mass are identified first, based on the approach taken in the automotive industry; see Reports EUR 22775 EN of the EC and ECE/TRANS/WP.29/GRPE/2007/8. Then, in a series of laboratory tests the RSG miniCAST Model 6201-C of Jing Ltd., Switzerland was investigated with respect to aerosol output reproducibility, which is known to be a very robust soot particle source. The main goal of this study was the investigation of instrument reproducibility in terms of mass and number emission properties.

4.2 Instrument Calibration Approaches

Definition of calibration

Calibration is the set of operations that establish, under specified conditions, the relationship between the values of quantities indicated by a measuring instrument and the corresponding values realized by standards. In general, the calibration of an instrument can be performed in two ways:

1. Checking of the measuring instrument against a traceable standard.
2. Comparison of the measuring instrument with a certified standard instrument.

Particle mass concentration

Conventional mass concentration measurement is based on the gravimetric method. Particulate matter is deposited on a highly efficient filter matrix. The increase in mass caused by the deposited PM is the principal measure for gravimetry. Filter holder and sample lines have to be designed to pre-defined construction criteria in order to minimize particle losses. Any calibration refers to the calibration of the balance in use by certified mass standards. Furthermore, the weighing of filters has to follow certain rules with respect to room temperature, relative humidity, and dew point, e.g., T = 295 ± 3 K and RH = 45 ± 8%, and dew point = 9.5 ± 3 °C (ECE/TRANS/WP.29/GRPE/2007/8).

Measuring non-volatile particulate matter by gravimetry requires the removal of all volatile matter prior to the filter sampling and consecutive gravimetric analysis. Calibration procedures are similar to those for conventional gravimetry. The removal efficiency of the volatile particulate matter remover has to be determined prior to the measurements in order to apply potential corrections to the mass measurement.

Measuring the mass of carbonaceous matter (= organic matter and elemental carbon) deposited on a quartz filter by means of a thermal-optical method requires a heating unit, or an oven, respectively, equipped with a specified gas supply in order to heat the filter sample under

controlled conditions under a specified atmosphere. The CO_2 evolving from the filter during the heating procedure is then measured by a non-dispersive IR absorption detector or – after conversion to CH_4 – by a flame ionisation detector (FID). The detector of the system is calibrated by a specified calibration gas, which is used as an external standard. Primary calibrations may be referenced against sucrose solutions or NIST traceable gas standards.

In all cases, the determination of a mass concentration requires also the use of a calibrated flow meter for determining the sample volume drawn through the filter matrix; see AIR6037 and references given there.

Light-absorbing black carbon
Measuring light-absorbing black carbon by an optical method, here Multi-Angle Absorption Photometry (MAAP) and Laser induced Incandescence (LII), is an indirect approach based on principal measures different from mass. The MAAP method measures aerosol absorption while LII measures incandescence radiation emitted from laser-heated black carbon particles. For both methods, the calibration for black carbon mass is performed against filter samples collected simultaneously which are analysed by an a-priori agreed thermal-optical method. As for the above-mentioned filter-based methods the system has to be supplied by a calibrated flow meter.

Particle number concentration
The current calibration method for condensation particle counters (CPC) is based on the method developed by Liu and Pui. The electrostatic classifier is used to deliver singly charged, monodisperse calibration aerosols of known size and composition. An aerosol electrometer and the CPC under calibration sample this aerosol in parallel downstream of the classifier. The particle number concentration is obtained from the aerosol electrometer current. This is the method used by most CPC manufacturers to determine CPC performance, including lower size detection limit, counting efficiency and linearity of response. Any CPC operated by users may be calibrated against a certified standard CPC which is calibrated against this primary method.

The CAST as a soot aerosol calibration source
So far the various CAST models provided by Jing Ltd (http://www.sootgenerator.com/) are the only commercially available compact carbon aerosol generators based on a flame process. They operate on a propane diffusion flame. The PALAS Defined Soot Particle Generator DSP 3000/3000H offers another option for generating soot particles in a premixed ethene-air flame. This generator however is of much higher complexity compared to the miniCAST and in the literature no data on particle characteristics are available so far. Commercial camping burners like the McKenna burner used by Slowik et al are not considered.

The PALAS GFG 1000 Graphite Aerosol Generator as discussed by Helsper et al produces carbon particles by a spark discharge between electrodes of high-purity graphite. This generator also emits particles of a size comparable to particles emitted from a flame, but of different OC-EC partitioning and of different optical properties (Petzold and Niessner, 1995). The latter study proved that the PALAS GFG1000 is not applicable to the calibration of optical methods. Thus, the generators of the CAST series are the only available compact source for combustion aerosols for instrument testing and calibration.

Referring to the previous discussion of calibration needs for mass-based and number-based measurement techniques, a soot aerosol generator is no indispensable pre-requisite for instrument calibrations in the framework of certifying the emissions of non-volatile particulate matter from aircraft engines. Particle number concentration measuring instruments can be calibrated by using any stable aerosol generator. For calibration purposes, a nebuliser or a vaporisation-condensation aerosol generator, as demonstrated by Scheibel and Porstendörfer (1983), are first choice. Mass-based methods do not require a soot aerosol generator as well. Gravimetry is calibrated by standardized balance weights, while thermo-optical methods require a certified gas or sucrose solutions for the detector calibration.

The potential use of the miniCAST is the production of test aerosol for instrument operational tests. Aiming at this application, the miniCAST was tested with respect to output stability and output reproducibility.

4.3 Experimental Part

In the DLR laboratories a Real Soot Generator RSG miniCAST 6201-C was set up and operated at various conditions. In the CAST burner, soot particles are formed within a co-flow diffusion flame due to the hydrocarbon pyrolysis that takes place as a consequence of the heat provided by the oxidation at the flame front. The CAST burner enables the soot particles to escape from the flame without contact with oxygen. Subsequently the particle stream is mixed with a quenching gas in order to prevent further combustion processes in the particle stream and to stabilize the soot particles. The quenching gas inhibits condensation in the particle stream at ambient air condition. To dilute the particle stream, compressed air is supplied to the quenched particle stream. Figure 1 shows a scheme of the CAST principle. Figure 2 shows a schematic and Figure 3 a photograph of the miniCAST set-up. The gas supply of the miniCAST was set up using Bronkhost mass flow controllers. Details concerning measurement range and uncertainties are compiled in Table 1.

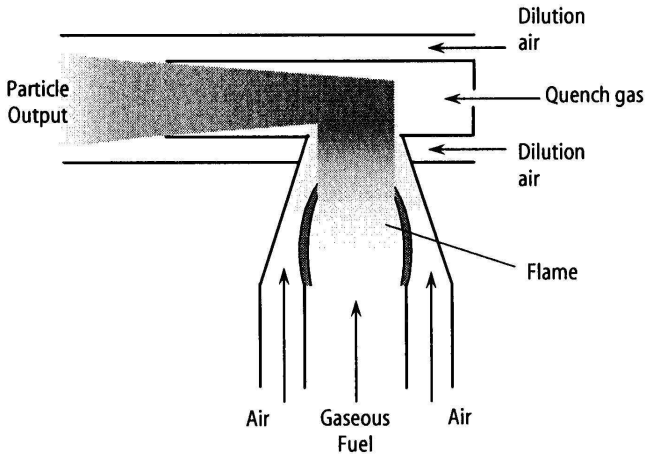

Figure 1 Working principle of the miniCAST burner.

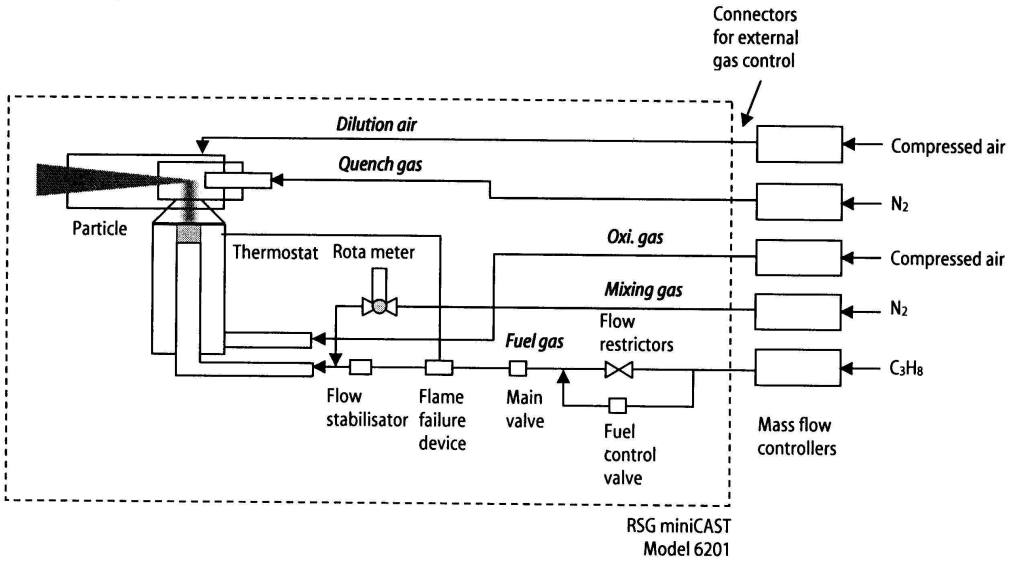

Figure 2 Schematic of the the RSG miniCAST Model 6201-C.

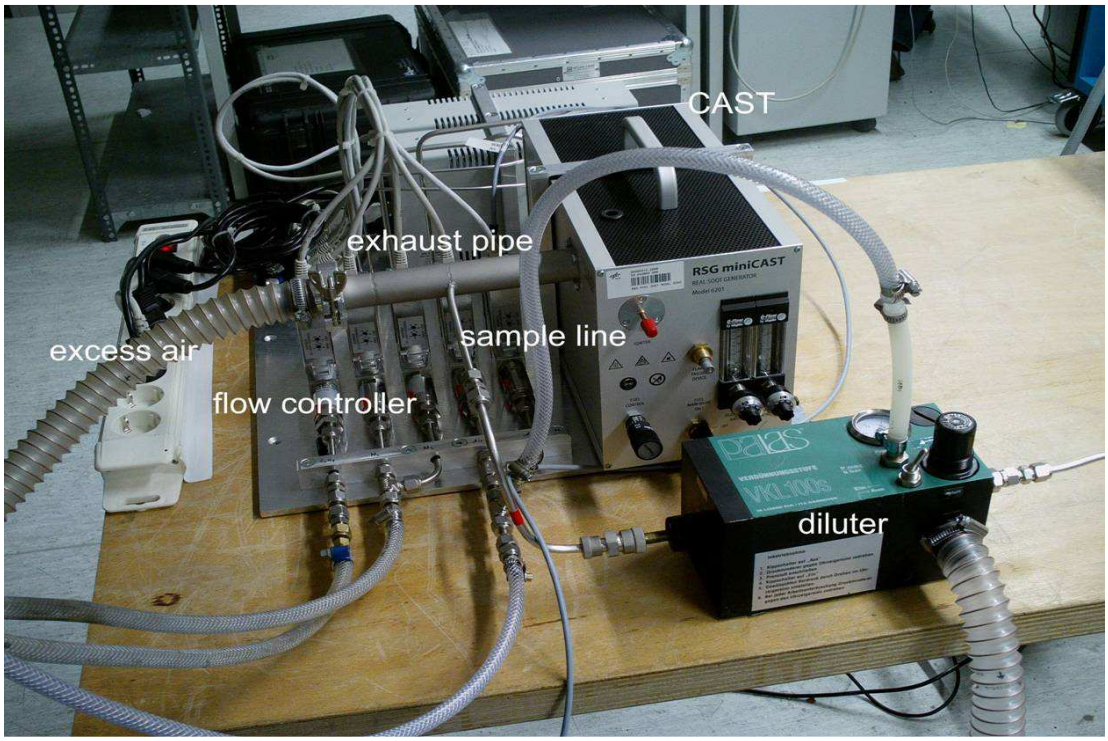

Figure 3 Photograph of the RSG miniCAST Model 6201-C.

Table 1 Gas supply system for the RSG miniCAST Model 6201-C.

Mass Flow Controller Bronkhorst Type F-201CV-100-RAD-33-V					
Gas	C_3H_8	Ox. Air	Mixing N_2	Quench N_2	Dilution Air
Flow, l/min	0 - 0.036	0 - 1.20	0 - 0.100	0 - 3.75	0 - 9.00
Deviation	± 0.6% max (of measurement range)				

The exhaust was sampled with a Multi-Angle Absorption Photometer (Thermo Scientific Model 5012) for the measurement of black carbon mass concentration and four Condensation Particle Counter (Grimm Model 5410) for the measurement of particle number concentrations. Two of the CPC were connected to a thermal denuder which was set to 250°C for removing volatile particulate matter prior to the measurement. Injection diluters of the type Palas VKL 10 (dilution ratio 1:10) and Palas VKL 100 (dilution ratio 1:100) were used for sample dilution in order to obtain particle number concentrations below the upper measurement range of the instruments (N_{max} =10^5 cm^{-3}). Particle size distributions were measured by a Grimm SMPS+E scanning mobility particle sizer connected to a Faraday cup electrometer. The dilution ratios were monitored by Pewatron CARBONDIO CO_2 sensors. The CO_2 volume mixing ratio of the raw exhaust gas was calculated for ideal combustion conditions.

Additional to the MAAP, the black carbon mass concentration was also monitored with a particle soot absorption photometer PSAP (Radiance Research; USA) and an Aethalometer (Magee Scientific, USA). The aerosol absorption coefficient σ_{ap} (530 nm) measured by the PSAP is converted into a black carbon mass concentration by division with the mass-specific absorption cross section of 7.5 m^2 g^{-1} [Bond and Bergstrom, 2006]. The particle scattering coefficient σ_{sp} was measured by an Integrating Nephelometer (TSI model 3563). The complete optical characterisation of the CAST output aerosol, however, is beyond the scope of this task.

The experimental set-up is shown schematically in Figure 4, and in Figure 5 as a photograph. The CO_2 mixing ratio in the burner exhaust gas was calculated assuming ideal combustion, i.e., all carbon contained in the fuel is oxidized to CO_2. The obtained volume mixing ratio of approx. 14300 ppm corresponds to a mass concentration of 7.7 g C m^{-3} at standard conditions of 273.15 K and 1013.25 hPa. Observed black carbon mass concentrations of approx. 1.4 mg C m^{-3} indicate a combustion efficiency of 0.9998, supporting the assumption of ideal combustion.

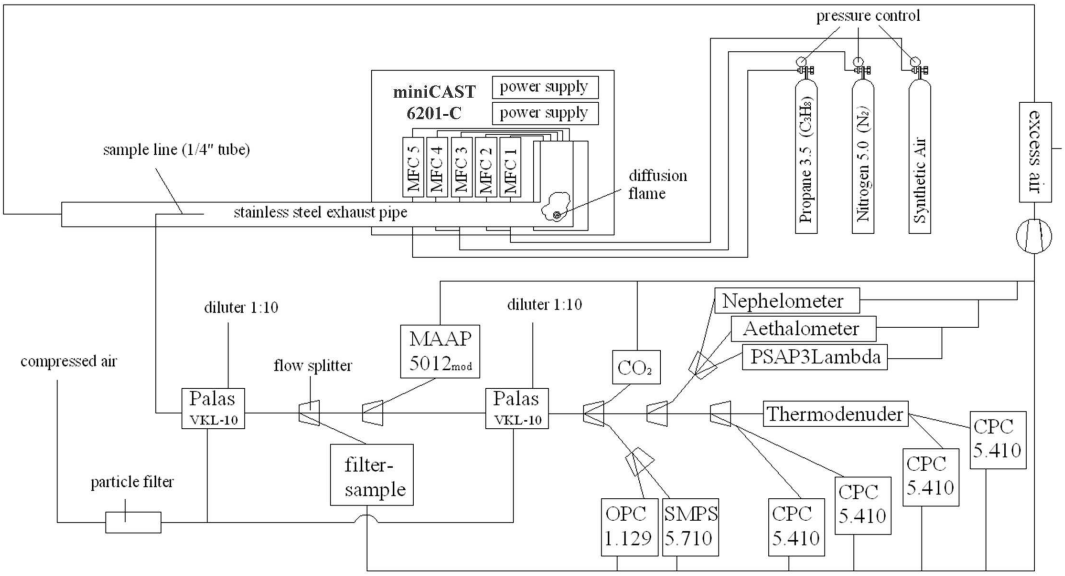

Figure 4 Experimental set-up in the DLR laboratories.

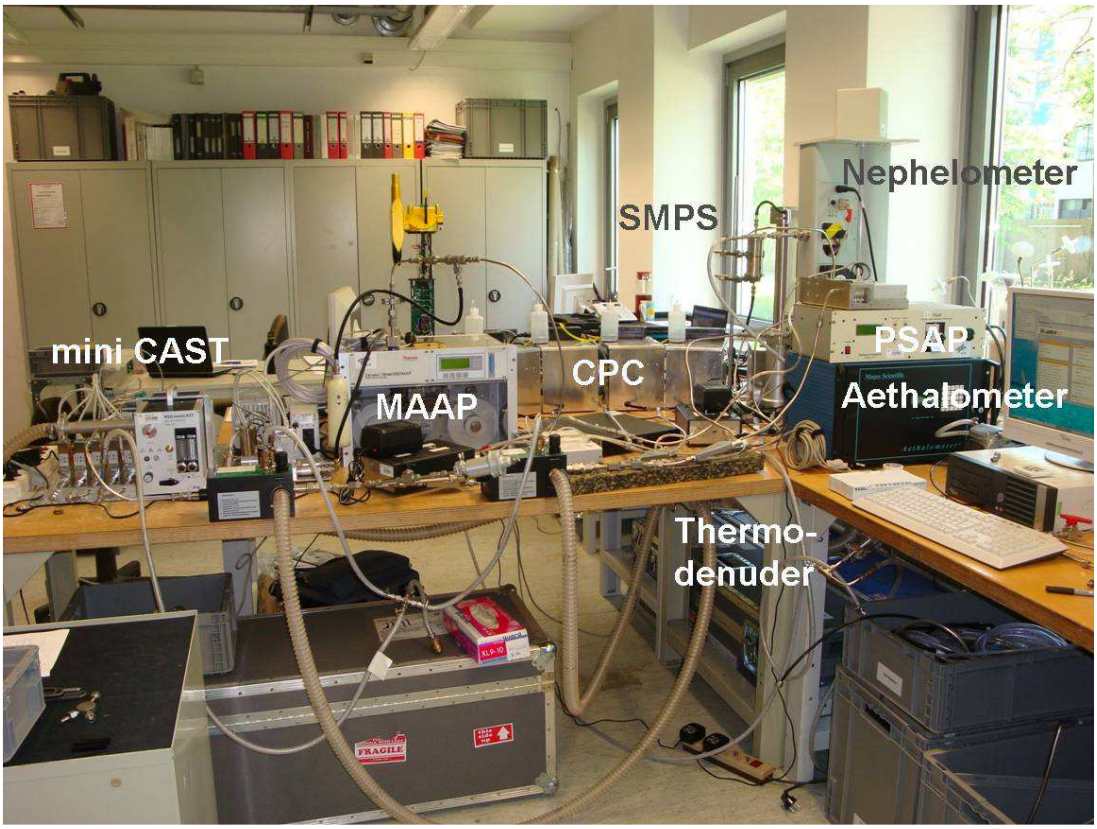

Figure 5 Photograph of the laboratory set-up.

4.4 Results

Table 2 summarises the operating conditions of the miniCAST burner during the tests which were selected for the reproducibility tests. In the course of SAMPLE (EASA.2008.OP.13) the group investigated the range of operation conditions for the RSG miniCAST by varying the fuel flow and the oxidation air flow. In the tests reported here the objectives were different. Here the intention was to vary the carbon-to-oxygen ratio over the widest possible range for producing aerosol with different elemental carbon-to-organic carbon ratios. Because of the different objectives the results cannot be compared.

At stoichiometric conditions the fuel propane (C_3H_8) is characterised by a ratio of carbon to oxygen atoms of 0.30. For the tests, the burner was operated at an equivalence ratios ϕ = 0.72. Respective values in terms of air-to-fuel ratio are AFR_{st} = 15.5 by mass for stoichiometric conditions and AFR = 21.5 for the selected conditions, which results in λ = 1.39.

Figure 6 shows the elemental carbon (EC) fraction of total carbon (TC) determined from collected quartz fibre filters via the SUNSET method [*Birch and Cary*, 1996]. The dashed line represents the stoichiometric ratio of carbon to oxygen atoms of 0.30. However, it has to be noted that in a diffusion flame there are always regions present which favour soot formation, even under stoichiometric conditions. Clearly, the ratio of EC to TC varies strongly with the ratio of carbon to oxygen (C / O) in the fuel. The behaviour is similar to that observed in an earlier study for an older model of the CAST soot generator [*Schnaiter et al.*, 2006], see short-dashed line in Figure 6. Thus, for the selected condition of C/O = 0.22 (ϕ = 0.72) the generated particles consist almost exclusively of elemental carbon with only minor fractions of organic carbon.

Table 2 Operation conditions of the CAST burner.

Condition; Date	Fuel (C_3H_8)	Oxidation Air	Fuel Mixing Gas (N_2)	Quench Gas (N_2)	Dilution Gas (air)	C/O	Equiv. ratio ϕ	Exhaust CO_2
	(l/min)	(l/min)	(l/min)	(l/min)	(l/min)			(ppm)
# 0; 14/06/2010	0.017	0.564	0.0000	1.236	1.080	0.22	0.72	14326
# 1; 15/06/2010	0.017	0.564	0.0000	1.236	1.080	0.22	0.72	14326
# 2	0.017	0.396	0.0000	1.236	1.080	0.31	1.02	15786
# 3	0.017	0.300	0.0000	1.236	1.080	0.40	1.35	16763
# 4	0.017	0.205	0.0000	1.236	1.080	0.59	1.97	17855
# 5	0.025	0.300	0.0000	1.236	1.080	0.60	1.98	24910
# 6	0.030	0.240	0.0000	1.236	1.080	0.89	2.98	31322
# 7; 22/06/2010	0.017	0.564	0.0000	1.236	1.080	0.22	0.72	14326

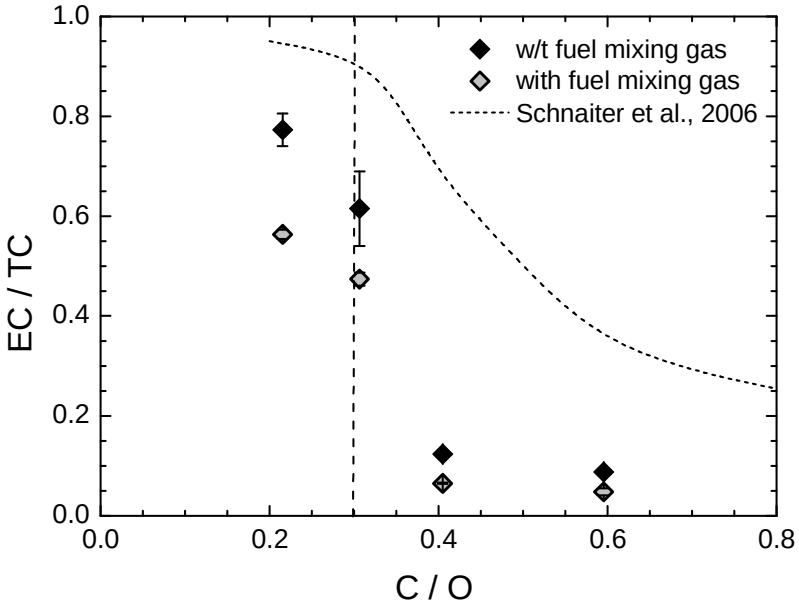

Figure 6 Elemental carbon fraction of total carbon (EC / TC) of particulate matter emitted from the burner for various ratios of carbon to oxygen (C / O) in the fuel.

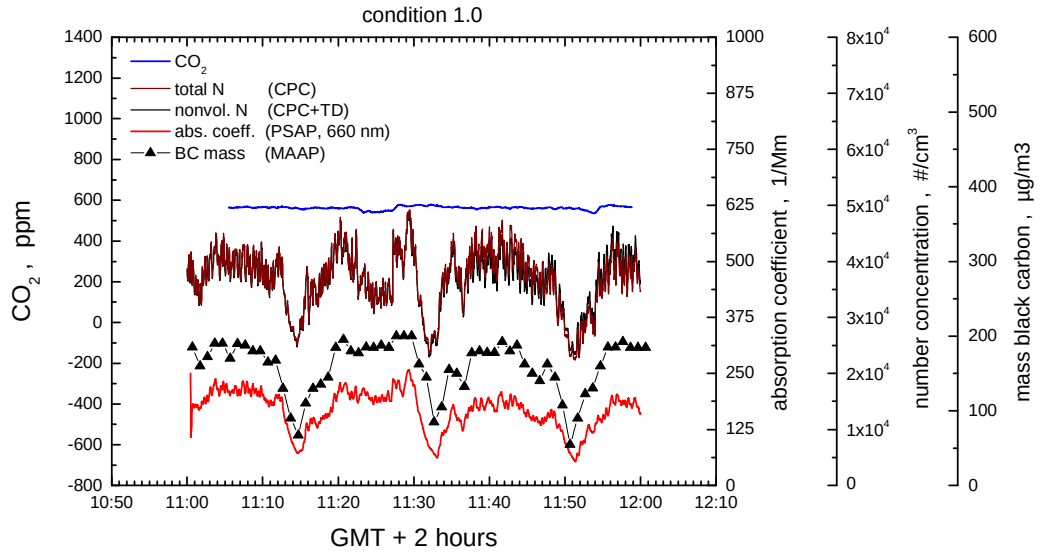

Figure 7 Time series of CO_2, CPC, MAAP and PSAP signals for Condition 1, Sequence 2; please note that values are not corrected for the different dilution ratios.

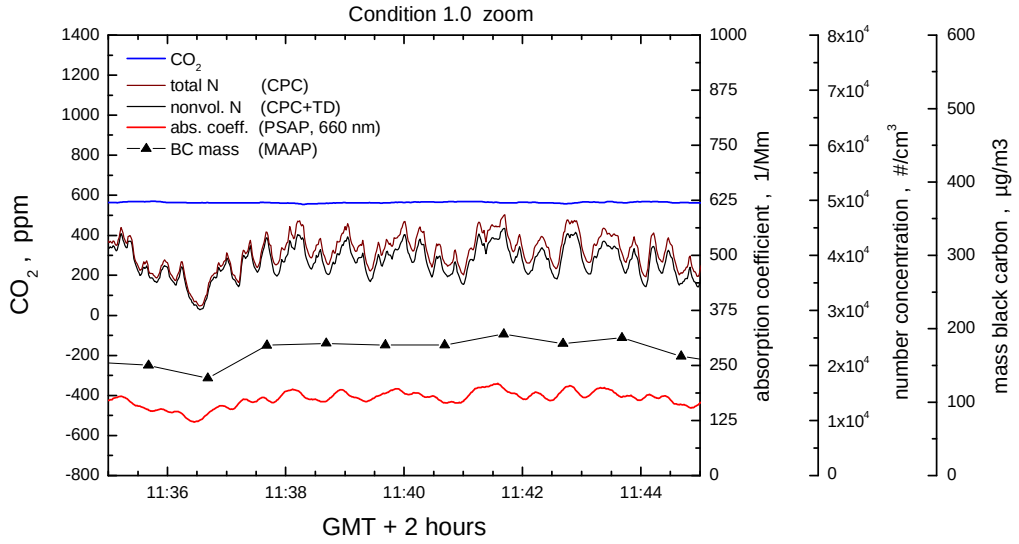

Figure 8 Zoom-In of the time series shown in Figure 7.

As is shown in Figure 7, during the operation of the CAST the output of particulate matter oscillated with various frequencies. During SAMPLE when a much simpler sampling line set-up was used no such oscillations were observed. The low-frequency oscillation with a period of approx. 20 min shown in Figure 7 is most likely associated to oscillations in the complex sampling system while the higher-frequency oscillation with a period of 1 min (see Figure 8) is associated to fluctuations of the flame caused by the mass flow control unit. However, all particulate matter instruments followed this oscillation which indicates that this effect is no artefact but a real property of the exhaust gas.

It turned out that the CAST output is extremely sensitive to any pressure fluctuations in the sampling line system. Therefore the miniCAST flame zone from the sampling system was decoupled by introducing a first VKL 1:10 injection diluter downstream the flame, see Figure 3. This diluter should protect the flame from any pressure perturbation occurring in the sampling line downstream the diluter. The low-frequency oscillation however was not linked to the operation of this injection diluter. In summary the combination of miniCAST and injection diluter worked well during the tests. It is interesting to note that Jing now produce a burner that works at a small positive pressure of 100 mbar.

The miniCAST was operated at similar conditions on two consecutive days and at the end of the tests. The results averaged over 20min sequences each for the different days is compiled in Table 3. Conditions 0 and 1 agree well while Condition 7 differs significantly. An inspection of the CO_2 of Condition 7, however, indicates that the observed CO_2 level is entirely different from those levels measured during Conditions 0 and 1. Furthermore, the particle number concentrations in the exhaust flow are increased by a factor of two compared to Conditions 0 and 1, while the mass concentration is increased by a factor of 2.4 indicating that the particles are of

larger size. This assumption is confirmed by the size distribution measurements by the SMPS system, showing an increase in the median diameter by 30% compared to Conditions 0 and 1. Concluding, Condition 7 exhibits different emission properties than Conditions 0 and 1 which refer to nominally the same operating conditions. Due to the fact that the CO_2 measurement is questionable for that condition, likely differences in the dilution system could not be resolved and in consequence this condition was excluded from the further discussion.

Comparing CPC#1 with CPC#2 connected to a thermodenuder, and CPC#3 with CPC#4 connected to a thermodenuder, no significant deviation is found, i.e., the aerosol consisted entirely of nonvolatile particles. Thermo-optical analysis of the collected filters indicates as well that the particulate matter consists almost exclusively of elemental or black carbon with only minor contributions of organic carbon (see Figure 6).

During Conditions 0 and 1, the number concentrations in the exhaust gas averaged for the individual sequences deviate by max. 10% (one standard deviation) from a sequence-average value. The internal correlation of the CPC instruments is very high as expected, see Figure 9. The average ratio of nonvolatile particles to total particles by number is 1.006, indicating an entirely nonvolatile aerosol on a number basis. The mass concentrations however show a larger scatter of about 20%.

Table 3 Results of the reproducibility tests

		Condition 0.0 14/06/2010		Condition 1.0 15/06/2010		Cond. 7.0 22/06/2010
Property	Device:	Sequence 1 15:45-15:53	Sequence 2 15:57-16:07	Sequence 1 11:02-11:12	Sequence 2 11:36-11:46	sequence 1 11:45-12:16
Number concentration	CPC#1	3.48 ± 0.19	3.22 ± 0.19	3.91 ± 0.23	3.85 ± 0.29	7.83 ± 0.30
(10^6/cm3):	CPC#2 TD	3.31 ± 0.18	3.06 ± 0.18	3.93 ± 0.23	4.04 ± 0.32	7.50 ± 0.29
	CPC#3	3.52 ± 0.20	3.26 ± 0.18	3.96 ± 0.23	3.91 ± 0.29	7.90 ± 0.30
	CPC#4 TD	3.38 ± 0.19	3.13 ± 0.18	3.59 ± 0.21	3.40 ± 0.25	7.76 ± 0.30
Black carbon (µg/m3):	MAAP	1444 ± 91	1127 ± 65	1794 ± 100	1686 ± 182	4132 ± 204
CO_2 content (ppm):						
Measured	CO_2	563.2 ± 5.8	566.6 ± 3.0	565.0 1.9	563.1 ± 2.9	410.6 ± 2.3
Calculated	CO_2	581.1 ± 2.3	581.1 ± 2.3	579.2 ± 2.2	579.2 ± 2.2	566.8 ± 2.6
Size distribution						
d_g, nm	SMPS	n/a	108	97	104	130
σ_g	SMPS	n/a	1.56	1.66	1.79	1.66

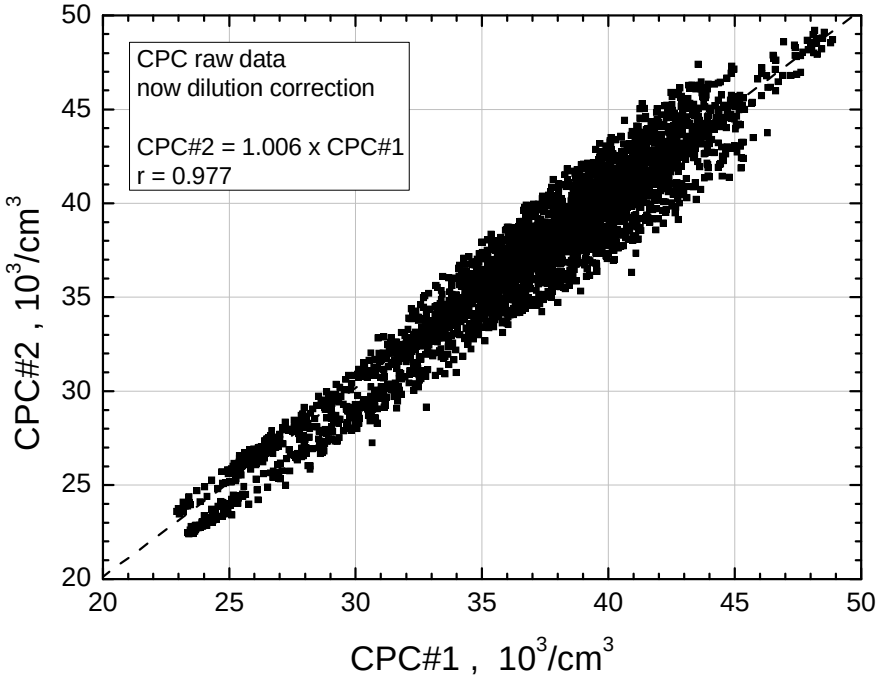

Figure 9 Correlation plot of CPC#2 connected to the thermodenuder (nonvolatile particles) vs. CPC#1 (total aerosol) for Condition 1, Sequence 1 and 2.

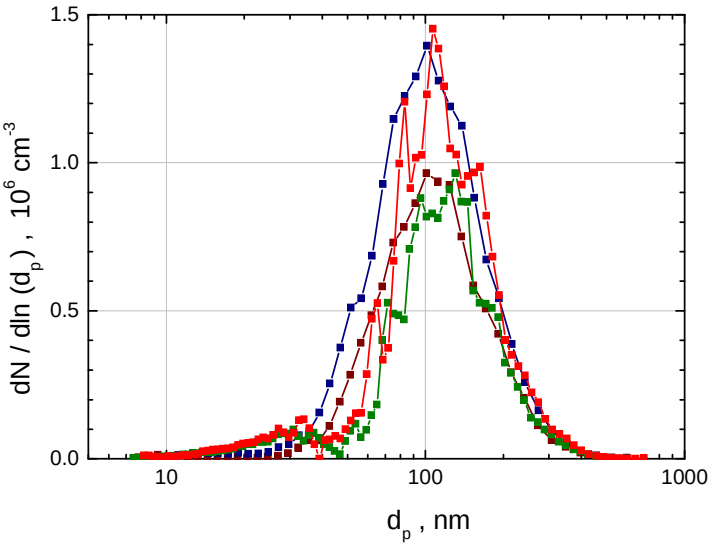

Figure 10 Size distributions measured during Condition 1, Sequence 1 and 2 (C/O = 0.22, EC/TC = 0.77 ± 0.03). The 4 plots are repeats at the same conditions.

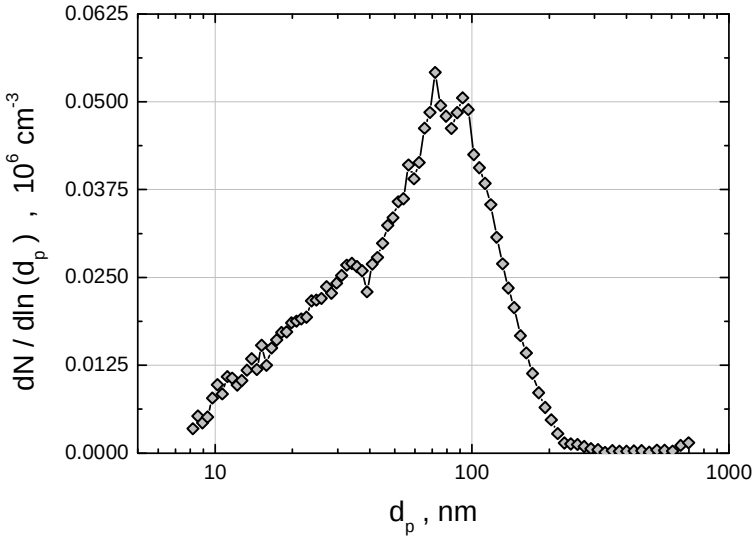

Figure 11 Size distributions measured during Condition 1.1 with fuel mixing gas added (C/O = 0.22, EC/TC = 0.56 ± 0.01).

Size distributions of emitted particles depend strongly on the C/O ratio of the fuel and on the addition of fuel mixing gas. Figure 10 shows the size distribution for the conditions generating almost entirely elemental carbon composed particles. One strong mode at d_g = 100 nm is clearly visible. Figure 11 refers to the same condition however with fuel mixing gas (fuel: 0.017 l/min; mixing gas 0.015 l/min) added. This modification results in the development of a second mode at smaller sizes around 40 nm which is accompanied with a lower ratio of EC/TC indicating a stronger contribution of organic matter. Even stronger modifications in the same direction are observed when operating the burner at a larger C/O ratio, which generates small-sized particles which are mainly composed of organic matter, see Figure 12.

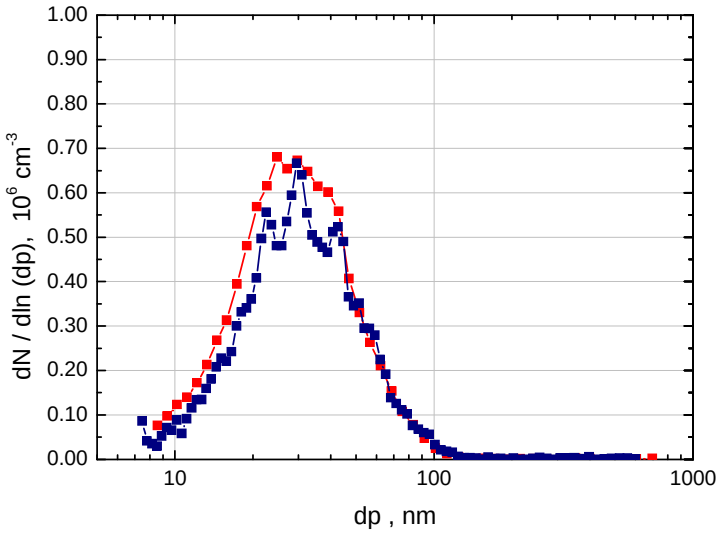

Figure 12 Size distributions measured during Condition 5 (C/O = 0.60, EC/TC = 0.09 ± 0.01). The 2 plots are repeats at the same conditions.

Based on a statistical analysis of the runs at C/O= 0.22, the geometric mean diameter d_g and the geometric standard deviation σ_g of the emitted aerosol turned out to be very stable, see Table 3 and Figure 10. For the selected conditions, the generator produces aerosol size distributions of a geometric mean diameter of 100 nm. Figure 12 shows the resulting size distribution when operating the miniCAST at C/O = 0.60. For this operation condition, particles consist to more than 90% of organic carbon and the average ratio of nonvolatile particles to total particles by number is 0.88, indicating the onset of formation for externally mixed organic matter particles.

4.5 Summary

The RSG miniCAST was successfully tested over a wide range of operation from C/O = 0.2 to C/O = 0.9 without substantial instrument failure.

The size distribution was shifted from CMD ≅ 110 nm at low C/O ratio to sizes below 20 nm at C/O approaching 1.0. Adding mixing gas to the fuel further reduces the average size of the particles and the modal distribution. Smaller particles are expected to be composed predominantly of organic matter and have been formed by nucleation/condensation of condensable organic cases.

Results from the CPC connected to a thermodenuder indicate the presence of a separate volatile particle mode at conditions with expected high OC content with non-volatile fraction of total decreasing from approx. 100% to 60%.

Condition 0/1 with highest EC content and an entirely nonvolatile exhaust aerosol on a number basis was select as being closest to non-volatile aerosol particulate matter for testing the burner's repeatability.

The RSG miniCAST 6201C is capable of producing a stable output of combustion particles with respect to black carbon mass and particle number concentration. Small fluctuations related to the mass flow controllers used for regulating the fuel flow have a direct impact on the exhaust properties. Furthermore, the flame stability depends crucially on pressure conditions in the exhaust line which makes the handling of the burner difficult. However, at the time of finalising the report, the production model 6201C, has been improved with a positive exhaust overpressure of around 100mbar, to make it more independent from pressure variations in the exhaust line.

Repetitive measurements at the same operating condition provided similar mass concentration values and chemical compositions of the aerosol. The variability of the burner output is of the order of 10% for particle number and 20% for black carbon mass measured by the MAAP. Compared to the criterion that filter weighing should produce repeatable results within ± 5 µg of mass, and that number concentration values shall agree within ±10% with the calibration value (ECE/TRANS/WP.29/GRPE/2007/8), these variabilities are at the upper limit tolerable for a traceable soot aerosol standard.

Jing Ltd. offers CAST burners which are calibrated for a given operation conditions. However, in case of proposing these calibrated CAST burners as instrument calibration standards, the performance of these burners would require extensive testing. Furthermore, since the miniCAST is based on a diffusion flame, considerable improvement may be achieved when switching to a premixed flame because for such a set-up much more stable and reproducible combustion conditions can be achieved (As shown in Glassman, 1996).

Summarising, the miniCAST is a valuable soot aerosol generator for instrument development and testing. The calibration of instruments for certification, however, should follow the procedures established by the responsible metrology institutions.

5. Experimental Approach – GTRC Hot End Simulator trials

5.1 Rig Description

The facility upstream of the rig under consideration comprises of the main air handing and treatment hardware. Air is introduced to the combustion chamber pre-heated and at the required mass flow. Pressure is controlled on the experiment, usually by a back-pressurising valve, but in the case of this experiment a choke-plate downstream of the combustor maintained the operating pressure (as described later). A compressor transfers the incoming air into a gas-fired non-vitiating heater, where it is raised to the required temperature for the test. The mass flow rate is measured using a coriolis meter, located upstream of the rig test section.

The rig conditions are monitored and controlled from a control room, which is remote from the rig room for the purposes of safety. The operators have full control over all of the operating parameters in the experiment using a computer controlled Supervisory Control And Data Acquisition (SCADA) system. Rig and plant conditions are logged once per minute and stored on the instrumentation and logging systems in the control room. This room also houses the gas analysis apparatus, as described in a later section of this report.

An overall schematic of the rig is shown in Figure 13 and a photograph is shown in Figure 14. These diagrams show the assembly of the rig, with locations of the combustion section, HES and exhaust gas sampling probes. The flow in the process is from left to right; pressurised, heated air is supplied to the combustion can where fuel is injected and burnt at constant pressure. The pressure in the can was maintained by a choke plate, which is a matrix of holes in a water-cooled assembly that holds the pressure in the upstream section.

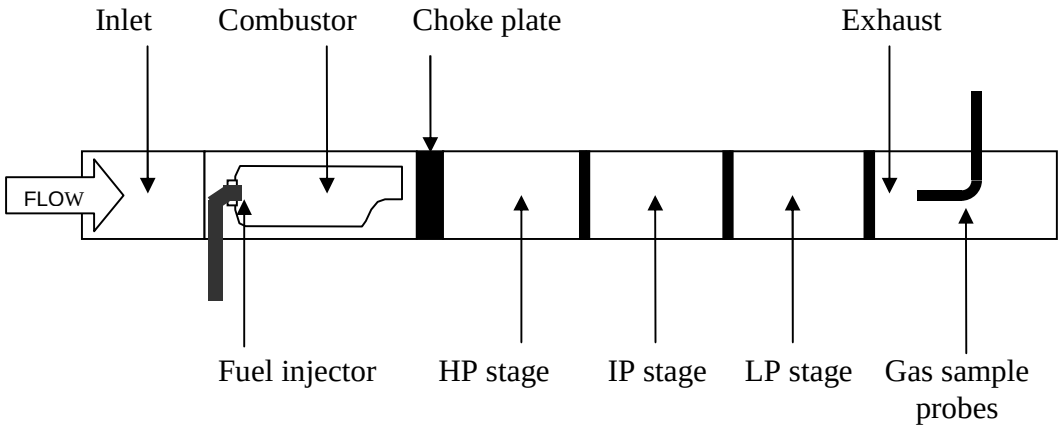

Figure 13 Schematic of the combustion system, HES and location of gas sampling probes.

For the combustion section of the rig, an aerospace cannular combustion chamber, constructed out of transpiration cooled steel was used for the tests. Fuel was provided into the can via an airblast atomizer, a modified version of the type used in an engine configuration. The fuel used in this trial was aviation grade kerosene, known as JP-10. A fuel analysis was conducted by QinetiQ (and is attached in Appendix B).

The Hot End Simulator (HES) is a facility that sits behind the combustor, mimicking the behaviour of a turbine section in a gas turbine. This component reduces the pressure and temperature of the exhaust gasses by removing heat rather than work from the exhaust gases. The HES is comprised of three separate heat exchanger stages. Each stage simulates the rotor workload while variation of the cross-sectional area and trimmer plates simulates the pressure stages in a turbine, referred to here as the high, intermediate and low pressure stages. Pressure was maintained in these sections via pressure trim plates, similar to the upstream choke plate, consisting of a matrix of holes, designating the effective blockage ratio.

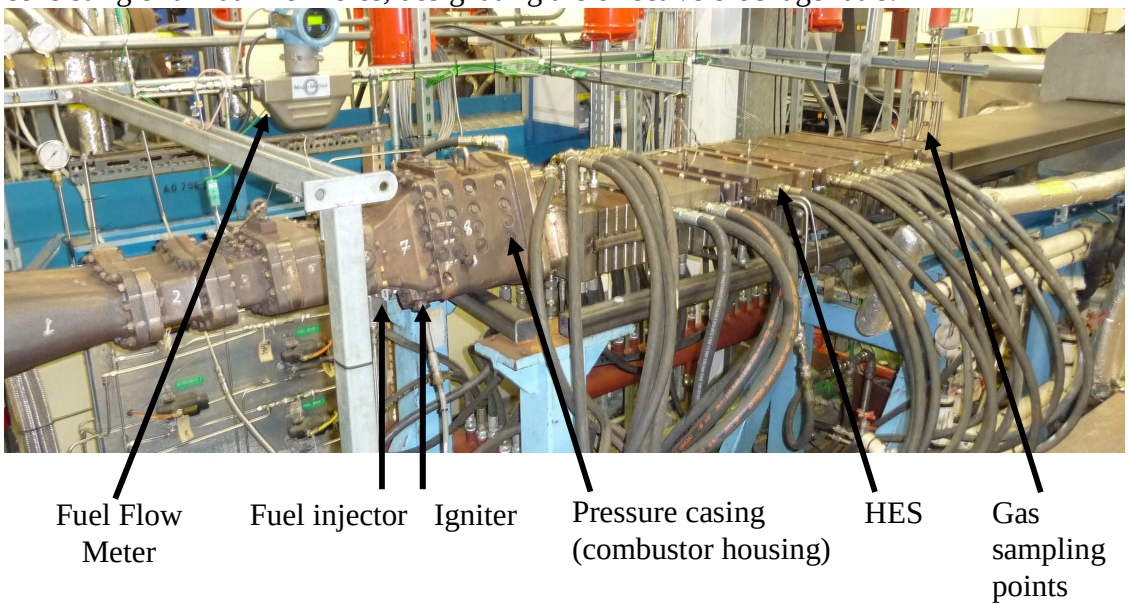

Figure 14 Photograph of the combustor, HES and gas sampling point.

The assembly was almost identical to that utilized in the SAMPLE I project tests conducted during 2009. More details are given in the SAMPLE I report (EASA Study - , Petzold and Marsh, 2009) and Petzold et al (2003). For the purposes of this experimental campaign the combustor and HES were used to provide a standard smoke source for the experimental programme. The main difference between this and the SAMPLE tests were that different gas sampling probes were used, which are described later in the report.
The location of the gas sample probes was such that they were under only a slight positive static pressure of 1.05 bar plus additional dynamic pressure from the flow of the gas stream. For this reason each partner provided an extractive pump downstream of the analyser to each sampling apparatus in order to draw the required sample flow through each analyser.

5.2 Test conditions

In total 3 conditions were selected for the trials. The aim of selecting the 3 was to provide tangible differences in the composition of the particulates emitted from the smoke source. Of particular interest to the research team was the difference in emissions for cases of varying organic (volatile) and inorganic (solid) carbon concentrations in the exhaust. These are summarised in Table 4.

Condition 1: Low particulates and high organic carbon loading (LS/HO).
Air flow = 1.0 kg/s; T_{in} = 400K; P_{in} = 350 kPa (abs); AFR = 65
This case (representative of most a modern civil aviation gas turbine) involved operating the combustor at a lean AFR and reduced temperature and pressure conditions when compared to the LS/LO case. The aim of this condition was for the smoke source to produce comparatively lower quantities of particulates but higher amounts of unburnt hydrocarbons in the exhaust. The target smoke number for this condition was 5.

Condition 2: Nominal particulates and organic carbon loading (LS/LO).
Air flow = 2.0 kg/s; T_{in} = 566K; P_{in} = 705 kPa (abs); AFR = 66
This condition was chosen since it represented a nominal cruise condition for the combustor when operating at a standard cruising altitude of around 11km. At this point the combustor is operating on the engine line and as such its emissions (both gaseous and particulate) should be within normal operating parameters. From the point of view of the experiment in question, the smoke source should be providing particulates with a target smoke number of around 13.

Condition 3: High particulates and low organic carbon loading (HS/LO).
Air flow = 2.6 kg/s; T_{in} = 660K; P_{in} = 1000 kPa (abs); AFR = 54
This condition involved operating the combustor at a richer AFR and increased temperature and pressure conditions when compared to the LS/LO case. The aim of this condition was for the smoke source to produce comparatively higher quantities of particulates but lower amounts of unburnt hydrocarbons in the exhaust. The target smoke number for this condition was 20.

Table 4 Summary of HES rig conditions.

Condition	Airflow (kg/s)	Combustor inlet temperature (K)	Combustor inlet pressure abs (KPa)	AFR	Target SN
LS/HO	1.0	400	350	65	5
LS/LO	2.0	566	705	66	13
HS/LO	2.6	660	1000	54	20

5.3 Sample line conditions

A bespoke gas handling and distribution system was developed and constructed for this project. This system was capable of controlling the sample temperature, flowrate and dilution ratio at a variety of locations. This included a tip-dilution probe, which was designed to allow dilution ratios from 1:1 to 100:1. However, due to time constraints experiments were only conducted at approximate dilution ratios of 10:1, 50:1 and 100:1. Likewise there was a non-ejector dilutor run at similar dilution ratios at 7m downstream. These dilutors were never used simultaneously during this experimental program.

Key conclusions from the SAMPLE I programme allowed the project partners to conclude that in order to provide a robust PM sample, dilution must be provided either at probe tip or downstream via a measured flow of inert gas or filtered dry air. This necessitated the need to provide a stringent way in which to dilute the sample and maintain an accurate measurement of flow rate through the system. As with the SAMPLE I programme, 2 sampling lines were used; one was diluted and one was undiluted. The purpose of the undiluted line was for instrumentation that requires comparatively high PM loading (e.g. Smoke Number and gravimetry).

To allow a rigorous investigation of the effect of dilution a new single point dilution probe was designed and manufactured for use during the combustor/HES test campaign. The design was based on lessons learnt from the SAE aerospace information report AIR6037, which evaluated a number of designs for tip diluted probes. A diagram of this dilution tip is shown in Figure 15.

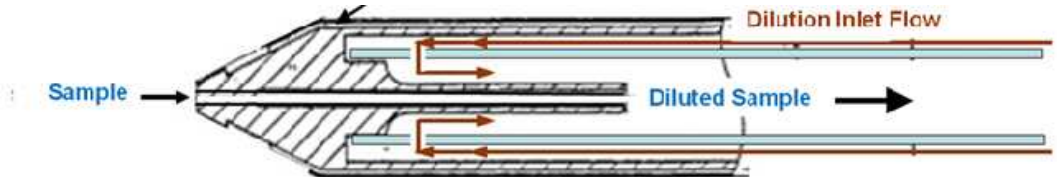

Figure 15 Diagram of HES probe tip, showing detail of dilution and sample flow.

Where bending or shaping of the sample lines was required the pipes were not subjected to bend radii smaller than 10 internal pipe diameters, thus adhering to the Aerospace Recommended Practice 1179 on aircraft gas turbine engine exhaust smoke measurement. The sample lines were temperature controlled by trace heating chords, such that the material temperature was controlled at required temperature on heated sections of smoke sampling lines (as discussed later). The pipe and heating chord were also lagged with a high-temperature mineral tubular insulation sheath. A schematic of the sample transport system is shown in Figure 16. The figure includes locations of: gas sampling probes, delta-P tappings (to provide flow measurement), diluters, flow splitters and gas analysis tappings.

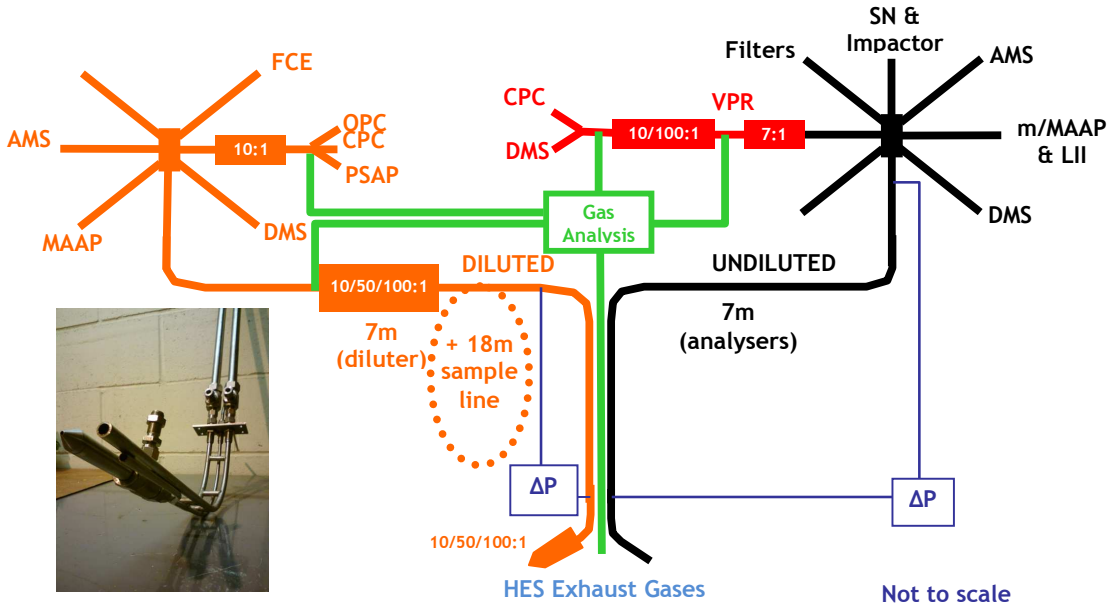

Figure 16 Sample transport system with photograph of diluted and undiluted gas sampling probes (inset).

The flow through the system was measured via 2 static pressure tappings in each sample line; these were located upstream of the sample distribution system. The tappings were used to measure the pressure difference over this distance, which was then used to calculate sample mass flow rate via a calibration test performed just before the tests. A coriolis flow meter was connected to the end of each line and the pressure differences between the tappings were calibrated over a range of flows and line temperatures using compressed air to simulate the sample flow. Sample flow rate was logged once per minute with the rig data.
The following dilution systems were used in the experiment:

- Tip dilution at the dilution probe, at dilution ratios of 10:1, 50:1 and 100:1.
- A bespoke non-ejector dilution system located 7m downstream of the probe tip, which was operated at nominal dilution ratios of 10:1, 50:1 and 100:1. Note tip dilution and 7m dilution were not operated simultaneously.
- A fixed 10:1 ejector dilutor (palas VKL-10) was positioned upstream providing a second stage of dilution necessary for the OPC, CPC, PSAP and MAAP apparatus.
- A fixed 7:1 hot diluent ejector at the upstream section of the VPR.
- An ejector system located at the downstream of the VPR, which was built using two 10:1 (palas VKL-10 & 10e) ejector dilutors which were designed to provide dilution ratios of either 10:1 or 100:1 to be studied. Note during experimentation dilution ratios of approximately 6:1 were witnessed at the primary palas VKL-10e dilutor resulting in overall VPR dilution ratios of 42:1 and 420:1.

The sample transport system was equipped with extension points whereby the line length could be altered. Hence the facility existed to increase the nominally 7m length lines to 25m in length.

This was used in order to assess the effect of line length and material on the sample and to evaluate the effects of 'bedding in' of sample lines (i.e. where PM is deposited on clean sample lines and the process of the PM depositing on the tube walls up to a point where the system reaches an equilibrium condition). The conditions evaluated in the undiluted, diluted and VPR sample lines are given in Table 5, Table 6 and Table 7 respectively.

Table 5 Conditions evaluated with the undiluted sample line.

Sample line temperature	60°C, 160°C, 350°C
Sample flow Reynolds Number	Laminar (<2000) Transition (approx 2800) Turbulent (>3000)
Sample line length from sampled gas to analyser inlets.	7m, 25m
Sample line external diameter and material	1/4 inch stainless steel 3/8 inch stainless steel 3/8 inch PTFE
Sample line 'bedding in'	7m, 25m

Table 6 Conditions evaluated with the diluted sample line.

Sample line temperature	60°C, 160°C, 350°C
Diluent temperature	Ambient (approx 20°C) Hot (>250°C)
Dilution ratio	10:1, 50:1, 100:1
Dilution location	At probe tip, 7m downstream, 25m downstream
Sample line diameter and material	3/8 inch stainless steel 3/8 inch PTFE

Table 7 Conditions evaluated with the Volatile Particle Remover.

VPR temperature	350°C
VPR residence time	0.5 sec, 1 sec, 2 sec.
VPR dilution ratio	40:1 to 400:1

Note that these parameters were typically tested in isolation in order to effectively de-couple the particular physical property under consideration. A complete evaluation of every possible physical property combination would have led to a prohibitively large number of permutations in the test programme.

5.4 Instrumentation used

Instrument reproducibility was successfully demonstrated for CPC and DMS 500 during SAMPLE I. Recent discussions in the SAE E31 sub-committee have highlighted that it would be desirable to measure the metrics of PM number and mass in future ARPs utilising an online 'real time' technique. Thus, it is perceived that the likely instruments are CPC for number and carbon

burn-off / MAAP / LII for mass. However, it may be necessary to derive the PM mass using an offline Carbon burn-off method. For SAMPLE II it was decided that other analysers would be included in the testing, measuring size and volatile matter, in order to broaden scientific knowledge on the transmission losses of PM. For the MAAP and LII this reproducibility was demonstrated in various inter-comparison studies, as demonstrated in SAMPLE I (EASA Study - Petzold and Marsh, 2009). The physical arrangement of the sampling apparatus is shown in Figure 17. The equipment used to measure the PM is listed in

Table **8**, with methodologies for measurement of PM shown in

Table **9**.

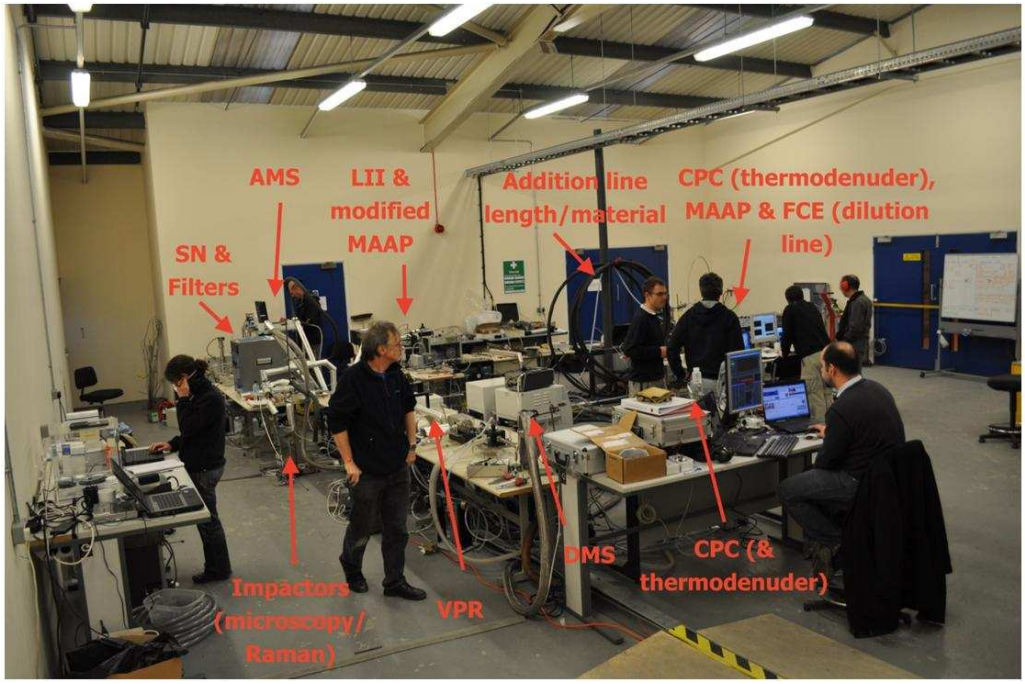

Figure 17 Photograph of sample analysis room detailing locations of key particulate analysers.

Table 8 Instruments used for measurement of PM in the study.

Equipment	Acronym	Measurements
Richard Oliver Smoke Meter	SN	Smoke Number
Aerosol Mass Spectrometer	AMS	Volatile PM
Differential Mobility Spectrometer	DMS	Size and number
Multi Angle Absorption Photometer	MAAP	Mass
Laser Induced Incandescence	LII	Size and number
Gravimetry*	GRAV	Mass
Optical Particle Counter	OPC	Number
Particle Soot Absorption Photometer	PSAP	
Condensation Particle Counter	CPC	Number
Thermo Gravimetric Analysis*	TGA	Volatile and non-volatile mass
Scanning Electron Microscopy*	SEM	Size
Faraday Cup Electrometer	FCE	Size
Micro-Raman Spectroscopy*	MRS	Graphitisation/chemical character

* indicates that the technique involves off-line analysis and that samples were captured during the trials for subsequent quantification.

5.5 Particle mass measurement

Non-volatile PM mass measurement methods can be divided into three general approaches:

- Gravimetric methods which measure total particulate mass (TM = OC + EC + inorganic compounds);
- Carbon-burn off methods which measure total carbon (TC = OC + EC) and elemental carbon (EC) particulate mass; and
- Optically-based methods which rely on light absorption by particles to measure the black carbon (BC) particulate mass, e.g., absorption photometry, laser-induced incandescence.

Table 9 Selected Methods for the Measurement of Particle Mass Concentrations in an Aircraft Engine Exhaust

Measurement Method	Measurement	Instrument / Reference
Smoke Number	smoke	ARP 1179 [*SAE*, 1997]
Gravimetric Analysis	total particulate mass (TMGRAV)	off line, filter samples
2-step combustion of filter samples	total carbon (TC) elemental carbon (EC)	off line, filter samples [*Schmid et al.*, 2001]
Thermo-Gravimetry (TG): Continuous combustion of filter samples	organic carbon (OC), elemental carbon (EC),	off line, filter samples [*Schmid et al.*, 2001]
Multi-Angle Absorption Photometry (MAAP)	Black carbon (BC), BC ≈ EC	THERMO ELECTRON Model 5012 MAAP * [*Petzold et al.*, 2005b]
Laser Induced Incandescence (LII)	Black carbon (BC)	Artium Technologies LII 300

* Note that 2 MAAP systems were used during the trial. One was a standard configuration, and one was a modified flow version.

Gravimetric Analysis

Time-averaging methods are used to sample the emitted particles on appropriate fibrous filters or membrane filters. Common practice is to use glass fibre, quartz fibre, or Teflon filters for exhaust particle sampling that show a filtration efficiency of >99% in the size range relevant for particulate matter emitted from gas turbines, i.e. for 10 nm < Dp < 500 nm. Applying gravimetry, the sampled particle matter is analyzed gravimetrically by weighing the filter before and after loading, which yields the total particle mass. The accumulated exhaust volume penetrating the filter is recorded for each sample in order to obtain a mass concentration measurement as defined in AIR6037 [*SAE*, 2009].

2-Step Combustion

Pre-conditioned quartz fibre filters are used for sampling exhaust particle matter. Particle-laden filters are analysed for the carbon content in a two-step combustion process. During the two-step combustion process the organic carbon is oxidized for 42 min at 340 °C in a pure oxygen atmosphere. The remaining carbon, defined as elemental carbon, is then determined at 650 °C (32 min) by a total organic carbon analyzer based on non-dispersive IR absorption of the evolving CO_2 [*Schmid et al.*, 2001].

Thermo-Gravimetry

Pre-conditioned quartz fibre filters are used for sampling exhaust particle matter. Particle-laden filters are analysed for the carbon content in a continuous combustion process. In an oxygen atmosphere, the sample is heated from room temperature to 1000°C using a gradient of 20K/min. The evolving CO_2 is detected by non-dispersive infrared absorption. Simultaneous to the heating of the filter, a laser beam is directed through the filter sample and records the change in filter transmission. The transmission of a clean particle-free filter is 1.0; increasing aerosol loading reduces filter transmission towards 0.0. Elemental carbon oxidation is assumed to start as soon as

the filter transmission increases from its initially very low value according to the black particle-laden filter [*Schmid et al.*, 2001].

Multi-Angle Absorption Photometry (MAAP)

Aerosol absorption photometry analyzes the modification of filter optical properties as transmittance or reflectance caused by the particles deposited on a filter matrix. Optical absorption methods are highly suitable for the measurement of combustion particles because the key component black carbon is a very efficient absorber of light in the visible spectral range. Since any particulate matter contains also a fraction of non-absorbing, i.e. light-scattering aerosol components, absorption photometry cannot be used for the measurement of total particle mass. The THERMO Model 5012 MAAP uses a multi angle absorption photometer approach to analyze the modification of radiation fields in the forward and back hemispheres of a glass-fibre filter caused by deposited particles. The MAAP data inversion algorithm is based on a radiation transfer method and compensates for the cross-sensitivity of aerosol absorption photometry to light-scattering aerosol components (Figure 18). [*Petzold and Schönlinner*, 2004; *Petzold et al.*, 2005b]. In the original set-up the MAAP instruments draws minimum 8 lpm through the instrument. At high BC mass loadings this high flow rate causes a high deposition of BC mass per unit time on the filter sample spot which requires frequent changes of the filter spot because the instruments allows for a minimum transmission of 20% which may be reached within less than 10 minutes at such high flow rates.

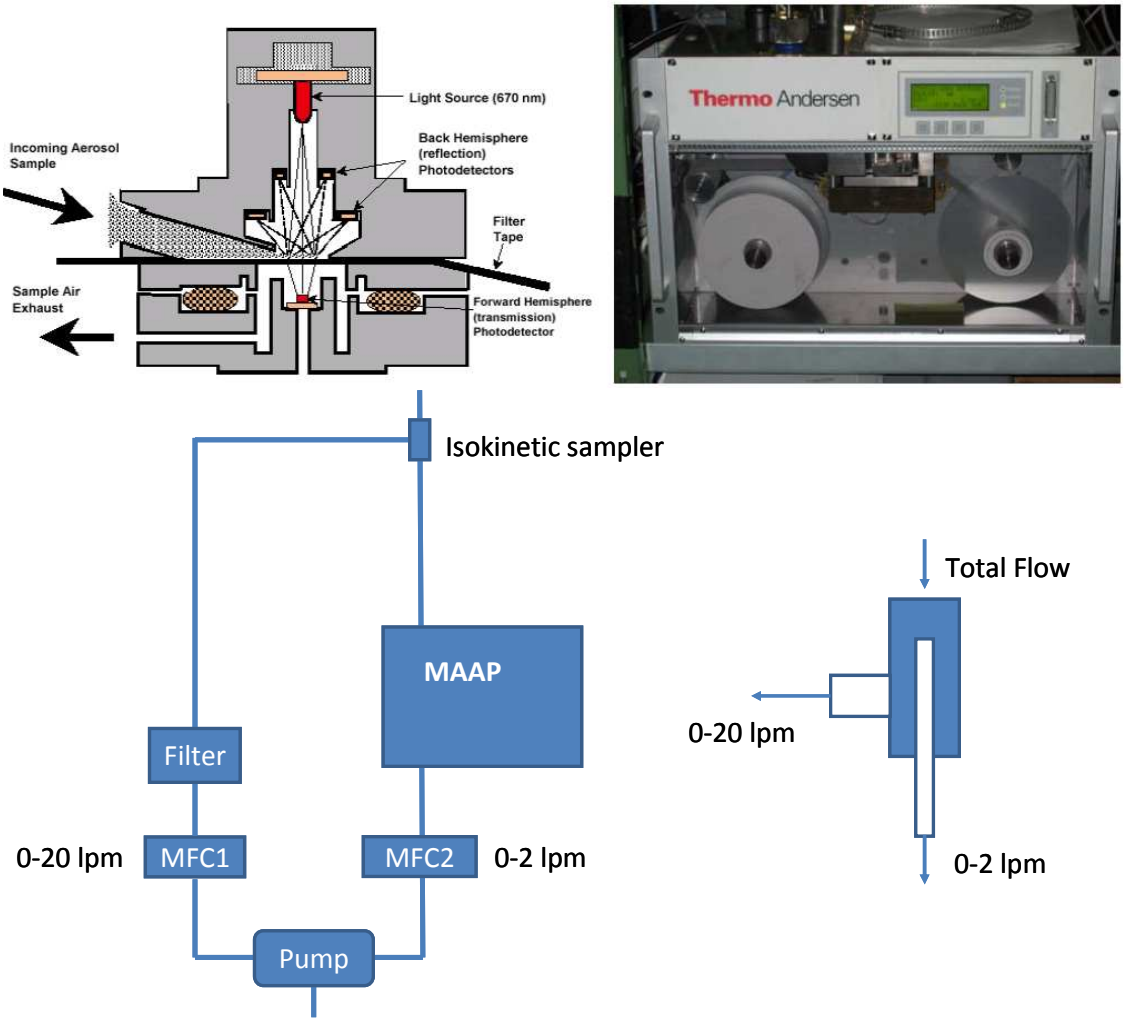

Figure 18 **Top:** Diagram and photograph of the MAAP instrument. **Bottom**: flow scheme and isokinetic sampler deployed by DLR.

In order to circumvent these frequent changes of the sample spot DLR has modified the flow scheme as shown in Figure 18, bottom. In the new configuration a variable flow is drawn through the filter spot which can be as low as 0.4 lpm, depending on the BC mass concentration. Mass flow controller 2 sets the flow through the instrument while mass flow controller 1 sets the bypass flow such that the entire flow into the system is kept at a constant level. For the flow split an isokinetic design was chosen.

The principal measure of any absorption photometer is the aerosol absorption coefficient σ_{ap}, given in units of 1/m. The conversion of an absorption coefficient measurement into a black carbon mass measurement requires the assumption on a mass-specific absorption cross-section

for black carbon, B_{BC}. For the MAAP the value B_{BC} = 6.6 m²/g was determined from calibration studies for the operation wavelength λ = 630 nm [*Petzold and Schönlinner*, 2004].
Using these values, the BC mass concentration is given as

$$BC = \frac{\sigma_{ap}}{B_{BC}}$$

Laser Induced Incandescence

Laser-induced incandescence (LII) is performed by measuring the thermal emission (incandescent light) emitted from particles heated by a pulsed laser to temperatures in the 2500 K to 4500 K range [*Snelling et al.*, 2005]. LII is highly selective, responding only to the presence of black carbon, making it decidedly appropriate for measuring the non-volatile particles produced as a combustion emission. This selectivity is due to the fact that the non-volatile particles are primarily black carbon. BC absorbs laser radiation over a broad spectral range, and is refractory, so that the nanoparticles survive heating to the temperatures necessary for the incandescence to be detected. At these temperatures, all volatile components that may have been condensed on the BC particles will be promptly evaporated, and most other non-carbonaceous particles will have also evaporated or undergone sublimation. Due to this selectivity, LII cannot be used for the measurement of total particle mass. Analysis of the LII signals results in the determination of the mass concentration, volume concentration, active surface area, and primary particle diameter of the particle emissions. A schematic of the LII process is shown in Figure 19.

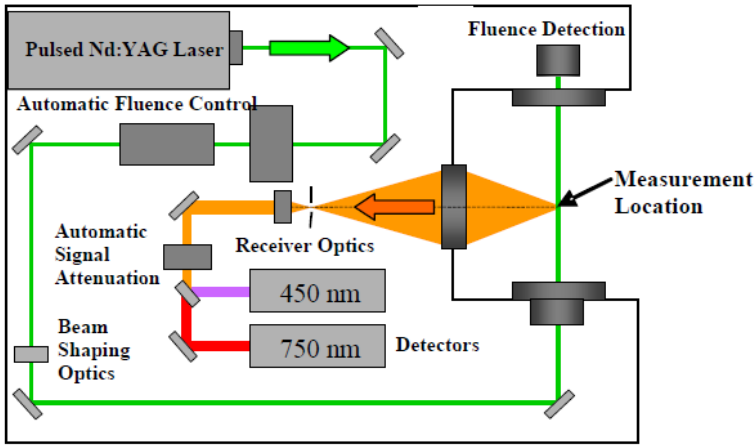

Figure 19 Diagram of the LII instrument

Mass Fractionation – Organic Matter

The total particulate mass (TM) emitted from a gas turbine is composed of organic carbon (OC), inorganic or elemental carbon (EC) and of inorganic species like sulphate (S). The distribution between organic carbon and elemental carbon depends on the operating conditions of the engine [*Petzold and Schröder*, 1998]. Since organic matter is composed of organic carbon with minor contributions of oxygen and hydrogen, the ratio of organic matter to organic carbon is calculated from the ratio of oxygen to carbon by [*Aiken et al.*, 2008]

$$\frac{OM}{OC} = 1.26 \times \frac{O}{C} + 1.18$$

For fuels with an O to C ratio of less than 1.0 weight-%, this relationship can be rewritten as

$$OM \cong 1.20 \times OC$$

Mass Fractionation – Particulate Sulphate

According to the First Order Approximation (FOA) Version 3 [*CAEP*, 2008], ε = 2.4 wt-% of the fuel sulphur is converted into particulate sulphate. This result is in agreement with PARTEMIS results [*Petzold et al.*, 2005a]. Knowing the sulphur content of the fuel was 0.030 wt%, the sulphate emission index (in g / kg) is estimated as

$$EI_{SO4-FOA3} = 10^3 \left[\frac{FSC \times \varepsilon \times MW_{SO4}}{MW_S} \right]$$

with molecular weights *MWSO4* = 96 g per mole and MW S = 32 g per mole. This approach assumes that all gaseous sulphuric acid is converted into particulate sulphate. From the comparison of non-volatile matter emission indices calculated by means of FOA 3 and elemental carbon values obtained during SAMPLE I it was shown that EI_{nonvol} - FOA ≈ EIEC. At conditions typical for gravimetric measurements (RH = 40%, T = 25°C), sulphate exists in its hydrated form as (H2SO4•6.5H2O) [*Agrawal et al.*, 2008]. Combining these findings and using the equivalence of FOA non-volatile matter emission index EInonvol-FOA3 and elemental carbon emission index EIEC the hydrated sulphate contribution to total aerosol mass is estimated as

$$SO4 \bullet 6.5H2O = \frac{EI_{SO4-FOA3}}{EI_{nonvol-FOA3}} \times EC \times \left[1 + \frac{6.5\, M_{H2O}}{M_{H2SO4}} \right]$$

Mass Fractionation – Total Particulate Matter

Total particulate matter is calculated from the sum of the single components as

$$TM_{SUM} = OM + EC + SO4 \bullet 6.5\, H2O$$

Mass Fractionation – Black Carbon

The light absorbing material, termed black carbon (BC), is strongly correlated to the EC fraction of the aerosol. Light absorption by combustion particles is therefore closely linked to the key traceable compound of the non-volatile fraction of the gas turbine exhaust aerosol, i.e.

$$BC \cong EC$$

Aerosol Mass Spectrometer

The instrument, shown schematically in
Figure 20, is composed of three main sections: (1) an aerosol sampling chamber, (2) a particle sizing chamber and (3) a particle composition detection chamber. Each chamber is separated by critical apertures and is differentially pumped. The AMS samples particles into high vacuum through an "aerodynamic lens" that contracts and expands the sampled air stream through a series of orifices. The particles have sufficient momentum to leave the streamlines and exit the "lens" in a well-defined beam. The particle beam is directed onto a resistively heated source and the aerosols are vaporised, then ionised by an electron impact ioniser and molecular fragments measured using a quadrupole mass spectrometer. The size of the particles is measured by synchronizing the molecular ions signals from the mass spectrometer with a chopper wheel positioned immediately behind the aerodynamic lens, approximately 50 cm in front of the heated

source. The size of the particles can be calculated from the delay time between the chopper wheel allowing a slug of air containing particles to enter the instrument and detection at the heater.

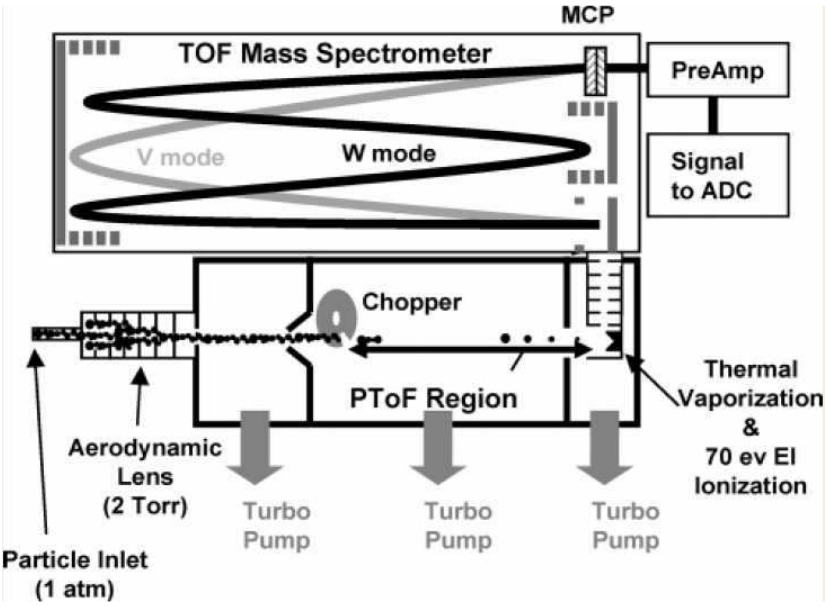

Figure 20 Aerosol Mass Spectrometer for size and composition analysis of submicron aerosol. Aerosols are sampled at ambient pressure by a unique aerodynamic lens. Aerodynamic particle size is determined from a time-of-flight (TOF) measurement. Size resolved particle composition is obtained by positive ion quadrupole mass spectrometry (QMS) following flash thermal particle vaporization.

5.6 Particle number measurement

Condensation Particle Counter

The operating principle of the saturator-condenser type CPC is depicted in Figure 21. Details of the CPC method are given in Appendix B of AIR 6037 [*SAE*, 2009]. With respect to the saturator, particle laden sample air is continuously passed through a tube where a liquid (the so-called working fluid) evaporates into the air until the air is almost saturated with vapour. Upon entering the condenser, the sample air becomes supersaturated by cooling or heating (depending on the working fluid) the walls of the tube, and this leads to condensation of vapour onto the particles to form droplets which grow to sizes suitable for optical detection. The minimum size of particles which are detectable by this method depends on the supersaturation realized in a single instrument according to the Kelvin equation [*Baron and Willeke*, 2001; *Hinds*, 1999]

$$\ln S^* = \frac{4\,\sigma_{liquid}\,M_{liquid}}{RT\rho_{liquid}\,D_p^*} \quad ; \quad S^* \geq 1 \quad ; \quad D_p^* \propto \frac{1}{\ln S^*}$$

S^* – critical supersaturation
M_{liquid} – liquid molar mass
σ_{liquid} – liquid surface tension
ρ_{liquid} – liquid density
D_p^* – minimum particle diameter for activation at S^*

After the sample flow has left the condenser the droplets are passed through an illuminated region and the light scattered by the droplets is detected with a photodetector, which converts the scatted light into an electrical pulse that is electronically recorded as a particle count. The flow rate through the CPC is controlled by the flow control system typically consisting of a pump combined with a critical orifice or a flow controller.

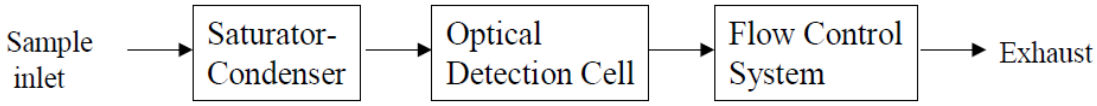

Figure 21 Schematic of a saturator-condenser type CPC [SAE, 2009]

Optical Particle Counter

The operating principle of any single-particle optical particle counter (OPC) is based on the concept that the intensity of scattered light is proportional to the particle size and can be predicted theoretically if the shape and refractive index of a particle is known as well as the wavelength of the incident light. Light scattering is the result of the interaction of the electromagnetic wave of incident light with the molecular structure of a particle that subsequently produces electromagnetic emissions with components of reflection, refraction and diffraction. The composite of these three components is a field of scattered light whose intensity varies as a function of angle with respect to the incident light. If the particle is spherical and of homogeneous composition, the scattered intensity is symmetric around the axis parallel with the incident wave but varies in intensity from 0 to 180º, where 0º is the most forward scattering and

180° is directly backward. This angular dependency of the scattering around a spherical particle can be calculated using the equations that were developed by for a specific diameter, refractive index and incident wavelength. The OPC of type GRIMM Model 1.129 applied in this campaign is capable of measuring particle sizes from 250 nm to approx. 32 µm in diameter. In this campaign, the OPC was mainly be used as a detector for large soot agglomerates which were not emitted from the HES but have formed in the sampling line. The OPC method is not applicable to size distribution measurements in fresh aircraft engine exhaust (typical particle diameter < 150 nm) due to its limited size resolution at the lower end of the scale.

5.7 Particle size measurement

Electrical mobility analysis is a well-established technique for sizing aerosol in the sub-micrometer size range. This method exposes charged aerosol particles to an electrostatic force resulting in a particle migration speed (proportional to electrical mobility *Z*), which depends among other parameters on particle size [*Baron and Willeke*, 2001; *Hinds*, 1999]. Hence, electrical mobility can be used for particle sizing. The electrical mobility of a charged particle, *Z*, is linked to particle size via the relationship

$$Z = \frac{n\, e\, C_C(D_m)}{3\,\pi\,\eta_g\, D_m}$$

ne – charge of particle
C_c – slip correction factor
η_g – viscosity of carrier gas
D_m – particle mobility diameter

For spherical particles, the electrical mobility diameter *Dm* is identical to the geometric diameter *Dg* (as measured by electron microscopy). The operation principle of mobility sizing methods is shown in
Figure 22. The Differential Mobility Spectrometer DMS 500, Differential Mobility Analysers DMA/DMPS and the Engine Exhaust Particle Sizer (EEPS) are based on this method. As an example, the DMS is described with more detail.

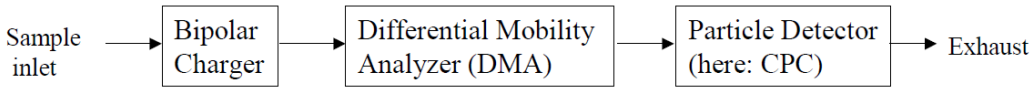

Figure 22 Schematic of a DMA coupled with CPC-based detector [SAE, 2009]

Differential Mobility Spectrometer

The DMS500 uses a classifier column (Figure 23) operating at sub-atmospheric pressure. Sample flow is drawn into the instrument through a conductive rubber sample tube. The DMS uses a cyclone that prevents particles larger than 1µm entering the sampling tube and the instrument. To measure the particles in the 5–1000 nm diameter range, steel restrictors with holes of 1.00 mm were placed upstream of the cyclones to maintain a flow rate of 8 standard litres/min (SLPM) and a pressure of 0.25 bar (the same as the instrument's classification column) inside the

sampling tube. This reduced pressure discourages particle agglomeration by reducing residency times [*Symonds et al.*, 2007] and helps isolate the instrument from fluctuating sample pressure. The sample gas passes through a corona discharge charger into the classifier column.
The charged particles flow within a particle-free sheath flow which is a uniform, cylindrical laminar column of air designed to carry the charged particles in a predictable manner. The particles are then deflected towards grounded electrometer rings by their repulsion from a central high voltage rod. Their landing position is a function of their charge and their aerodynamic drag. The particles yield their charge to the electrometer amplifiers and the resulting currents are translated by the instrument's user-interface into particle number and size data. Using a 5 m sample line, a 300 ms response can be achieved.

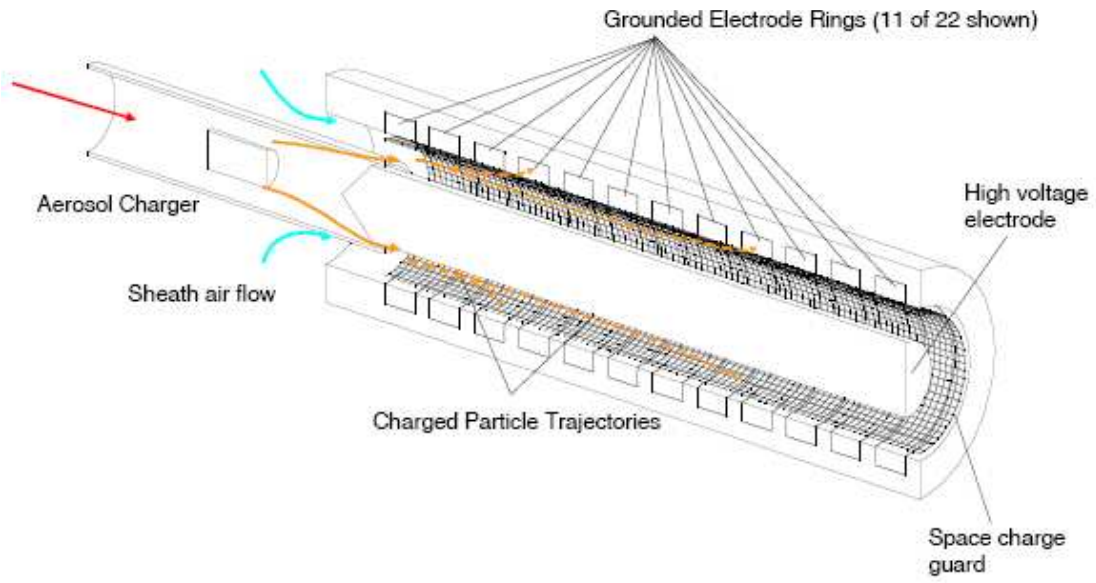

Figure 23 Diagram of the Differential Mobility Spectrometer classifier column.

The use of PTFE tubing allows sampling temperatures as high as 200 ºC. It requires an external supply of clean, dry compressed air at 3 bar gauge, for primary dilution of compressed air, up to 4:1 ratio. A precipitator inside the instrument removes charged particles below approx. 30nm in diameter. The charger consists of a corona discharge wire suspended along the major axis of a perforated cylinder. The corona discharge produces a large number of positive ions. These ions collide with and charge the incoming particles.
The classifier separates the charged particles according to their electrical mobility. Although the classifier is operated at reduced pressure the aerodynamic drag of the particles is significant, it classifies by charge to drag ratio, or by electrical mobility i.e. using the diameter of a spherical particle with the same charge to drag ratio as the particle being measured. The main advantage of the DMS is the real-time (up to 10Hz) sampling capability allowing immediate analysis of the data, which is of prime concern as expensive rig running may be reduced if erroneous data points are observed early in the test.

5.8 Micro-Raman Spectroscopy

The Micro-Raman spectrometer is designed to apply Raman spectroscopy to microscopic areas and samples. It is a purpose built instrument that integrates an optical microscope (along with a digital imaging system) to a Raman spectrometer. The principal of operation (shown in Figure 24) is as follows: The sample is illuminated through the objective of the microscope with a laser, the objective of the microscope also collects the Raman scattered light from the sample. The collected light is then focused to form an image on the entrance aperture of the Raman spectrometer. The beam of light collected from the sample enters the device and is separated into its Stokes shifted frequencies by a diffraction grating. The separated light is focused onto a Charge Coupled Device (CCD) array detector where the intensity of each frequency is measured by an individual pixel on the array. The output of the CCD is then processed to produce a spectrum which displays the intensity of the in-elastically scattered light relative to the wavelength of the exciting laser.

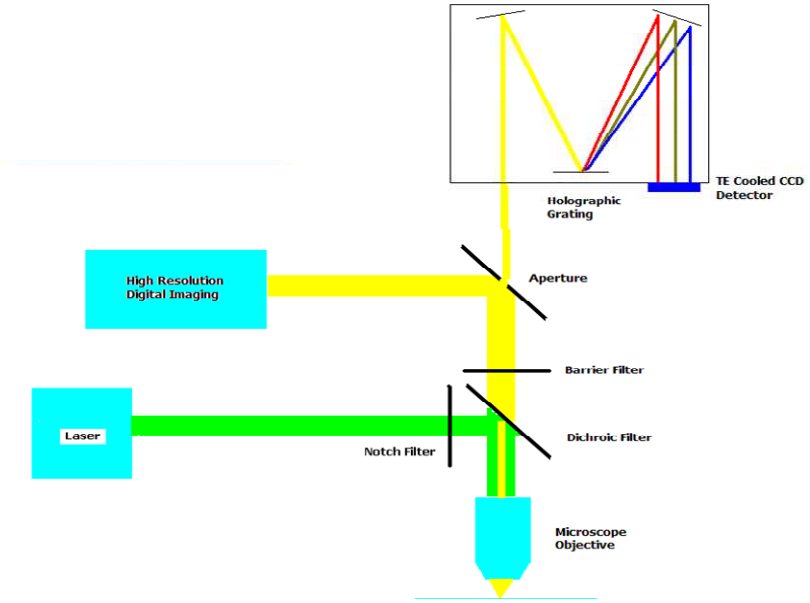

Figure 24 Schematic diagram of Micro-Raman spectrometer setup

Micro-Raman spectroscopy is a highly sensitive technique and can be used to identify different molecules and functional groups within larger molecules since the bonds formed between atoms have specific vibrational frequencies (dependent on atomic masses and bond strengths). In this work, Micro-Raman spectroscopy is used to determine the level of graphitisation in the non-volatile particulate matter for each of the sampling condition. This measurement will indicate the chemical character of the particles and highlight any chemical changes that may occur for different sampling conditions.

Samples for Micro-Raman analysis are collected via impaction on to the surface of a Scanning Electron Microscope SEM sampling stub. Analysis is done ‘off-line’ were samples captured during the trials are subsequently processed and quantified. It should be noted that impaction is a collection technique that is biased towards the sampling of larger particles. Small particles are able to better follow the streamlines in the flow because of their lower momentum, and so are

less likely to impact upon the surface. Consequently the number of ultra fine particles that are collected on the stub is reduced, and the sample is not a strictly accurate representation of the particle distribution in the flow.

5.9 Volatile Particle Remover

To remove the volatile particle component of the exhaust stream a volatile particle remover was constructed using the sequential hot dilution/evaporation tube/cold dilution apparatus shown in Figure 25. The setup conforms to current PMP UNECE VPR specifications and was similar to that utilised within SAMPLE I.

SAMPLE I analysis showed that between 10 and 15% of the number of particles exiting the VPR were volatile – the VPR was not efficient enough. In order to understand why this result had occurred, in SAMPLE II the VPR was designed in such a way that the residence time in the hot (350°C) evaporation chamber (1.5m x 3/4" OD) could be varied (0.5 and 4s) by adjusting the flow valve upstream of the coriolis mass meter/pump. Also the cold downstream dilution ratio could be switched between a low (nominally 10:1) and high (nominally 100:1) dilution ratio. When the SAMPLE II experiment of changing sample line temperature is also included, a third variable (VPR inlet sample temperature) was also added. A DMS and a CPC were placed after the VPR to analyse the size distribution and total particle number concentration. Prior to the inlet of the CPC a thermal discriminator was placed (a simple tube heated to 300°C as used in SAMPLE I) such that the sample could be diverted through it to analyse the volatile removal efficiency. The VPR sample inlet was located on the splitter off-take 7m downstream of the probe tip. Unfortunately due to technical difficulties the originally planned CPC could not be used and instead a CPC was used which was not capable of measuring number concentrations higher than 105 number/cm3 (TSI 3025A). Thus the CPC was incapable of measuring the number concentrations when the secondary diluter was set to 10:1. Therefore CPC data is only available for the 100:1 case. A second DMS was connected to the undiluted sample line at the 7m splitter allowing comparisons of size distribution data to be made, up and downstream of the VPR.

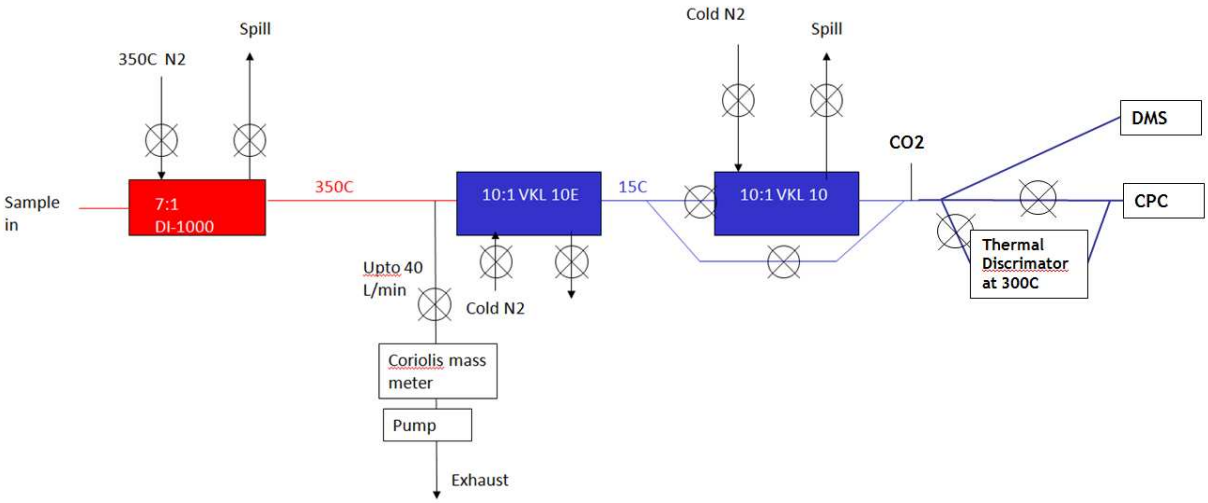

Figure 25 Volatile Particle Remover Setup

6. Experimental Results - GTRC Hot End Simulator trials

6.1 Undiluted sample line

6.1.1 Rig condition

The rig conditions studied are illustrated in the HES experimental approach. In total 3 conditions were examined, including nominal particulates and organic carbon loading (LS/HO), Low particulates and low organic carbon loading (LS/LO) and High particulates and low organic carbon loading (HS/LO). In all 3 cases a standard sampling system configuration was used, i.e. 7m 3/8" stainless steel pipe heated to 160°C as shown in Figure 16.
Figure 26 shows the variation in smoke number measured according to ARP 1179C (SAE smoke number) over the 3 HES rig conditions tested. During this series of tests, the original composition of the sample is subject to change, since HES conditions such as inlet air temperature, inlet air pressure, air mass flow, fuel mass flow and inlet air dew point can marginally vary thus affecting the resulting PM. This change is often not observed in the corresponding gas analysis data. Hence, during this test, the sampling system conditions have been maintained constant. The data in Figure 26 shows that the supposed lowest condition of PM (LS/HO) produced a smoke number of 4.1 with the LS/LO providing a smoke number of 13.9 and HS/LO providing a smoke number of 18.3. The smoke number method appears to correlate well with the rig performance, since the target conditions in Table 4 are well met.

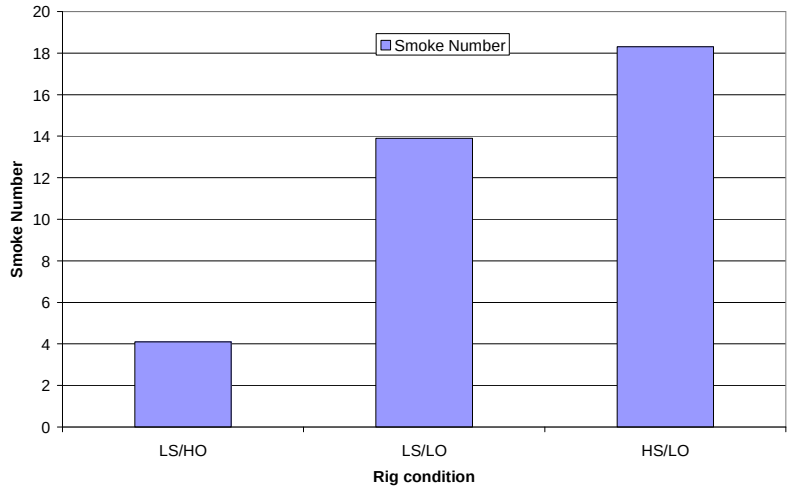

Figure 26 Effect of HES rig condition on undiluted SAE smoke number of exhaust gas.

Figure 27 shows the MAAP and LII data for the 3 different rig conditions tested during the HES trials. Both instruments clearly show an increase in PM as the rig condition is increased from low smoke / high organic, to low smoke / low organic and high smoke / high organic.

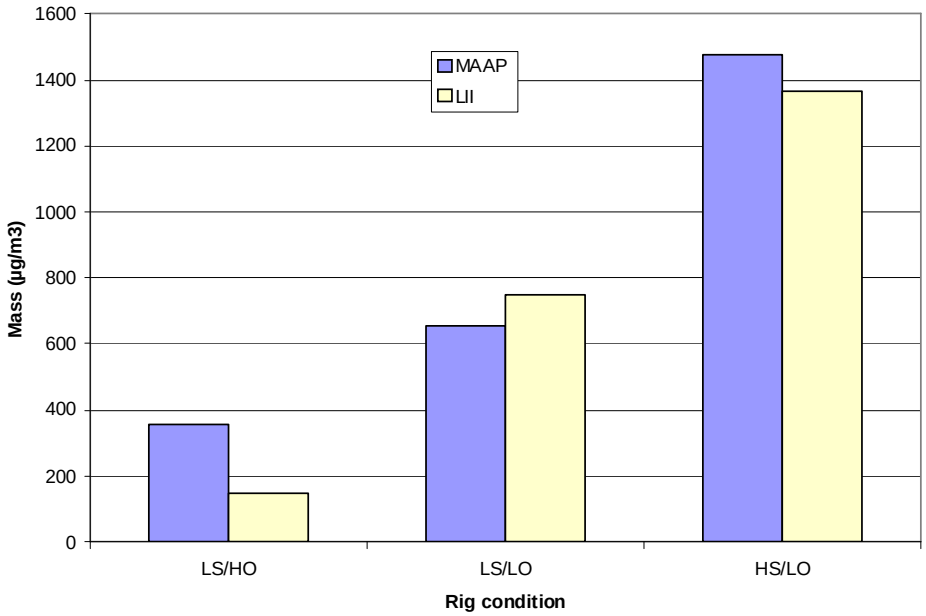

Figure 27 Effect of HES rig condition on undiluted PM mass loading of exhaust gas.

Figure 28 shows the various HES rig conditions with respect to total PM number (accumulation and nucleation), as measured by the DMS instrument. The data suggests that the largest number of particles were generated during the LS/LO condition, despite this condition generating the middle quantity of mass. This could suggest a shift in the nature of the PM over the 3 conditions. Further to this, Figure 29 shows the size distribution of the PM over the 3 conditions tested. It is clear that the shapes of the PM size profiles corroborate with all of the data presented in this sub-section regarding the HES condition inasmuch as during conditions where large amounts of organic carbon are produced by the rig, greater quantities of small particles are detected by the DMS. This is evidenced by the large nucleation peak in the LS/HO conditions, which suggests that the nucleation peak is partly formed by condensed organic particles, the large agglomeration peak in the HS/LO condition and the comparatively equal peaks in the LS/LO condition.

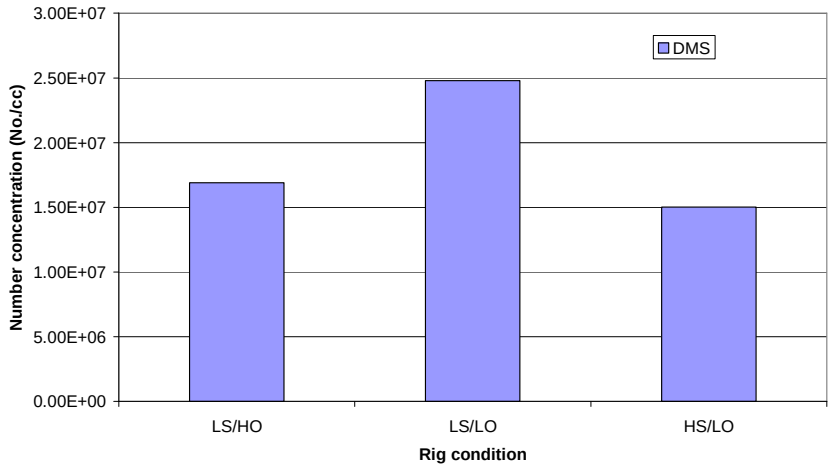

Figure 28 Effect of HES rig condition on total undiluted PM number loading of exhaust gas.

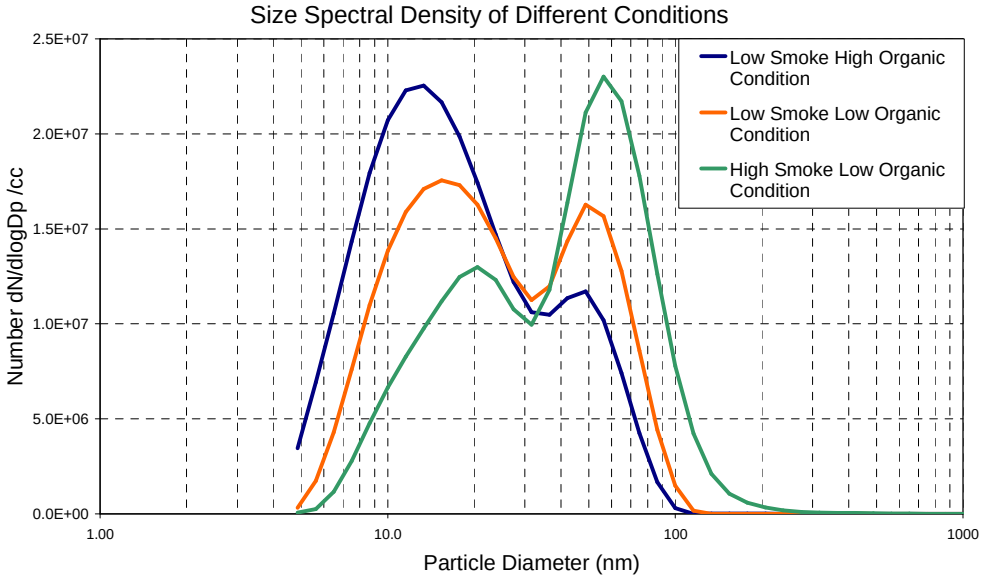

Figure 29 Size distribution of HES rig condition on undiluted PM number loading of exhaust gas.

Figure 30 shows the effect of rig conditions on the organic and SO_4 products. There is a strong correlation with the LII data. In all cases the data implies that higher smoke number conditions produce larger quantities of organics and SO_4. These are considered as symptomatic of higher fuel mass flow rates providing greater throughputs of sulphur and an increased tendency for intermediate products of combustion.

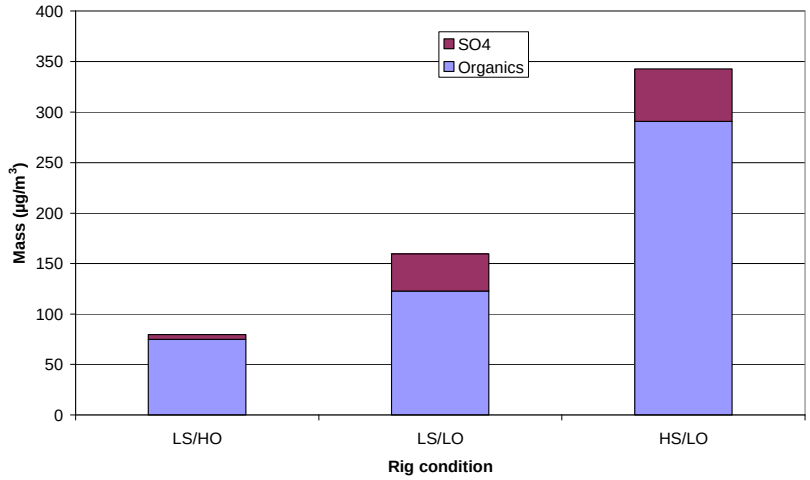

Figure 30 Effect of HES rig condition on undiluted PM organics and SO_4 mass loading of exhaust gas for AMS instrument.

6.1.2 Sample line temperature

The following measurements were conducted at the LS/HO condition and thus any variations on the nature of the PM sample should be attributed to the sampling system, rather than changes in the HES rig condition.

The sample line temperatures studied in all cases were 60°C, 160°C and 320°C with the sampling system in its standard configuration. Figure 31 shows the different values of SAE smoke number for the 3 line temperatures investigated during the tests.

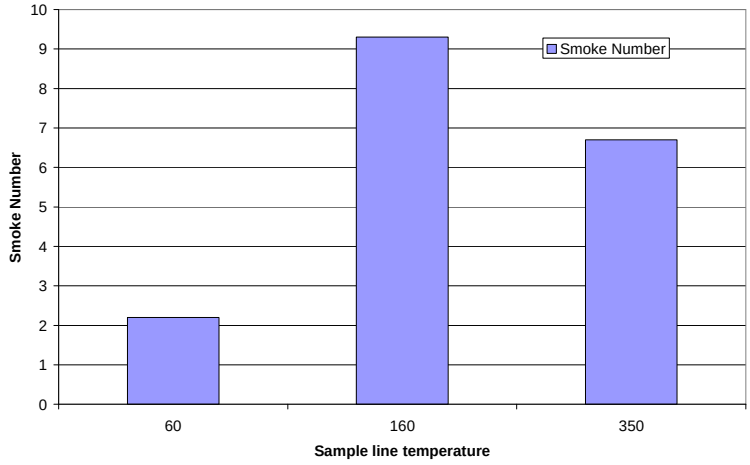

Figure 31 Effect of undiluted sample line temperature on PM mass loading of exhaust gas on SAE smoke number.

It is interesting to note that the changes in SN (and hence losses in the sampling system) are not straightforward. It is possible that low sample line temperatures increase PM losses, since

volatile matter is more likely to condense on the sample lines. Note that the error in measurement of SN is ±3.

Figure 32 shows the effect of sample line temperature on the LII and MAAP instruments. Results show that there is an acceptable level of agreement between the instruments at the 60°C and 160°C line temperatures, but there is a slight difference between them at 350°C. The data indicates that PM mass losses are slightly reduced as the sample line temperature is increased.

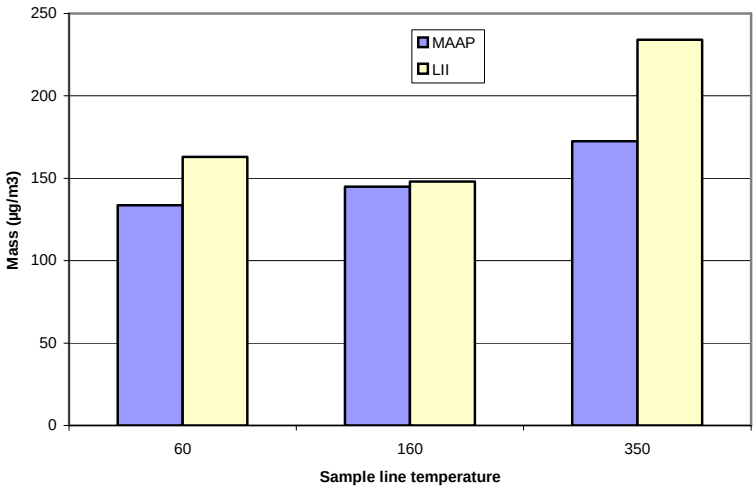

Figure 32 Effect of undiluted sample line temperature on PM mass loading of exhaust gas for LII and MAAP instruments.

Figure 33 shows the effect of sample line temperature on total number concentration as measured by DMS. The data shows that there is clearly more loss (in terms of particle number) at lower temperatures. It should be borne in mind that the number concentration was sensitive to HES rig fluctuations, and the data presented in Figure 33 was selected based on the results witnessed for the 3 different line temperature conditions at comparable Reynolds number.

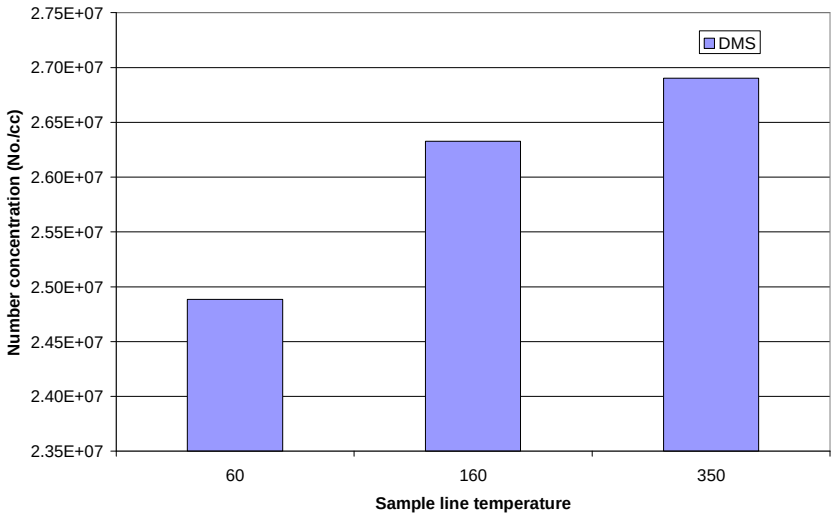

Figure 33 Effect of undiluted sample line temperature on PM number loading of exhaust gas

Figure 34 shows the effect of sample line temperature on the organic material detected in the gas sample. Whilst there appears to be little difference between the conditions at 60°C and 160°C, there is an increased amount of organic matter at 350°C. This is potentially due to the higher line temperatures causing volatilisation of the organic carbon in the sample, whereas below 350°C the organic carbon was retained by the sample lines. The detected quantity of SO_4 showed a decreasing trend with increasing sample line temperature.

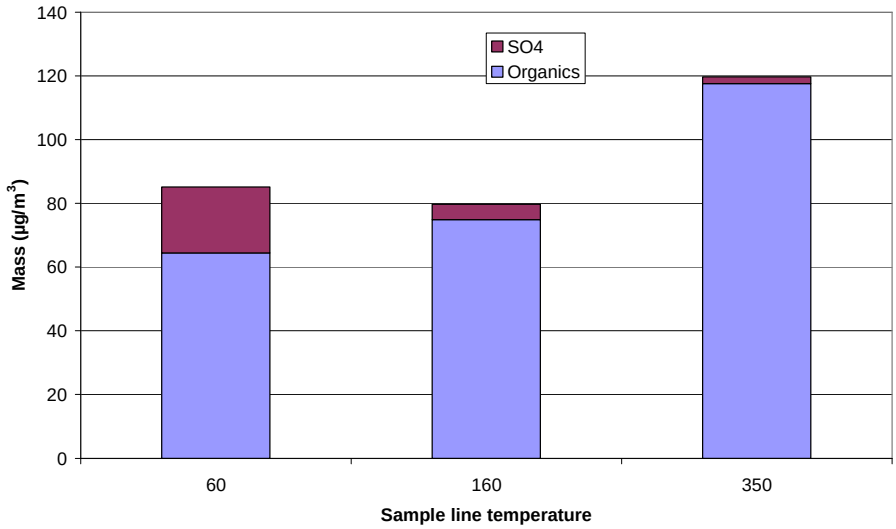

Figure 34 Effect of undiluted sample line temperature on PM organics and SO_4 mass loading of exhaust gas for AMS instrument.

6.1.3 Sample flow regime

The following measurements were conducted at the LS/HO condition and thus any variations on the nature of the PM sample should be attributed to the sampling system, rather than changes in the HES rig condition. This was conducted at the baseline condition of 160°C, 3/8 SS line 7m.
Figure 35 shows the effect of the sample flow regime on the LII and MAAP instruments. The three conditions studied were laminar, transition and turbulent flow. The data show that the flow condition will have an effect on PM losses in the sampling system, although this result does not identify the specific cause of this loss. There is a small discrepancy in the turbulent case, which was attributed to HES rig fluctuations.

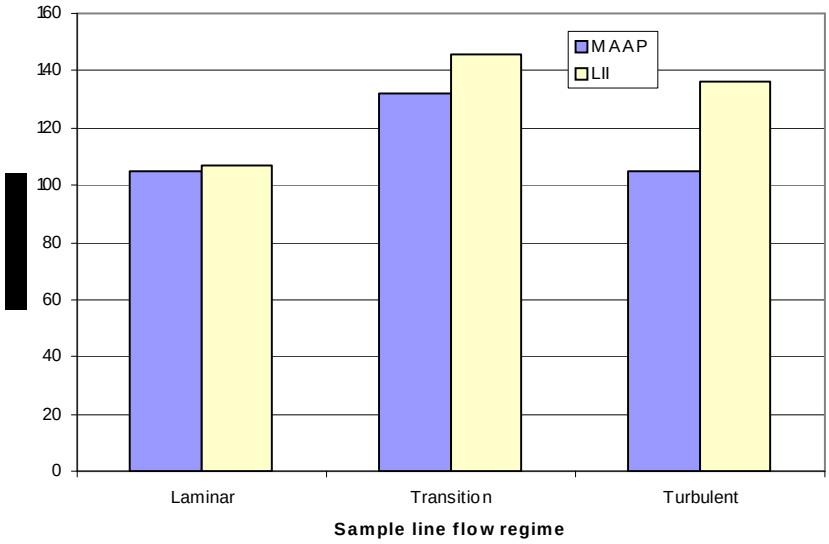

Figure 35 Effect of undiluted sample line flow regime on PM mass loading of exhaust gas for LII and MAAP instruments.

Figure 36 shows the effect of sample flow regime on the DMS instrument. There is a correlation between this result in terms of number and the MAAP mass data provided in Figure 35, thus implying that lowest PM losses are witnessed in the transitional regime.

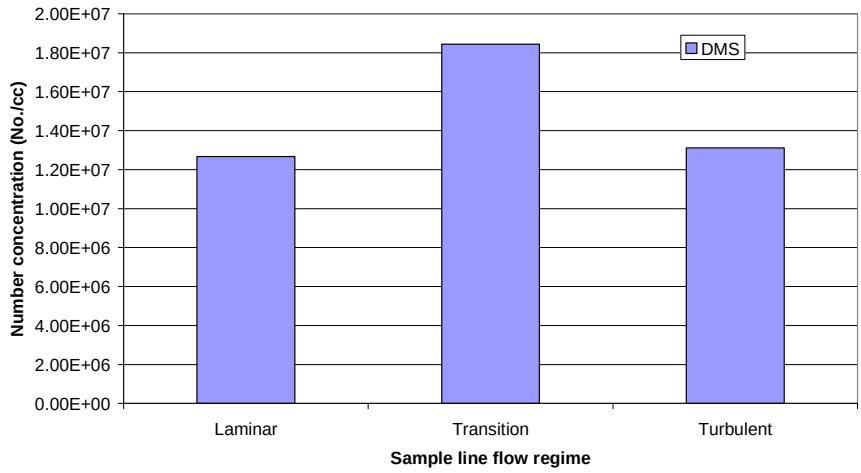

Figure 36 Effect of undiluted sample line flow regime on PM number loading of exhaust gas for DMS instrument.

Figure 37 shows the effect of flow regime on the quantities of organics and SO_4 in the gas sample. There is a clear trend between the flow regime (i.e. Reynolds number) and concentration of these species, with the higher levels of organics being witnessed at higher Reynolds numbers.

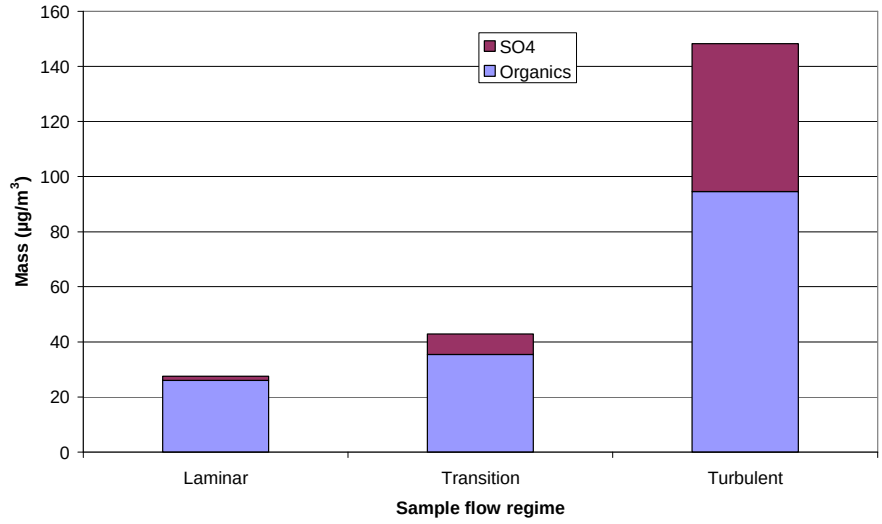

Figure 37 Effect of undiluted sample line flow regime on PM organics and SO_4 mass loading of exhaust gas for AMS instrument.

Figure 38 shows the effect of exhaust sample flow regime on the SAE smoke number. Data for the transition regime is not included as the corresponding measurement was deemed unreliable as there was insufficient time to conduct repeatable experiments. The SN results appear to show no major differences in the flow regimes, given the error of ±3 in the measurement technique.

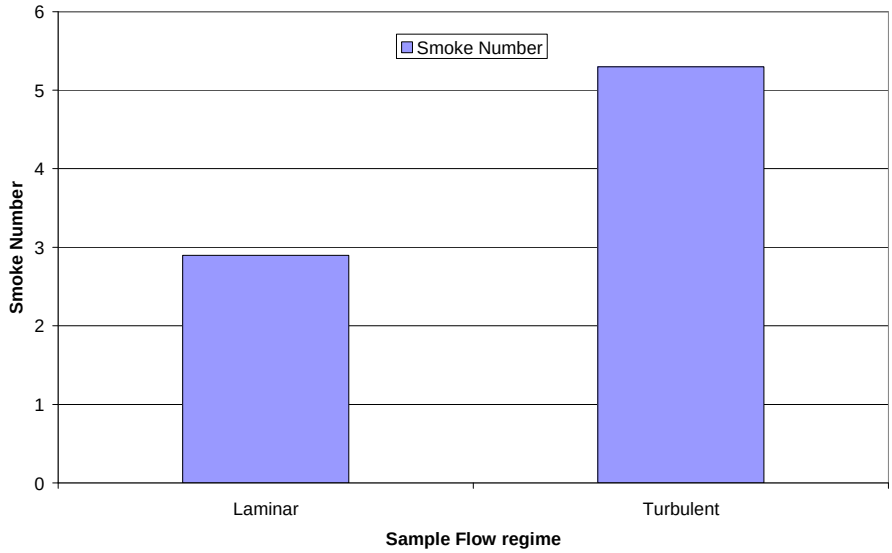

Figure 38 Effect of undiluted sample line flow regime on SAE smoke number.

6.1.4 Sample line length, diameter and material

The following measurements were conducted at the LS/HO condition and thus any variations on the nature of the PM sample should be attributed to the sampling system, rather than changes in the HES rig condition. This was conducted at the baseline condition of 160C, Reynolds number <2000 (Laminar).

Figure 39 shows the effect of the sample line length and diameter on the LII and MAAP instruments. Clearly the data demonstrates that sample line length, diameter and material have an effect on the losses of PM. When extending the sample line from 7m to 25, a small loss in PM mass is shown, although this appears to be minor in comparison to effect of line material (PTFE v SS) and line diameter (3/8” v 1/4”). The use of PTFE material in the sample line appears to increase the PM losses, since the system is dimensionally identical to that of the 3/8” stainless steel case. The use of the 1/4” tube also has a significant effect on the PM losses, although it should be borne in mind that smaller tube diameter will give a higher wall surface area to sample volume ratio, increase the volumetric flow rate of the gas and increase the Reynolds number of the flow in order to maintain a constant mass flow rate in the system.

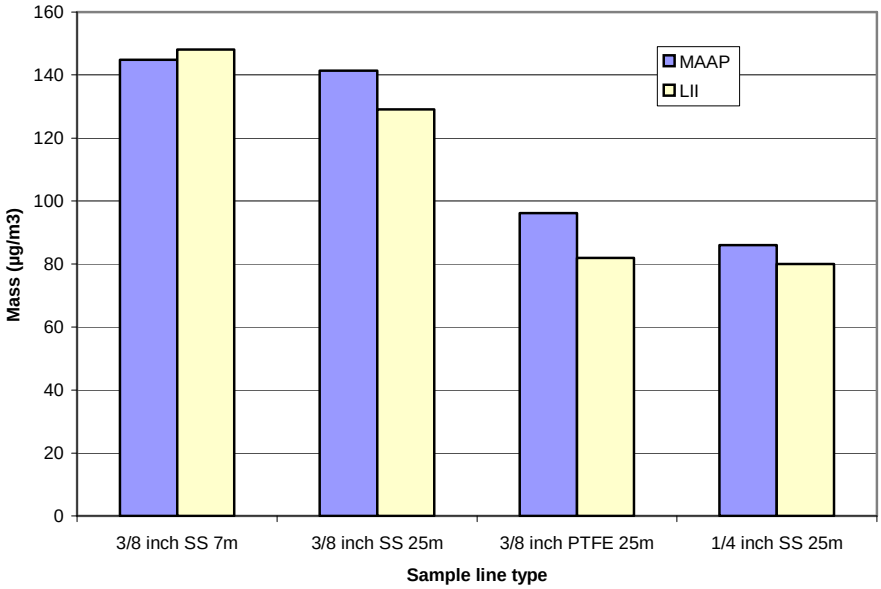

Figure 39 Effect of undiluted sample line length and diameter variations on PM mass loading of exhaust gas for LII and MAAP instruments.

Figure 40 shows the DMS results during the line size, length and material experiment. The data indicates that 8.9 x 10^5 particles were lost per metre of line when the sample line was increased from 7 to 18m. When a 1/4" line extension was used, the losses were higher at 10 x 10^5 lost per metre. The addition of the PTFE line demonstrates that number losses are higher than when using stainless steel.

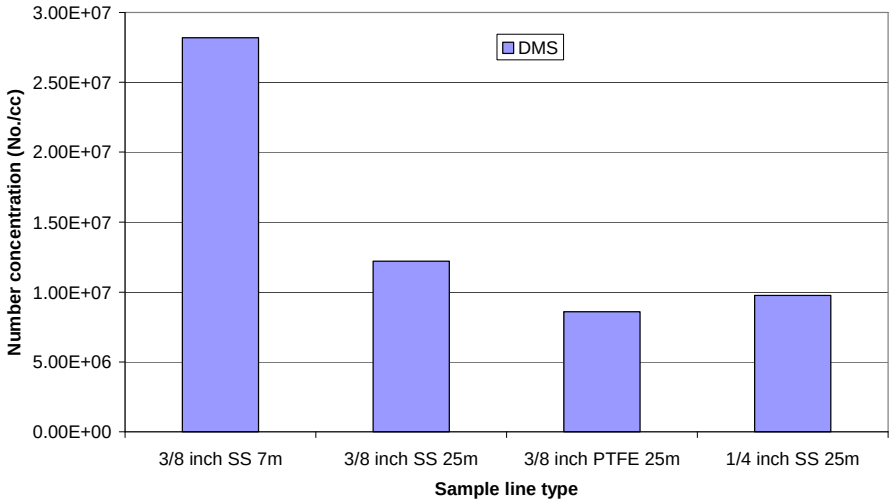

Figure 40 Effect of undiluted sample line length and diameter variations on PM number loading of exhaust gas for DMS instrument.

Figure 41 shows the concentrations of organic and SO_4 species during the test to determine the effects of line length, diameter and material on volatile losses in the sampling system. The data shows that the increase of line length from 7m to 25m substantially increases losses of volatile materials. The effect of PTFE line material is interesting since the losses do not appear to be as significant as is the case for 25 of stainless steel. The inclusion of 1/4" tubing reduces losses with respect to using 3/8" tubing. Also note how the trends presented in this data are not consistent with the mass data shown in Figure 39, hence the potential for PM losses is not identical between volatile and non-volatile PM, according to this data.

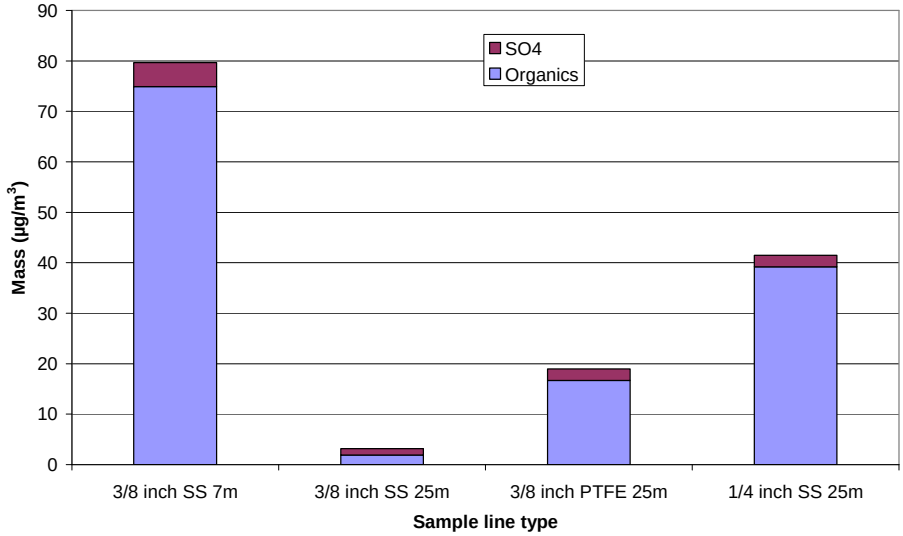

Figure 41 Effect of undiluted sample line length and diameter variations on PM organics and SO_4 mass loading of exhaust gas for AMS instrument.

Figure 42 shows the effect of changes in the sample line diameter, length and material. The data indicates that small particles are preferentially lost as line length increases, given the significant change in profile shape for the 25m lines.

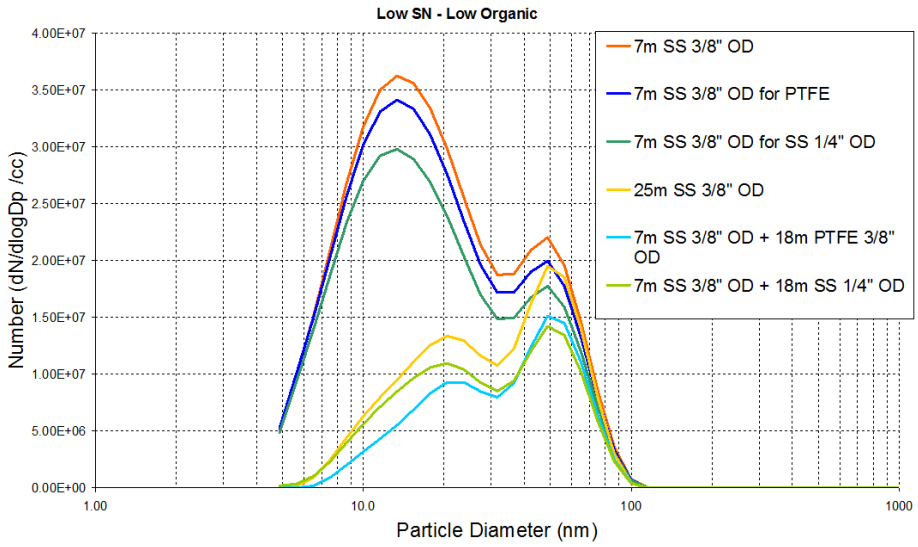

Figure 42 Size distribution as measured by DMS, demonstrating the effect of changes in sample line dimensions and material.

6.1.5 Line deposition ('bedding in') experiments

Figure 43 shows the PM size distribution at the LS/HO condition during a 65 minute deposition test using the DMS instrument. Due to time constraints it was decided that a higher SN condition would allow the experiment to be conducted over a shorter duration. These experiments were conducted at the baseline case of 160°C. Whilst the size distribution appears to be unaffected, it is clear that the PM concentrations are changing over time. On initial inspection the size distribution appears to stabilize after 35 minutes, when then the variations in size as seen in Figure 43 for both peaks appear to be comparable to variations caused by fluctuations in the HES rig inlet conditions.

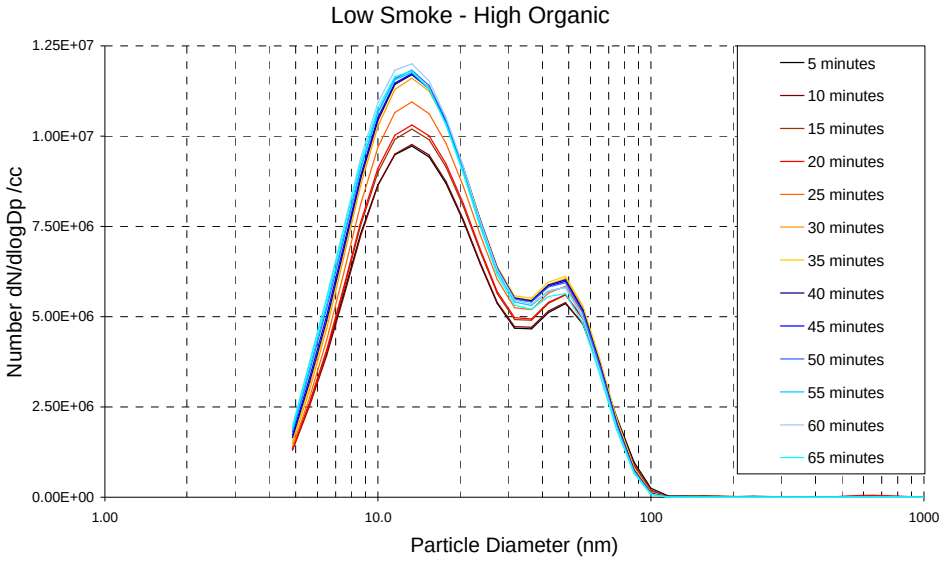

Figure 43 Size distribution of LS/HO condition on the 7m stainless steel line 1 at undiluted sampling flow.

Examining the bedding in effect in terms of number concentration of the two peaks (the nucleation mode and the accumulation mode) is shown by analysing the data based on the split between the two peaks at 31nm. Initially the Accumulation mode peak in Figure 44 looks to have reached a peak at that 35 minute mark, followed by a steady decline.

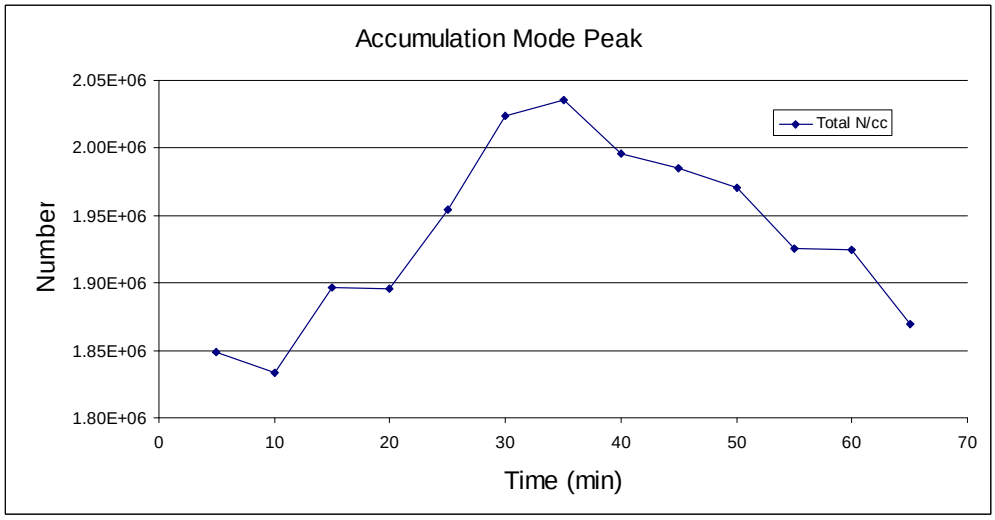

Figure 44 Total Number Concentration with respect to time for the Accumulation Peak for the LS/HO condition.7m stainless steel line at undiluted sampling flow.

The nucleation mode shown in Figure 45 has a steep gradient for the first 30 minutes then the growth slows down for the next 30 minutes until reaching a peak on 60 minutes.

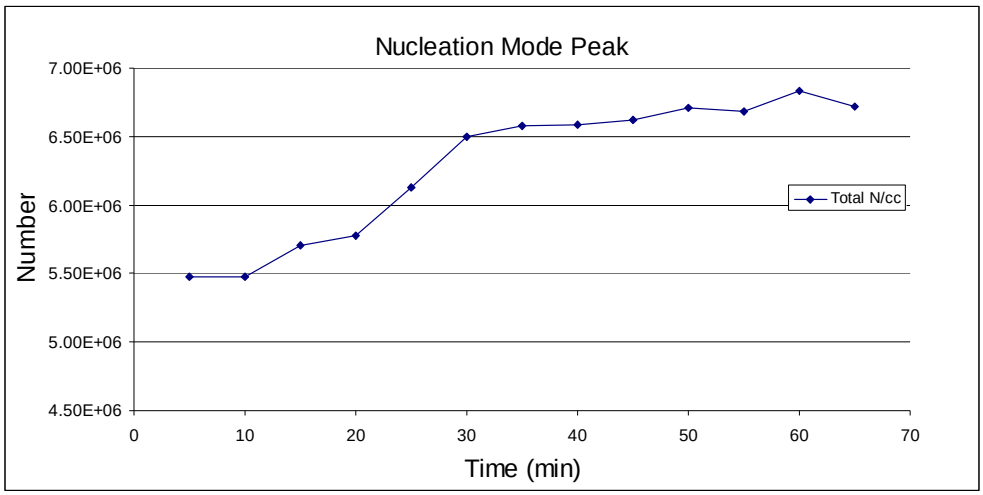

Figure 45 Total number concentration with respect to time for the Nucleation mode peak for the LS/HO condition. 7m stainless steel line at undiluted sampling flow.

Given the different effects that the two significant peaks are showing, further inspection of their respective Geometric Mean Diameters and their variation with time show markedly different behaviours. Figure 46 over the whole time range shows a steady decrease in from 50nm to 48nm.

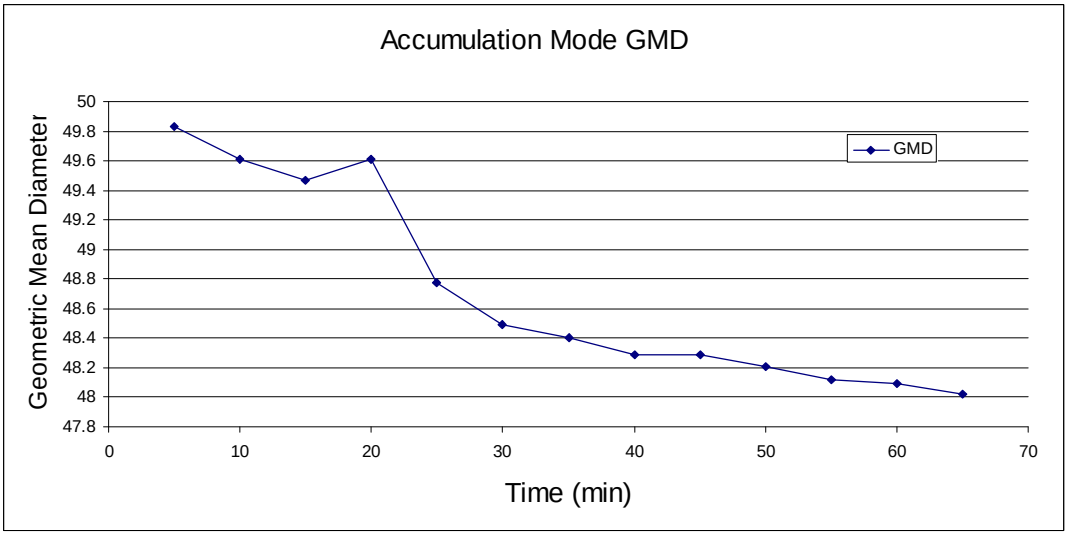

Figure 46 Plot of Geometric Mean Diameter of the Accumulation Mode with respect to time in the LS/HO condition. 7m stainless steel line at undiluted sampling flow.

Figure 47 however shows two different trends – an increase initially to 13.55nm at the 10-15 minute time and then a steady decrease to 13.15nm over the next 45 minutes.

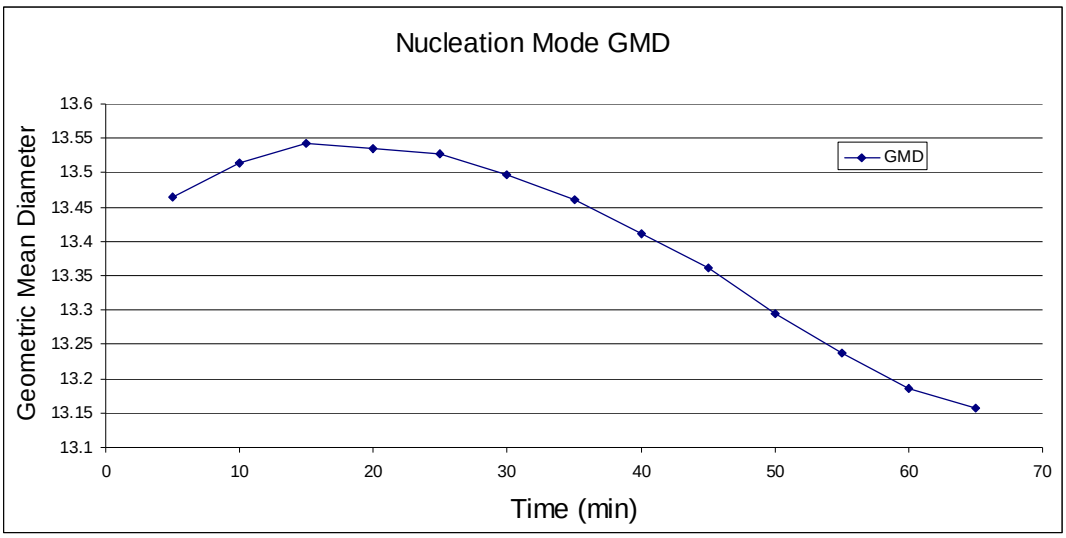

Figure 47 Plot of Geometric Mean Diameter of the Nucleation Mode with respect to time in the Low Smoke – High Organic condition on the 7m stainless steel line at undiluted sampling flow.

These trends could be indicating that while the overall number distribution could have reached a plateau, that the deposition is size dependant with the effects of the nucleation mode and agglomeration having a continuing effect.

6.1.6 Other measurements

Degree of Graphitisation

In any given sample, there is considerable variation in the extent of agglomeration and size of the collected particulate matter. This variation is shown in Figure 48. In consequence, the analysis was two fold and is reported in terms of: 1) Big particles – those particles that are agglomerated and have a diameter greater than 1 µm. 2) Small particles – the individual particles that are distributed all around the surface and have a diameter less than 0.1 µm.

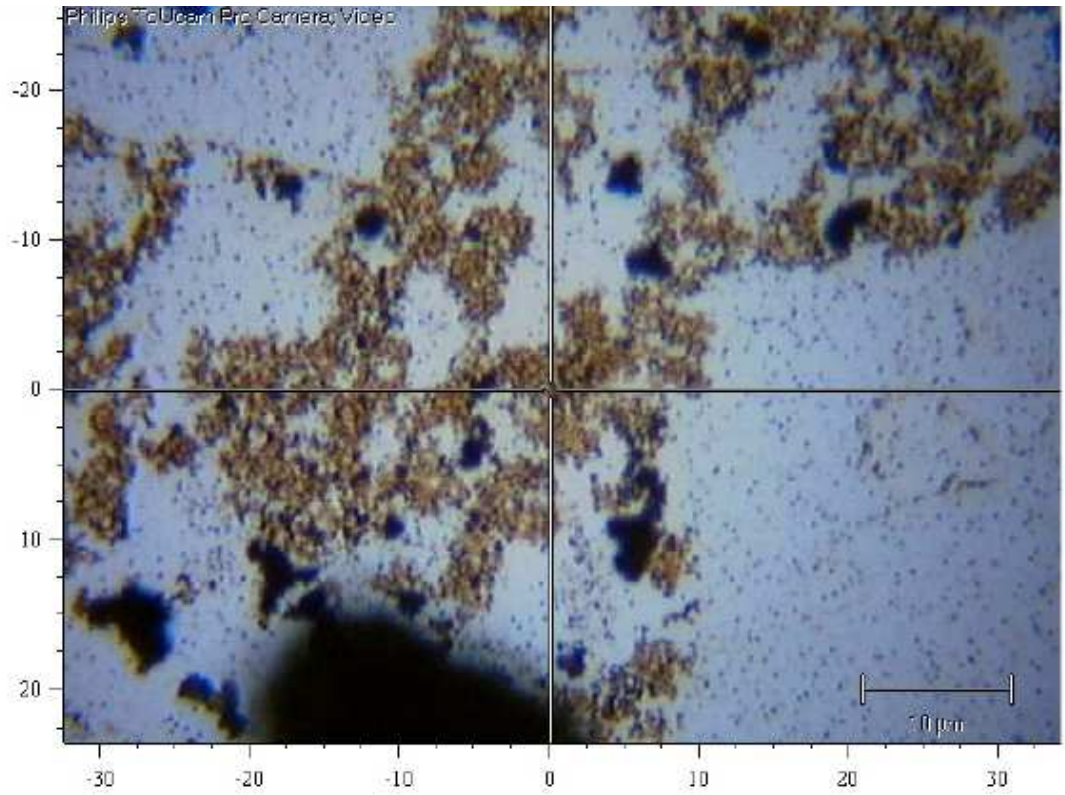

Figure 48 Image showing the typical variation in the agglomeration and size of the collected particulate matter.

The graphitic content of a particle is determined from the ratio of the amplitude of the G band (graphitic) to the amplitude of the D band (amorphous) in the Raman spectrum. This analysis is performed for a number of individual particles in each of the samples. Data for a given sample shows that there can be considerable variation in the graphitisation between individual and neighbouring particles.

Averaged over all the experiments, the non-volatile particulates emitted from the Hot End Simulator have a composition that is typically 30% to 35% graphite, the remaining balance is principally amorphous carbon.

Figure 49 shows the degree of graphitisation in the particulate matter collected on the undiluted sample line and determined by Micro-Raman spectroscopy for three different experiments: The effect of line aging, the effect of sample flow, and the effect of line temperature. For the assessment of line aging effects the two samples were collected approximately 30 minutes apart

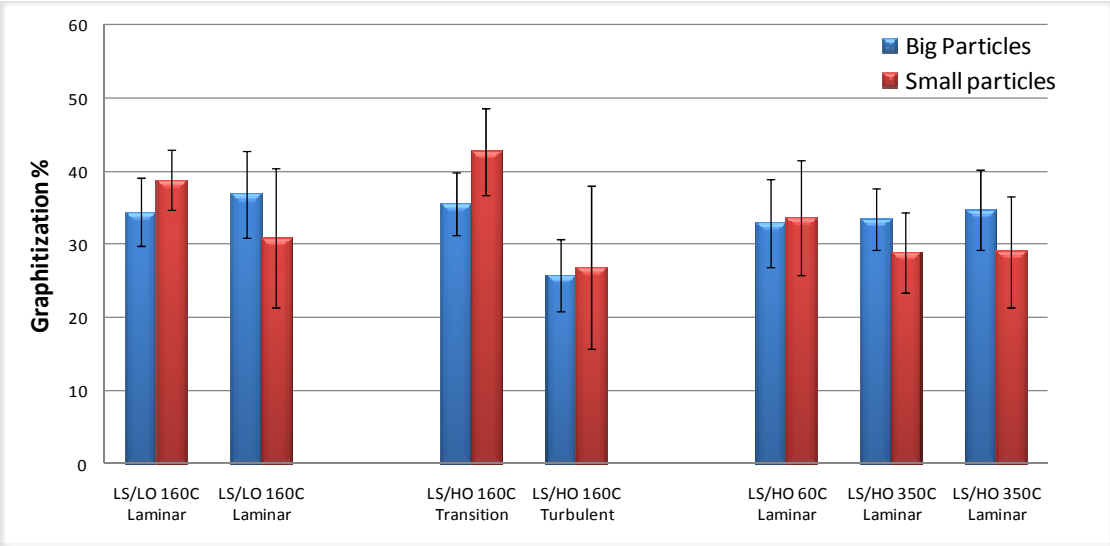

Figure 49 The average extent of graphitisation in the non-volatile particulate matter for different collected samples: Effect of line aging (left), Effect of sample flow (centre), Effect of line temperature (right). Rig condition is indicated.

Within the experimental error, the chemical character of the particulates does not change with sample line aging. Furthermore, the chemical state of the particulates does not change with different sample line temperature. However, the chemical character of the particulates does appear to show a discernible change with differences in the sample line flow. In this case, particles sampled from a turbulent flow have a reduced graphitic content in comparison to particles sampled from a transition flow. Nevertheless a degree of caution is required in the interpretation of the data, since each sample did show considerable variation in the graphitisation between individual and neighbouring particles, and the statistical extent of the difference is small. Further analysis of many more particulates in each sample will be required to reduce the experimental errors and isolate any clear differences in the chemical character of the particulates to changes in the sampling flow.

Unfortunately it was not possible to obtain a sample in Laminar flow under these conditions as there was insufficient flow to supply all instruments whilst maintaining the laminar flow condition.

Ion Chromatography and Gas Chromatography-Mass Spectrometry results

These offline techniques were applied once during the tests to give an indication of the relative performance of chemical analysis versus on-line methodologies. The Ion Chromatography (IC) technique involved passing the gas sample through de-ionised distilled water followed by subsequent analysis using a commercially available IC apparatus located at Cardiff University. Results showed that at the LS/HO condition, with sample lines at 160°C and laminar flow, sulphate concentrations were 27.4 mg/m^3, nitrates were 1.61 mg/m^3 and chlorides were not detected.

Gas Chromatography-Mass Spectrometry (GC-MS) was undertaken on 2 of the used gravimetry filters. The filters and smoke were dissolved in Dichloromethane and analysed in a commercial GC-MS apparatus at Cardiff University. Results showed a clear peak of naphthalene, with no other PAH compounds detected, as show in the chromatogram in Figure 50. The concentrations of naphthalene measured from the filters were 0.4 ml of naphthalene per Nm^3 of exhaust gas (0.4 ppmV) at the LS/HO condition and 0.2 ml of naphthalene per Nm^3 of exhaust gas (0.2 ppmV) for the HS/LO condition. Hence, it may be shown that 100% more naphthalene is observed at the LS/HO condition compared with the HS/LO condition.

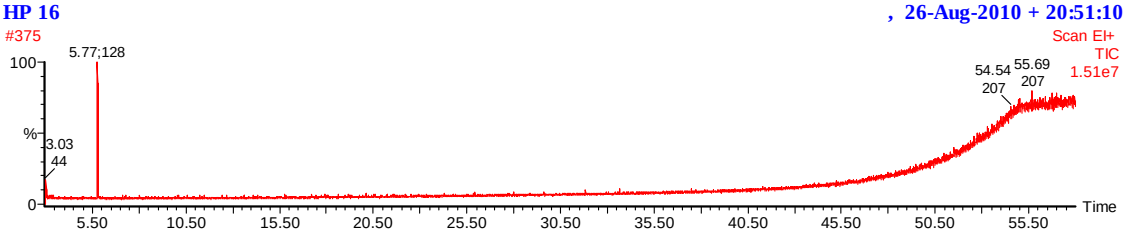

Figure 50 GC-MS chromatogram of PM sample from used gravimetric filter. The Napthalene peak is shown on the far left of the image.

Scanning Electronic Microscopy analysis

SEM analysis of the PM typically captured during the HES tests. The images in Figure 51 illustrate that the primary particle size is of the order of 20nm, which is in good agreement with the LII data, that predicted primary particle sizes of around 18nm.

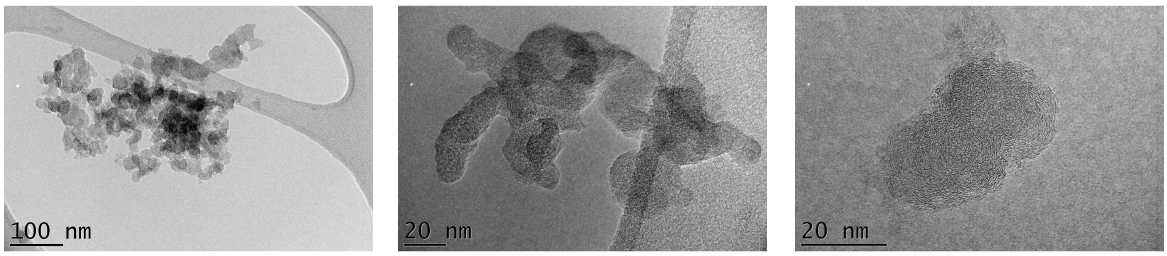

Figure 51 SEM images of smoke particles.

Instrument intercomparison

Figure 52 shows the comparison between gravimetric (total mass) measurements and 3 instrument techniques including black carbon via MAAP and LII, and estimated total mass via DMS. This data is from a series of HES rig and sample line conditions during the test campaign. The diagonal line represents a 1:1 (perfect agreement) relationship. These results compare favourably with SAMPLE I data and highlight that the HES rig was operating in a comparably similar regime as was witnessed during the SAMPLE I test campaign.

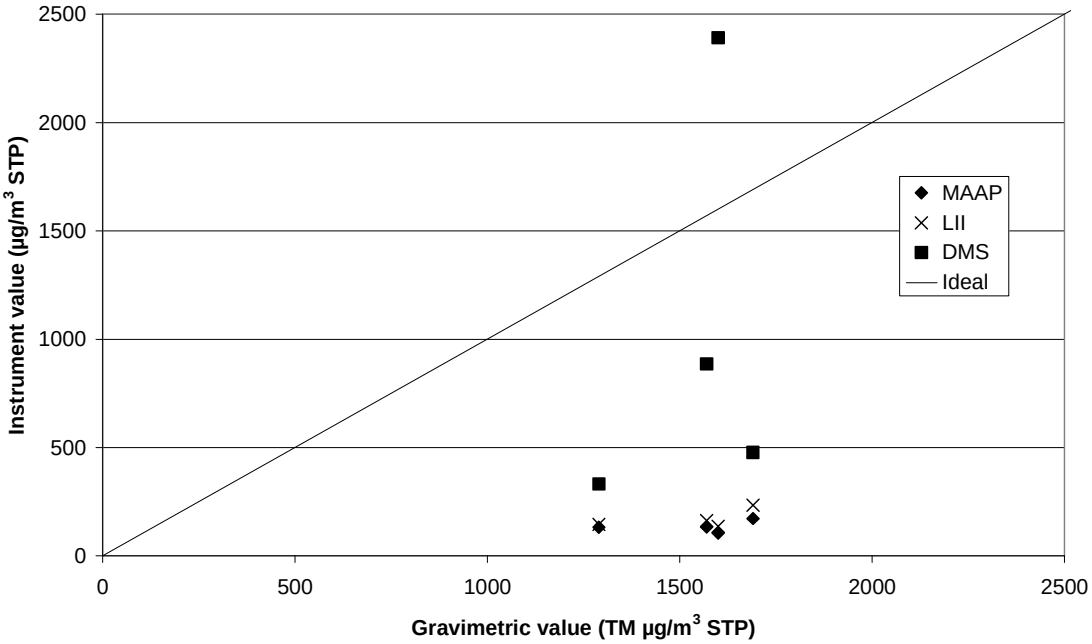

Figure 52 Comparison between the Gravimetric filter deposition method and the MAAP, LII and DMS instruments during the trials.

6.2 Diluted sample line

The application of a variable condition dilution sample line was utilised in the compilation of the following data. The details of this system can be found in the methodology section, and the conditions that were varied are shown in Table 10. It is clear from the number of variables that a substantial dataset can be produced from every possible permutation available. Hence the following figures are a representative summary of the key trends shown in the experimental data. It is also important to note that all concentration data in this section has been re-calculated to take into account the effect of dilution, e.g. at 50:1 dilution, the concentrations will be multiplied by 50 in order to normalise back to the undiluted values. This was done to aid in evaluating changes in PM concentration during dilution.

Table 10 details of variables used for the diluted line test from which CPC, MAAP, OPC and FCE data was produced.

Engine conditions	LS/HO, LS/LO, HS/LO
Dilution temperature	<40°C (cold), >200°C (hot)
Line temperature	60°C, 160°C, 335°C
Dilution ratio	10:1, 50:1, 100:1
Location of dilution point	Probe tip, 7m downstream, 25m downstream

It is important to note that comparisons between the above conditions are only made per piece of evidence submitted (i.e. per figure). It is not always consistent to make comparisons between the graphs, since smoke generation conditions may have changed slightly between experimental tests.

6.2.1 Effect of rig condition on PM at various dilution ratios

Figure 53 (a) shows the CPC number concentrations at various dilution ratios with cold tip dilution measured at after a 7m 3/8" SS sample line operated at 160ºC. For the cases of the LS/HO and LS/LO condition it is clear that 10:1 dilution causes a higher PM number loss compared with the 50:1 and 100:1 dilution cases.

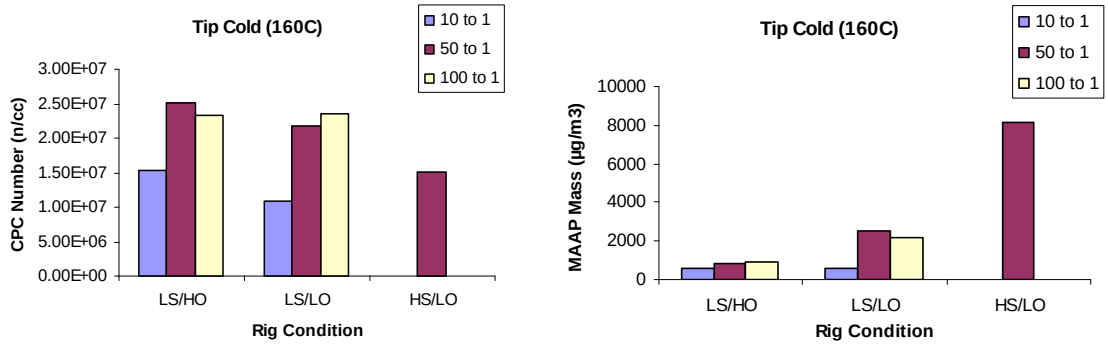

(a) **(b)**

Figure 53 (a & b) PM number (CPC) and mass (MAAP) loadings at different dilution ratios over three rig conditions, Dilution cold introduced at tip

In terms of mass concentration, Figure 53 (b) shows the MAAP data for various dilution ratios with cold tip dilution. Again it is witnessed that there appear to be lower PM mass concentration losses when higher levels of dilution (>50:1) are used in both the LS/HO and LS/LO rig conditions.

It is noted that the highest mass occurs at the HS/LO condition compared to the lowest number measurement, which suggests that there is a shift in particle size towards larger particles. This trend is confirmed in the OPC data given in Figure 54, where it is seen that more large particles are measured at HS/LO.

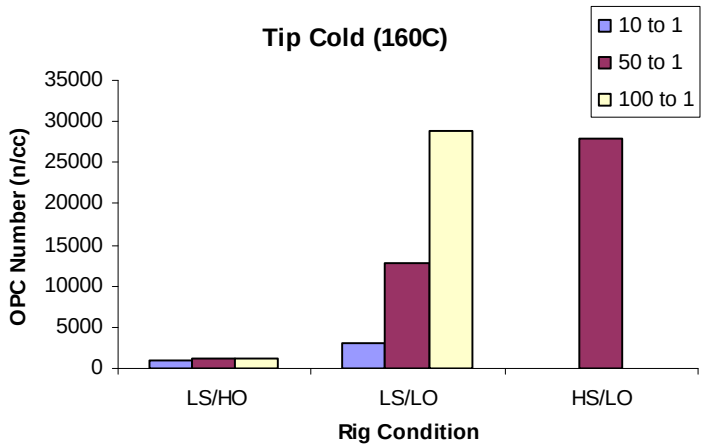

Figure 54 PM number concentration at different cold diluent tip dilution ratios over three rig conditions, as measured by OPC.

Unfortunately there was not sufficient time to examine dilution ratio effects for each of the 3 engine conditions; however, it is observed that the OPC data shows a similar trend to the MAAP data set whilst giving an opposite trend to CPC data. These trends imply that there is a definite shift in particle size distribution for the 3 engine conditions with the LS/HO displaying large numbers of small (nucleation) particles and comparatively fewer large (accumulation) particles, LS/LO displaying moderate numbers of both small and large particles and HS/LO having larger numbers of large particles with relatively few small particles as demonstrated earlier by comparative DMS data (Figure 29).

It is also observed that there seems to be a definite trend for both mass and number conservation with a minimum dilution ratio of 50:1 being necessary to reduce PM losses within the sample line as discussed later in the report.

6.2.2 Effect of line temperature and dilution ratio with tip dilution.

The following measurements were conducted at the LS/HO condition and thus any variations on the nature of the PM sample should be attributed to the sampling system, rather than changes in the HES rig condition.
Figure 55 to Figure 58 shows the effect of line temperature on the conservation of PM in a diluted sample line. It can be noted in terms of CPC measured number concentration that the

lowest losses appear to occur when using a line temperature of 160˚C is utilised when diluting at tip as shown in Figure 55 (a & b). This trend is different to that witnessed by the DMS on the undiluted line (Figure 33) which showed very little line temperature effect on number concentrations. Also there is corroboration with the previous result that higher levels of dilution ratio cause lower PM losses within the diluted sample line in terms of CPC measured number concentration if dilution occurs at the tip as demonstrated by Figure 55 (a& b).

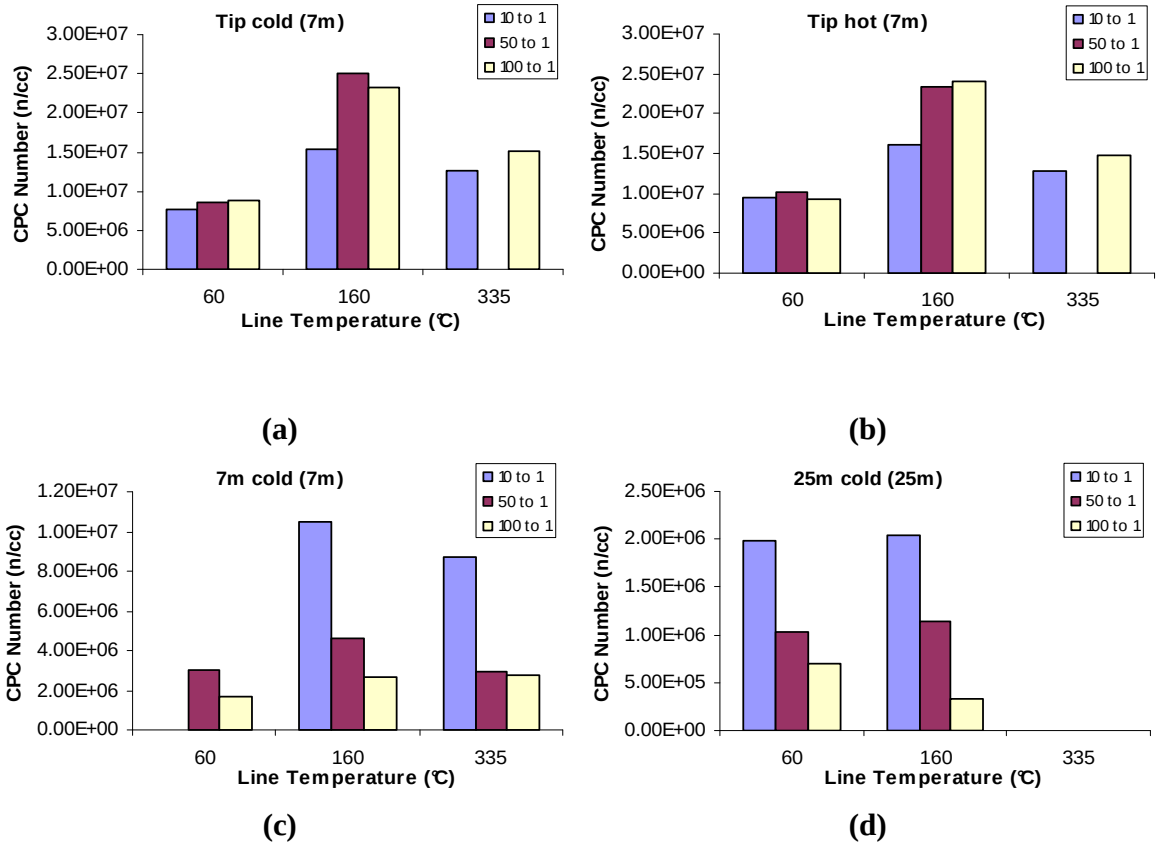

Figure 55 (a-d) Effect of line temperature on PM number concentration (CPC) at numerous dilution ratios and locations respectively.

Unfortunately due to the analysers preset sample flow requirements then using non ejector dilution systems it is not possible to keep the residence time constant for variable line temperatures. However, it is observed in Figure 55 (c & d) that if dilution occurs downstream of the tip then there appears to be little effect of line temperature to the PM number losses occurred. It is also observed that there is an unexpected reverse in trend towards dilution ratio with the lowest dilution ratio (10:1) exhibiting the lowest observed losses in PM, this is in contradiction to the trends noted for tip dilution in Figure 55 (a& b).

Figure 56 shows the effect of dilution ratio and temperature on the Geometric Mean Diameter (GMD) of the PM in the sample, as measured by the Faraday Cup Electrometer (FCE).

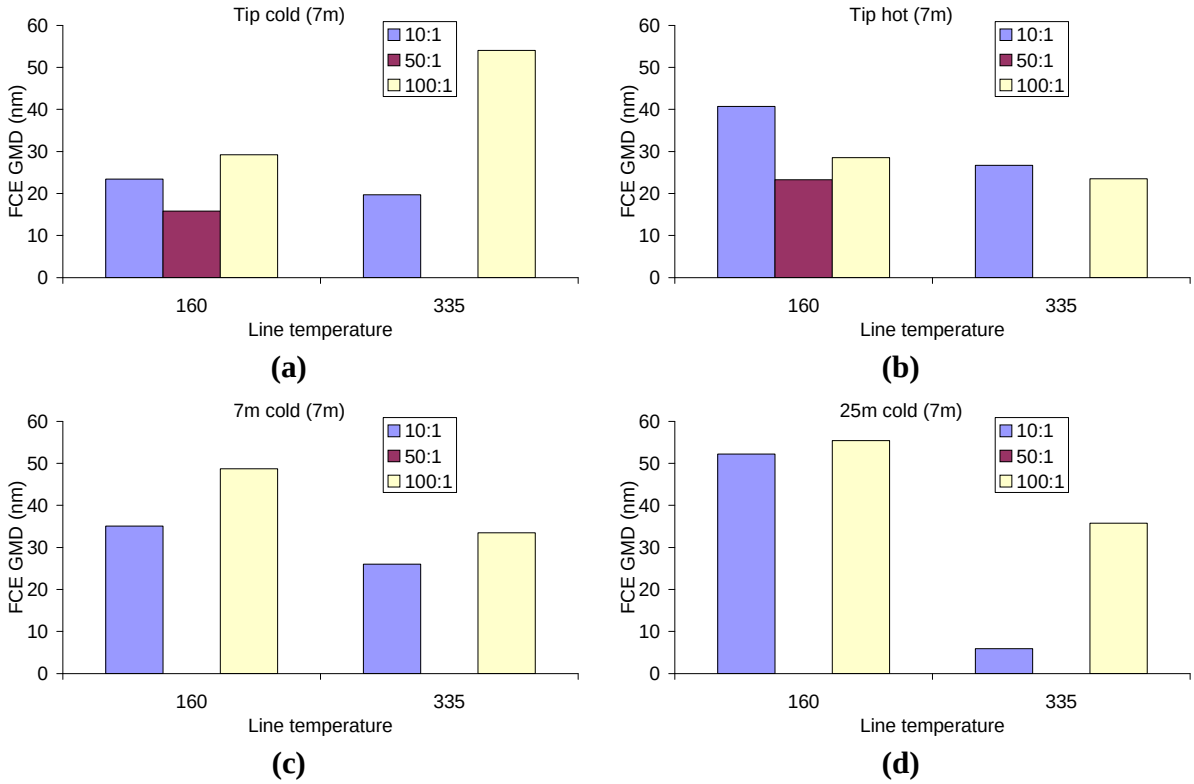

Figure 56 Effect of temperature on PM size expressed as Geometric Mean Diameter (GMD) at numerous dilutions ratios and locations respectively.

It is thought that this effect is attributed to an associated increase in residence time in the sample line with increased dilution ratio as lower levels of exhaust sample are drawn through the system as dilution ratios increase using a non-ejector style dilutor. Thus, the residence time in the 7m line is 10 times longer for the 100:1 dilution ratio case compared to the 10:1 case.

As can be seen the trends witnessed earlier for PM number concentration with regards to line temperature are observed in Figure 57 (a-d) for MAAP measured mass concentration. It is again witnessed that the lowest losses in terms of mass occur at a line temperature of 160˚C with high dilution ratios (>50:1) with greater losses observed for both the 60˚C & 335˚C line temperature cases. This is in agreement with smoke number data witnessed on the undiluted line discussed earlier (Figure 28), but again does not fully correlate with mass data observed using a secondary MAAP and LII on the undiluted line (Figure 32) demonstrated little sensitivity to line temperature on PM mass concentration losses and witnessed the lowest losses occurring at the 335˚C line temperature case.

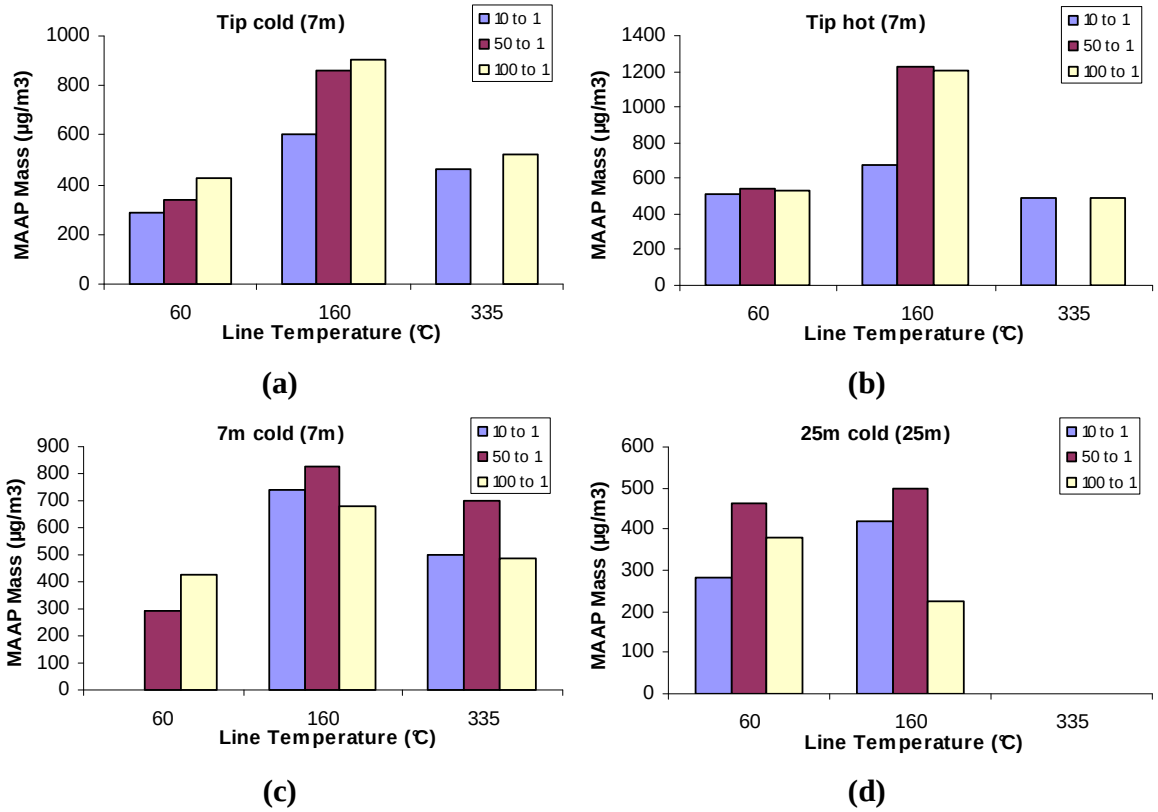

Figure 57 (a-d) Effect of line temperature on PM mass concentration (MAAP) at numerous dilution ratios and locations respectively.

The downstream diluted cases for MAAP measured mass are presented in Figure 57 (c& d). It is observed that the losses associated with dilution ratio (and corresponding residence time) shown in the number concentration data discussed earlier (Figure 55 (c &d) are not witnessed in the mass measurement.

The 160˚C line temperature data at 7m dilution downstream presented in Figure 57 (c) exhibits little dependence of dilution ratio, with the lowest observed losses being recorded at 50:1 dilution ratio. This result could be explained by the high residence time within the sample line associated with the higher dilution ratio allowing the smaller sized particles to be lost to the sample line. However, it could also be hypothesised that the small particles are agglomerating along the length. Thus, allowing the total number of particles to decrease whilst conserving mass. A similar trend is witnessed for the 25m dilution case and is given by Figure 57 (d). In this case the 100:1 dilution case witnesses much higher losses than those observed at the lower dilution ratios which may be explained by the extra residence time witnessed in the longer pipe.

The OPC data is given in Figure 58 (a-d) and suggests there is little difference in the number of large particles (>0.25-32µm) between the 60°C and 160°C cases when diluting at the tip with cold diluent highlighted in Figure 58 (a). It is observed that there is a slight gain in larger particles at the higher line temperature of 335°C. The hot dilution case depicted by Figure 58 (b) witnesses a jump in the number of larger particles for the 160°C line temperature case. This

trend replicates and offers an explanation for the similar trend witnessed in the representative MAAP derived mass concentration case (Figure 57 (b)).

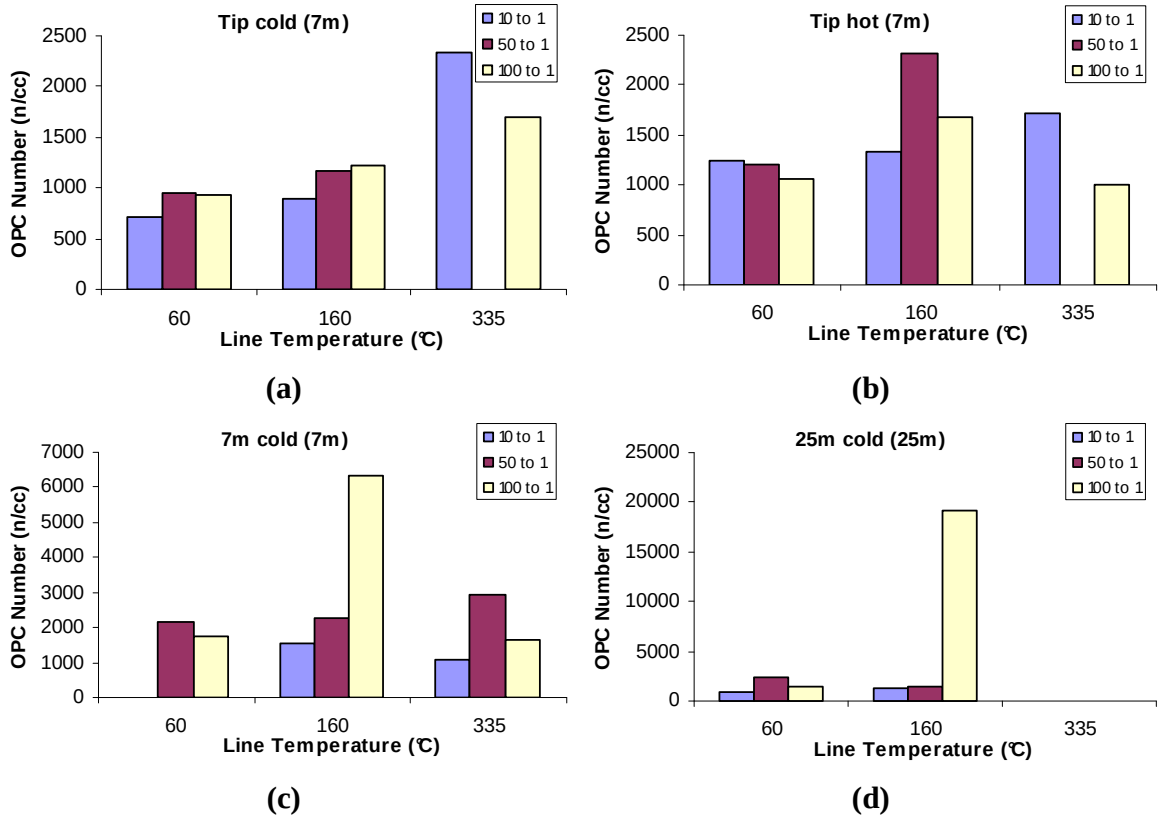

Figure 58 (a-d) Effect of line temperature on PM number concentration (OPC) at numerous dilution ratios and locations respectively.

It is also noted that there seem to be some very large number counts for high dilution cases (100:1) of large particles (>0.25-32μm) when dilution is performed upstream in the sample line with the effect being higher at 25m than 7m line length. This once again could be attributed to the long residence times allowing agglomeration to occur during transport along the line. However, on looking at the data set it can be seen that these high values are not constant but come in periods of very high readings for short periods during the sampling period. This could imply that what is being witnessed could be a transient line shedding event which has been witnessed and discussed previously in the Sample I test campaign (Petzold & Marsh (2009)). It is noticed that these events are only witnessed during the 160°C line temperature however, this could be coincidental. It is noted that the other OPC loadings for the 7m and 25m cases seem to be slightly higher than the levels witnessed at tip dilution.

6.2.3 Effect of dilution location and diluent temperature.

The following measurements were conducted at the LS/HO condition and thus any variations on the nature of the PM sample should be attributed to the sampling system, rather than changes in the HES rig condition.
The following data demonstrates the effect of changing the dilution temperature and location at 3 dilution ratios with the sample line temperature constant at 60°C. Figure 59 (a& b) shows the CPC and MAAP data for tip cold, tip hot, 7m and 25m dilution conditions. It is witnessed for both number and mass that the lowest PM losses are witnessed when dilution occurs at the tip with hot dilution gas.

Figure 59 (a) shows that there is a consistent agreement that the PM number losses increase the further from the tip that dilution is conducted, this is observed for each of the various dilution ratios. It is observed that in terms of number concentration up to 5.52E+06 particles/cm^3 are lost within 7m of sample line if diluting at 7m cold at 50:1 compared with the comparable tip dilution case, and this figure increases to a loss of 7.5E+06 when dilution is conducted at 25m.

However, in terms of mass (Figure 57 (b)) it is noted that there seems to be no obvious trend in terms of PM loss if diluting cold at tip, 7m or 25m.

As discussed earlier it can be seen that there seems to be a distinct advantage in using high dilution ratios (>50:1) of hot gas at the tip.

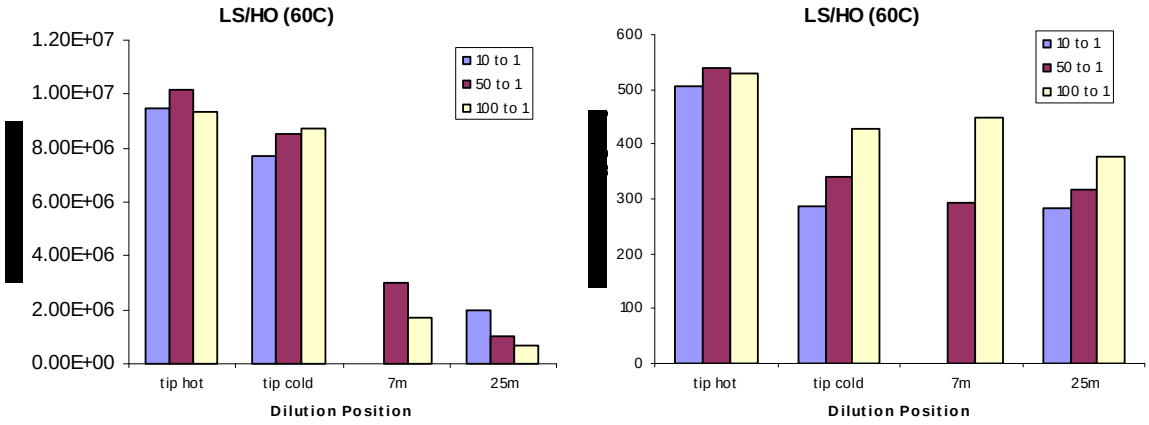

(a) **(b)**

Figure 59 (a & b) Effect of dilution location and diluent temperature on PM number (CPC) and mass concentration (MAAP). Sample Line temperature 60°C

Figure 60 (a & b) shows data taken at the same conditions as Figure 59 (a & b), but with the sample lines at a higher temperature of 160°C. Direct comparisons between sample line temperatures have been highlighted previously so will not be discussed further at this time. Figure 60 (a) shows the CPC number concentrations at 160°C for various dilution temperatures and conditions. Note that the effect of dilution temperature is less profound when compared to

the 60°C case shown earlier (Figure 59 (a)). However, again it is seen that losses increase the further from the tip the point of dilution is conducted.

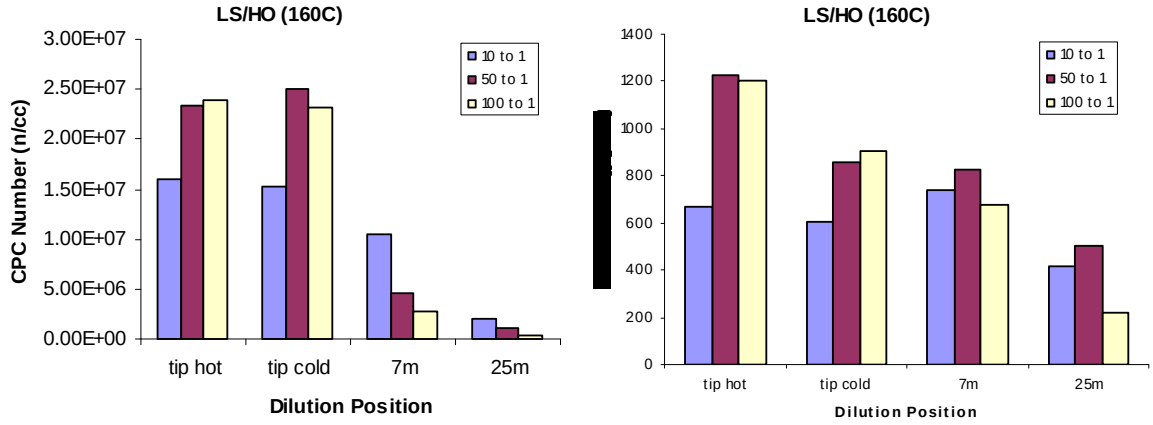

(a) **(b)**

Figure 60 (a & b) Effect of dilution location and diluent temperature on PM number (CPC) and mass concentration (MAAP). Sample Line temperature 160°C

Figure 60 (b) shows the equivalent MAAP data for 160°C sample lines. In this case, there is reasonable agreement with the CPC data with losses in terms of mass being witnessed as the point of dilution moves from tip to 25m which did not seem so prevalent in the 60°C case discussed earlier (Figure 57 (b)).

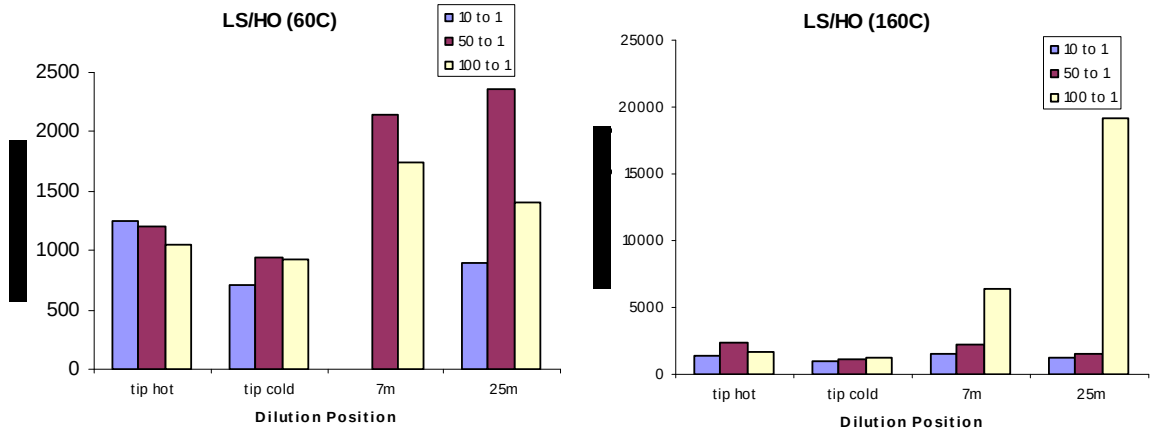

(a) **(b)**

Figure 61 (a & b) Effect of dilution location and diluent temperature on PM number (OPC) Sample Line temperature 60°C & 160°C respectively

Figure 61 (a & b) show the number concentrations measured using an OPC at different locations. It can again be witnessed that there appears to be higher loadings of large (>0.25-32μm) particles

if the point of dilution is at 7m or 25m downstream with highest loadings occurring when a dilution ratio of 100:1 on a 160°C line is utilised. This again highlights the possibility of agglomeration and line shedding occurring when the lines are longer with comparatively longer residence times. Particle growth by condensation of volatile vapours on pre-existing soot particles is assumed to be not sufficient enough for providing the observed particle growth.

Figure 62 shows the effect of the dilution temperature and location as measured by the FCE. It can be seen that PM size is increasing with line lengths, given the larger GMD values at 7m and 25m downstream of the probe tip. This supports the theory that dilution at increasing downstream location supports the loss of small particles.

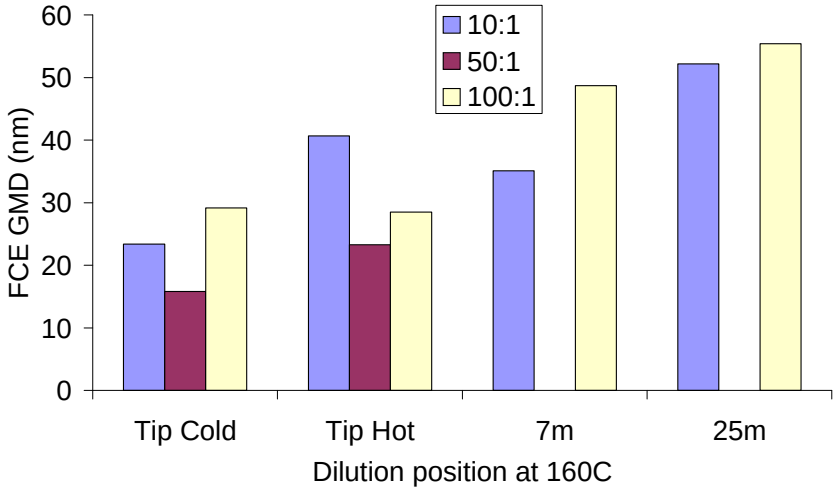

Figure 62 Effect of dilution temperature and location on PM GMD as measured by the FCE.

Unfortunately due to the manufacture of the longer 18m lines it was not possible to heat these lines to 350°C for this reason experiments could only be performed with points of dilution at tip and 7m. Figure 63 (a& b), show PM number (CPC) and mass (MAAP) concentrations for 335°C sample lines. Note that timing constraints precluded the 50:1 dilution ratio data, but good comparisons are available between the 10:1 and 100:1 dilution ratios. Figure 59 (a) shows CPC data at the 335°C sample line temperature. At this temperature there seems little effect between the use of hot and cold tip dilution, which is logical, since the diluent and line temperatures are virtually identical. A loss is shown in the PM number concentration at 7m dilution but once again this could be an effect of the extended residence time in the sample line.
It is again observed that in terms of number there are lower PM losses witnessed when high levels of dilution are used at the tip with the trend reversing when diluting at 7m due to the associated extra residence time witnessed when increasing dilution ratio.

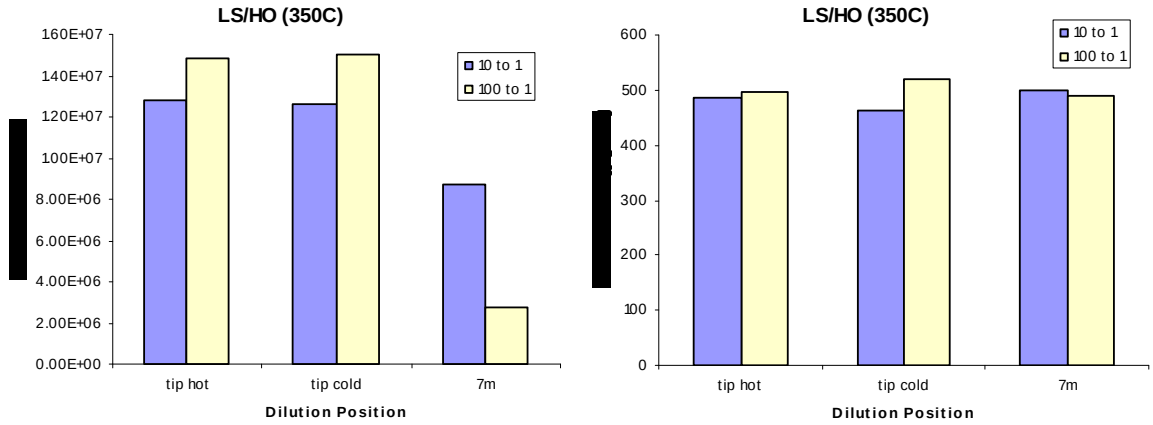

(a) **(b)**

Figure 63 (a& b) Effect of dilution location and diluent temperature on PM number (CPC) and mass (MAAP) loadings. Sample Line temperature 335°C

It is noted in Figure 63 (b) that again in terms of mass measured by MAAP that there appears to be no extra PM loss when diluting at 7m compared with at tip if the lines are held at 335°C which is in agreement with the two earlier observations at line temperatures of 60°C and 160°C (Figure 59 (b) & Figure 60 (b)).

The OPC data for the 335°C case is given in Figure 64 and it is seen that there are comparable figures of loadings of large (0.25-32µm) particles as was witnessed in the 60°C and 160°C line temperature cases with slightly higher numbers witnessed if cold tip dilution is used.

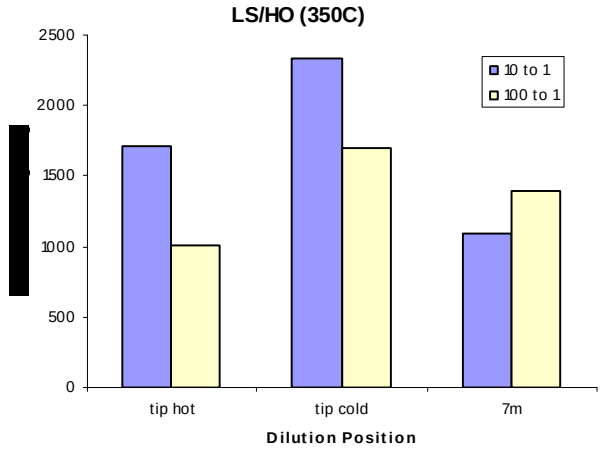

Figure 64 Effect of dilution location and diluent temperature on PM number (OPC). Sample Line temperature 350°C

The downstream dilution measurement data seems to indicate high non-volatile particle loss when compared to tip dilution. However, if residence time is taken into account, analysis shows

that downstream dilution data points had longer residence time than for tip dilution. The trend for higher particle penetration for smaller residence times is not unexpected. Fortunately over the HES testing period two similar residence times were encountered for both tip and 7m downstream dilution. Regardless of dilution location the penetration efficiencies were comparable. This suggests that for non-volatile particles sample line residence time is more critical than where the point of dilution occurs (up to 7m downstream). This effect for dilution location >7m downstream cannot be verified with these results.

6.2.4 Effect of Line Length and Line Material on PM

The effect of line length and material were investigated at different dilution locations (tip& 7m) using cold diluent. The initial 7m stainless steel section, which was heated to 335°C, sample was then passed through a further 18m of either stainless steel or grounded carbon loaded PTFE line both of which were heated to a sample line temperature of 160°C. Measurements were made at both 7m and 25m downstream of the sample probe. Due to time constraints only dilution ratios of 50:1 were investigated at two rig operating conditions of LS/LO and HS/LO.

PM number data measured by CPC is presented in Figure 65. It can clearly be seen that for both rig conditions there are increases in losses observed in terms of number as the point of measurement is moved from 7m to 25m downstream of the sampling probe, with larger losses being witnessed in the grounded PTFE line than the comparative stainless steel case.

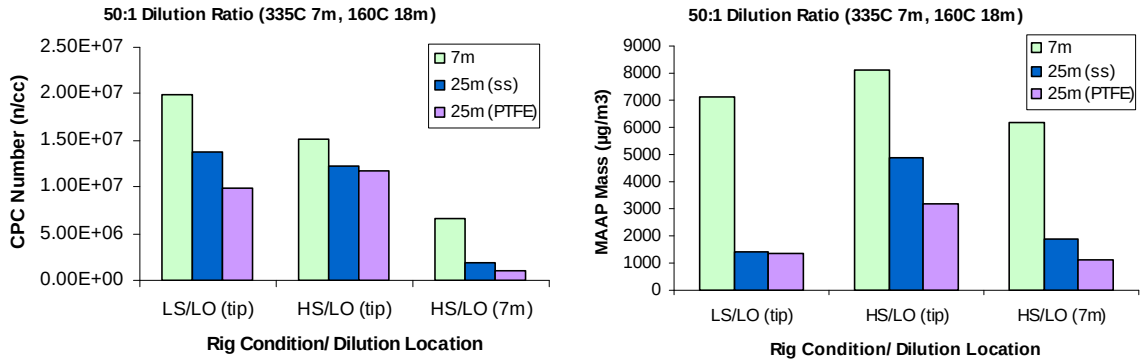

(a) **(b)**

Figure 65 (a & b) Effect of line length and line material and dilution location on PM number (CPC) and mass (MAAP) loadings respectively. Sample Line temperature first 7m 335°C. Dilution ratio 50:1

MAAP mass loading given in Figure 65 (b) also demonstrates a consistent loss in PM as the sample line changes from 7m to 25m long with the PTFE again showing the highest losses. This trend is consistent with the trends witnessed for the MAAP measurements made on the undiluted line (Figure 39). However, there seems a much greater loss between the 7m and 25m sampling points witnessed on the diluted sample line compared with the undiluted tests. Some of this difference may be attributed to thermphoretic losses as the sample travels from the hot 335°C 7m section into the cooler 160°C 18m line which was not the case in the undiluted case which was a constant temperature over the whole line.

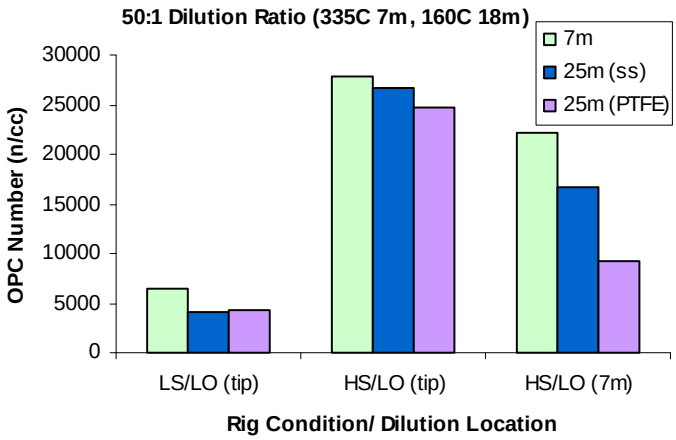

Figure 66 Effect of line length and line material and dilution location on PM number (OPC) Sample Line temperature first 7m 335°C. Dilution ratio 50:1

OPC PM number data is shown in Figure 66 it can be seen that the number of large particles (0.25-32μm) measured decreases with line length. In this set of experiments all dilution occurred at the same point therefore the velocity in the lines is constant all the way to the point of sampling so any residence time differences are directly proportional to the length of line.

6.3 Volatile particle remover results

Analysis of DMS total number concentration shows that the VPR removes approximately one third of the particles but the concentration is not dependant on residence time or dilution ratio when compared to the scatter of data points within the measurement timeframe. This is shown in Figure 67 to Figure 69.

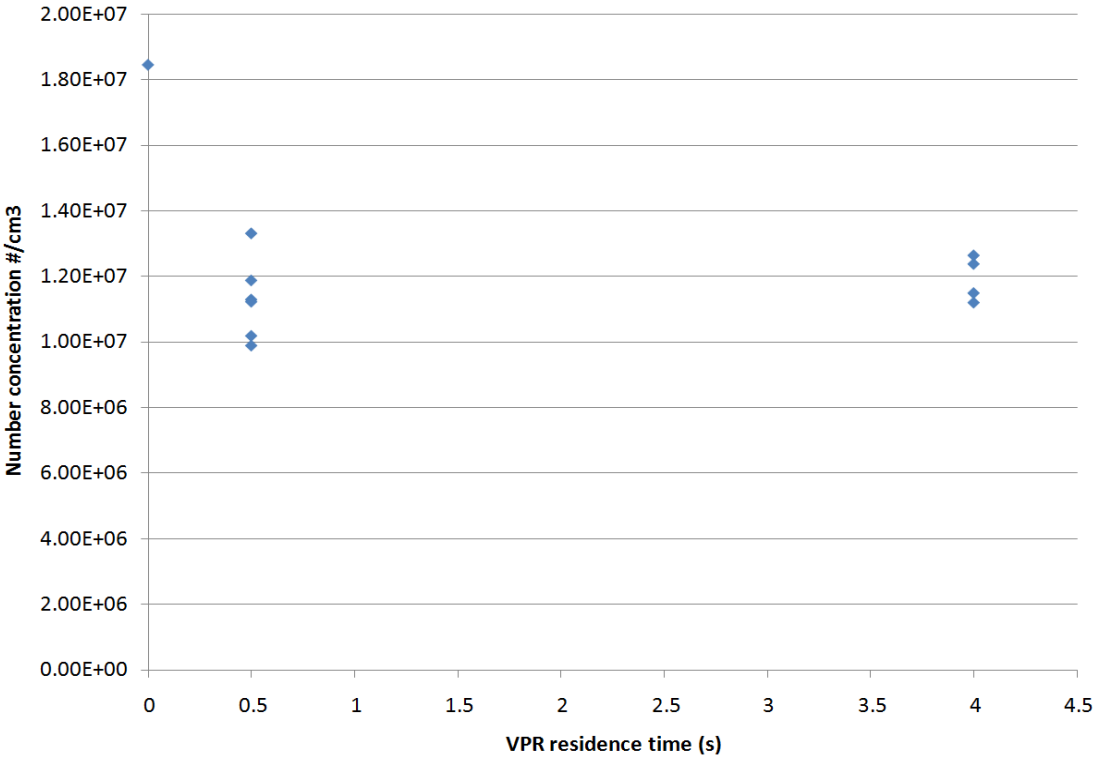

Figure 67 VPR efficiency with respect to residence time (DMS data)

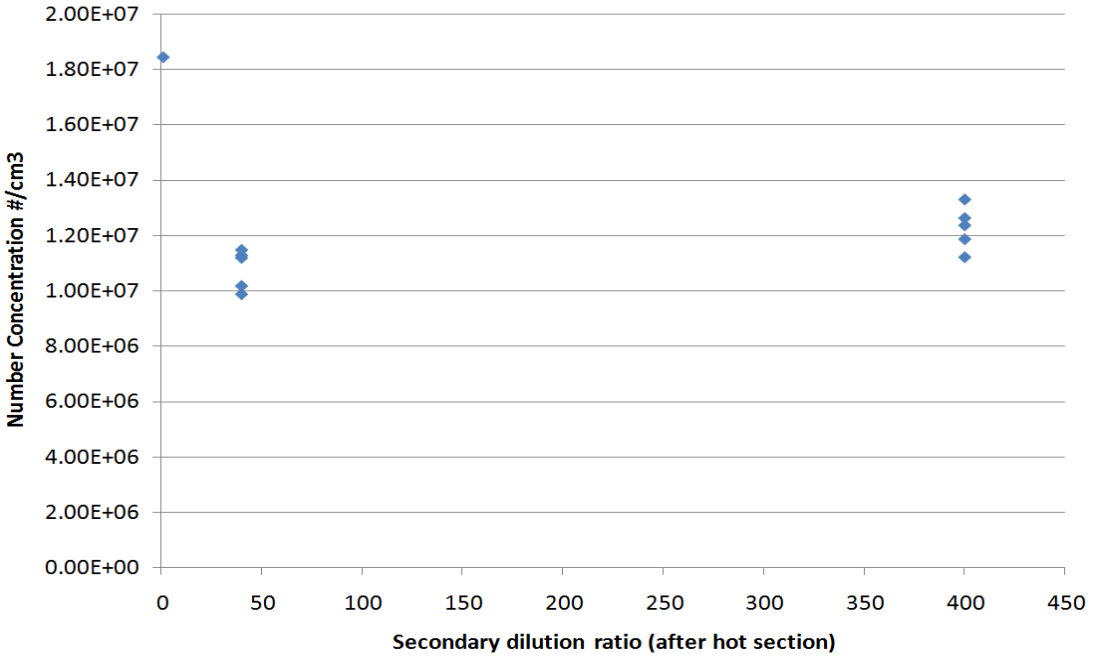

Figure 68 VPR efficiency with respect to secondary dilution ratio (DMS data

Detailed analysis of the DMS size distribution data always displayed a bi-modal distribution. Further examination of the size distribution characteristics with respect to varying the VPR residence time are shown in Figure 69. It can be seen that the number concentration of the nucleation mode is over double that of the accumulation mode (even after the VPR) and perhaps surprisingly both modes show a decrease after the VPR. The geometric peak sizes do not change at all before and after VPR. If the accumulation mode is only comprised of solid soot particles with an organic coating then the VPR would shift the geometric peak size but there would be no change in total number concentration.

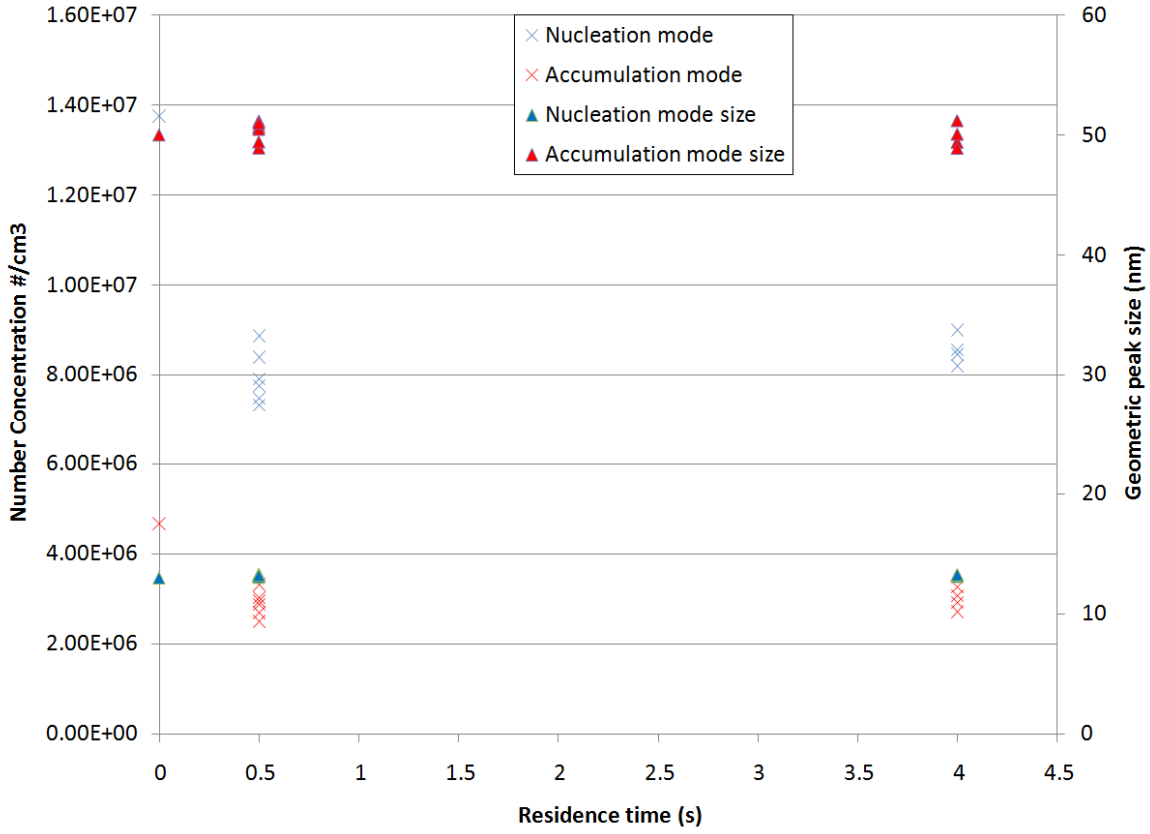

Figure 69 Nucleation and Accumulation modes VPR efficiency (DMS data)

The CPC data is shown in
Table 11. Examining the data which is close to the original SAMPLE I VPR setup (0.5s residence time) it can be seen that small, but significant differences are observed using the thermal discriminator (TD), ~5% of particles exiting the VPR are volatile. This difference increases to ~9% when the sample inlet temperature is cool at 60°C, but at an inlet temperature of 350°C, no difference is observed using the TD. Whereas when the longer residence time setup is applied, then no difference is observed when the TD is switched on and off. In addition, VPR efficiency is not dependent upon inlet flow regimes.

Table 11 CPC data for PM measured in VPR experiment.

Reynolds regime	Inlet line Temperature (C)	Thermal Discriminator	VPR Residence time (s)	CPC No. Conc. #/cc	% difference
laminar	160	n	0.5	1.52E+07	
laminar	160	y	0.5	1.45E+07	4.6
laminar	160	n	4	1.40E+07	
laminar	160	y	4	1.40E+07	-0.1
turbulent	160	n	0.5	1.90E+07	
turbulent	160	y	0.5	1.80E+07	5.3
turbulent	160	n	4	1.70E+07	
turbulent	160	y	4	1.70E+07	0.0
laminar	60	n	4	2.90E+07	
laminar	60	y	4	2.90E+07	0.0
laminar	60	n	0.5	3.00E+07	
laminar	60	y	0.5	2.75E+07	8.3
laminar	350	n	4	2.80E+07	
laminar	350	y	4	2.80E+07	0.0
laminar	350	n	0.5	2.80E+07	
laminar	350	y	0.5	2.80E+07	0.0

The conclusion of this analysis depends upon the composition of the nucleation mode:
If the nucleation mode is ONLY composed of volatile particles (which is the current SAE-E31 understanding) -

(i) The VPR suppresses the volatile particles BUT is not efficient at preventing the nucleation mode from persisting.

(ii) The VPR evaporation tube residence time appears to be significant but even with long times is still not capable of removing nucleation mode completely.

(iii) The inlet sample line temperature does make a difference which indicates that prevention of volatile condensation before VPR is beneficial (and that volatile condensation does take place at 160°C)

(iv) Higher secondary dilution does not make a significant impact on VPR efficiency

(v) Using a simple thermal discriminator does not remove the nucleation mode entirely from the CPC measurement (from the DMS data removing the nucleation mode would result in a reduction of total number concentration of >50%)

If the nucleation mode contains ‘some’ solid carbon particles (i.e. the non-volatile particle distribution is bi-modal) -

(i) The VPR is removing volatile particles when the evaporation tube residence time is long enough

(ii) The inlet sample line temperature does help to increase VPR efficiency

(iii)Higher secondary dilution does not make a significant impact on VPR efficiency

Understanding the composition of the nucleation mode would help to define which conclusions to come to. Unfortunately an AMS does not measure the nucleation mode size range, thus other composition techniques need to be found which help to solve the understanding of particles <25nm.
Background measurements of SO_2 were not constantly measured, but a one-off ambient measurement obtained through the rig inlet compressor and no flame/fuel in the combustor (using the SO_X analyser as part of the combustion gas analysis system) showed a level of approximately 3ppm. This is an exceptionally high ambient level but can be attributed to industrial processes within the nearby steel works. It is possible due the high sulphur levels encountered in the combustor inlet air that the nucleation mode would always form with only 7:1 hot primary dilution in the VPR. Larger primary dilution ratios and a higher evaporation tube temperature could help prevent the nucleation mode from re-condensing after the VPR when high sulphur levels are encountered during rig or engine testing.

6.4 Conclusions from the combustor HES testing

The data shown in this section has led to the following conclusions:

- Rig condition, sample line temperature, flow rate, dilution location and line material all have an effect on the mass, number and size data surrounding PM measurement.
- Sample line temperatures above 350°C appear to show the least amount of PM loss.
- The grounded PTFE tubing evaluated during these tests appeared to cause a noticeable loss in PM.
- PM losses were also observed when using a 1/4" diameter sample line, but this could be attributed to effects such as changes in residence time and surface area per unit sample volume.
- Whilst some evidence exists to demonstrate that residence time has a significant effect on the condition of the PM sample, definitive data can’t be provided and as such a specific test would need to be carried out.
- In terms of ‘bedding-in’, results indicated that stabilisation occurred relatively quickly during a period of tens of minutes.
- Hot tip dilution appears to minimise PM losses in terms of mass and number.
- Dilution at downstream locations appeared to increase PM losses, but this can’t be de-coupled from line residence time, given the difficulties in measuring residence time mentioned above.
- A dilution ratio greater than 50:1 appeared to limit PM losses in terms of both number and mass.
- The VPR suppresses the volatile particles but is not efficient at preventing the nucleation mode from persisting altogether.

7. Experimental Approach – Large Modern Civil Aero Engine trials

7.1 Introduction

The large modern engine trials took place at the Rolls-Royce Derby development test beds facility. This facility was capable of operating gas turbine engines over a range of power settings in a controlled environment, such that PM emissions analysis could be conducted in an adjacent temporary laboratory facility.

The engine test programme took place under ICAO certification conditions. This involved using a certified ICAO Annex 16, centres of equal-area sampling probe (Rotating cruciform rake) and a heated sampling system. The sampling system conveyed the gas sample to a suite of analysers, as described in the next section.

7.2 Engine Test Bed Description

Due to the complexity of a full engine test and rake system, it was not possible to incorporate dilution at the probe tip. Therefore dilution was added approximately 5 metres downstream of the sampling probe, which is within the current SAE E31 guidelines of 8 metres for engine PM sampling. A schematic representation of the sampling setup is shown in
Figure 70. A photo-sketch of the test bed is shown in Figure 71; the Figure is represented in this way in order to remove details of proprietary hardware, for reasons of Roll-Royce commercial confidentiality.

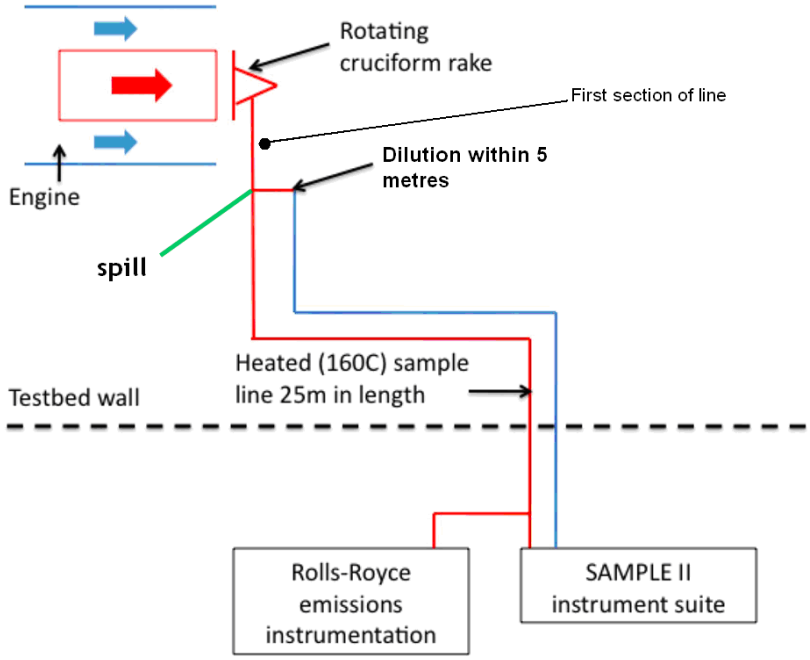

Figure 70 Schematic of engine test setup. (diluted line in blue; undiluted Annex 16 line in red)

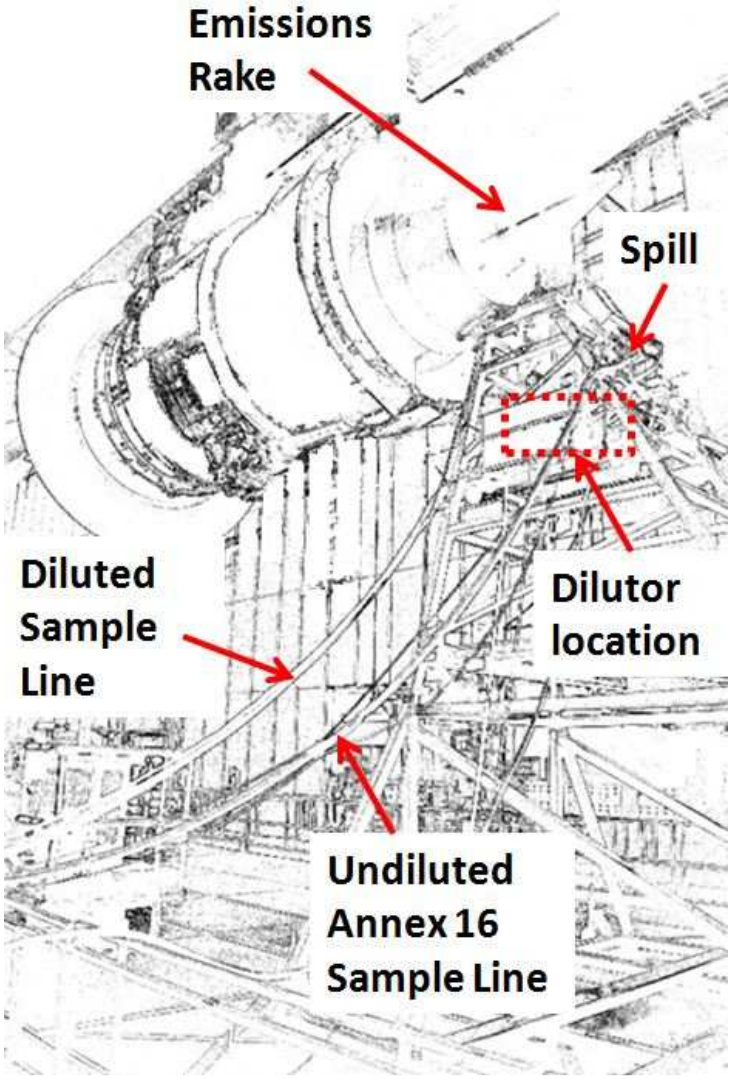

Figure 71 Photo-sketch of engine and sampling system on test bed.

In total two gas samples were provided to the analysis suite; an undiluted sample and a diluted sample (which are represented in more detail later in the report). The lines carrying these samples were capable of being trace heated to 160°C. The undiluted sample line was the existing Rolls-Royce Annex 16 gas/smoke sample line; the diluted line was specifically added for this test, adhering to current SAE E31 PM measurement guidelines.

7.3 Test Conditions and experimental variables

Table 12 shows the variables that were altered during the test in order to quantify the effects under consideration.

Table 12 Variables examined during the engine test campaign

Variables	Diluted line	Undiluted line
Engine power setting	ICAO 1: 7% ICAO 2: 30% ICAO 3: 80% ICAO 4: 100% Cruise type T Cruise type P	
Downstream dilution ratio	10:1, 100:1	NA
Diluted line temperature	160°C, 60°C	NA
Diluent temperature	160°C, 60°C	NA
Stages of dilution	1, 2	NA
Undiluted line temperature (orange line in Figure 76)	Between annex 16 line and diluted line: 300°C, 160°C	NA

The most challenging sampling point to measure was at a low power engine condition due to there being very little exhaust dynamic pressure entering the sample probe. This was also the condition with the perceived highest quantities of volatile particles that need to be removed in order to conduct non volatile PM number measurements.

Due to the considerations mentioned above along with the fact that this was the lowest fuel flow condition (therefore maximising project monies in terms of fuel consumption) a complete experimental matrix examining all of the line variables was undertaken at this low power engine condition. Owing to there being limited time available at the higher ICAO engine powers included pseudo-type cruise conditions a limited set of the important variables (as deduced from the earlier HES tests in Chapter 6) were tested.

In order to be able to test the sampling variables listed above, a remotely operated dilution system was required to be situated within 5 metres of the rake exit. The built system is shown in Figure 72 before and after trace-heating and lagging was added. Two Palas VKL 10E diluters were used with special Kalrez high temperature (323°C) seals inserted in order to allow high temperature sample input and dilution. High temperature pneumatically remotely controlled ball-valves (Swagelok T63M series) were used to switch between one diluter or two diluters in series. A Watlow ceramic heater (Cast x-1000 3Kw) was used to pre-heat the nitrogen diluent when required. Ejector-type dilutors create suction on their sampling inlet, thus a pump is not required to obtain a sample from the existing Annex 16 sampling line. The temperature of each section of the sampling system within the dilution box was independently controllable.

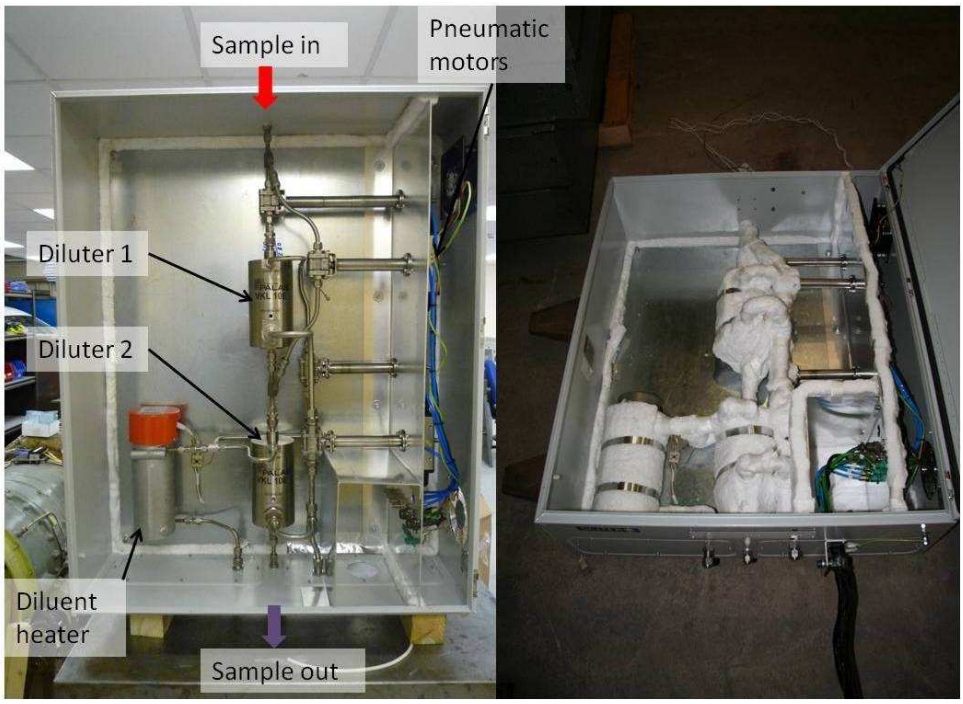

Figure 72 Photograph of engine dilution system, below with trace heating and lagging added on right.

The particulate measurement instruments for the engine testing are shown and annotated in Figure 73. Note that some instruments in the photograph are located on the undiluted line splitter but were placed onto the dilution line when required.

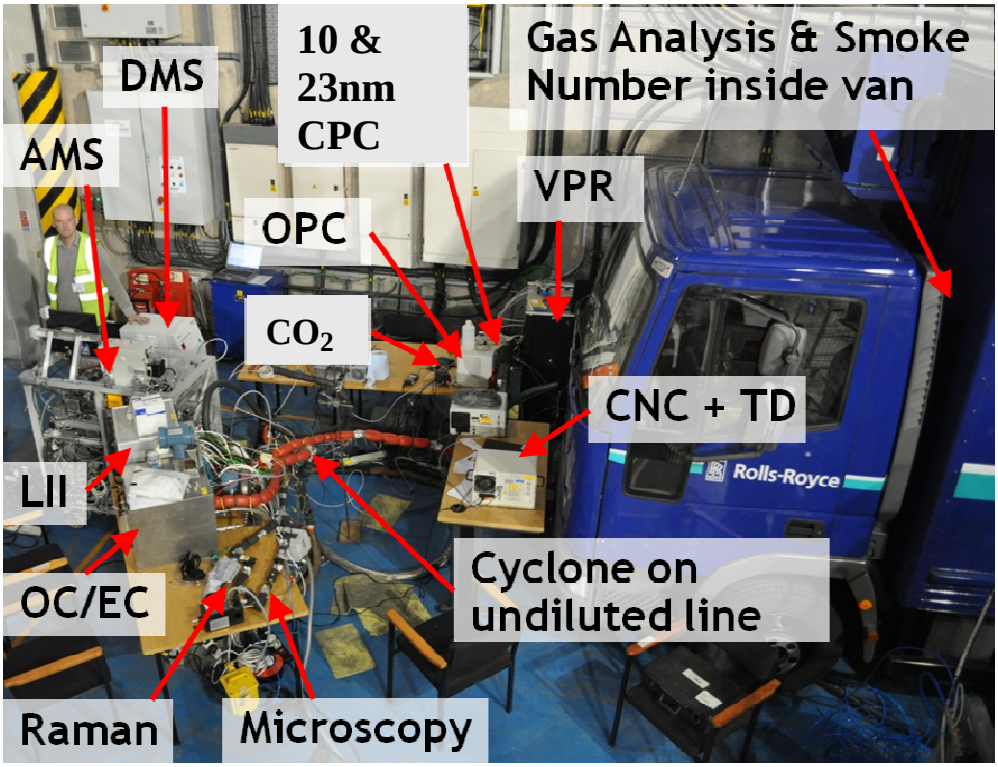

Figure 73 Photograph of initial engine particulate measurement setup before trace heating was added to undiluted splitter.

A closer-detail image of the AVL VPR system (discussed later in the report) and 7-way splitter as used in the HES test campaign (discussed earlier) is shown in Figure 74.

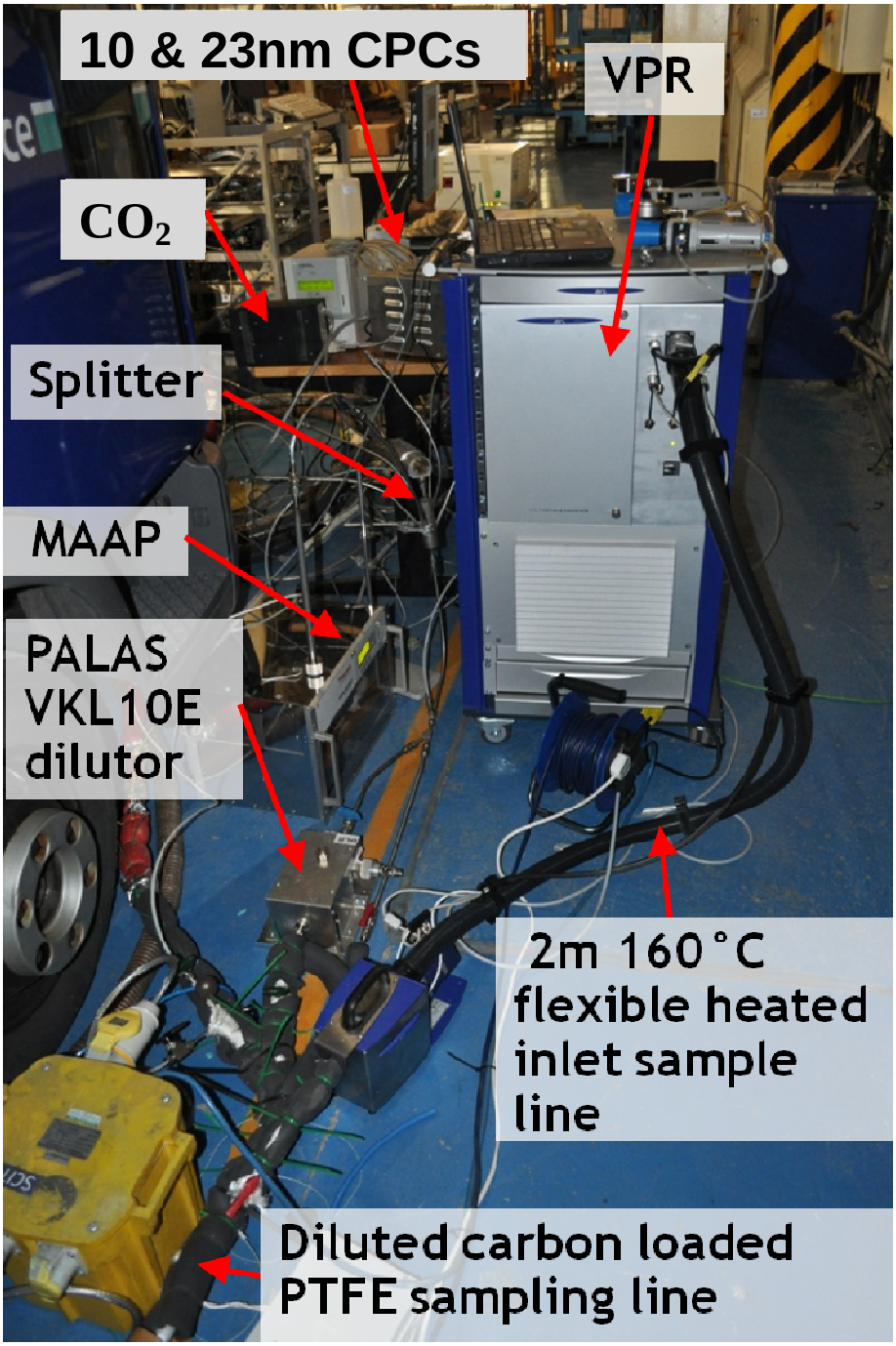

Figure 74 Photograph of dilution particulate system with the AVL volatile particulate remover.

Figure 75 Photograph of diluent Nitrogen banks and calibration gas (including 5000ppm and 500ppm CO2 for dilution analysers)

Two Nitrogen banks (99.99%) containing 11 cylinders were coupled together with the outlet fed through a particle (HEPA) filter (as shown in Figure 75) before being split to the various dilution points on the sampling system. Throughout the 3 days of testing, approximately 180m^3 of Nitrogen was used.

7.4 Sample line set up

Numerous CPCs (with different D_{50} lower cut-off limits) and a DMS were utilised during the large scale modern engine test to measure number concentration. Due to the forthcoming SAE E-31 PM measurement guidelines being based only on non volatile PM measurements, it was necessary to utilise a VPR to remove the volatile fraction of the exhaust gas. As there has been limited work conducted in the area of volatile particle removal in the aero industry it was decided that a commercially available PMP approved automotive VPR should be used. Thus an AVL unit, which uses an internal rotating/chopper diluter, was obtained and tested (Note that the evaporation tube within the VPR was maintained at 300°C). However, the PMP approach adopts a lower size cut-off of 23nm which is considered by current SAE E31 members to be too high for the measurement of aero exhausts owing to the relatively smaller PM witnessed in aero exhausts compared to those produced by reciprocating diesel engines. For this reason the VPR was

modified to allow both the standard 23nm counter along with a nominally identical 10nm counter to be tested simultaneously.

A schematic of the diluted and undiluted sample line set up is shown in
Figure 76. The set up was designed to take into account findings from the comprehensive HES sampling variables investigation (as highlighted earlier in this report) and was also based upon the expected 'Non volatile PM measurement methodology concept system' from ongoing SAE-E31 discussions.

Using existing Annex 16 methodology for the initial part of the sampling system, a splitter (with 30° off-takes and no internal shoulders) was placed as close as possible to the probe. Considering the physical geometry constraints of sampling from a large gas turbine engine, this distance was ~4m from probe tips to allow a second heated sampling line (as depicted by the orange line in
Figure 76 to connect to a variable dilution system and provide a diluted sample line for the particulate number measurements. This is depicted by the pink line in
Figure 76). The residence time from probe to the splitter for the inlet to the VPR, indicated by the dotted line and seen in the photograph of Figure 71, was 6.7s. This residence time includes the distance from the Annex 16 probe to the splitter for the dilution and along the 25m carbon loaded PTFE line. Variable heating of the initial sampling system (probe tip to splitter) up to 300°C was possible due to this particular emissions rake design, which allowed the emissions sample to cool sufficiently before entering the standard Annex 16 carbon-loaded PTFE heated line (to prevent melting of this line).

The design of the system was created prior to the Nov 2010 SAE-E31 Particle subcommittee meeting. During that meeting the decision was made to focus all (mass and number) particulate measurements onto the dilution line until there was evidence to suggest mass measurements can be taken on the existing undiluted Annex 16 line without further loss compared to the diluted line. Taking this decision into account, alterations were made to the sample system design to allow LII measurements to be made on the dilution line using an additional splitter and heated line. In order to obtain a sharp size cut-off of 1μm before the mass instruments on the Annex 16 line (note that the DMS already has a 1μm cyclone on the inlet to the instrument), two Cambustion cyclones were used in parallel. The reason for using two cyclones is due to the critical need to keep the flow through a cyclone at a specific rate (in this case 8 SLPM) to keep the cut-off at the prescribed size. However, the instrument flow requirements of 16 SLPM meant that obtaining one commercially available cyclone for this task was not possible, so two 8 SLPM cyclones in parallel were used instead.

Due to the scarcity of current large modern engine testing being dedicated to particulate emissions testing, a variety of PM characterising measurements were obtained. This setup is thus not identical to the current SAE E31 proposed non volatile PM measurement procedure, as multiple methods will not be required to measure the metrics of PM size and mass. A detailed schematic, including the operational sample flow rates of the diluted line PM measurement system is shown in
Figure 77. The additional 5:1 diluter was placed upstream of the 7-way splitter due to the need to reduce the sample temperature down to a required ambient level necessary for the CPCs and MAAP (without incurring thermophoretic losses). It was also undertaken to attempt to keep the

CPCs in their relevant 'single count' measurement ranges (no VPR present to provide additional dilution) especially when only using the low (10:1) dilution ratio at the primary dilution location.

The use of this additional instrumentation was carefully scheduled to ensure minimal impact on the primary objectives of the test. The addition of the instrumentation makes the sampling setup appear complicated and unlike the expected certification PM measurement sampling system. However, careful scheduling and operation of the system provided both comparisons of expected PM certification data and also full characterisation of the non volatile and volatile particle fractions. The total sample flow in the PM sample line was kept constant as possible (24 SLPM) thus providing similar line losses for every test point.

On a technical note the Palas VKL 10E diluter operated downstream of the 25m line as shown in
Figure 77 provided a 5:1 dilution ratio, rather than the expected designed 10:1 dilution ratio. Modifications of diluent pressure appeared to make no significant difference. This practical issue should be considered in future testing, since it was also witnessed during the HES campaign using a different manufacturer's (Dekati) eductor diluter system.

An example of a specific sampling setup (with a total of 24 SPLM) is shown in
Figure 78, where the system was configured to obtain a non volatile PM number measurement (not mass) where the particulate measurement suite is only being used as 'make up' flow to ensure the 24 SLPM condition was met. This type of setup ensured that sample line flow rates and pressures were replicated throughout the various test points allowing good data comparisons of non volatile PM number across numerous engine power conditions to be made. Note when the additional diluter was utilised, the dilutor inlet flow was 5 SPLM therefore the LII/AMS line was connected to ensure the 24 SLPM condition was met.

As can be seen in
Figure 77, CO_2 is measured in numerous positions along the sample line in order to assess the dilution ratios of the various dilutors. Typically there was the requirement for 3 different CO_2 analysers in order to cover the ranges of CO_2 to be expected after each stage of dilution (raw exhaust, after 5m diluter & after 25m diluter). For the lowest levels of CO_2 witnessed after the two stages of dilution where dilution ratios were of the order to 500:1, levels of CO_2 are of the order of 70ppm. As the lowest range analyser that was available for this study was 1000ppm it meant that the expected associated measurement errors (±2% of range) meant that the uncertainty could be as high as 30%. This has a significant impact on the final uncertainty of a particulate measurement. The uncertainty of measurements of dilution ratios above 1000:1 using standard commercially available analysers would incur final particulate measurement uncertainties of >100%. Careful attention should be shown when comparing datasets obtained with high dilution ratios.

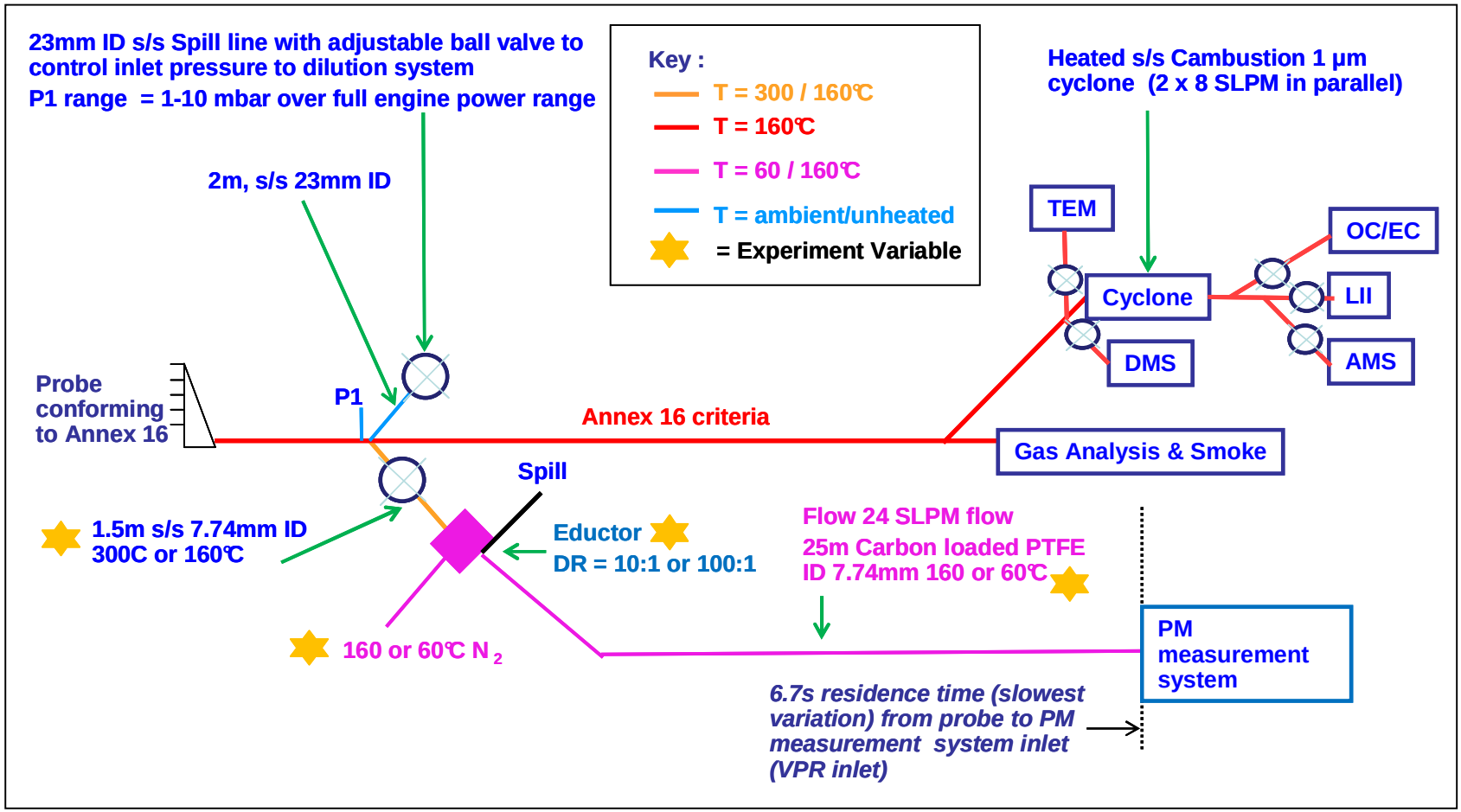

Figure 76 Schematic of sampling system detailing both current Annex 16 line along with additional diluted PM measurement line

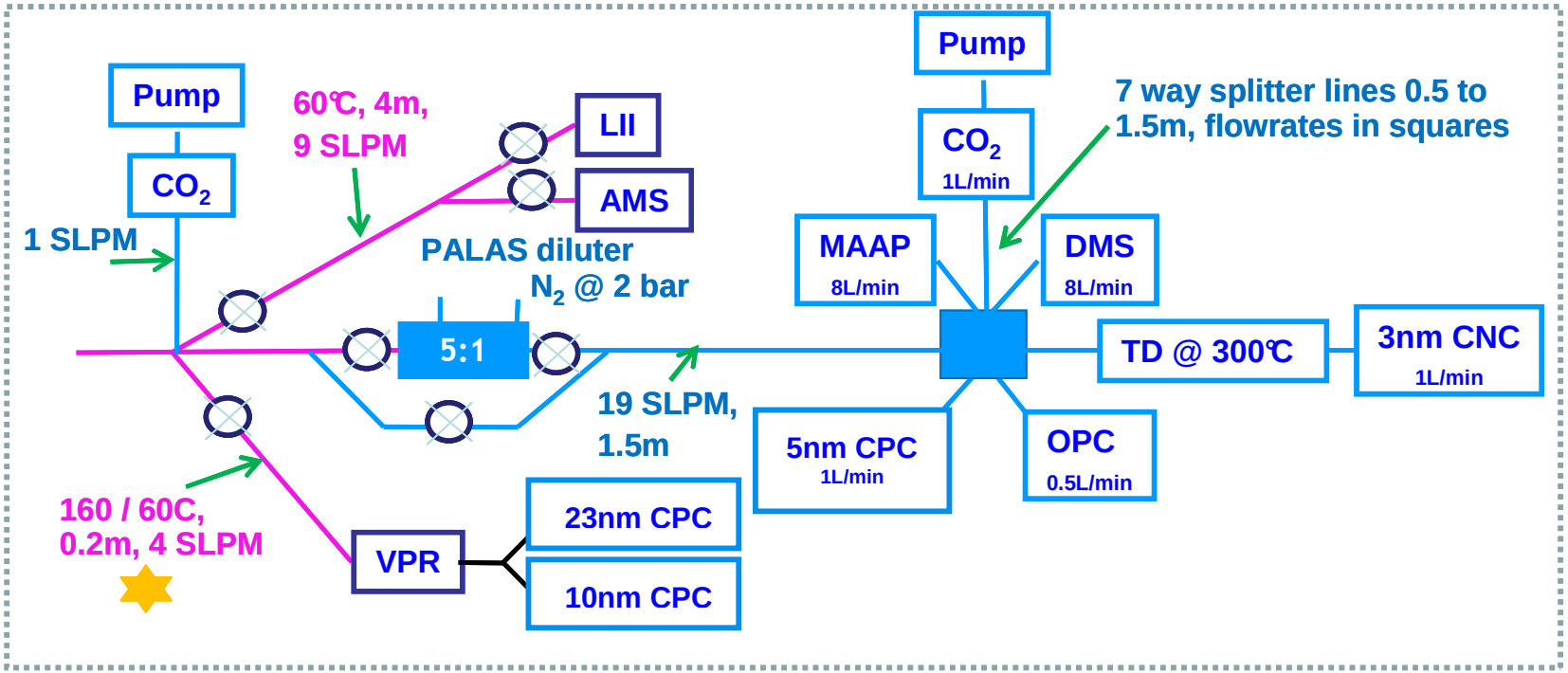

All lines s/s 7.74mm ID except for black colour = conductive flexible tubing 4mm ID (same colour key as previous slide)

All splitters straight-through with 30° angle

Figure 77 Flow rates within the various branches of the 7 way splitter are indicated by the numbers in each instrument box (SLPM)

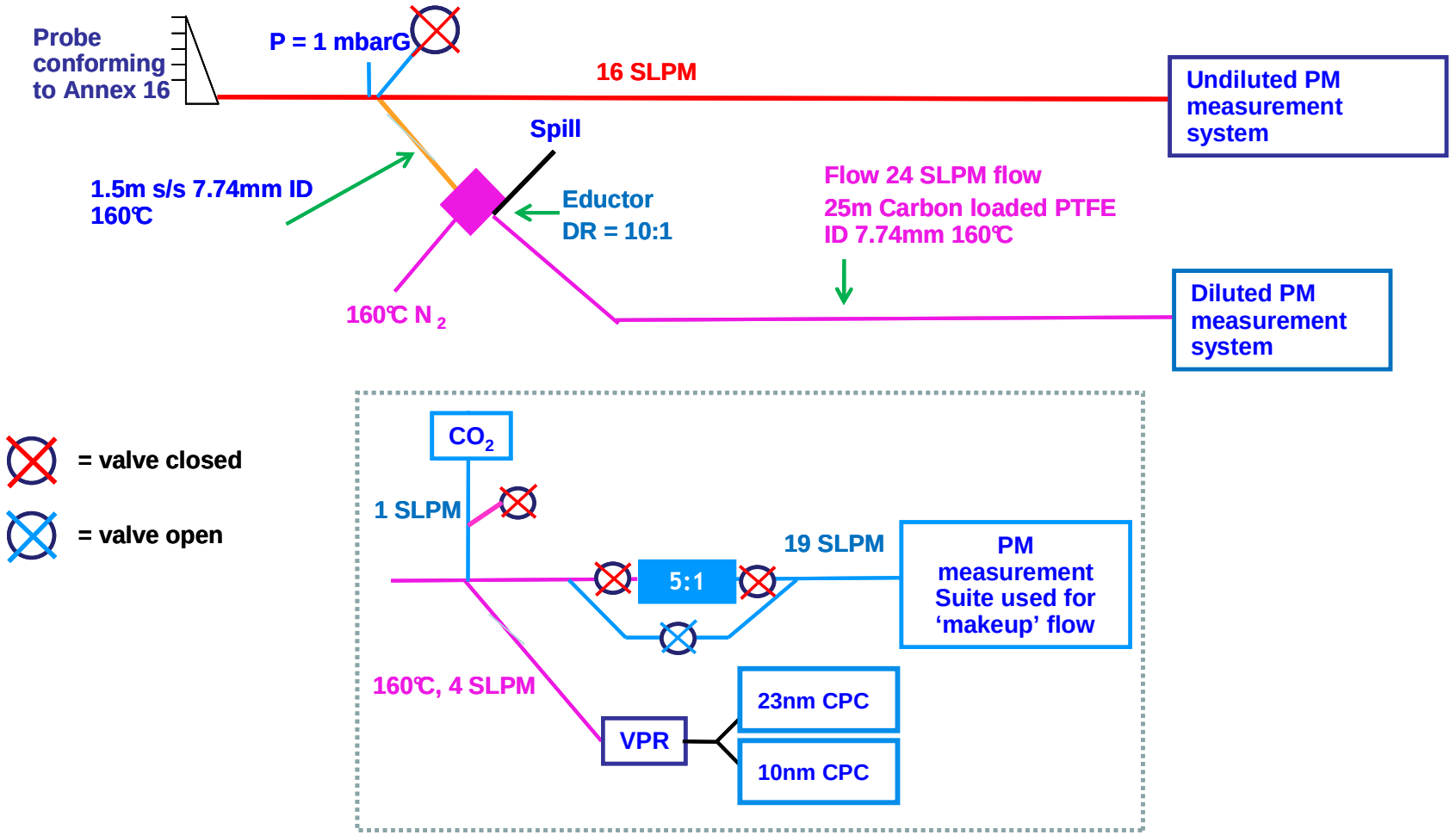

Figure 78 Simplified example of experimental layout for low power engine condition, 160°C sample inlet temperature, 160°C diluent and sample line temperature, dilution ratio 10:1

8. Experiment results - Large Modern Civil Aero Engine trials

8.1 PM number measurements

Figure 79 shows the number concentrations measured using both the 10 & 23 nm counters positioned after the PMP approved AVL VPR system, where numerous trends can be observed. At 10:1 dilution there is always a greater measured number concentration utilising the 10 nm lower cut-off CPC compared with the 23 nm lower cut-off CPC over all of the temperature ranges tested. Typically this offset shows a 20-30% increase in number count using the 10 nm lower cut-off CPC. There are a number of plausible explanations depending on whether the particles in the range of 10-23 nm are volatile or elemental carbon. If it is believed that the particles in this range are volatile then the data would suggest that the VPR is not completely removing all volatile PM. However, the microscopy and LII results from the HES test campaign (as discussed earlier) suggested that the primary particle PM size is approximately 15 nm which supports the possibility that there may be elemental carbon particles in the 10-23 nm size range which would account for the discrepancy in number concentration.

At 100:1 dilution there was a reduction in both 10 nm and 23 nm particles compared to 10:1 dilution with typically a 10% reduction witnessed in both counters. This reduction is consistent with the associated losses expected by adding an additional eductor dilution stage. However, once again this could be attributed to the more efficient removal of volatiles if a higher primary dilution ratio is utilised.

At 100:1 dilution, with the diluter inlet temperatures at 300°C it is observed that there is a marked reduction in the measured number concentrations of both the 10 & 23 nm lower cut-off CPCs. Interestingly for this case both counters show the same number concentration, which is different to all other cases. This seems to support the theory that the majority of particles in the 10-23 nm size range are predominantly volatile and the VPR is not fully removing the volatile fraction of the exhaust. If this data is to be believed then it suggests that the most effective method to remove the volatile fraction would be to keep the exhaust sample hot (~300 to 400°C) thus preventing the volatile component from condensing and then diluting at a high ratio (100:1).

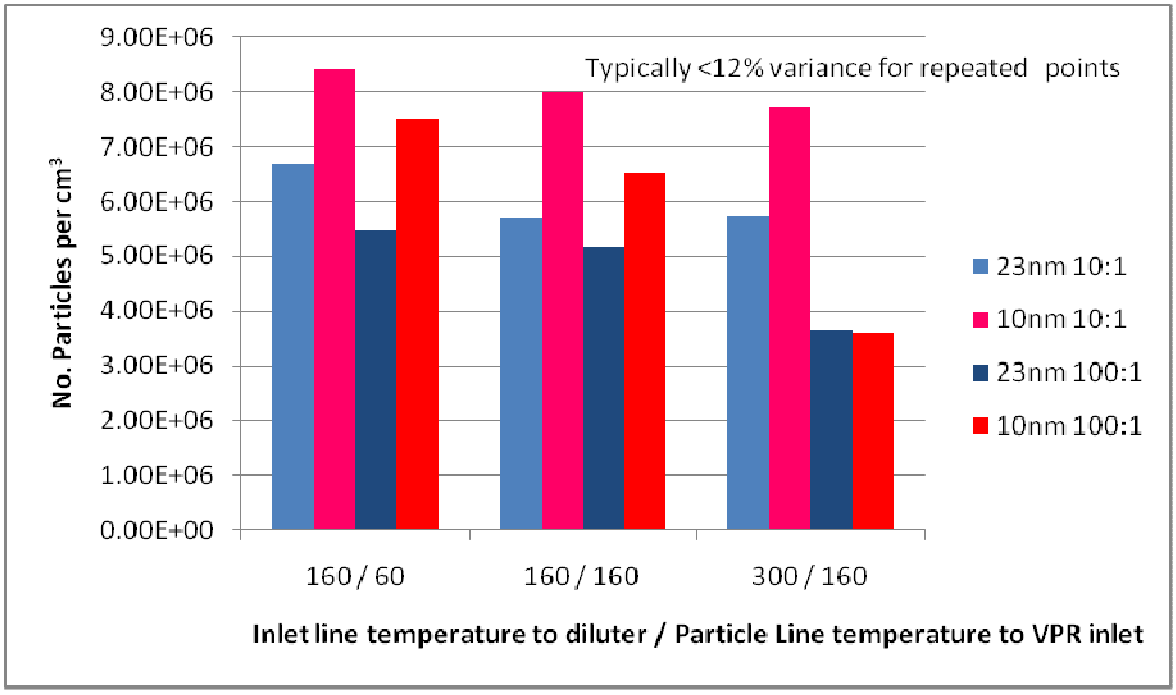

Figure 79 CPC number concentration results from VPR experiment showing effect of diluter inlet temperature and diluted sample line temperature over a series of particle cut-off sizes and dilution ratios.

The data from Figure 79 is represented in a different format in Figure 80 to illustrate the typical offsets in number concentration between the 10 & 23 nm lower cut-off CPCs. The y-axis shows the ratio of number concentration as measured by the 10 nm lower cut-off CPC normalised against the comparable value measured by the 23 nm lower cut-off analyser. It should be noted that if the particles in the 10-23 nm range are purely volatile and the VPR is 100% effective at removing the volatile fraction it would be expected that all the discrete data points should lie on the blue 1.00 ratio line. However as can be seen only the data points taken at the 300°C inlet temperature lie on this line (with good repeatability at the higher 100:1 dilution ratio). Data below the line are within instrument uncertainties (each CPC is ±5%, therefore 10% is within experimental error). This again supports the statement that the VPR may not be effectively removing the volatile fraction and the most effective way of conducting this is to keep the sample hot (>300°C) and dilute with a high ratio (100:1) to ensure there is no chance of condensation of volatiles in the remaining 25m sample line.

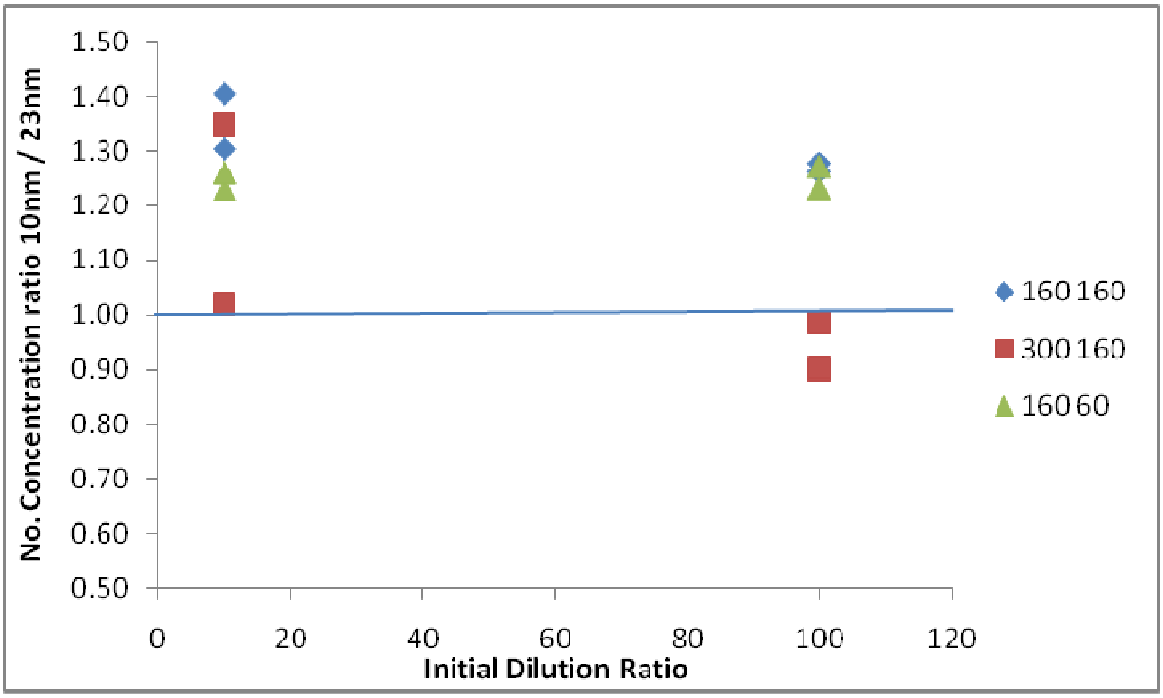

Figure 80 CPC number concentration results from VPR experiment showing effect of dilution ratio over a series of diluter inlet temperature and VPR inlet temperatures.

Figure 81 shows the CPC Emissions Index (EI) PM number concentrations, as measured downstream of the VPR for the 6 engine conditions studied during the trial. As can be seen it was observed that the maximum number concentration is witnessed at the ICAO 2 engine power and the minimum witnessed at the ICAO 4 condition. It was also noticed that again the 10 nm lower cut-off returned greater number concentrations than that of the 23 nm cut-off. The missing 10 nm cut-off data (at ICAO 3, 4 and Type Cruise T) is attributable to low butanol levels in the CPC reservoir. On a practical note, the design of the CPC system does not adequately alert the user to this problem and hence it should be borne in mind for future PM testing. These observed number EIs fit generally within the expected range compared to measurements made upon legacy engine technology. Even though sampling systems of previous experimental particulate campaigns did not match the current expected SAE-E31 PM measurement methodology.

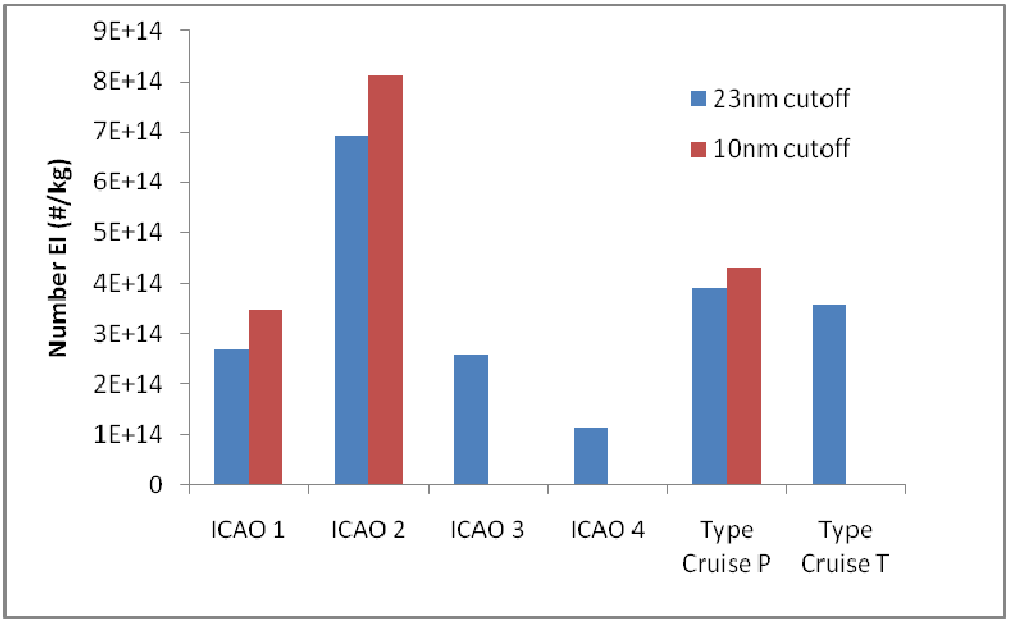

Figure 81 CPC Emissions Index number concentration over a series of particle cut-off sizes for the 6 engine conditions tested.

Comparisons between a variety of CPCs with different lower size cut-offs were made when the dilution ratios were high enough to bring all the instruments into their detectable range limits (and single count rather than photometric mode). This occurred when the dilution ratio was nominally set at 500:1 (100:1 at initial dilution point plus 5:1 at downstream dilution). The 23 & 10nm CPCs behind the VPR were placed on the 7 way splitter with the 5nm CPC. Table 13 shows the normalised comparison to the 5nm CPC, as expected significant differences are observed between 23 and 10 nm (20%), but almost no difference between 10 and 5 nm (2%). In addition, as expected when compared with Figure 79, when the inlet sample line temperature is high the volatile number component is much reduced and very little difference is observed between utilising a 23 or 5 nm lower size cut-off.

Table 13 Normalised comparison (5nm absolute values were 6.25 x 10^6 and 3.92 x 10^6 #/cc for 160/160 and 300/160 conditions respectively) of three different lower size cut-off (D50's) CPCs for different sampling line conditions (Note CPCs not behind VPR) with dilution ratio nominally at 500:1

	23nm	10nm	5nm
160/160	0.77	0.98	1.00
300/160	0.98	0.99	1.00

Due to the multitude of experimental variables it was only possible to test the simple thermo-discriminator (short heated pipe at 300°C) at a couple of measurement points in front of a 3nm CPC. In
Table **14**, it can be seen that volatile material is removed from the PM sample (as sown in

Figure 77 the thermo-discriminator was not after the VPR). The amount of volatile material removed is very likely to depend on engine power condition, due to there being higher volatile fraction at lower power as demonstrated in the HES tests.

Table 14 Effect of using thermal discriminator to assess the effective volatile particle number reduction. Measurements obtained with 160°C sampling lines and 10:1 dilution ratio.

	Thermodiscriminator @ 300°C		
	With	Without	Volatiles %
ICAO 1	3.55E+06	4.12E+06	13.83
Type Cruise P	2.94E+06	3.16E+06	6.96

Eductor dilutor particle losses were assessed by switching in additional eductor diluters and keeping the flow rates constant such that losses in the sampling system were similar. Again due to the multitude of experimental variables, this assessment was only performed on a limited number of measurement points. The data is summarised in Table 15.

Particle losses are generally higher (or at least comparably the same) for the lower size cut-off (10nm) CPC. This is unsurprising as aerosol diffusion loss theory dictates higher losses for smaller particles, hence the expectation that the losses would be higher for the lower size cut-off.

Assuming that the VPR performs efficiently (which is a big assumption due to the data shown in Figure 79), the observed losses for the higher temperature sampling condition case look much larger than the rest of the data. However, this can be explained by the likelihood that the VPR has not removed all of the volatile material and the effect of adding in a higher dilution ratio is prevention of condensation rather than particle losses due to the addition of a diluter. Therefore to perceive the effective particle loss effect of an eductor dilutor, comparable data for 160/60 and 160/160 conditions with identical sampling systems should be analysed. Averaging the two datasets for the CPCs behind the VPR across both conditions, it was observed that for a single PALAS VKL10E dilutor, total number particle loss for a 23 nm cut-off was 10%, and for a 10 nm cut-off it was 15%.

Table 15 Particle losses (%) due to inclusion of additional eductor dilutor. The dataset was obtained on a low power condition with measurements obtained by comparing test point data from using either one or two dilutors in series.

	23nm	10nm	
160/60	11	10	CNC's behind VPR
160/160	9	18	CNC's behind VPR
300/160	36	53	CNC's behind VPR
160/60	17	19	no VPR
160/160	4	11	no VPR
300/160	13	34	no VPR

8.2 PM mass measurements

8.2.1 PM 'Black Carbon' mass measurements

Non volatile mass measurement was attempted utilising both the MAAP and Artium LII-300 black carbon mass measurement techniques. Due to limited testing times on each of the conditions (5 to 10 minutes) it was found that there was insufficient time for the MAAP to stabilise to a statistically reliable result using the commercially available onboard logging algorithms. The LII instrument samples at a much higher rate (20Hz) thus was successfully used to measure mass for each of the ICAO power conditions, this data is represented in Figure 82. As can be seen once again as witnessed with the non volatile number data (Figure 81) the highest values witnessed during the four ICAO power settings are witnessed at the ICAO 2 power setting. The general trend of EI mass follows that observed for EI number for the ICAO power curve. However, it should be noted that in the case of EI mass there is a marked difference observed at the two pseudo 'cruise' type conditions which was not the case in the EI number measurements. It is noted that the Type T cruise condition witnessed the highest values of mass. However, on comparison with the number data it is noted that comparatively low number concentrations are observed on the same condition (Figure **81**). This discrepancy indicates that there must be shift in size distribution between the two cruise type conditions with the T type condition exhibiting a larger size distribution than the comparative P Type condition (see Section 8.3).

Unfortunately due to operator error the Auto-Range option was switched off in the LII instrument. This resulted in the majority of the signals obtained being saturated at the point of on-board processing, resulting in the lack of accurate mass comparison data between the current undiluted Annex 16 and 'new' PM diluted line at different dilution ratios. However, following discussions with the instruments manufacturer, it was determined that the LII analysis software allows for an estimation of mass concentration using the unsaturated tail-end of the data signals. Using this method the absolute mass concentration will be under-predicted but are well within the order of magnitude (for example possibly up to 3 or 4 times higher) and the trends will be reasonably correct.

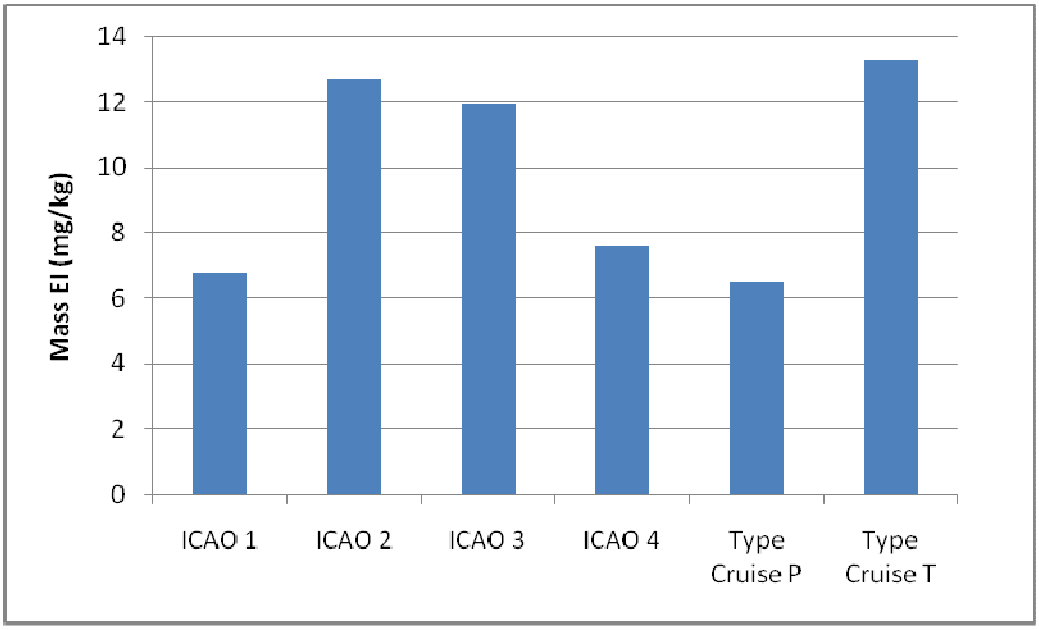

Figure 82 LII Emissions Index mass concentration over a series of particle cut-off sizes for the six engine conditions tested.

When the LII was located on the PM dilution line (at a lower power condition only) with a 100:1 dilution ratio the data signals were not saturated, above the detectable limit (mass concentration >0.5µg/m^3), and therefore suitable for quantitative analysis. This had two benefits;

(i) Proving measurement capability of LII-300 at very low non-volatile mass concentrations (raw data ~3 µg/m^3).

(ii) Excellent data was obtained which was used to assess the impact of line temperature on non-volatile mass concentration and is shown in Table 16. It can be clearly seen that there is no impact of line temperature on non-volatile mass concentration.

Table 16 Non-volatile mass concentrations (dilution corrected) for different sampling line temperatures

°C	EI (mg/kg)	σ
160/60	33	5
160/160	30	5
300/160	32	6

8.2.2 Volatile PM measurements

8.2.2.1 PM Volatile Mass measurement

Volatile particle mass was measured during the engine testing using an Aerosol Mass Spectrometer (AMS) similar to that utilised in the HES testing. The instrument fluctuated between being placed on the Annex 16 and PM line. The graphs shown below in Figure 83 illustrate the volatile mass spectra at various engine power conditions. The similarity in fragmentation shape indicates that the composition of the volatile aerosol does not change across the engine power curve. The only change observed was the height of mass peaks which relates to the total amount of volatile and is shown on the individual graphs within Figure 83 per power condition. The trend is that volatile mass concentration peaks at mid-to-high power conditions. This trend was not foreseen due to previous published measurement data from APEX3 indicating that highest volatile mass concentrations are usually associated with low engine power conditions. More understanding is required on how the sampling system may impact volatile mass measurements. Unfortunately due to an instrument malfunction, data was not obtained for the Cruise Type T condition.

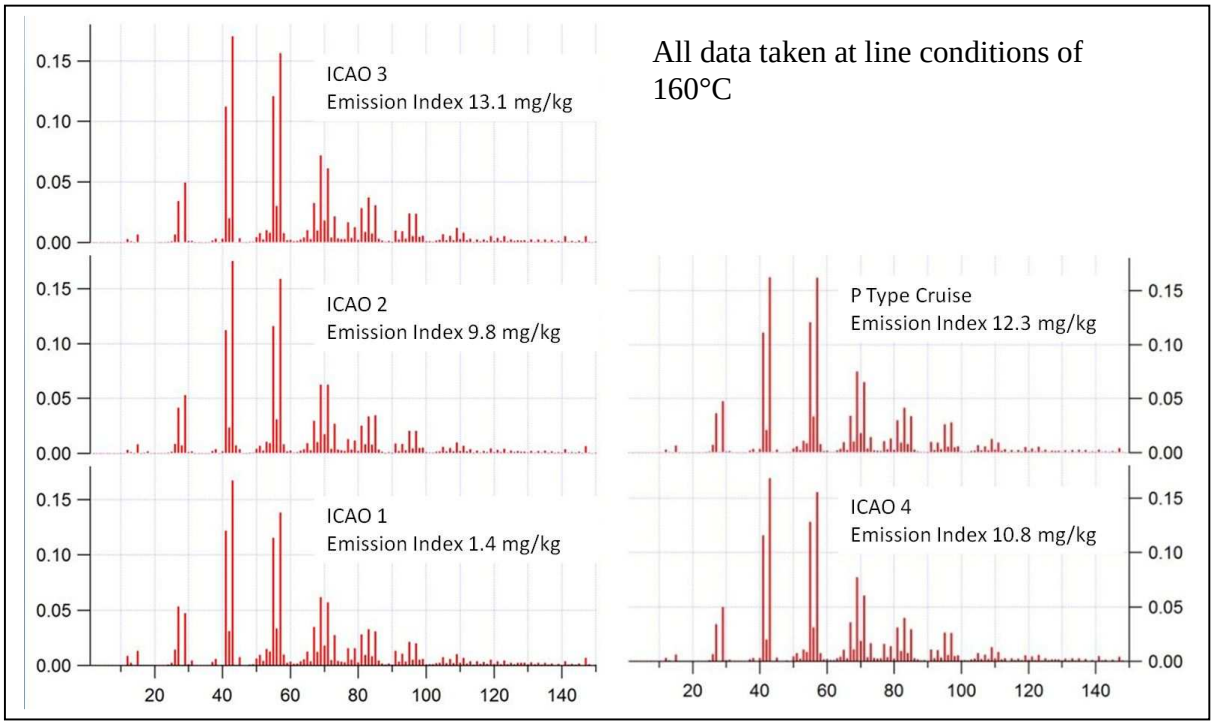

Figure 83 Volatile aerosol mass fragmentation spectra obtained with No. of ions per channel on y-axis and m/z (mass/charge ratio) on x-axis. Stated total masses is the sum of all peaks.

8.2.2.2 Ion Chromatography and Gas Chromatography-Mass Spectrometry results

Offline techniques were applied once during the tests to give an indication of the relative

performance of chemical analysis versus on-line methodologies. The Ion Chromatography (IC) technique involved passing the gas sample through de-ionised distilled water followed by subsequent analysis using commercially available IC apparatus located at Cardiff University. Results showed that at the ICAO 1 condition, with sample lines at 160°C and laminar flow, sulphate concentrations were 71.1 mg/m^3 and nitrates were 9.0 mg/m^3.

Figure 84 shows the Gas Chromatography Mass Spectrometer (GC-MS) results for the filter that was collected. It is interesting to note that in this case, a series of organic compounds were detected over the PAH (Polycyclic Aromatic Hydrocarbons) range analysed. Additionally to this filter, a sample of the engine lubrication oil was processed with the same GC-MS methodology. The results indicated that there were no PAH-range organic species present in the engine oil.

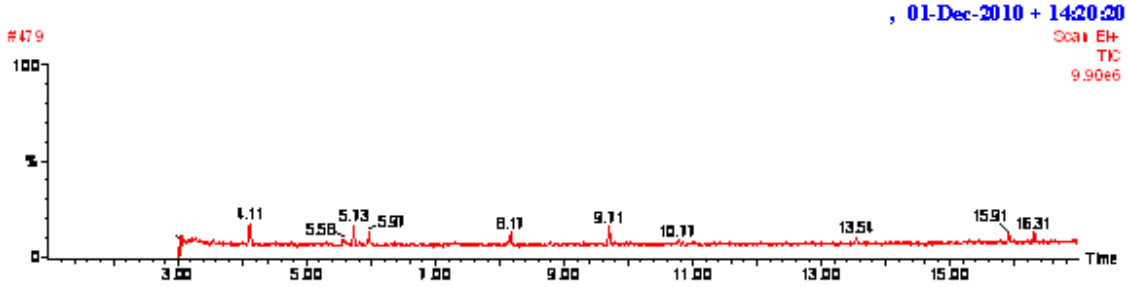

Figure 84 GC-MS chromatogram of PM sample from filter.

8.2.3 Total mass measurements (DMS)

Assuming particle sphericity with a carbon material density of 1.8g/cm^3 and an effective density of 1, total (volatile and non volatile) aerosol mass was calculated from DMS data and is shown in Table 17. Comparing the two inlet line temperatures (to the initial dilutor) it can be seen that the higher line temperature results in a lower total mass for all dilution ratio conditions. This is expected (see Section 8.1) due to the higher line temperature preventing condensation of organic aerosol from gas-phase precursors before dilution, where sample chemistry is 'frozen'.

Comparing the average data difference (15.3 vs 10.2 mg/kg) indicates a volatile mass fraction of ~5mg/kg. For the AMS low engine power condition (ICAO 1), the volatile mass fraction was 1.4 mg/kg, so approximately one third of the DMS size distribution calculation. However, this difference is probably attributable to the DMS assumption of material density for solid carbon rather than a mixture of solid carbon, organic carbon and sulphate aerosol.

It should also be noted that there may be minor differences between the techniques due to the sampling lines and flows being different (particle penetration losses different) and in addition the lower size cut-off of the measurement range for the AMS is around 40nm whereas for the DMS it is 5nm.

Table 17 Total aerosol mass in EI mg/kg (corrected for dilution) for different inlet sampling line temperature (160 & 300°C) and dilution ratio conditions (nominally 10, 50 & 500:1) at low engine power

	10:1	50:1	500:1
160/160	11.2	21.2	13.5
300/160	9.3	12.4	8.8

8.3 PM size measurements

Both the DMS and OPC were used to observe and understand the particle size distributions within the large modern aero engine exhaust. The DMS measured in the 5-1000nm size range and the OPC measured in the 250-32000 nm range. The size distributions for different sample line conditions and dilution ratios were measured on a low engine power condition using the DMS are given in Figure 85 and Figure 86. The size distributions measured over the entire engine power range are shown in Figure **87**.

Comparing the two inlet line temperatures in Figure 85, the number concentration is reduced by 13% (above experimental error) indicating that the first mode (at 23nm) contains volatile aerosol (whether in the form of solid particulate coating or in homogeneous form is unknown). In addition, the slight shrinkage in the second mode from 53 to 51 nm is probably due to the higher line temperature preventing growth of PM due to organic coating and matches with the data shown in Table 17.

The size distributions in Figure 86 show insight into the 'mixed' first mode phenomena. Tri-modal distributions are observed as the dilution ratio is increased. The higher dilution ratios are much more successful at 'freezing'/preserving the particle size distribution within the sampling system. According to conventional aerosol theory, coagulation growth rates at these relatively low particle concentrations are much larger than the order of seconds, observed in this sampling system. Therefore this phenomena (merging the purely volatile mode with soot particles) is likely due to the condensation of volatile aerosol, with a 10:1 dilution ratio not being high enough to prevent condensation at a low engine power (high unburnt hydrocarbon) condition.

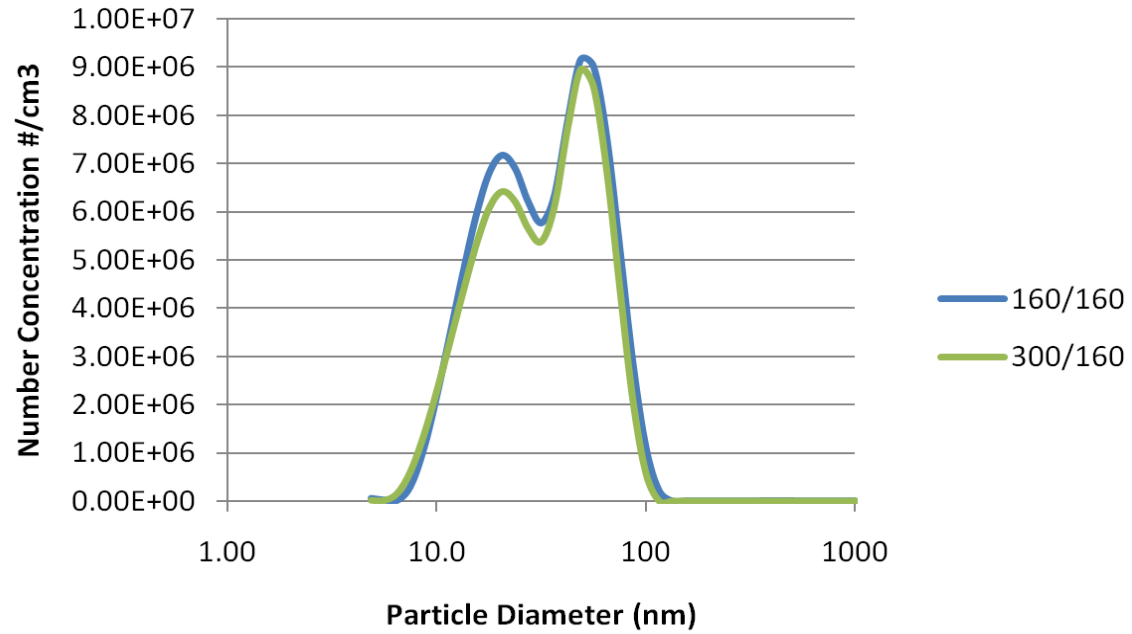

Figure 85 Size distributions measured using DMS for different sample line conditions with 10:1 dilution ratio at low power condition

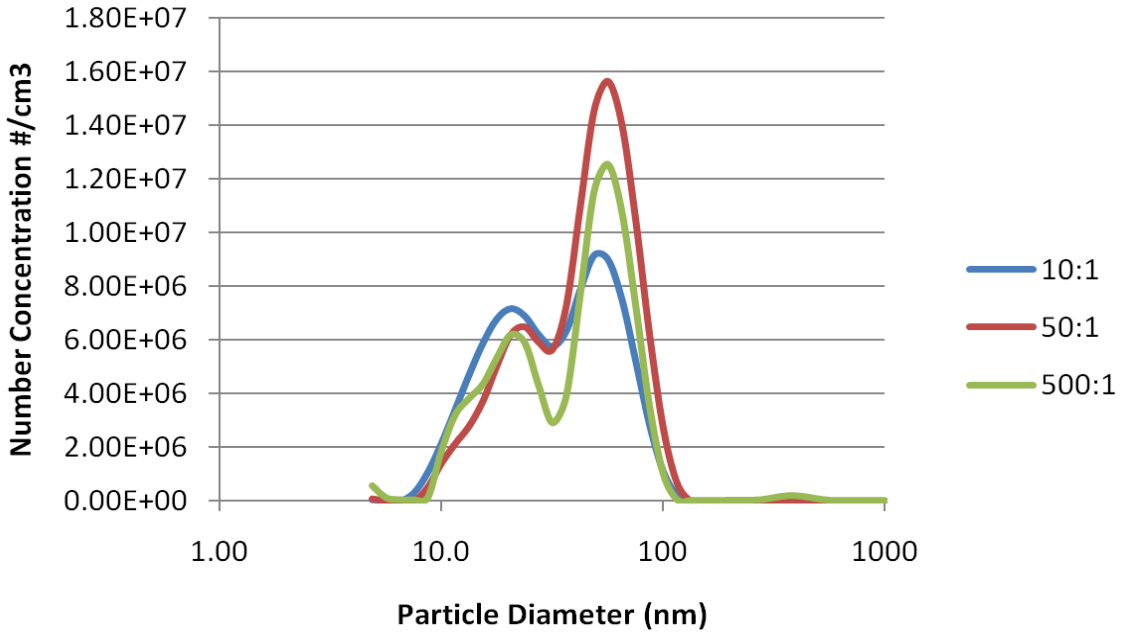

Figure 86 Size distributions measured using DMS for different dilution ratios with 160°C (160/160) sample line conditions.

The size distributions measured across the engine power range (Figure 87) all have a similar bi-modal shape (note all data taken at 10:1 dilution ratio) with no distinct third 'purely' volatile

mode (expected at <15 nm). The third mode could be underlying the distribution but is masked by the first mode which peaks at ~17 – 20 nm

The first mode drastically reduces in number concentration with increasing engine power condition. This is to be expected if the particles in this mode are assumed to be volatile or a form of mixed non volatile/volatile, due to the hydrocarbon measurements decreasing to virtually negligible levels as the engine power increases (Note that the AMS does not measure particles below 40nm, so therefore does not detect this variation).

For the second mode, there are significant shifts in distribution (from 50 – 60 nm), specifically the location of the right-hand-side of the second mode, this has a huge impact on the relevant particle mass and corresponds to the differences noted in Figure 82. The general trend is for higher engine power conditions to have larger GMD's (for both first and second modes).

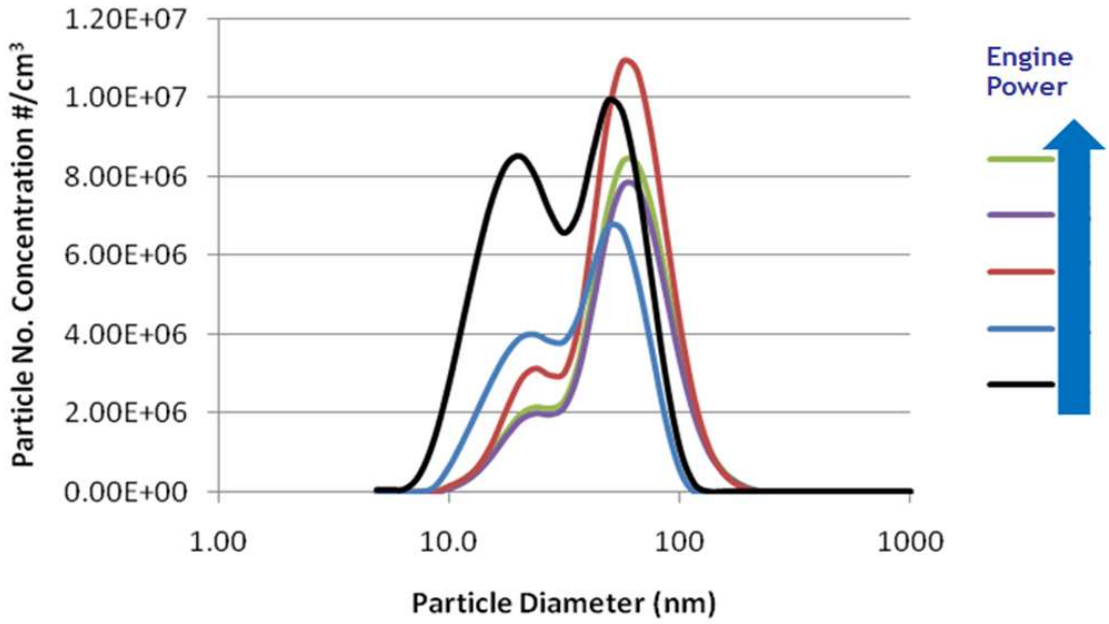

Figure 87 Size distributions measured using a DMS across the range of engine power settings, Sample line conditions at 160/160 with a 10:1 dilution ratio

Figure 88 shows the number concentration distribution for the different size bins measured using an OPC. As can be seen it is witnessed that the majority of the particles are counted in the <1000nm range for each of the line conditions. This agrees well with the expectations of current scientific opinion (within SAE E31) which suggests that all aero exhaust PM is in the range of 1-1000 nm. It is most likely that the particles are shedding from the walls of the sampling system or possible background aerosol ingested into the engine (the data is not corrected for ambient measurements). It should be noted that the number concentrations are very low (by several orders of magnitude) at these larger (>250 nm) size ranges when compared to the numbers witnessed at the lower (<100 nm) size bins .

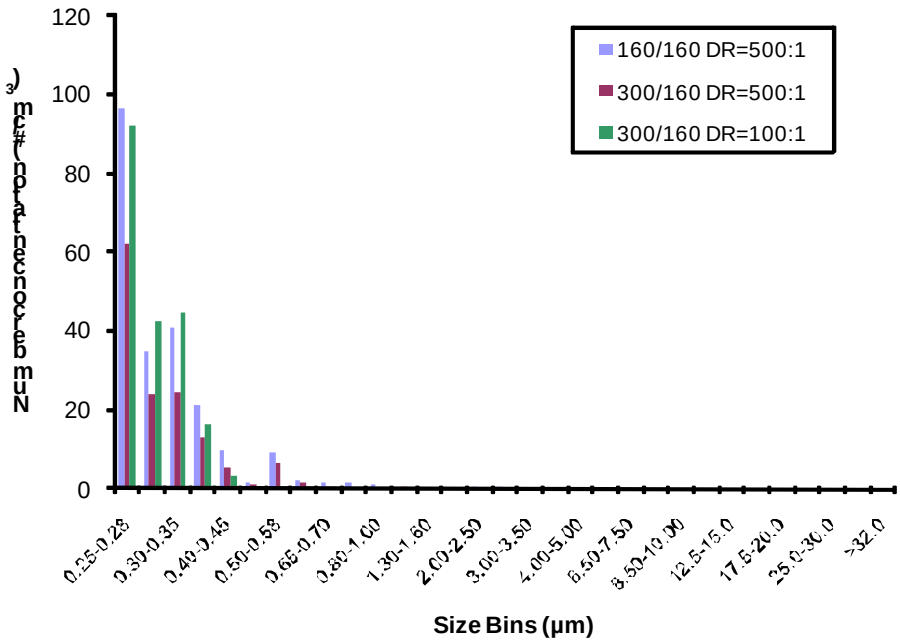

Figure 88 OPC Number concentrations for various sampling conditions at a low power engine condition

If a mass is assumed from the particle measurement performed by the OPC as given in Figure 89 then it can be seen that in certain circumstances it appears that not all the mass is measured within the 1000nm cut-off point. It can be seen in the 160/160 low engine power case that it appears that nearly 40% of the mass occurs for particles of greater than 2000 nm, this is surprising as the number concentrations for this size bin are minimal. However, due to volume, and thus mass, being calculated as a cubic of the measured size it is highlighted that a few relatively large particles (the OPC was not downstream of the 1µm cyclone) can massively skew the mass data, as was witnessed in the LII data performed in the SAMPLE I test campaign.

This 40% accumulation of mass of particles greater than 1000nm was accounted for by only 0.2% of the total number counted for all size bins measured using the OPC, highlighting the need to understand the requirement of ensuring large artefacts from shedding in the sample line need to be removed before performing a mass measurement.

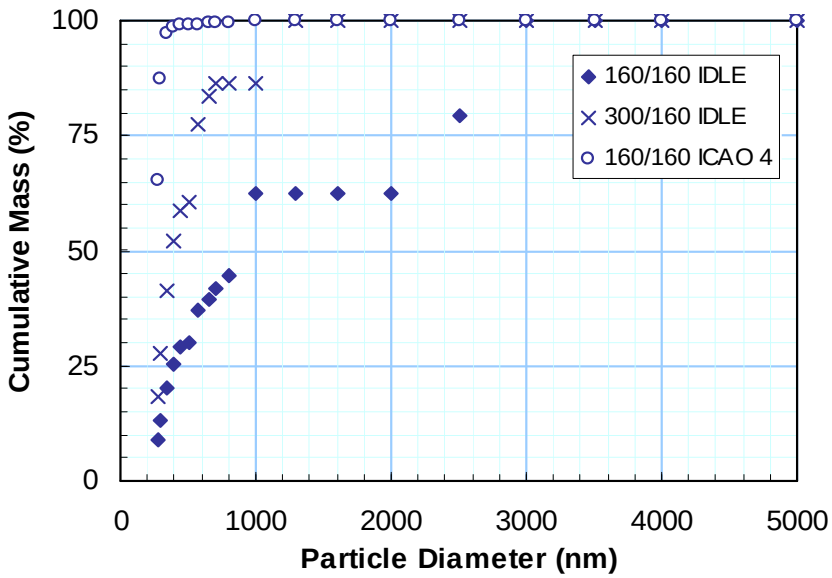

Figure 89 Cumulative Mass undersize plots for OPC data

8.4 Conclusions - Large Modern Civil Aero Engine trials

The principal conclusions from the engine tests are as follows:

- A successful demonstration of an eductor-type PM system in conjunction with a modified Annex16 sampling system (as currently proposed by SAE E31) to measure non-volatile PM number and mass has been undertaken.
- In agreement with the HES test campaign, where dilution was added at 7m downstream of the sampling probe, it was observed that a dilution ratio of greater than 10:1 promoted significantly lower number counts (above the expected losses of an additional diluter stage), suggesting that the volatile particles are not fully removed at low dilution ratios.
- Overall non-volatile PM measurements are not influenced by sample line temperature with almost no difference in the 160/160°C and 160/60°C cases for the Number measurement, and no difference between the 300/160, 160/160 and 160/60°C cases for the Mass measurement. This is confirmed by HES test data.
- When operating eductor-type dilution systems, it is difficult to achieve a specified dilution ratio. This has been attributed to the balances of pressures between the inlet, outlet and diluent flow. Hence in the case of this test, and in agreement with trends witnessed during HES testing, the 25m downstream dilutor produced lower than expected dilution ratios.
- It was observed that there was a 20% – 30% discrepancy in number concentration measured using the 10 nm and 23 nm CPC behind the AVL VPR system. However, this trend was not witnessed when the sample temperature was kept high (>300°C before dilution and 160°C between dilution and VPR) and dilution was high (>100:1). This may

indicate that the VPR is not 100% effective at removing the volatile fraction for aero engine exhausts.
- There are potential problems with calculation of true PM number and mass concentration when dilution factors are calculated using CO_2 measurements at less than 100ppmV. This is due to the associated errors when using gas analysers.
- Single eductor diluter losses witnessed in this experiment were of the order of 10% to 15% (for 23nm and 10nm cut-off respectively).
- In its current configuration, the MAAP instrument does not have a fast enough response time to give statistically reliable data during mid to high power testing conditions as potential PM certification measurement windows are less than 4 minutes.

8.5 Recommendations - Large Modern Civil Aero Engine trials

The key recommendations from the engine tests are:

- Further work is required on understanding the volatile removal efficiency of commercially available VPR systems for use with modern large civil aero engines.
- Greater understanding of the use and losses associated with eductor-type diluters is required.
- The measurement of non-volatile mass concentrations either on existing Annex 16 hardware or PM dilution lines should be assessed in order to provide scientific evidence concerning the comparative line losses, such that the losses of the proposed sampling concept can be appraised.
- Line loss penetration characteristics of the PM measurement system (both the existing Annex 16 hardware and the PM dilution line) are required.
- Bespoke measurement suites are required in order to return consistent and reliable data when comparing engine systems using different PM measurement hardware.

9. The modelling of sample line effects.

9.1 Introduction

This report summarizes the main results obtained on the sampling line modelling during the SAMPLE II project. The behaviour of combustor exhaust gases has been studied using numerical simulations. These have focussed on the gases and particulate matter interactions during transport in the line, from the probe tip to measurement instruments.

9.2 Code description

The code used is based on previous work done on the SAMPLE project. It has been adapted from a 1D aircraft plume microphysical model to the specific thermodynamic conditions met in a sampling line, as a function of the settings (dilution, temperature etc.) (see Vancassel et al., 2004). The flow is assumed to be homogeneously distributed on the tube section so that average properties can be determined such as gas concentration, particle concentration, and temperature. The simulation can be seen as a temporal simulation as the sample average velocity and the line length determines the time of residence of the sample in the tube.

Gas species

Some of the exhaust gases are critical for particulate matter formation and can therefore modify the sample properties. This study has focussed on some of the most efficient gases for nucleating new particles, sulphuric acid and water vapour. As organic compounds are also thought to promote particle growth, they have been taken into account. Water vapour emission index has been set close to typical values, 1.4 kg/kg fuel.
The sulphuric acid amount at the probe tip has been deduced from the fuel sulphur content (700 ppm), and the sulphur conversion factor. This one has been taken within the range provided by the PartEmis experiment, close to the average value (2.5%) (Wilson et al., 2004).
The initial amount of organics has been set at 80 ppm, in the range of generally suggested values. It should be noted that sulphur contained in the ambient air, in the industrial area where the experiment took place, is likely to enhance the concentration of sulphuric acid in the sampling line.
Chemi-ions have also been considered with an initial emission index of the order of 10^{17} for one electrical charge. Negative charges have been assumed to be mainly related to sulphate clusters whereas positive charges have been attributed to organic compounds.

Particles

Exhaust primary particles have been assumed to be soot particles. They have been initialized using both the data provided by instruments during the campaign and the data from PartEmis (Wilson et al., 2004), using the same combustor. The particles have been distributed on a size bin grid following a log-normal law, with a mean diameter of 45 nm, a total concentration close to $10^{13}/m^3$.
Some other particles have been considered from nucleation, condensation and of course coagulation processes which tend to mix the different type of species.

As described in the SAMPLE previous report, the different types of particles considered are:

- Soot primary particles assumed to be initially dry
- Mixed soot (soot covered by volatile material, sulphuric acid, water and organics $(soot)(H_2SO_4)_a(H_2O)_b(OM)_c$) OM= organic matter)

Volatile particles :

- Sulphuric acid clusters and particles (hydrated sulphuric acid $(H_2SO_4)_a(H_2O)_b$)
- Organics clusters and particles $((OM)_a(H_2O)_b)$
- Negatively charged sulphate clusters and particles $((HSO_4^-)_a(H_2O)_b)$
- Positively charged organic clusters and particles $((OM^+)_a(H_2O)_b)$
- Mixed volatile particles (neutral, no charge: $(H_2SO_4)_a(H_2O)_b(OM)_c$)
- Mixed negative volatile particles $((HSO_4^-)_a(H_2O)_b(OM)_c)$
- Mixed positive volatile particles $((OM^+)_a(H_2SO_4)_b(H_2O)_c)$

Where a, b and c are the respective number of molecules of the different compounds composing the particle.

Physical processes

Particles in the sampling line will undergo various transformations. Their concentration change can be given by:

$$\frac{dN}{dt} = \left(\frac{dN}{dt}\right)_{dilution} + \left(\frac{dN}{dt}\right)_{coagulation} + \left(\frac{dN}{dt}\right)_{nucleation} + \left(\frac{dN}{dt}\right)_{loss}$$

Their composition change mainly depends on coagulation and material exchange between gas phase and condensed phase. As a result, the number of molecules *i* per particle will vary as follows:

$$\frac{di}{dt} = \left(\frac{di}{dt}\right)_{evaporation} + \left(\frac{dN}{dt}\right)_{condensation} + \left(\frac{dN}{dt}\right)_{coagulation}$$

Details on the processes can be found in the literature (Kärcher, 1995; Yu et Turco, 1998, Yu et al., 1999; Vancassel et al., 2004)

The loss process has been treated by calculating the fraction of the particles passing through the tube (i.e. penetration efficiency). For small sized particles, diffusion processes are dominant compared to inertial deposition, gravitational settling that occur for particles generally much larger than 1 micron, in elbows for example. Although the main applicable loss processes have all been used (see SAMPLE1 report), this study has focussed on diffusion for laminar and turbulent flows. For such cases, loss processes have been significantly changed. The penetration efficiency of the entire line used to be calculated by integrating the contribution of *n* smaller line sections (each time step corresponds to a section of the line) so that the efficiency of a line of length L is

$$\eta(L) = \eta\left(\frac{L}{n}\right)^n$$

However, the efficiency is strongly correlated to the Sherwood number. The Sherwood number is a dimensionless number representing the ratio between convective and diffusive mass transfer. For turbulent processes, the Sherwood number depends on the Reynolds number and the Schmidt number which are independent from the line length. Therefore, the above formula applies. But for laminar flows it cannot apply as the Sherwood number is a function of the line length.

For a turbulent flow, the following equations were used to determine the penetration efficiency, with L the length of the considered line.

$$\eta(L) = \exp\left(-\frac{\pi DL}{Q} \times Sh\right) \quad (1) \qquad \text{where} \qquad Sh = 0.0118\left(\frac{Ud}{\nu}\right)^{7/8}\left(\frac{\nu}{D}\right)^{1/3} \quad (2)$$

As the Sherwood number does not depend on the line length in this case (turbulent), for a line length equal to L/n, the penetration efficiency becomes :

$$\eta\left(\frac{L}{n}\right) = \exp\left(-\frac{\pi DL}{Qn} \times Sh\right) \quad (3)$$

and finally $\eta\left(\frac{L}{n}\right) = \eta(L)^{1/n}$ or $\eta(L) = \eta\left(\frac{L}{n}\right)^n$ (4)

The final penetration efficiency at the end of the line is the product of the penetration efficiencies worked out for the sampling line sub sections as the line is divided according to the time steps used during the simulations. But for a laminar flow, equation (4) does not apply because the Sherwood number depends on the length of the line, therefore:

$$\eta\left(\frac{L}{n}\right) = \exp\left(-\frac{\pi DL}{Qn} \times Sh\left(\frac{L}{n}\right)\right) \neq \exp\left(-\frac{\pi DL}{Q} \times Sh(L)\right)^{1/n}$$

The line penetration efficiency must therefore be first calculated for the whole line length and must be worked out each time step afterwards from the previous result. Intermediate results (e.g. middle of the line) may therefore be looked at with care. Results can be improved as a function of the sample flow rate.

The calculation strategy has been modified in order to get the correct value for the whole line length but not necessarily on a single section.
The particle transport efficiency has been determined using the following :

Laminar flow

$$\eta_{diff} = 1 - 2.56\mu^{2/3} + 1.2\mu + 0.177\mu^{4/3} \quad (\mu < 0.02)$$

$$\eta_{diff} = 0.819\exp(-3.657\mu) + 0.097\exp(-22.3\mu) + 0.032\exp(-57\mu) \quad (\mu > 0.02)$$

with $$\mu = \frac{\pi DL}{Q}$$

where D is the diffusion coefficient, L the line length and Q the sample flow rate

Turbulent flow

The penetration efficiency is given by

$$\eta_{diff} = \exp(-\mu \times Sh)$$

where Sh is the Sherwood number given as

$$Sh = 0.0118 \times \mathrm{Re}^{7/8}\, Sc^{1/3}$$

with

$$\mathrm{Re} = \frac{Ud}{\nu} \text{ and } Sc = \frac{\nu}{D}$$

where υ is the kinematic viscosity and U the average flow velocity.

9.3 Results

Effect of line length and temperature

The effect of the sampling line length has been studied by varying only the line length but keeping the experimental parameters constant. Calculations have been performed for 7 m and 25 m lines. Results have been analysed at the DMS location, indicated in Figure 90.

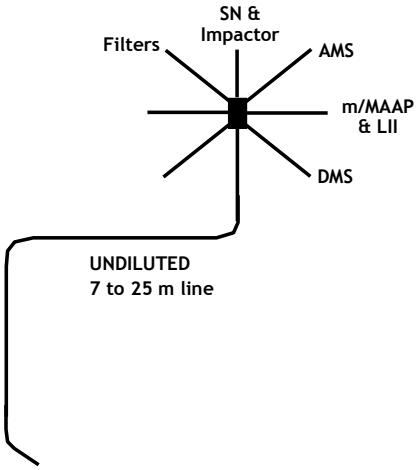

Figure 90 Schematic diagram of the undiluted sampling line.

The main influence of a lengthened line lies in the fact that the time of residence increases at constant sample flow rate, as shown in Figure 91.

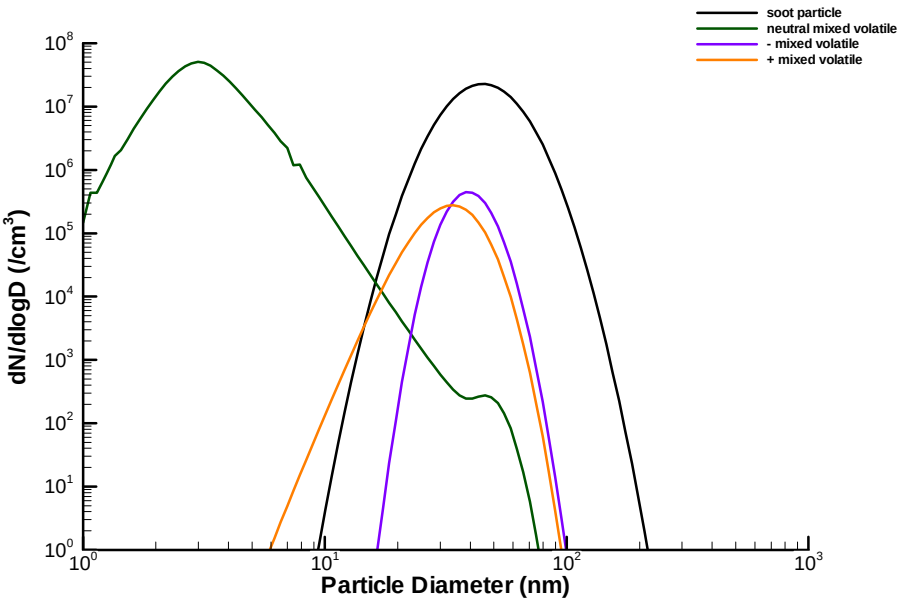

Figure 91 Particle size distribution (volatile and non volatile) for the 7m undiluted line at 60°C (333K)

Therefore, loss processes of particles, like coagulation and line wall losses are increased. The general trend can be foreseen as being a decrease of the number concentration and a size distribution being shifted to larger sizes.

The line temperature has been set to 60°C (333K) which is the most favourable case for nucleation to occur, over the range of tested temperature. When no dilution occurs, this temperature remains low enough in order to form new particles, driven by sulphuric acid. For the aforementioned initial conditions, the model predicts that at the DMS location, some volatile particles are present at quite large concentrations, even larger than soot particles number density. These volatile particles are composed of neutral mixed volatile, negatively and positively charged volatile droplets (made of organic matter, sulphuric acid and water). The charge concentrations are initialized at the same value, whether they are positive or not. But the particle self collision efficiency depends on their composition, especially on their affinity. Negative sulphate particles are more likely to condense on sulphate neutral clusters than on organic material. As organics and sulphuric acid are not in same concentrations at the combustor exit, this leads to distributions of positive and negative mixed volatile being not superimposed. The case presented in Figure 91 assumes that soot particles cannot grow (hydrophobic), leading therefore to distribution centred on the initial mean value (45 nm).

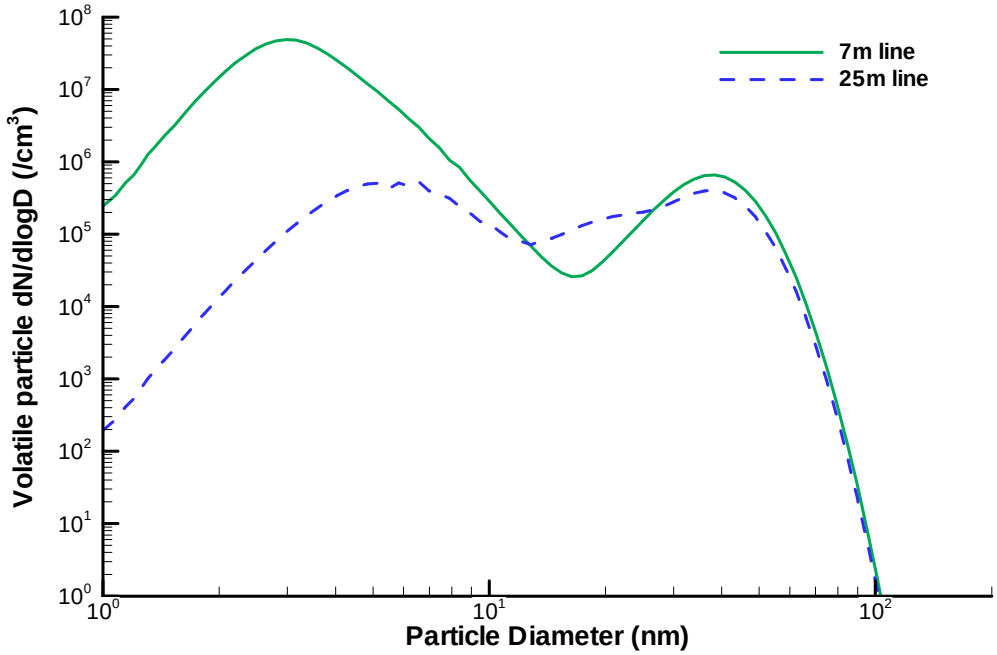

Figure 92 Total volatile particle size distribution after 7m and after 25m undiluted line at 60°C.

As expected, changing the 7m line for the 25m line, leads to a decrease of the volatile particles total concentration. The bimodal structure still appears. The first mode is shifted to larger sizes for the 25m case (from 3nm to 5nm) and peaks 2 orders of magnitude below the 7m case maximum. Soot particles, not represented here, do not undergo severe concentration decrease in comparison as coagulation is not very efficient at their size range (close to 40-50 nm). Therefore,

the main loss process affecting them is diffusion on the line walls, which has been predicted to be close to 15% at 25m and 5% at 7m for a turbulent flow.

The coagulation efficiency is indeed better at smaller sizes but also at higher concentrations. The characteristic time of coagulation (time needed to lose half the initial number concentration) is higher than the time of residence of the sample in the line. FOCA/DLR studies indicate only slight shift to larger sizes attributed to soot coagulation. Therefore coagulation is not expected to play an important part (as discussed in Wahl et al, 2007.)

The time of residence plays the major part in the volatile particles size distribution change. As it can be seen in Figure 93, the size distribution is initially composed of very small droplets and clusters. These are depleted by line losses and by coagulation, also leading to particle growth.

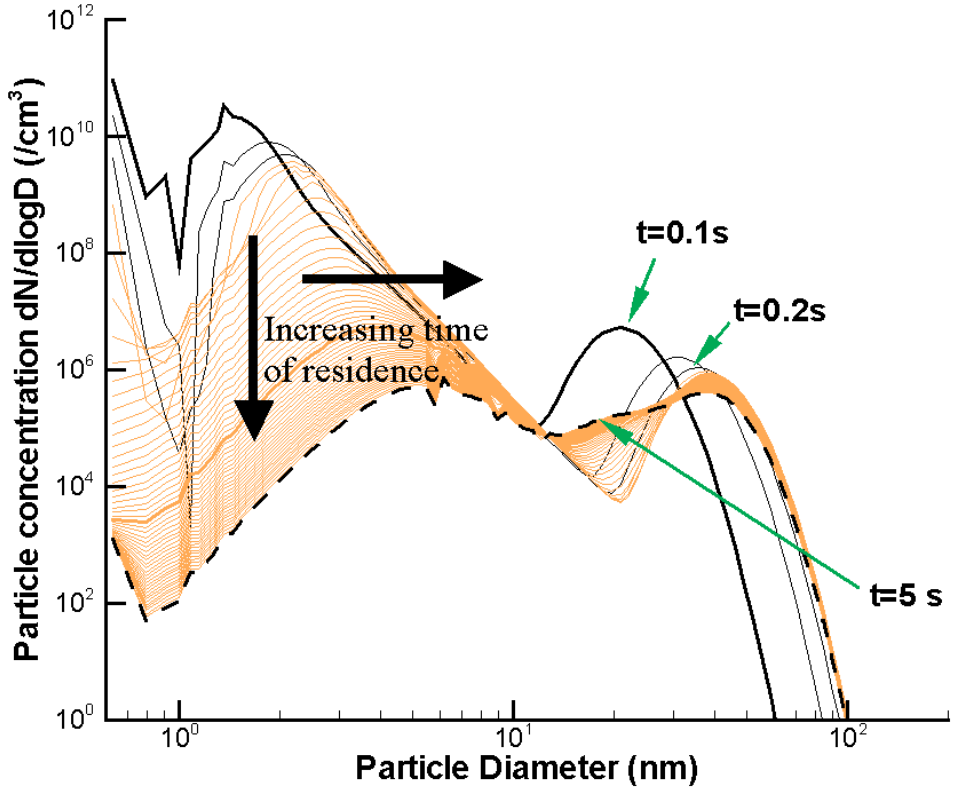

Figure 93 Evolution of the volatile particles size distribution in the 25m line as a function of time.

The second mode rapidly forms and the difference between 0.5s and 5s remains small (the maximum size are very close) contrarily to the first mode which loses several orders of magnitude in the meantime. This is due to enhanced coagulation (large concentration and high mobility leads to large coagulation coefficient) and diffusion losses which are quite important for small particles (diffusion increases with decreasing size).

Effect of line temperature

Volatile particles are predicted to form when temperature is kept at 333 K. This temperature is rather high for nucleation to occur but sulphuric acid and water vapour makes a very efficient nucleating mixture and the sample was not diluted, keeping concentrations of vapours quite high. A simple test has been performed in order to look at the effect of increasing temperature. It has been increased on the 7m line case up to 160°C (433K) which is another tested temperature at GTRC Cardiff.

For the 7m case (and subsequently for the 25m as well) the model does not predict any new particle to get formed before the end of the line as shown in Figure 94. Gaseous clusters composed of sulphuric acid hydrates and organic matter are visible at high concentration but cannot form stable particles due to strong evaporation processes.

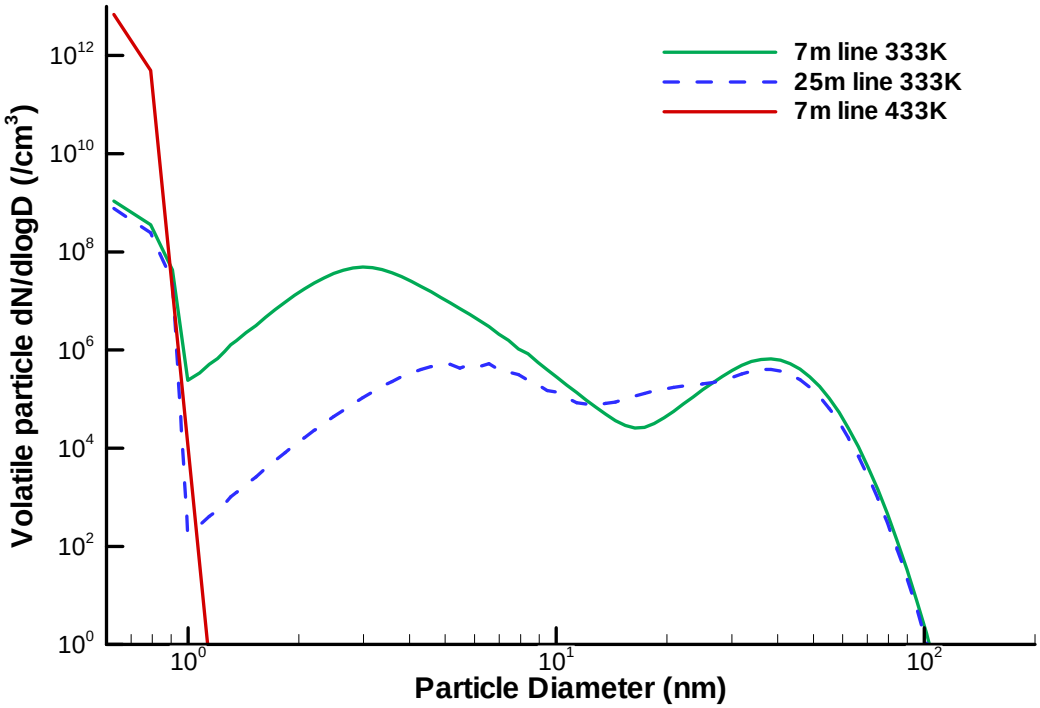

Figure 94 Size distribution for 7m and 25m line at two different sample temperatures (60°C and 160°C, respectively 333K and 433K)

It should also be noted that with the 433K temperature (maintained constant), even a 15% sulphur conversion factor does not lead to significant nucleation events and therefore to the formation of new particles. This very high factor is not in agreement with previous experiments but may reflect an upper limit and a sulphured ambient air. However even in that case, the model used here does not predict new particle formation.

Effect of the VPR

A volatile particle remover has been used in order to eliminate volatile particles from the sample. This is based on high temperature-high dilution ratio stages, placed on the line (see Figure 95).

The 60°C temperature has been used to make sure that the model could form particles, which is necessary to test the VPR ability to remove them. The VPR has been modelled as a simple device, changing particles and gas concentrations by dilution and increasing temperature. No other physical processes occurring in the diluters for example (such as enhanced particle loss by turbulence) have been taken into account.

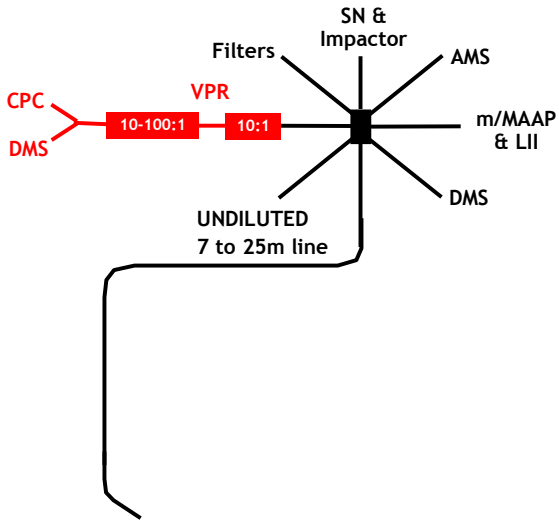

Figure 95 Schematic diagram on the sampling line with the VPR, note that in practice the dilution ratio was variable depending on the test conditions, as outlined in Figure 16.

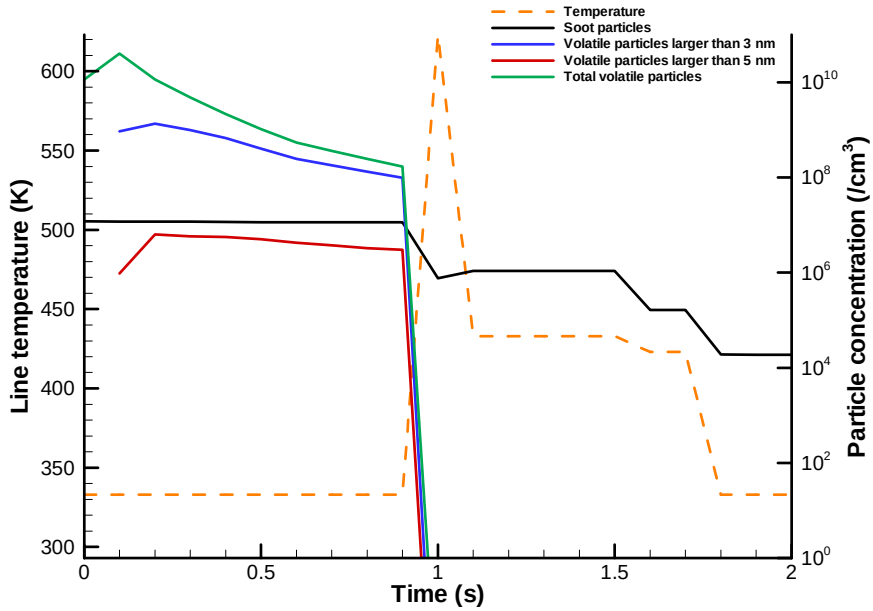

Figure 96 Evolution of temperature and volatile particles concentration in the sampling line using the VPR.

The temperature change as a function of time has been plotted in Figure 96. The VPR is modelled by a sudden increase of temperature which rises up to 633K before being cooled down to 433 K. It is kept at a nearly constant value until another change bringing it back to the initial 333K. Soot particles number concentrations are only affected by the VPR through expansion or

shrinkage of the sample (due to temperature change) and dilution, responsible for number density decrease. The soot particles number density follows all the steps where sample changes apply.

The total volatile particles concentration (larger than 1nm) and the concentration of volatile particles larger than 3 and 5 nm, respectively, have also been plotted in Figure 96. These particles form very quickly and their concentration exhibits a maximum at 0.2s. Then their concentration decreases due to line losses and coagulation. At the VPR, a 1:400 dilution is gradually applied (1:6, 1:7, 1:10 at respective temperatures of 623, 433 and 333K). From the data provided, the second stage (dilution 10-100) is actually composed of two 1-10/1-10 dilution stages. Thus the ratio used are in agreement with Figure 95.

The first effect is due to the temperature sudden increase, which evaporates all the condensed material from the particles, removing all the volatile fractions. The second effect is due to dilution, which decreases the concentration of condensable vapours by several orders of magnitude. As a result, even if temperature gets low enough for nucleation to occur downstream, vapours concentration cannot get supersaturated any more and nucleation does not take place or is extremely low. This is the reason why after 1.8s particles do not form anymore, even if the sample has been cooled down to 333K. It should be noted that the dilution air has been considered free of particles and condensable matter (the sample is composed of the material initially emitted by the engine only).

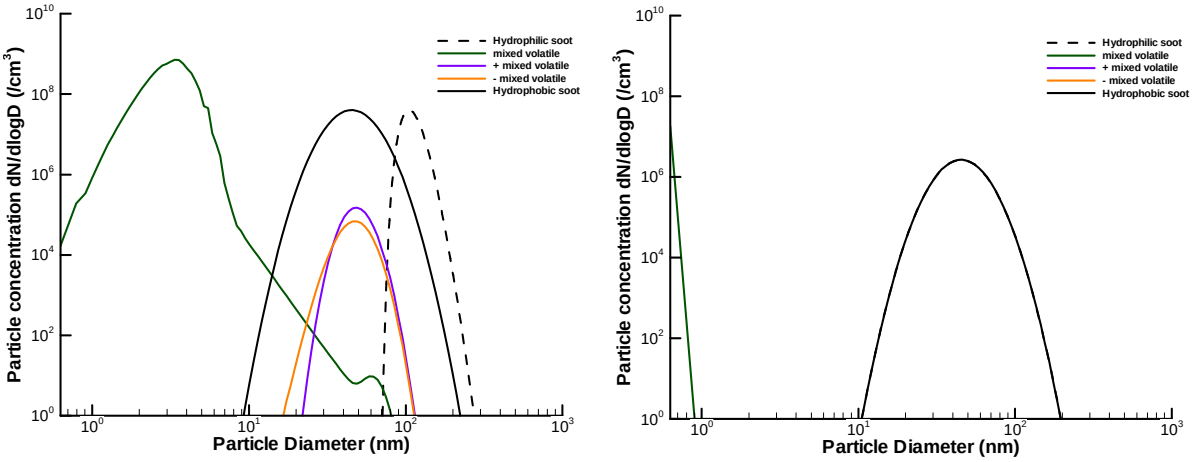

Figure 97 Particles size distribution before the VPR (left) and immediately after the first stage (right) (T=633K)

Figure 97 shows the particles size distribution before and after the VPR, showing the effect of the first stage (hot dilution at 633K). The volatile particles evaporate, gaseous clusters only remain. If soot particles are assumed to be hydrophilic, the model predicts they can grow by water uptake on a sulphuric acid and organics layer at sizes of the order of 100nm. The volatile fraction evaporates as well.

Effect of sample flow rate and time of residence

The sample flow rate is very important regarding particle loss in a sampling line. This is even more important when different regimes are considered (laminar or turbulent). Simple simulations

have been performed using different sample flow rate on the simplified Rolls–Royce sampling line. One important point is that instruments requirements are slightly different in terms of mass or volume flow rate. This difference can make comparisons difficult as these requirements involve different sample behaviour.
Considering the undiluted line, two cases have been studied, respectively 14l/mn and 8l/mn dedicated to filter sampling and DMS-LII measurements. Although the flow rates were only different on a small section of the line, the behaviour of a sample through a 7 m long line with the same parameters has been simulated. A 25l/mn flow rate (used for the diluted line) has also been used.

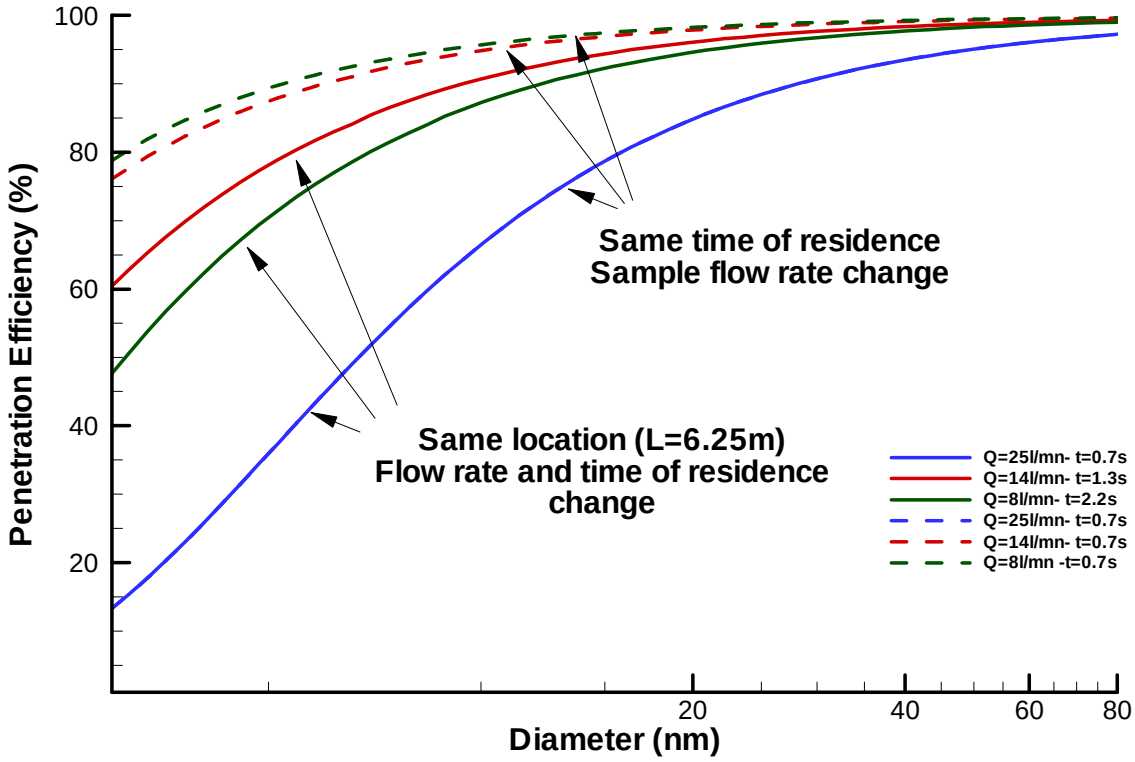

Figure 98 Overall penetration efficiency of the line at different flow rates (Rolls-Royce line flow rates 8, 14, 25 l/mn) at different locations

The results shown in Figure 98 first indicate that the penetration efficiency varies as a function of the time of residence and the sample flow rate. The largest particle losses at the end of the line have been obtained for the 25l/mn case that was considered as turbulent, although the time of residence was quite small (0.7s). Looking at the line efficiency at the same location implies to take into account both the sample flow rate effect on particles diffusion but also the time of residence of the sample. As a result, the line penetration efficiency shows a different trend. Reducing the flow rate from 25 to 14l/mn seems to increase the penetration efficiency. On the other hand, decreasing the flow rate from 14 to 8l/mn has an opposite effect when the particle concentrations are evaluated at the location. This is due to the increasing time of residence. This is confirmed by the penetration efficiencies plotted in Figure 98, not taken at the same location but for a similar time of residence. The main effect evaluated here is the sample flow rate. The lower the sample velocity is, the larger the penetration efficiency.

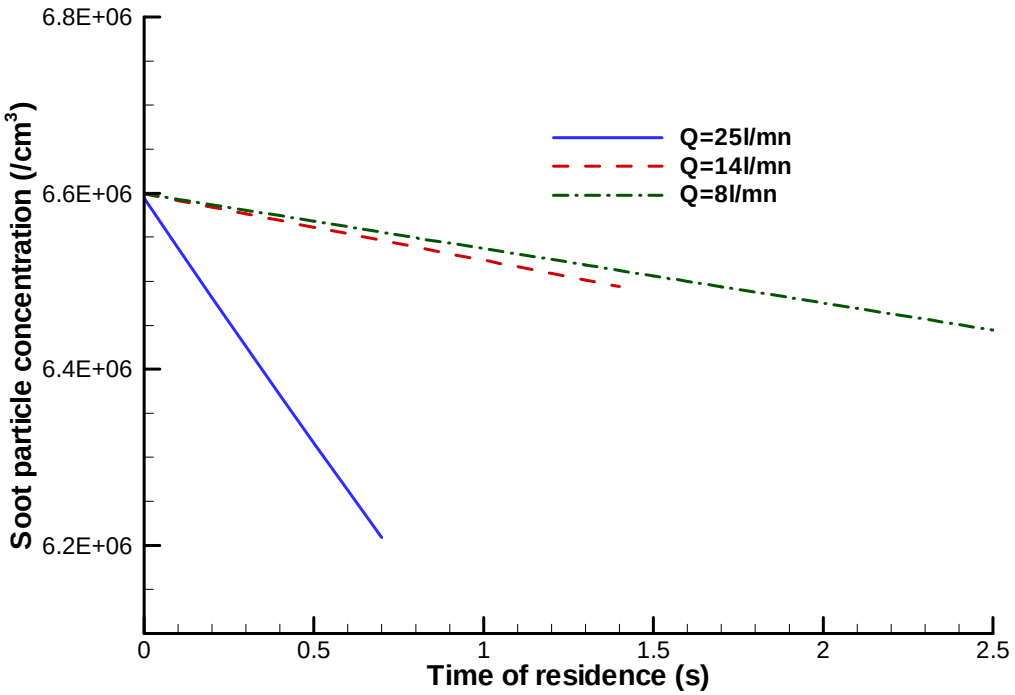

Figure 99 Soot particles concentration as a function of the time of residence for three different sample flow rates (Rolls-Royce line).

This is also clearly shown in Figure 99. At 0.7s, the particle concentration decreases with increasing sample flow rate. But taken at the end of the line, the concentration at 2.5s for the 8l/mn case is smaller than the 14l/mn one, corroborating the behaviour seen in Figure 98. It is not straightforward to experimentally decouple the effect of the time of residence from the sample flow rate. The simulations show that at 0.7s (i.e. same time of residence for 3 different sample flow rates), particle losses increase with increasing sample flow rate, so Loss(25lpm) > Loss(14lpm) > Loss(8lpm). This is the effect of the sample flow rate only. Close to the end of the line 6.25 m (same line length for the 3 sample flow rates), the effects of the sample flow rate and the time of residence are mixed, it is therefore obtained that Loss(25lpm)>Loss(8lpm)>Loss(14lpm). Thus the results do not conclusively prove that loss is a function of residence time.

9.4 Conclusion

Several simulations of the combustor exhaust sample evolution in sampling lines have been performed. The main conclusions that can be drawn at this time must be appreciated regarding the assumptions made. This concerns the initial composition of the exhaust, the physical processes used, the uncertainties associated to the data provided etc.
From the calculations performed during this project:

- Volatile particles can form in the undiluted line when temperature is maintained at 60°C
- They do not form at higher temperature even for a very large sulphur conversion factor
- The volatile particles are mainly formed by neutral mixed droplets (organic matter, sulphuric acid, water) for the smaller sizes, by electrically charged mixed particles for larger sizes
- A difference in the volatile particle concentrations can be observed between a 7m and a 25m line (change by several orders of magnitude); it can be attributed to diffusion losses and coagulation losses due to increased time of residence
- Volatile particles are removed by simulating the effect of the VPR on sample dilution and temperature; they do not reform afterwards with the conditions used in the simulations
- The sample flow rate plays a significant part in particles concentration change in the line because of the flow regime and the associated time of residence

Finally dilution has also been tested, looking the effect of tip dilution or 7m dilution. The model, based on thermodynamic evolution of the sample did not predict significant differences. Observed changes as a function of the dilution location may be due to the different diluters technology, especially between the tip of the probe diluter and more conventional “in line” diluters.

Several things can however be improved. The effect of small cluster not colliding to the line wall is not well known (rebound effect). The effect of the Sherwood number is also to be evaluated more carefully as the total line length determines the overall penetration efficiency. A discrete approach of the line in different sections is not applicable in a straightforward way.

10. A study into the agreement between smoke number and carbon dioxide measurements at some spatial locations in the exhaust of a gas turbine.

10.1 Introduction

When certifying new aircraft gas turbine engines, manufacturers must provide evidence to the regulatory authorities that gas analysis and smoke number measurements made at specific locations in the exhaust plume are representative of the whole engine [ICAO, 1993]. This is currently a relatively straightforward task. However, when new quantitative smoke measurement techniques are introduced in the future, the time taken to acquire samples may significantly increase. Thus placing an added burden on engine manufacturers.

As a potential means of reducing quantitative smoke sampling time, it has been suggested by members of the SAE, E-31 [SAE, 2002] aircraft emissions committee that if it can be proven that smoke emission trends and plotted symmetry are the same as gas analysis patterns, it would only be necessary to measure smoke at a reduced number of pre-determined spatial locations. Interpolated values could then be used to represent the whole engine.

The objective of the work presented in this report was to examine a limited amount of archive data to determine whether gas analysis and smoke number trends show similar symmetrical patterns in the exhaust plume. To achieve this, archive data acquired from the QinetiQ-TRACE engine was analysed at two power settings which were idle and cruise. The measurements were made using a single-point traversing probe along the horizontal centre-line of the engine only, and not the whole engine. However, although limited, this provides an ideal comparison of symmetry between both sides of the engine along the centre-line.

It should be noted that the results presented herein are for a single engine test only. This data does not necessarily stand for any gas turbine and more data would be required in order to have a high degree of confidence in the results.

10.2 Experimental set-up

The data used in this report was acquired in 2001 at what is now QinetiQ Farnborough, utilising the TRACE (Transport and Chemical Evaluation Engine). The engine was a hybrid mixture of components, however the combustion system was relatively modern and consisted of ten interconnected tubo-annular combustors coupled with modern airspray fuel atomisers.

A single-point, water-cooled, traversing sample probe was used to simultaneously transport conditioned gaseous and smoke to the respective instruments. The probe and the sample lines were conditioned at a temperature of 150°C± 10°C and the analysis was undertaken in accordance with ICAO [ICAO, 1993] regulations [SAE, 2002]. The gas sample probe was incrementally moved in 50mm steps along the horizontal centreline of the engine. at a distance equivalent to half of the nozzle diameter downstream of the exhaust exit. The power conditions tested were equivalent to idle and cruise.

10.3 Results

Idle

Figure 100 to Figure 103 shows results obtained at the idle power setting for carbon dioxide, carbon monoxide, unburned hydrocarbons and smoke number respectively. In these plots, the X-axis shows the horizontal distance in mm, either side of the centre line of the exhaust nozzle, whilst the Y-axis shows the specific species concentration.

Figure 100 shows a plot of carbon dioxide and it can be seen that the symmetry between the left and right hand side of the engine is satisfactory. A similar result is observed when carbon monoxide is plotted against distance as shown in Figure 101. Large localised carbon monoxide and unburned hydrocarbon concentration values indicate combustion inefficiency and should also highlight any potential combustor/fuel injector anomalies. If, for example, a fuel injector were slightly misaligned or partially blocked, the resultant fuel-jet would be miss-aligned and could potentially result in localised regions of poor mixing resulting in an unsymmetrical plot of the respective species. However, Figure 101 shows that the carbon monoxide distribution is symmetrical and Figure 102 shows the same trends for unburned hydrocarbon.

This suggests that the engine efficiency is evenly distributed and there are no localised regions of inefficiency in this area. Therefore, it would be expected that smoke distribution would follow similar trends. However, Figure 103 shows a plot of smoke number against spatial location and in this instance it can be seen that the plot is only partially symmetrical. From about –150mm to +150mm the plot appears satisfactory. Up to +450mm, the actual smoke values appear reasonable, but from about –200mm to –300mm the smoke number increases significantly.

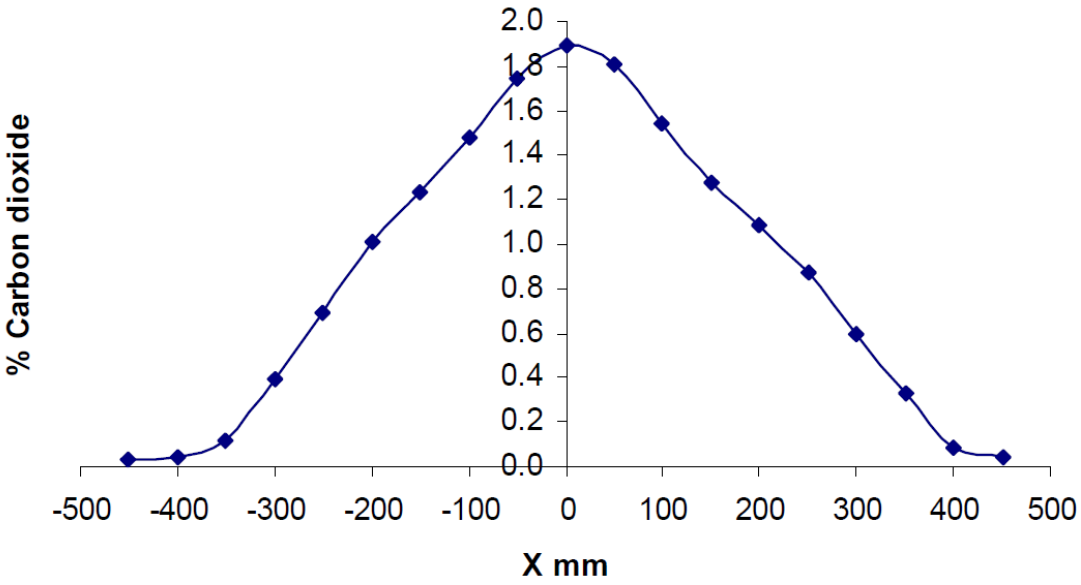

Figure 100 Carbon dioxide against horizontal distance at idle

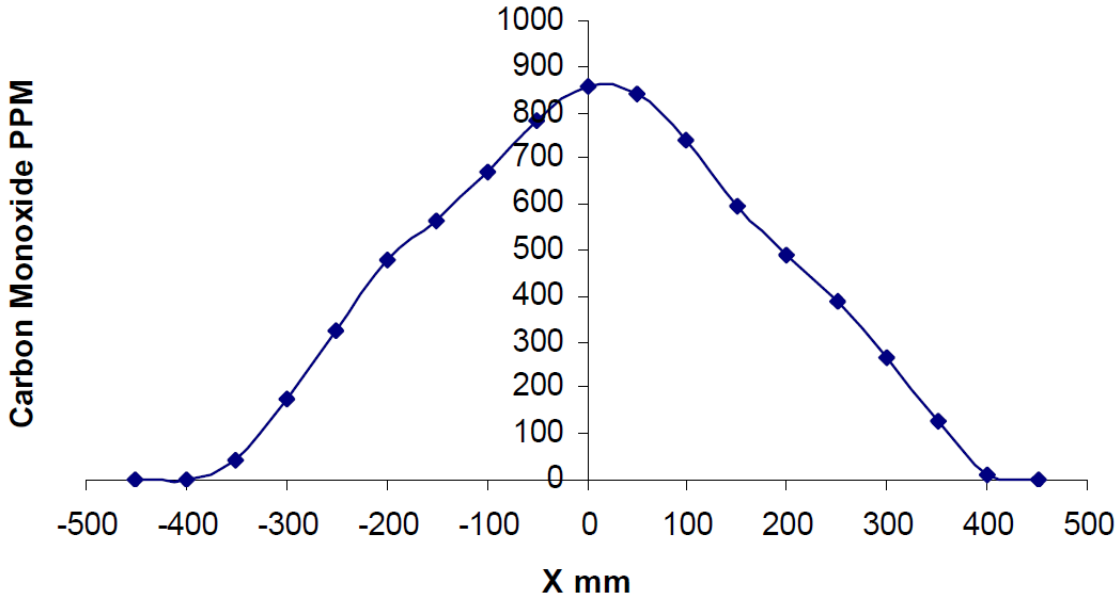

Figure 101 Carbon monoxide against horizontal distance at idle

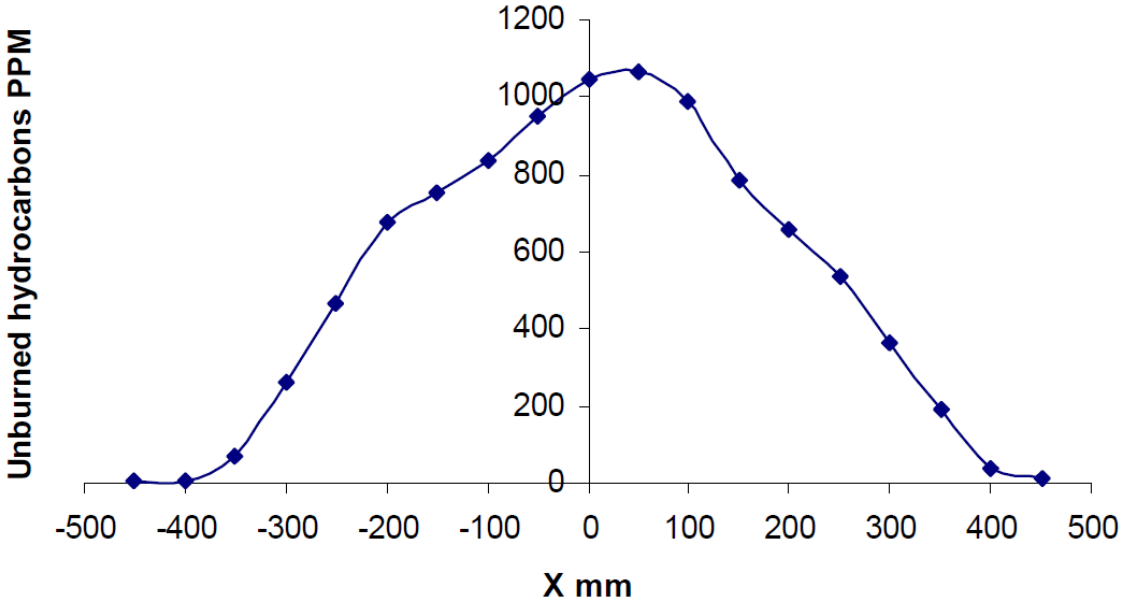

Figure 102 Unburned hydrocarbons against horizontal distance at idle

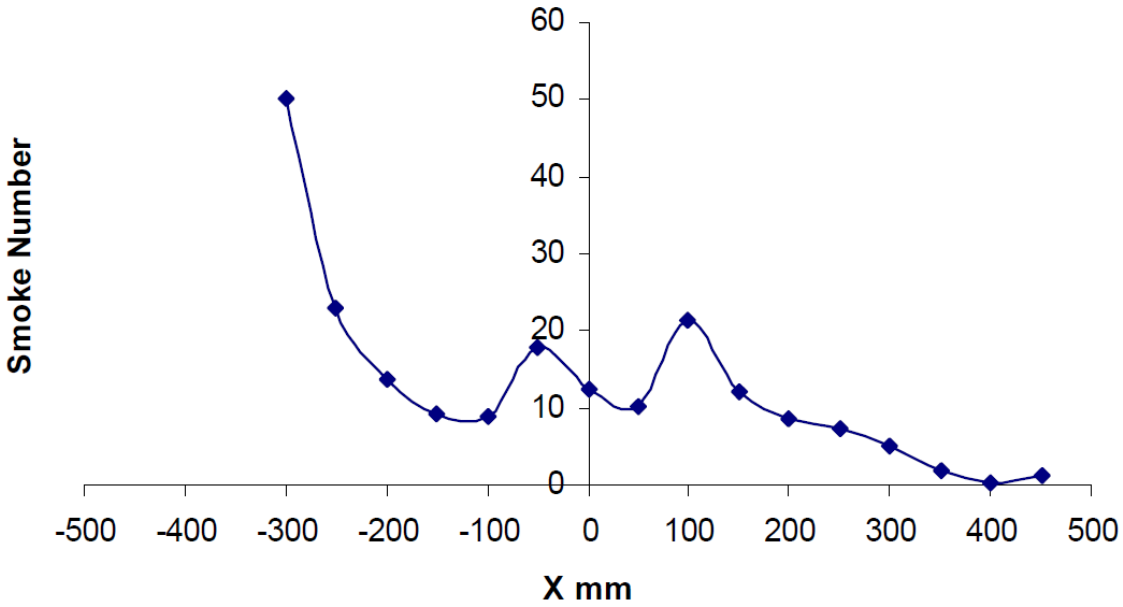

Figure 103 Smoke number against horizontal distance at idle

Figure 104 to Figure 107 shows plots of carbon dioxide, carbon monoxide, unburned hydrocarbons and smoke number respectively at the cruise power condition. As would be expected, raising the engine power has resulted in an increase in carbon dioxide values and a reduction in both carbon monoxide and unburned hydrocarbons when compared to idle. Good symmetry is again evident with respect to the gaseous species. However, smoke number shows non-symmetry around the combustor centre-line.

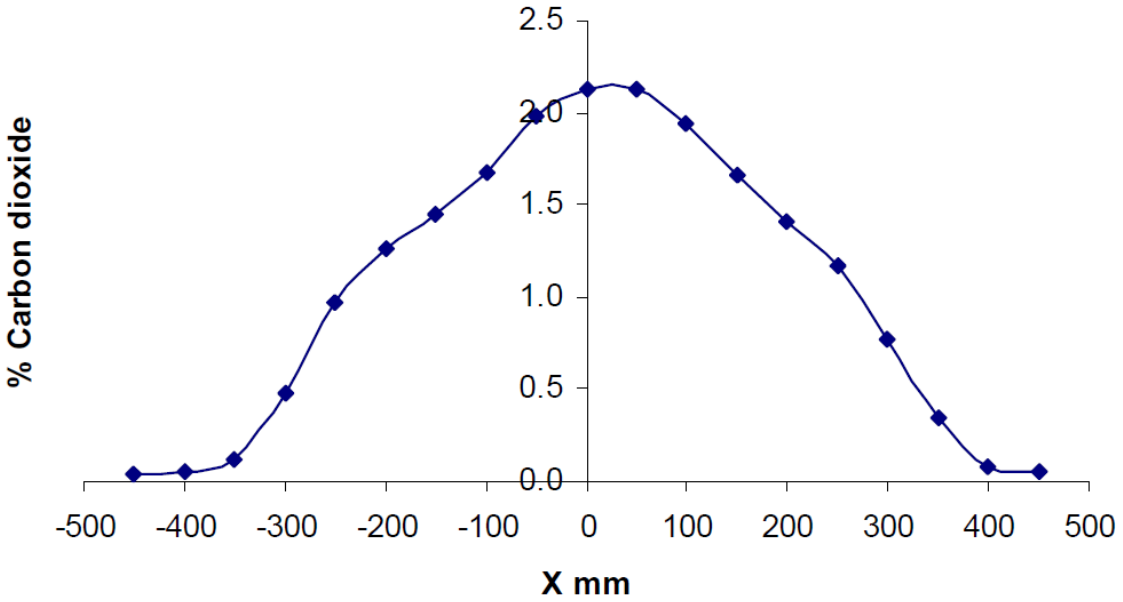

Figure 104 Carbon dioxide against horizontal distance at cruise

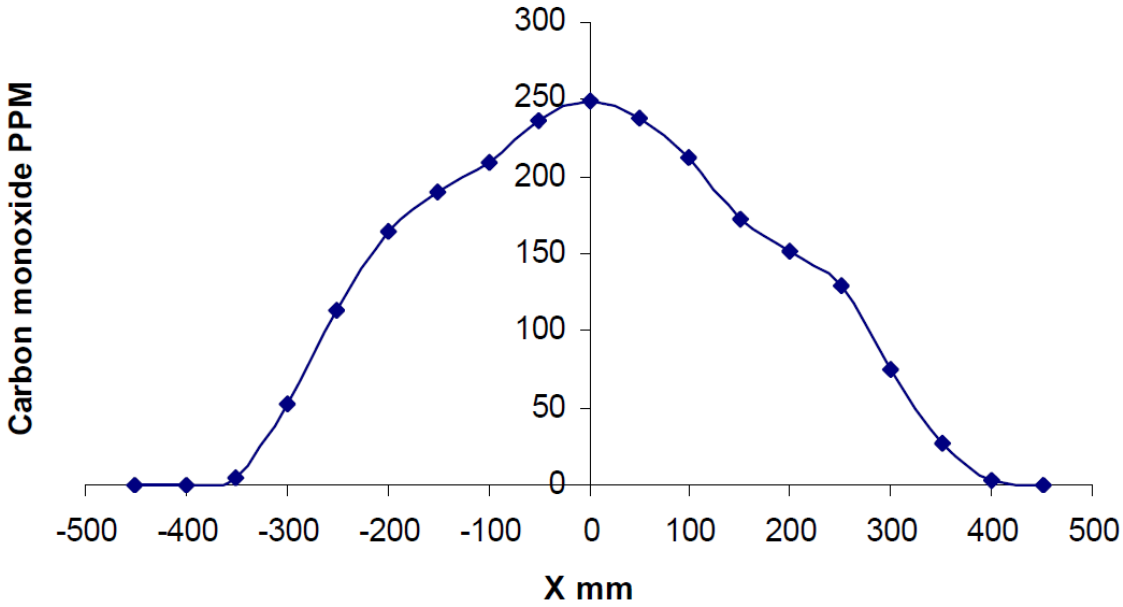

Figure 105 Carbon monoxide against horizontal distance at cruise

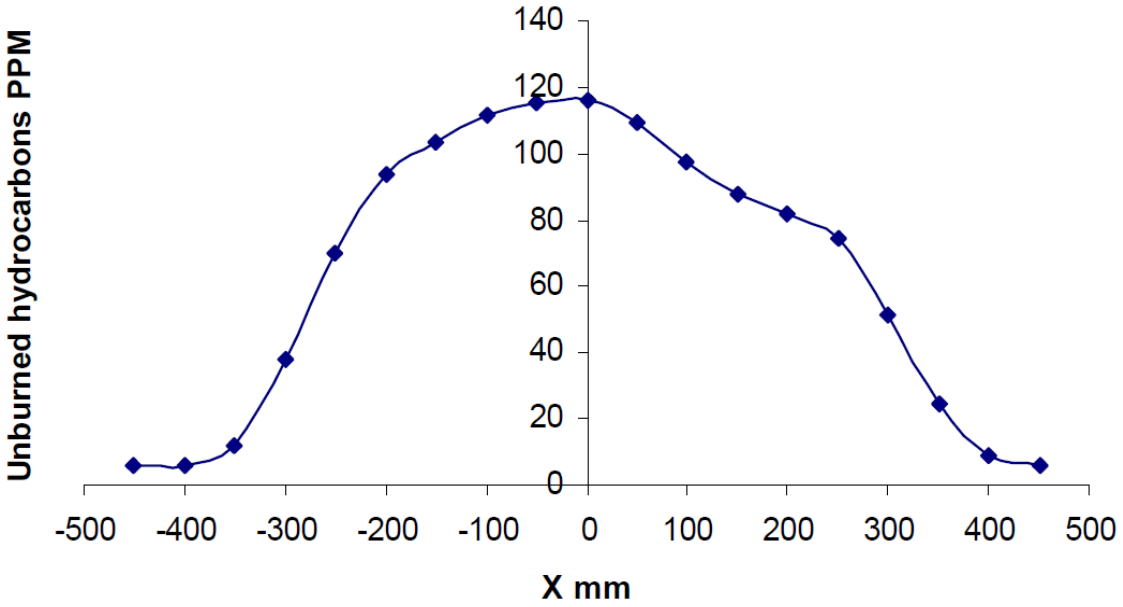

Figure 106 Unburned hydrocarbons against horizontal distance at cruise

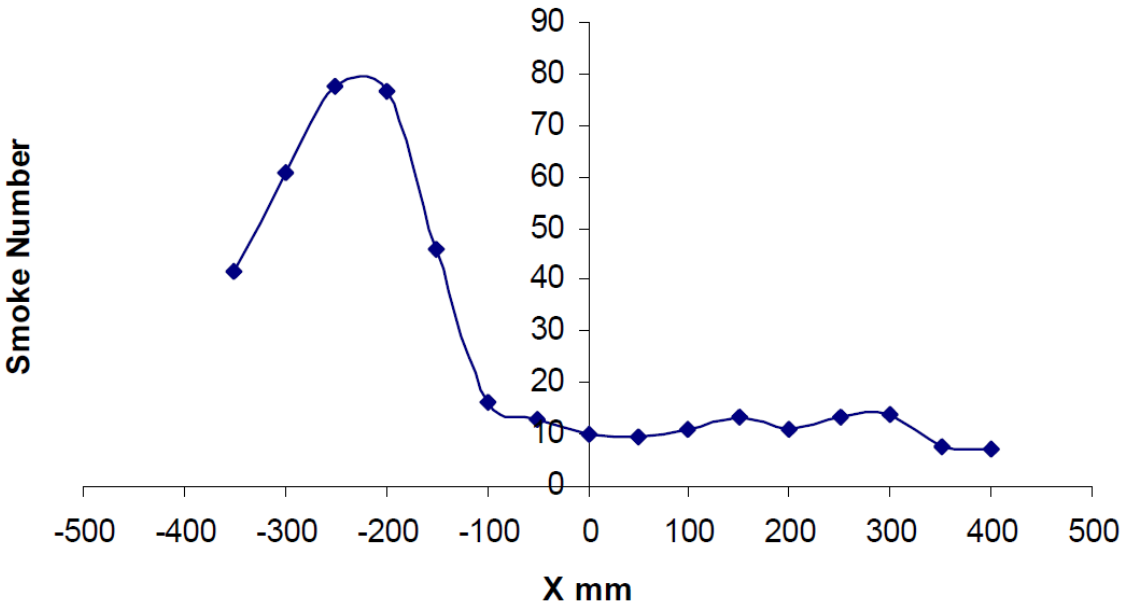

Figure 107 Smoke number against horizontal distance at cruise

10.4 Discussion of results

At both power settings, carbon dioxide, carbon monoxide and unburned hydrocarbons show symmetrical plots. Smoke number measurements show a limited symmetry, but also very high values on one side of the engine only. Potential reasons for the anomaly could be:

- Faulty fuel injector
- Faulty combustion chamber
- Carbon shedding from certain regions of the engine
- Carbon shedding from the gas sample lines

Looking at these items sequentially: it is unlikely that a fuel injector or combustor were malfunctioning in the spatial locations where the measurements were made as this would have been obvious from both the carbon monoxide and unburned hydrocarbon measurements. It is however possible that large ballistic particles were transported into this region of the exhaust plume from another locality, either by shedding or the real-time combustion process. Whilst gaseous species would all follow similar aerodynamic trajectories, ballistic smoke particulates could unexpectedly arrive from anywhere within the engine.

Carbon shedding within the sample line is unlikely as it is only apparent on one side of the engine. Due to the limited data set it is not possible to draw any firm conclusions. The objective of this work was to ascertain whether smoke and gaseous emissions show similar symmetrical patterns, this small study has shown that regardless of the reason for the high smoke number values they do not.

10.5 Conclusions

For this particular example, gaseous species show good symmetry around the horizontal centre-line of the engine. However, this is not the case with respect to smoke number, which at both power settings has shown abnormally high values on one side of the engine. The distribution of carbon monoxide and unburned hydrocarbons suggests that there are no localised points of combustion inefficiency in this measurement region. Therefore, large smoke number values would not be expected. Several potential reasons have been postulated for the localised high smoke number but there is insufficient data to draw any firm conclusions.

The reason that this work was undertaken was to provide evidence as to whether symmetrical plots of gaseous species were a good indication as to whether smoke would follow similar trends. In this instance, this has not proven to be the case. It is recommended that additional studies be undertaken as more data is required for analysis.

11. Intercomparison of Carbon Burn-Off and Optical Methods

11.1 Methods

During the test performed in SAMPLE II several filter-based carbon burn-off methods were compared in order to determine the precision of their results. Investigated methods were:

Gravimetric Analysis
Time-averaging methods are used to sample the emitted particles on appropriate fibrous filters or membrane filters. Common practice is to use glass fibre, quartz fibre, or Teflon filters for exhaust particle sampling that show a filtration efficiency of >99% in the size range relevant for particulate matter emitted from gas turbines, i.e. for 10 nm < D_p < 500 nm. Applying gravimetry, the sampled particle matter is analyzed gravimetrically by weighing the filter before and after loading, which yields the total particle mass. The accumulated exhaust volume penetrating the filter is recorded for each sample in order to obtain a mass concentration measurement [SAE, 2009].

2-Step Combustion
Pre-conditioned quartz fibre filters are used for sampling exhaust particle matter. Particle-laden filters are analysed for the carbon content in a two-step combustion process. During the two-step combustion process the organic carbon is oxidized for 42 min at 340 °C in a pure oxygen atmosphere. The remaining carbon, defined as elemental carbon, is then determined at 650 °C (32 min) by a total organic carbon analyzer based on non-dispersive IR absorption of the evolving CO_2 [Schmid et al., 2001].

Thermo-Gravimetry
Pre-conditioned quartz fibre filters are used for sampling exhaust particle matter. Particle-laden filters are analysed for the carbon content in a continuous combustion process. In an oxygen atmosphere, the sample is heated from room temperature to 1000°C using a gradient of 20K/min. The evolving CO_2 is detected by non-dispersive infrared absorption. Simultaneous to the heating of the filter, a laser beam is directed through the filter sample and records the change in filter transmission. The transmission of a clean particle-free filter is 1.0; increasing aerosol loading reduces filter transmission towards 0.0. Elemental carbon oxidation is assumed to start as soon as the filter transmission increases from its initially very low value according to the black particle-laden filter [Schmid et al., 2001].

SUNSET Analyser
The commercially available SUNSET Lab OC/EC Aerosol Analyser is another thermal-optical technique for analysis of the carbonaceous fraction of particulate matter and operates similar to thermo-gravimetry. This technique uses a proven thermal-optical method to analyze for organic and elemental carbon aerosols collected on quartz filters. The samples are thermally desorbed from the filter medium under an inert helium atmosphere followed by an oxidizing atmosphere using controlled heating ramps. A flame ionization detector (FID) is used to monitor the analysis. The instrument supports both the NIOSH Method 5040 (Issue 3 from 30 September 1999) [Birch

and Cary, 1996] and the IMPROVE protocol (as shown by Chow and Watson, 2001). NIOSH Method 5040 uses optical filter transmittance for the correction of pyrolytic conversion of OC into EC and is referred to as TOT (thermal-optical transmission), while the IMPROVE protocol uses optical reflectance for corrections and is referred to as TOR (thermal-optical reflectance). The major difference to thermo-gravimetry as used here is that removal of carbon is achieved by heating the sample in an oxygen-free He atmosphere. An example thermogram is shown in Figure 108. The evolving CO_2 is detected by a Flame Ionisation Detector (FID) after catalytic conversion to CH_4. The onset of elemental carbon removal is either detected by laser transmission or by laser reflectance.

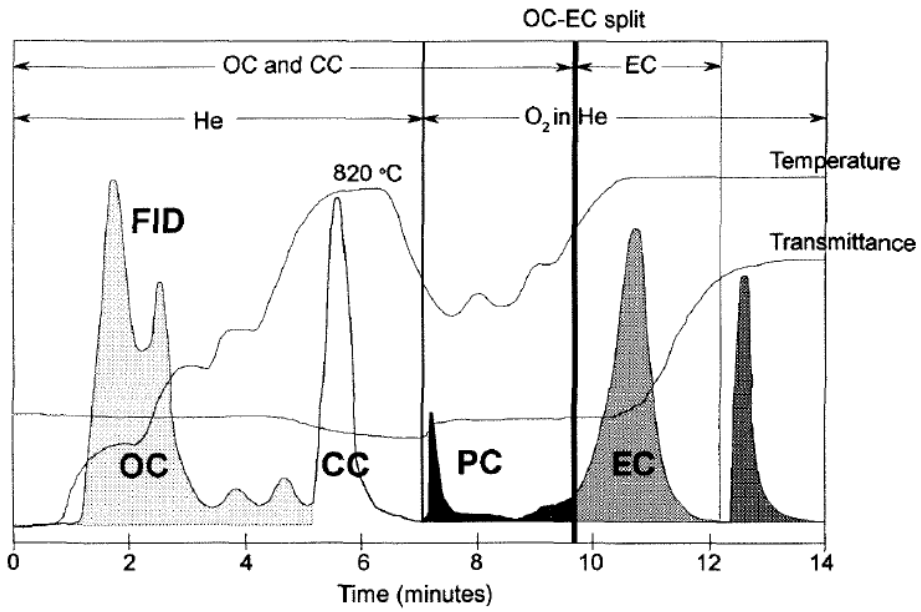

Figure 108 Example thermogram for sample containing rock dust (carbonate source) and diesel exhaust. Three traces correspond to temperature, filter transmittance, and detector (F1D) response. Peaks correspond to organic (OC), carbonate (CC), pyrolytic (PC), and elemental (EC) carbon [Birch and Cary, 1996].

Particle Soot Absorption Photometry (PSAP*)*

The Particle Soot Absorption Photometer (PSAP) is based on the measurement of the transmission of a filter [Bond et al., 1999]. The PSAP is a simplified version of the MAAP which requires additional correction for particle scattering. Similar to the MAAP the PSAP instrument measures the aerosol absorption coefficient σ_{ap} which is converted into a BC mass concentration by means of a mass absorption efficiency b_{ap} in units of m^2/g, see also the section on PM metrics for engine certification and their relation to Smoke Number of this report. The absorption coefficient was measured at a wavelength of 535 nm which was converted into a BC mass concentration using mass absorption efficiencies of 7.5 m^2/g and 10 m^2/g for fresh and aged soot particles, respectively [Bond and Bergstrom, 2006]. The PSAP was used as another optical method in order to provide photometric intercomparison data with the MAAP instrument.

11.2 Results

Results for filter-based methods

The carbon burn-off methods were compared for all operation conditions tested during SAMPLE II. In total 45 quartz fibre filter samples were collected and analysed by four different carbon burn-off methods. Table 18 summarises the results from the method intercomparison. The values refer to the average over the four applied methods which are themselves based on the averages over all filter samples collected during the trials. Single values of filters are summarised in Table 19.

Total carbon is determined within a maximum standard deviation of 10% between the four methods. The deviation of the applied methods from a method average for elemental carbon is maximum 14%. This analysis supports the conclusion that all applied methods are well applicable to this subject of measurement. Method- introduced uncertainties in the determination of EC are below 15%.

Table 18 Intercomparison of carbon burn-off methods and gravimetry for the conditions operated during SAMPLE II.

Day	Condition	No. of samples	TC av (µg/m³)	TC sd (µg/m³)	TC rel sd (%)	EC av (µg/m³)	EC sd (µg/m³)	EC rel sd (%)	Gravimetric (µg/m³)
12/04/2010	LS/LO	8	1542.3	149.1	9.7	1227.2	48.7	4.0	n/a
13/04/2010	LS/HO	8	1407.1	51.5	3.7	716.6	101.0	14.1	1575
14/04/2010	LS/HO	6	1635.7	68.2	4.2	1043.9	86.8	8.3	1630
15/04/2010	LS/HO	13	1573.7	66.0	4.2	868.2	64.7	7.5	n/a
16/04/2010	LS/LO	6	2299.2	116.6	5.1	1761.6	124.7	7.1	n/a
16/04/2010	HS/LO	4	5938.7	234.3	3.9	4983.9	88.6	1.8	n/a

Table 19 Results from carbon burn-off method analysis.

Date	Filter #	Condi-tion	Start time	Dura-tion	flow rate	2-Step Combustion		Thermogravimetry		SUNSET TOR		SUNSET TOT	
				min	l/min	EC µg/m³	TC µg/m³	EC µg/m³	TC µg/m³	EC µg/m³	TC µg/m³	EC µg/m³	TC µg/m³
12/04/2010	42	LS/LO	13:19:00	5	8	1922.6	2095.4	1994.5	2095.4	2055.0	2690.8	2007.6	2690.8
12/04/2010	43	LS/LO	13:28:05	5	8	bdl	bdl	bdl	bdl	n/a	399.5	n/a	399.5
12/04/2010	34	LS/LO	13:37:00	5	8	144.7	175.9	135.1	175.9	n/a	412.9	n/a	412.9
12/04/2010	48	LS/LO	13:51:20	5	8	1614.0	1754.2	1642.4	1754.2	1526.8	2022.9	1468.3	2022.9
12/04/2010	44	LS/LO	14:29:50	5	8	1056.4	1020.0	793.0	1020.0	780.8	1291.5	782.1	1291.5
12/04/2010	11	LS/LO	14:38:35	5	8	1042.4	1193.8	980.8	1193.8	1033.1	1580.0	1009.0	1580.0
12/04/2010	31	LS/LO	14:55:00	10	8	1352.8	1657.0	1222.0	1657.0	1403.1	1712.2	1381.4	1712.2
12/04/2010	39	LS/LO	15:10:00	10	8	1417.1	1441.0	1293.3	1441.0	1375.2	1750.4	1370.1	1750.4
13/04/2010	17	LS/HO	17:23:00	18	8.05	989.2	1337.7	n/a	n/a	891.7	1364.4	701.7	1364.4
13/04/2010	13	LS/HO	18:15:00	18	8.05	634.7	1068.9	574.5	1068.9	612.3	1124.0	504.5	1124.0
13/04/2010	36	LS/HO	18:30:00	18	8.05	1076.2	1683.8	n/a	n/a	1109.5	1715.4	911.6	1715.4
13/04/2010	32	LS/HO	20:05:15	10	8.05	638.2	1079.5	590.2	1079.5	563.4	1181.9	426.2	1181.9
13/04/2010	35	LS/HO	20:20:00	18	8.05	1161.0	1636.1	1056.7	1636.1	1019.6	1916.6	919.2	1916.6
13/04/2010	38	LS/HO	20:36:30	10	8.05	635.5	1523.9	609.1	1523.9	677.4	1528.1	553.8	1528.1
13/04/2010	46	LS/HO	22:45:00	18	8.05	906.9	1415.7	557.0	1415.7	729.7	1471.0	597.7	1471.0
13/04/2010	49	LS/HO	22:45:00	18	8.05	679.6	1340.5	529.6	1340.5	439.3	1291.9	328.6	1291.9
14/04/2010	33	LS/HO	12:23:00	18	8.07	1228.7	1467.3	1027.9	1467.3	1112.7	1789.5	897.1	1789.5
14/04/2010	2	LS/HO	13:38:30	10	8.07	703.4	1283.9	855.1	1283.9	844.0	1442.2	714.6	1442.2
14/04/2010	1	LS/HO	14:32:00	18	8.07	1369.8	2158.8	1338.8	2158.8	1315.8	2173.9	1133.6	2173.9
14/04/2010	14	LS/HO	16:46:00	18	8.07	1607.8	1959.6	1421.5	1959.6	1602.0	1989.5	1343.8	1989.5
14/04/2010	3	LS/HO	18:17:00	18	8.07	1140.0	1458.0	874.0	1458.0	1065.4	1586.0	923.1	1586.0
14/04/2010	9	LS/HO	18:35:30	10	8.07	615.7	1132.3	734.9	1132.3	665.4	1187.5	519.7	1187.5
15/04/2010	4	LS/HO	10:50:50	10	8.09	670.0	1344.9	710.4	1344.9	756.0	1364.8	674.8	1364.8
15/04/2010	29	LS/HO	11:06:35	10	8.09	716.8	1360.0	630.7	1360.0	792.5	1594.8	702.5	1594.8
15/04/2010	19	LS/HO	11:33:00	10	8.09	619.0	1137.6	602.3	1137.6	597.7	1237.1	522.3	1237.1
15/04/2010	QQ#01	LS/HO	12:28:00	17	8.09	1249.3	1633.1	1169.5	1633.1	1106.0	1832.1	1062.5	1832.1
15/04/2010	QQ#02	LS/HO	12:28:00	17	8.09	n/a	n/a	n/a	n/a	n/a	n/a	n/a	n/a
15/04/2010	QQ#03	LS/HO	14:00:00	17	8.09	1519.6	2231.3	1250.5	2231.3	1394.7	2262.9	1238.4	2262.9
15/04/2010	QQ#04	LS/HO	14:00:00	17	8.09	876.5	1061.8	743.7	1061.8	779.4	1133.4	747.0	1133.4
15/04/2010	QQ#05	LS/HO	16:37:00	17	8.09	1099.8	1580.5	921.2	1580.5	946.5	1745.2	976.3	1745.2
15/04/2010	QQ#06	LS/HO	16:37:00	17	8.09	637.7	922.2	617.1	922.2	586.5	1162.6	568.5	1162.6
15/04/2010	QQ#07	LS/HO	18:25:00	17	8.09	1493.0	2257.6	1143.6	2257.6	1211.6	2236.4	1085.1	2236.4
15/04/2010	QQ#08	LS/HO	18:25:00	17	8.09	1246.7	2431.4	1003.9	2431.4	1032.3	2343.3	933.4	2343.3
15/04/2010	QQ#09	LS/HO	18:25:00	17	8.09	576.3	1016.5	503.5	1016.5	492.5	1027.9	478.7	1027.9
15/04/2010	QQ#10	LS/HO	19:20:00	17	8.09	748.3	1221.7	539.5	1221.7	n/a	n/a	n/a	n/a
16/04/2010	QQ#11	LS/HO	09:15:00	12	8.01	595.4	842.9	590.9	842.9	535.3	1056.3	496.3	1056.3
16/04/2010	QQ#12	LS/LO	10:03:00	10	8.01	936.4	1032.1	875.3	1032.1	997.0	1376.0	868.7	1376.0
16/04/2010	QQ#13	LS/LO	10:03:00	10	8.01	1933.9	2365.0	1397.1	2365.0	1975.5	2458.7	1707.5	2458.7
16/04/2010	20	LS/LO	10:29:50	5	8.01	1767.1	2119.4	1518.2	2119.4	1831.6	2456.4	1626.7	2456.4
16/04/2010	15	LS/LO	10:39:00	5	8.01	1191.7	1587.4	1193.3	1587.4	1346.4	1860.4	1192.8	1860.4
16/04/2010	QQ#14	LS/LO	11:16:00	10	8.01	3250.4	3887.1	3114.0	3887.1	3372.9	3849.5	3135.0	3849.5
16/04/2010	QQ#16	HS/LO	14:13:00	5	8.01	8144.2	8518.8	7674.3	8518.8	7593.3	8585.4	7460.5	8585.4
16/04/2010	QQ#17	HS/LO	14:13:00	5	8.01	4567.9	5423.4	5063.9	5423.4	4837.7	5811.3	4872.8	5811.3
16/04/2010	40	HS/LO	14:13:45	3	8.01	3068.8	3399.5	2919.5	3399.5	3074.4	3871.9	2952.7	3871.9
16/04/2010	41	HS/LO	15:17:20	3	8.01	4591.3	5601.3	4013.1	5601.3	4570.1	6298.0	4338.4	6298.0

Results for optical methods

The agreement between filter based methods and optical-based methods was studied during a dedicated run when the dilution in all sampling lines was kept at a constant value. In this BC intercomparison run the quartz fibre filters were collected from the undiluted sampling line upstream the VPR. The PSAP was connected to the undiluted line downstream the VPR with another VKL 10 dilution stage connected upstream to the PSAP. The MAAP was connected to the diluted line with two VKL10 stages connected upstream. The MAAP modified by DLR for operation at high mass concentrations was connected upstream the VPR directly to the raw exhaust line.

The respective dilution ratios were determined from measured CO_2 volume mixing ratios in the sampling lines. The overall dilution in the VPR branch upstream the PSAP was 439 ± 7, while the dilution in the diluted line was 106 ± 4. Thus the dilution ratios were very stable during this test. The results of this intercomparison is summarised in Table 20.

Table 20 Summary of the EC – BC intercomparison test at low smoke – high organics conditions on 15 April 2010.

Method		Mass concentration	
		average (µg/m³)	std deviation (µg/m³)
2-Step Combustion	EC	619	93
TG	EC	602	90
SUNSET TOR	EC	598	54
SUNSET TOT	EC	522	50
MAAP	BC	565	50
PSAP (@7.5 m^2/g)	BC	695	60
PSAP (@10 m^2/g)	BC	521	45
MAAP modified	BC	138	50

Excluding the modified MAAP, the method average mass concentration is 589 ± 60 µg / m³. All methods agree within an uncertainty range of 10%. The modified MAAP will be studied in a separate test in order to improve the set-up for the planned application.

12. PM metrics for engine certification and their relation to Smoke Number

12.1 Introduction

The Smoke Number SN is a proxy for the visibility of the plume emitted from the aircraft engine under certification. The visibility is defined by the Koschmieder law as [Seinfeld and Pandis, 1998].

$$x_v = \frac{3.912}{\sigma_{ep} + \sigma_{em}} \qquad \text{(Eq. 1)}$$

with the visibility x_v given as distance in m and the extinction coefficients for particles σ_{ep} and gas molecules σ_{em} given as inverse length in 1/m. Thus, the visibility of an exhaust plume is governed by the light attenuation caused by particulate or gaseous constituents. Since this focus is on particulate matter emissions the following discussion of properties is limited to aerosol particles.

12.2 Principal optical parameters

Optical properties of aerosol particles are related to the different interaction processes of particulate condensed matter and electromagnetic radiation. All optical properties of particles can be traced back to the interaction of the electric charges distributed in the condensed matter and the oscillating electromagnetic wave. The excited electric charges reradiate energy in all directions by scattering processes and may convert a part of the incident radiation into thermal energy by absorption processes.

In terms of plume visibility, the major processes of interest are elastic scattering and absorption of incoming radiation. Conservation of energy requires that the light removed from the incident beam by the particle is accounted for by scattering in all directions and by absorption. The combined effect is referred to as extinction. Conservation of energy requires

$$\sigma_{ep} = \sigma_{sp} + \sigma_{ap} \qquad \text{(Eq. 2)}$$

with σ_{ep}, σ_{sp} and σ_{ap} in units of 1/m being the extinction, scattering and absorption coefficients of the aerosol [Bohren and Huffman, 1983]. Indices *ep*, *sp* and *ap* refer to extinction, scattering and absorption of light by particles. Extinction, scattering and absorption by gas molecules are referred to by indices *em*, *sm*, and *am*.

For spherical particles, these coefficients are calculated from an analytical solution of electromagnetic theory which was published by Gustav Mie in 1908. A comprehensive description of Mie theory is given in the textbook of *Bohren and Huffman* [1983]. The calculation of single-particle cross sections for extinction (C_{ep}), scattering (C_{sp}) and absorption

(C_{ap}) requires knowledge of the two key properties complex refractive index and size parameter. The size parameter *x* is defined as the ratio of particle diameter d_p to the wavelength of light λ with $x = \pi\, d_p / \lambda$.

The complex index of refraction $m = n + i\ k$ is closely related to the particle chemical composition. The absolute value of *m* defines the scattering properties while the imaginary part *k* may equal zero for non-absorbing particles and $k > 0$ for absorbing particles. Values for *m* are listed in the literature [Hess et al., 1998; Seinfeld and Pandis, 1998] for a variety of chemical substances and wavelengths. Particularly the refractive index of black carbon which is the most important particulate absorber in the atmosphere is extensively reviewed by *Bond and Bergstrom* [2006]. Mixing rules which apply for calculating properties of mixed particles are described by Ouimette and Flagan [1982] and by *Bohren and Huffman* [1983].

For an aerosol described by the particle size distribution $n_N(d_p)$, the extinction coefficient is related to the cross-sections accessible by theory via the relationship

$$\sigma_{ep} = \int C_{ep}\ (m, x)\ n_N\ (d_p)\ d\ \log d_p \quad \text{(Eq. 3)}$$

with complex refractive index *m* and size parameter *x*. Similar relationships hold for scattering and absorption cross sections. The widely used *aerosol optical thickness* of a plume of thickness z is simply the integral of σ_{ep} over thickness *z*, i.e.

$$\delta(\lambda) = \int \sigma_{ep}\ (\lambda, z)\ d\ z \qquad \text{(Eq. 4)}$$

Particles may extinguish radiation by scattering and/or absorption with $\sigma_{ep} = \sigma_{sp} + \sigma_{ap}$. The fraction of scattering to extinction is defined by the *single-scattering albedo*

$$\omega_0 = \frac{\sigma_{sp}}{\sigma_{ep}} = \frac{\sigma_{sp}}{\sigma_{sp} + \sigma_{ap}} \qquad \text{(Eq. 5)}$$

12.3 Particle metrics

For particulate matter of known chemical composition, i.e., of known effective refractive index *m*, the extinction can be related to the particle mass concentration by the mass extinction efficiency b_{ep} in units of m^2/g as [Ouimette and Flagan, 1982]

$$\sigma_{ep} = c_{mass} \times b_{ep} \quad \text{(Eq. 6)}$$

If the particulate matter under consideration is mainly absorbing ($\omega_0 < 0.3$), this relationship can be approximated by considering absorption only

$$\sigma_{ap} = c_{mass} \times b_{ap} \quad \text{(Eq. 7)}$$

The approximation by an entirely absorbing aerosol is applicable to combustion particles. Following Bond and Bergstrom [2006] the mass absorption efficiency b_{ap} for fresh combustion aerosol particles at an wavelength of 550 nm is 7.5 m^2/g. If other wavelengths have to be considered, this property scales with the inverse wavelength, i.e.

$$b_{ap} \propto \frac{1}{\lambda} \quad \text{(Eq. 8).}$$

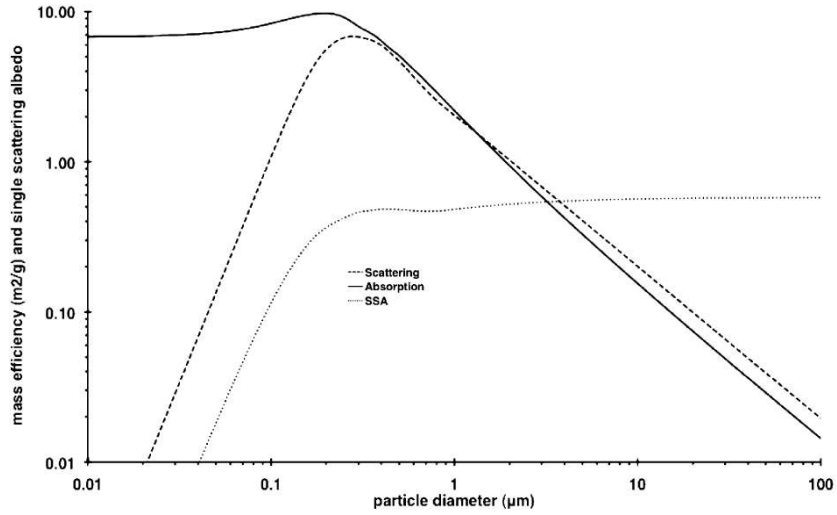

Figure 109 Mie calculation of mass scattering efficiency b_{sp}, mass absorption efficiency b_{ap} and single scattering albedo (SSA) ω_0 as function of particle diameter for a spherical BC particle with a refractive index of m = 1.74+0.44i, a wavelength of λ = 550 nm, and a density of ρ = 1.8g/cm^3 [Moosmüller et al., 2009].

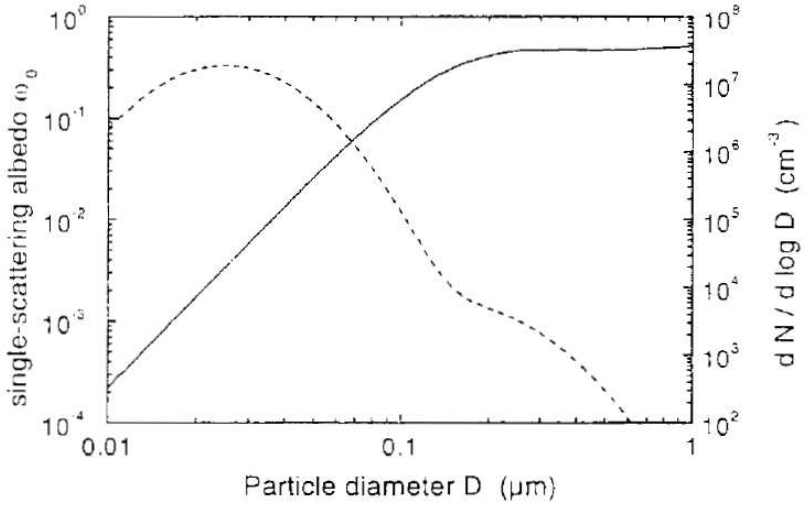

Figure 110 Single-scattering albedo for spherical BC particles at a wavelength of 545 nm. Also given is the size distribution of BC particles in the exhaust plume of a B737-300 at cruise [Petzold et al., 1999].

One key pre-requisite for relating particle mass concentration to particle optical properties is the absence of a particle size effect, i.e., if the mass absorption efficiency b_{ap} depends on particle size, then the unambiguous relation of aerosol absorption to particle mass concentration requires an additional measurement of the particle size distribution. Figure 109 shows the Mie calculation of mass scattering efficiency b_{sp}, mass absorption efficiency b_{ap}, and single scattering albedo ω_0 as function of particle diameter for a spherical BC particle. Figure 110 shows similar calculations for ω_0 only, but combined with a typical size distribution of BC particles in aircraft engine exhaust.

Combining both Figures it is obvious that for the size range relevant for BC particles in the exhaust of aircraft engines (d_p < 0.1 µm) the mass absorption efficiency is independent of particle size, the mass scattering efficiency shows a strong dependence on particle size, and the single-scattering albedo is below a value of 0.2 for a wavelength of approx. 550 nm (green). The independence of the respective mass efficiency parameter from size is given only for absorption by small BC particles, but not for scattering.

In the Rayleigh limit of particles being small compared to the wavelength λ the dependence of particle optical properties on particle diameter d_p, can be summarised as [Bohren and Huffman, 1983]

$$Q_{scat}\,(m,x) \propto \left(\frac{d_p}{\lambda}\right)^4 \;;\; C_{scat} = \frac{\pi\, d_p^2}{4} Q_{scat} \;\Rightarrow\; b_{sp} \propto \frac{d_p^3}{\lambda^4}$$
$$Q_{abs}\,(m,x) \propto \frac{d_p}{\lambda} \;;\; C_{abs} = \frac{\pi\, d_p^2}{4} Q_{abs} \;\Rightarrow\; b_{ap} \propto \frac{1}{\lambda} \qquad \text{(Eq. 9)}$$

with scattering and absorption efficiencies Q_{scat} and Q_{abs}, respective cross sections C_{scat} and C_{abs} and the resulting mass-related efficiencies b_{sp} and b_{ap}.

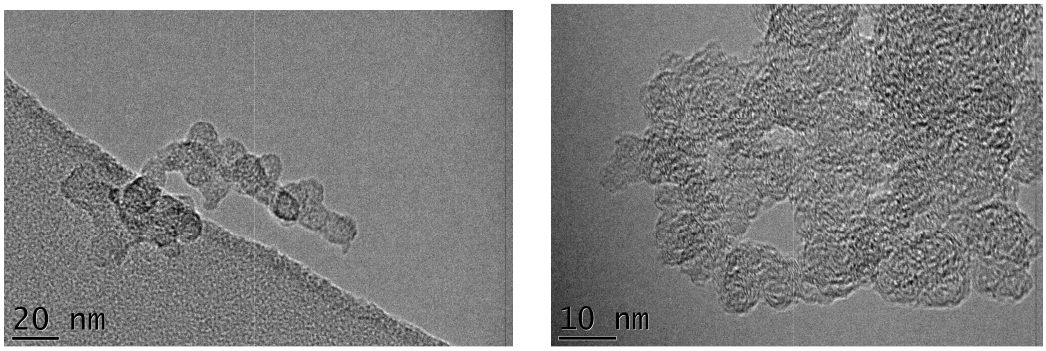

Figure 111 Transmission electron microscopy images of gas turbine exhaust soot particles [*SAMPLE 1 Final Report, 2009*].

Concerning fractal-like clusters which are typical for BC particles emitted from combustion sources Berry and Percival [1986] (see also *Moosmüller et al.*, 2009 for a summary) showed that absorption properties of fractal clusters are governed by the size of the primary particles while scattering properties depend on the size of the cluster. In turn, particle absorption fulfils the requirements for the Rayleigh limit so that the mass absorption efficiency b_{ap} is independent of particle diameter d_p while the clusters can reach sizes comparable to the wavelength λ and the mass scattering and extinction efficiencies b_{sp} and b_{ep} show strong dependencies on particle size d_p.

12.4 Conditions at high relative humidity

The discussions in the previous section are valid only for dry particles or for conditions at low relative humidity which corresponds to conditions at engine certification work. If plume visibility studies are conducted by means of a Lidar instrument at ambient conditions the effect of particle growth by the uptake of water from the gas phase has to be considered.
Usually particles are composed of various substances as an internal mixture. Some of the substances as ammonium sulphate $(HH_4)_2\ SO_4$ or sulphuric acid H_2SO_4 show considerable growth in size at high relative humidity, see Figure 112.

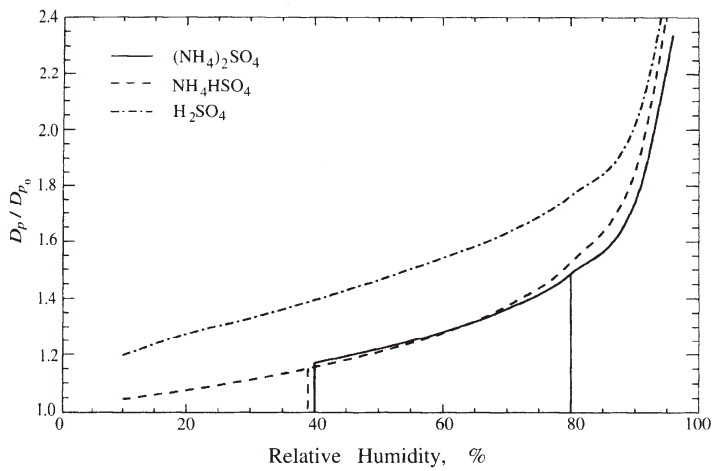

Figure 112 Particle humidity growth factor D_p / D_{p0} for various substances [Seinfeld and Pandis, 1998].

Particle growth is expressed as the ratio of the particle diameter at humid conditions d_p versus the particle diameter at dry conditions, d_{p0}. The extinction in a humid environment has to be calculated from Eq. 3 using the humid diameter d_p instead of the dry diameter d_{p0}. Furthermore, adding water to the particle, the refractive index has to be matched to the new conditions by

$$m_{hum} = \phi\, m_{dry} + (1-\phi)\, m_{water} \quad \text{(Eq. 10)}$$

with the volume fraction of dry mass $\phi = V_{dry}/V_{hum}$. The volume fraction of dry mass can be calculated directly from the particle growth factors.

The increase in particle extinction by uptake of water is a well-known effect observed by Lidar measurements because exhaust plumes are easier to detect at high relative humidity conditions due to particle growth from the emitted sulphuric acid. However, this effect is of minor importance for engine certification issues and can be neglected in our discussion.

12.5 Conclusion

Potential particle metrics related to plume visibility are in the order of relevance:

1. Particle size distribution and the particle refractive index, and
2. Particle mass concentration and particle mass-specific absorption coefficient b_{ap}.

The particle size distribution is difficult to measure and is therefore excluded from the current list of potential particle metrics in AIR 6037 [*SAE*, 2009], the only particle property applicable to plume visibility is the particle mass concentration. Number concentration cannot be used as a surrogate because number and size are not linked. Size distribution measurement techniques are not mature enough for being applied in certification measurements. Furthermore, size distributions are affected by processes like coagulation in the sampling lines causing large uncertainties in the gathered information.

The pre-requisite of a size-independent mass-specific efficiency parameter with respect to the considered optical property is valid only for particle absorption while particle scattering shows a strong dependence on size. Since the smoke number SN is related to extinction (= scattering + absorption) and depends therefore not only on particle mass but also on the particle size distribution there is no direct measurable particle property available which links particle mass to optical extinction in an unambiguous manner. Concluding, the theoretic approach, showing how SN is related to extinction confirms that a particle number-size distribution would be necessary, to reconstruct a visibility criteria. However, the combination of particle mass concentration and number concentration of nonvolatile particles permits an approximation of light absorption by the exhaust plume, which dominates extinction at least in the near field after emission.

13. Experimental data to suggest the difference between cooled and un-cooled sampling probes.

13.1 Introduction

To study the effect of probe cooling, data analysis has been performed on previous Rolls-Royce emission measurements, which were taken on a turbofan engine exhaust with a water-cooled and un-cooled cruciform rake.

13.2 Results

A range of engine power conditions (low to high) were performed with engine exhaust temperatures between 700 and 750°C. Emission measurements were obtained using ARP1256 and ARP1179 specifications. The water-cooled rake resulted in cooling the sample temperature down to 40 to 70°C (depending upon power condition). Subtracting the water-cooled data from the un-cooled data allows the results for each emissions species to be compared as shown in Figure 113 and Figure 114.

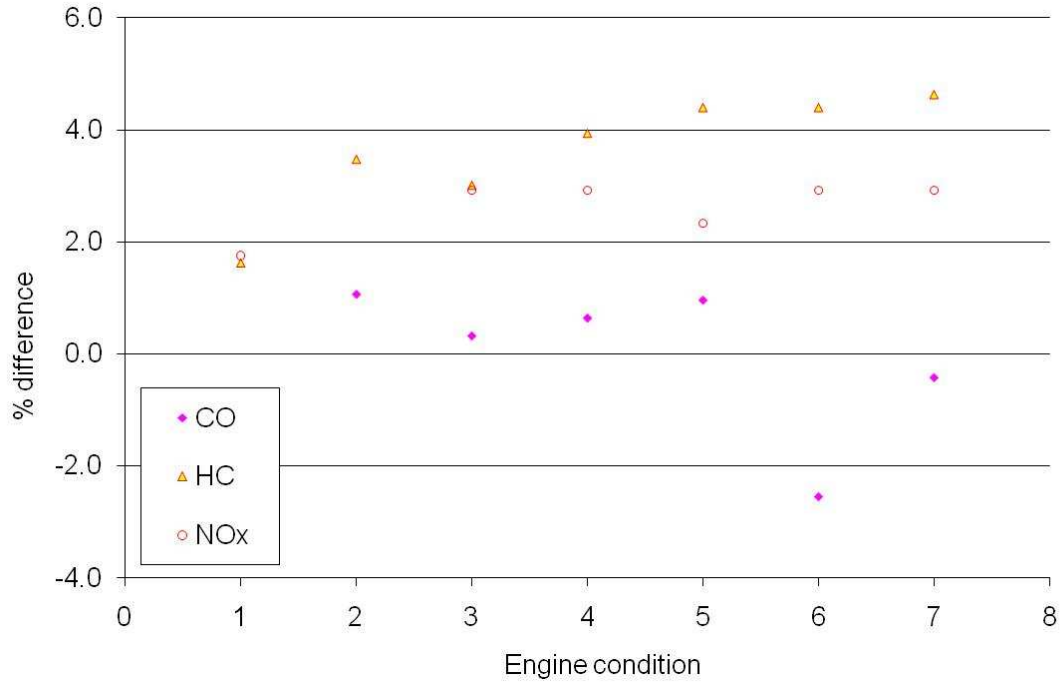

Figure 113 Percentage differences between gas species measurements extracted from cooled and un-cooled sampling probes.

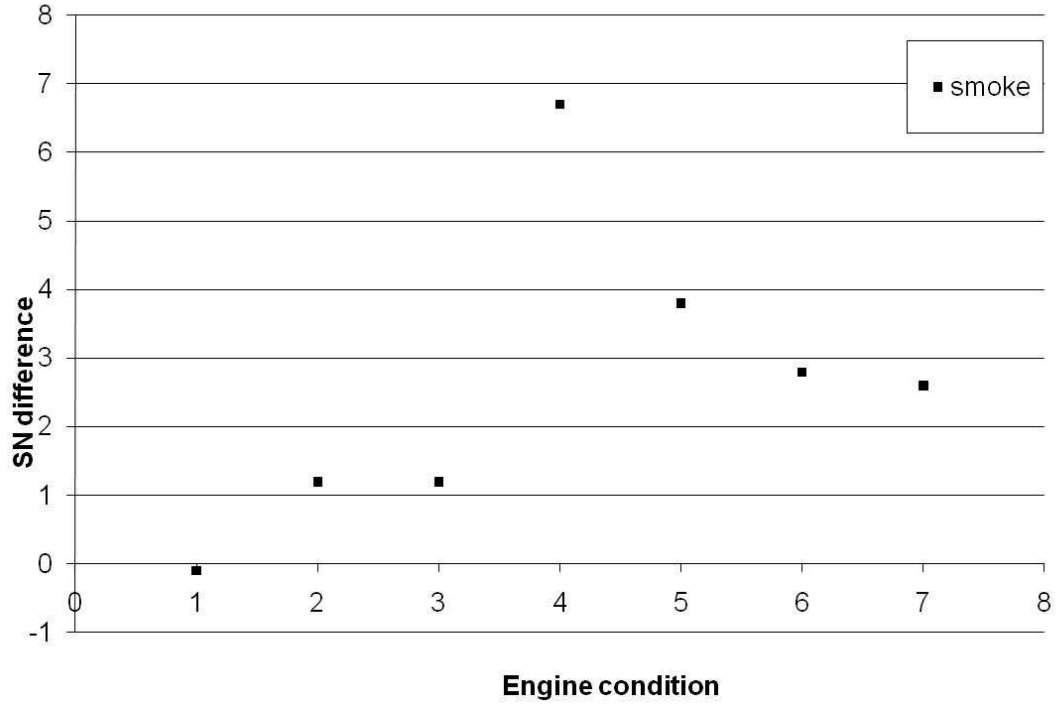

Figure 114 Differences between Smoke Number measurements extracted from cooled and un-cooled sampling probes.

Analysis of the CO data indicates negligible difference, with the exception of one close data point, the results are all within the 2% accuracy of the methodology. Analysis of the NO_x data suggests a small (~2.5%) consistent loss of NO_x in the water-cooled probe but this magnitude of difference is similar to uncertainty of the measurement. Analysis of the HC (Hydrocarbon) data shows a similar trend to NO_x but with a slightly larger loss for a cooled probe, which increases with engine exhaust temperature (from 2 to 4%). Analysis of the SN (Smoke Number) data reveals that the particulate loss is also encountered for the water-cooled probe, again generally with larger losses at higher exhaust temperatures.

13.3 Conclusion

In conclusion, cooling the sampling probe results in small losses of NO_x and HC and impacts the loss of smoke particulates. It is unsurprising to see these losses due to some condensation of HC/ NO_x coating the smoke particulates, thermophoretic losses of hot particles to cold sampling walls (the greater the temperature gradient the larger the loss) then partially removes the sample from reaching the analysers. If 'burn-out' of gaseous species had been observed in the uncooled probe, then the data analysis would have indicated minus differences – this was not the case. Thus it is concluded that probe cooling is not required in exhaust sampling temperatures of <750°C.

14. Experimental Approach – UV Lidar tests at Manchester airport

14.1 Rig Description

The Lidar used in these trials was MMU's Rapid-Scanning UV Lidar (Figure 115). This has been used previously in a series of field campaigns (at Heathrow, Manchester and Cranfield airports) to study the dispersion of engine emissions from commercial aircraft (Bennett *et al.*, 2010).

Figure 115 Lidar on field trials at Heathrow, May 2005. The 10 m meteorological mast at the rear could not be fully deployed at the Ringway site for reasons of aviation safety. The hood on the roof has been lifted off the steering mirror, partially obscuring it from this angle. Note that the vehicle has been jacked down for stability. Right: Dr Simon Christie; left: Dr Mike Bennett.

The Lidar is built around a frequency-tripled Nd:YAG laser, emitting in the UV-A at 355 nm. As such, it is effectively eye-safe. The laser fires at 30 Hz, at up to 33 mJ/pulse. The beam can be steered in elevation or azimuth with a plane mirror. The optics are co-axial, with the output beam being along the axis of a Newtonian telescope: this collects the return signal using a parabolic mirror of 254 mm diameter. The signal is then split between two photomultiplier tubes (PMT) whose output may then be digitized at up to 125 MSamples/s. In the field trials for the SAMPLE II project, a single PMT was used, being digitized at 60 MSamples/s and 10 bits: this gave a range resolution of 2.5 m.

As may be seen from Figure 115, the system is mounted in a Mercedes van. This has onboard power generation, so the system can operate autonomously. On arrival on site, the vehicle is jacked down for stability, and its alignment then set against the horizontal and against defined landmarks. Timebase and location are taken from the GPS. A 10 m inflatable mast allows the standard meteorological variables also to be monitored.

As at present configured, the Lidar operates in simple backscatter mode. A laser pulse is emitted and is scattered elastically by atmospheric aerosol. The magnitude of the return signal then gives an indication of the concentration of such aerosol, while the delay between emission and return indicates its range. By scanning the steering mirror while the laser fires, it is possible to obtain a horizontal or vertical cross-section of the aerosol distribution; such cross-sections may be repeated at 5 s intervals for as long as is desired – for several hours if necessary. A suite of analysis programs has been written to permit aerosol dispersion to be monitored qualitatively and quantitatively (Bennett *et al.*, 2010).

A fundamental problem with backscatter Lidar is that the backscatter cross-section of the aerosol depends both upon its size spectrum and on its complex refractive index. In general, neither of these is known, so one cannot directly interpret the Lidar signal as a gravimetric concentration of aerosol. In the case of aircraft engine emissions, some progress has been made by Eberhard *et al.* (2005). If it is assumed that the aerosol in the plume consists largely of elemental carbon, its refractive index may be taken as $2.0 + 1.0i$. For uniform spheres, the backscatter per unit mass of aerosol has its greatest value when the circumference of the particles is approximately equal to the wavelength of the scattered radiation. For our Lidar (or Eberhard's) this then gives a rather flat maximum of ~0.2 m^2 g^{-1} sr^{-1} for soot particles of diameter, $d \sim 100$ nm. For larger particles, this calibration falls off as d^{-1}; for smaller particles, it falls off as d^3. Assuming that the 'black smoke' in an engine emission test consists largely of elemental carbon and that it typically consists of spheres of 40-100 nm diameter, it should thus in principle be possible to relate the integrated Lidar backscatter across a plume to the mass emission rate of 'black smoke' within it.

As noted, the above approach assumes that the observed visual nuisance of an engine emission arises from elemental carbon only. This seems not to be the case, in as much as the signal strength obtained by the Lidar is frequently greater in cool conditions, the implication being that much of the UV backscatter arises from volatiles. (These of themselves may have health implications.) In the field trials within SAMPLE II, therefore, the group was attempting to appraise a different approach, namely to monitor the visual optical density (OD) of the plume simultaneously with obtaining Lidar backscatter cross-sections. The Lidar cross-section thus enables us to locate the chord along which optical density is measured within the dispersing plume and to integrate up to obtain a total flux of optical obscuration.

14.2 Instrumentation used

For the measurements of optical density, an array of Kipp & Zonen SP Lite2 Silicon Pyranometers was used - effectively suitably packaged and calibrated silicon photodiodes. These provide a cost effective method of monitoring short-wave solar radiation, with a sensitivity down to 60 $\mu V\ W^{-1}\ m^2$. If an engine plume passed briefly between the solarimeter and the sun, then the relative loss of signal should be a direct measurement of the plume's optical density. A shortcoming of this instrument, for this application, is that the maximum sensitivity of the pyranometer is in the near infra-red. (It measures within the spectral range 400-1100 nm.) This is of little use, since infra-red would be only weakly scattered by submicron aerosol and is anyway not visible to the eye. The visual optical density of the plume would thus be grossly underestimated. The instruments were therefore adapted with the use of standard photographic visible filters (Figure 116). Such filters are centred on the green and thus gave the pyranometers a response much closer to that of the human eye.

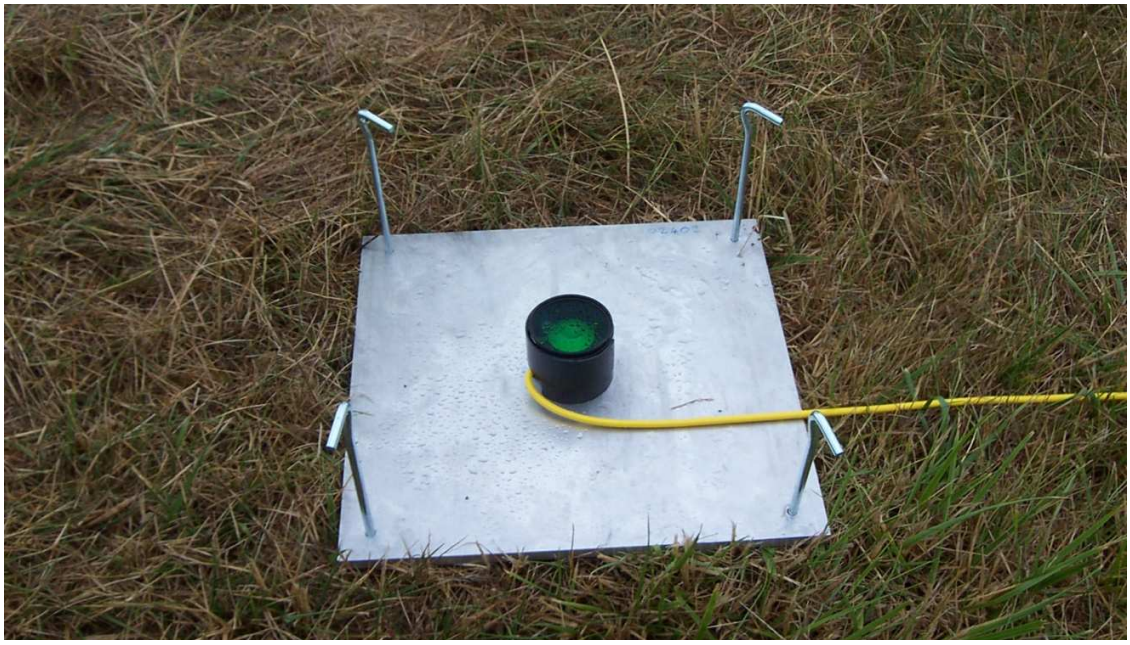

Figure 116 Individual solarimeter *in situ*.

The outputs of the pyranometers were logged at 2 s intervals in differential mode to 12-bits accuracy by two CR1000 Campbell Scientific recorders. The gain of the analogue/digital converter was set to approximately capture the maximum possible solar intensity in the period of the measurements. As such, the system should have had a maximum sensitivity of an OD of as little as 2.4×10^{-4}. Assuming that most optical scattering arises from Mie scattering in the lowest (say) 2 km of the atmosphere, this implies a sensitivity equivalent the scattering from a path length of ~0.5 m in the boundary layer.

The Lidar and solarimeters were then deployed at Manchester (Ringway) airport close to the end of Runway 2, as shown in Figure 117 and Figure 118. To avoid any interference with the airport's navigation systems, the solarimeters were placed along the boundary of the prohibited area. Instruments were spaced at 20 m intervals with the two loggers between pairs 1-2 and 3-4. The Lidar was installed outside the airfield at the location shown. Calculation then showed that the sun would shine directly from the Lidar towards the various solarimeters at the (local) times shown.

In operation, the Lidar would scan in elevation from the ground upwards, with the scanning azimuth being incremented from time to time so that the sun's rays striking a solarimeter lay within the Lidar scanning plane. Given a clear blue sky and light winds, the solarimeters should thus be able to detect the loss of solar flux arising from the engine emissions of an aircraft at the start of its take-off run, at the same time as the Lidar was obtaining complete and detailed plume cross-sections.

Note that Runway 2 is only currently used at peak hours. In the morning this extends up to about 1000 local time. Because of the constraints of the site, useful measurements could not be made much before 0900, or in the afternoon peak. There is a bias to westerly operations, but in the event of a significant NE component to the wind, aircraft would be obliged to take off from the far end of the runway, and well away from our instrumentation.

Manchester Airport supplied us with a file of aircraft traffic movements (ATM) over the period of the measurements. A specific list of aircraft and registration numbers in relation to the Lidar scans was compiled.

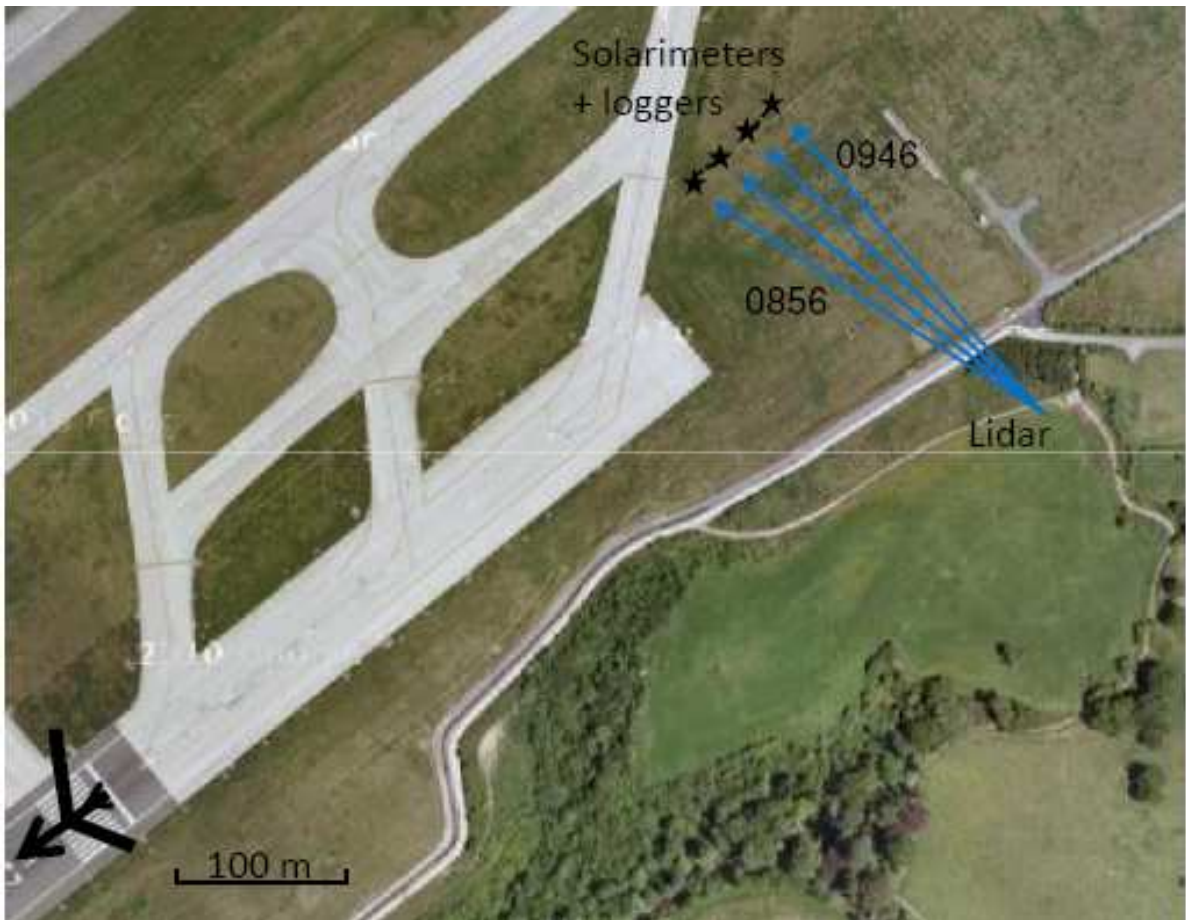

Figure 117 Arrangement of Lidar and solarimeters for the Sample II experiment at Manchester airport, 12-16 July 2010. Solarimeter locations are marked with black stars. Each logger services two solarimeters, as indicated with the dashed lines.

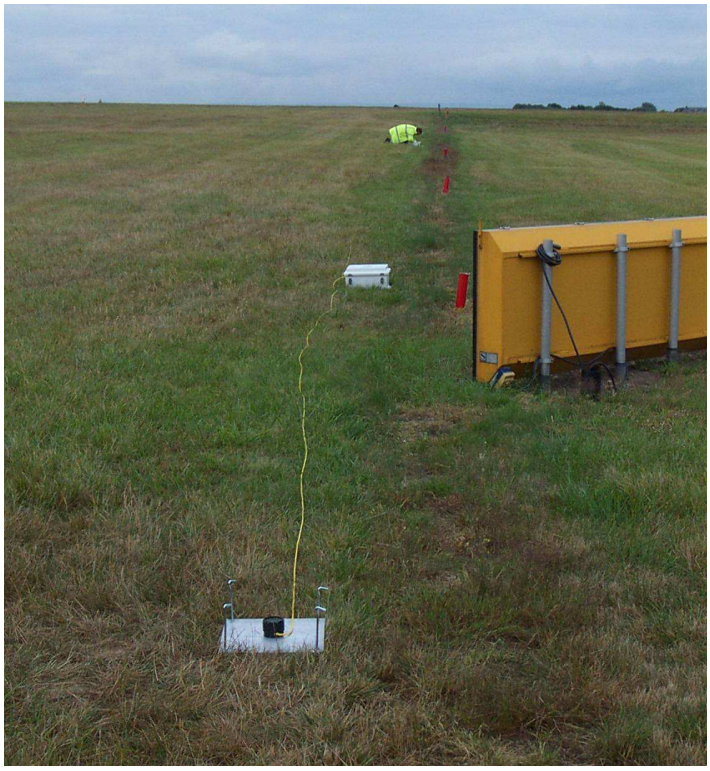

Figure 118 Line of solarimeters on airfield. The box in the middle distance houses a logger.

14.3 Test conditions

Permission was granted from Manchester Airport to carry out the field trial in the week 12-16 July 2010. The solarimeters were deployed and the loggers initiated on the first day, leaving four mornings to make useful Lidar measurements. Unfortunately, the weather was unfavourable on all of these four days, with rather little sunshine, intermittent rain and, early in the week, easterly winds.

14.4 Experimental results

We had the benefit of some intermittent sunshine with westerly operations on the mornings of 15 and 16 July. Figure 119 shows the solarimeter record for 0915-0945 BST on 15 July. Aircraft departures are also shown (as diamonds).

Unfortunately, this time series was about as good as it got in terms of steady insolation over the measurements period. There was some broken sunshine between clouds but the natural variability was too great to permit dips in insolation to be related to aircraft movements.

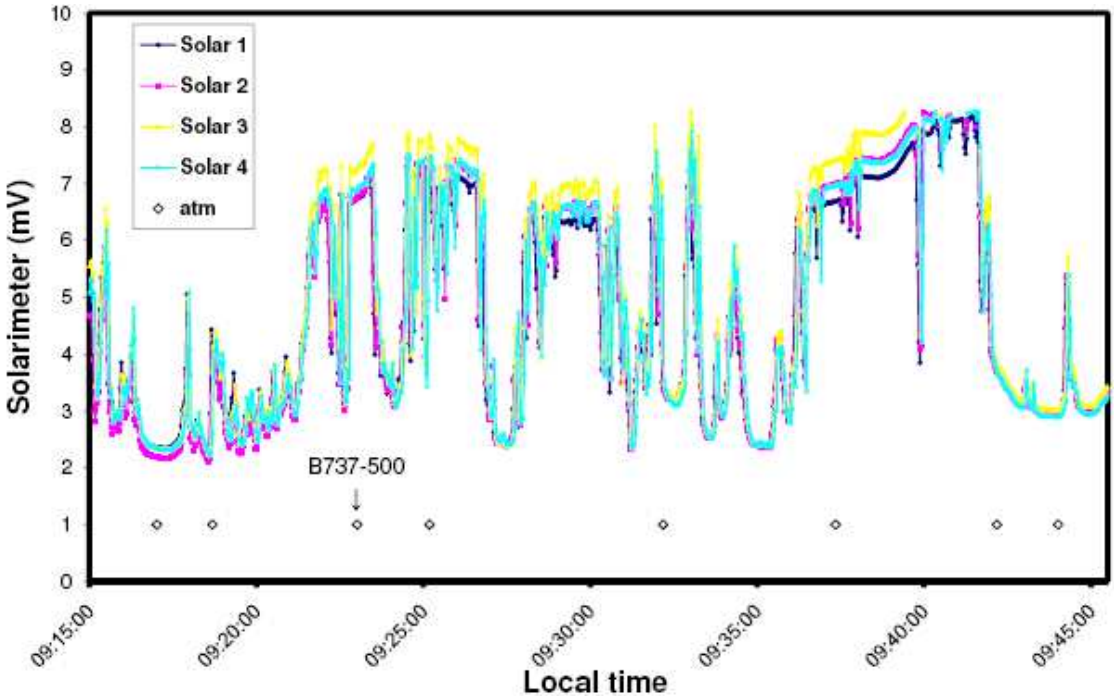

Figure 119 Output from solarimeters on morning of 15/7/10 in relation to aircraft departures from runway 2.

A typical Lidar cross-section of the engine emission is shown in Figure 120. The location of the relevant solarimeter in this diagram and the chord that the sun's rays would have followed to reach this solarimeter is indicated. The scale on the Lidar signal corresponds to the additional backscatter provided by the plume relative to the backscatter provided by the ambient air. Crudely, one may take the line integral of this along the chord, to see that this corresponds to an additional scattering path length of 50% × 10 m = ~5 m through the boundary layer. This is an order of magnitude larger than the nominal precision of the solarimeter-logger system, but is orders of magnitude smaller than the changes in scattering arising from elements of cloud passing in front of the solarimeters.

Had the sky been clear enough to provide a measurable optical density along this chord, it should thus have been possible to calibrate the Lidar signal in terms of this optical density and hence integrate up the cross-section to obtain a measure of the total visual obscuration emitted by the aircraft. Given the weather conditions pertaining at the time of the trial, however, it was not possible to do this.

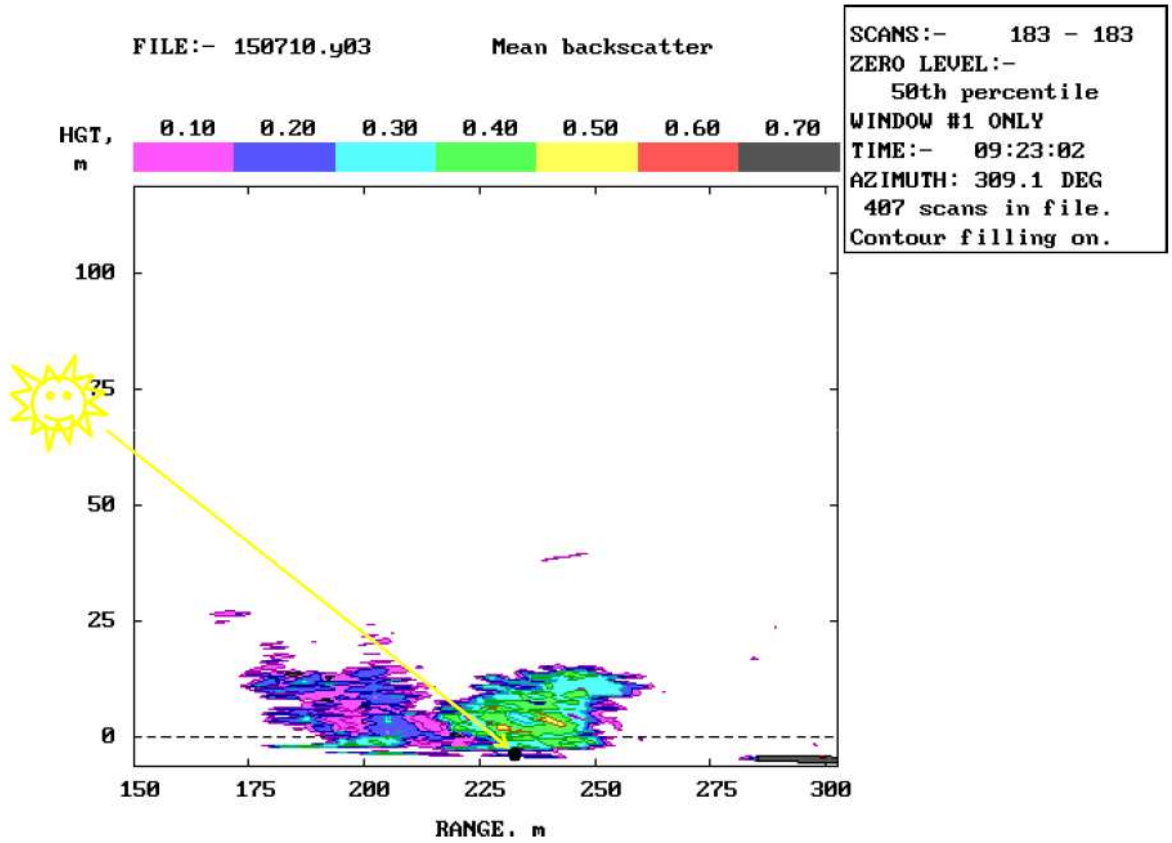

Figure 120 Lidar cross-section of plume from Lufthansa B737-500 following a rolling start. The solarimeter (at 233 m from the Lidar) was struck by the sun's rays following the path shown: the solar elevation was 38° at this time.

14.5 Conclusions

The logistics and instrumentation to monitor simultaneously the optical density of an engine plume and its backscatter cross-section have been set-up. Instrumentally, such joint measurements seem to be feasible. Successful implementation of this system, however, is very sensitively dependent on the meteorology: any future trials of this methodology should be prepared to leave the instrumentation in place for several summer weeks in order to obtain useful measurements.

15. Conclusions of the report

The experiments, studies and reviews presented in this report have allowed for an enhanced understanding of the nature of aircraft PM emissions. Most significantly this report has quantified some of the key causes of PM loss and transformation in typical sampling systems. The significant conclusions include:

1. The miniCAST model 6201 C is a valuable soot aerosol generator for instrument development and testing. More research is needed to establish whether such a device could be used as a calibration source. Given the current state of the market of potential calibration sources it is still not entirely possible to produce a definitive source of representative PM by which all instruments and sampling systems could be calibrated.
2. Future testing of the nature of the work undertaken in this report requires the application of a certified standard instrument in order to describe the variability of soot generators, rigs and engines.
3. Rig condition, sample line temperature, flow rate, dilution location and line material all have an effect on the mass, number and size data surrounding PM measurement.
4. Whilst some evidence exists to demonstrate that residence time has a significant effect on the condition of the PM sample, definitive data can't be provided and as such a specific test would need to be carried out.
5. In terms of 'bedding-in', results indicated that stabilisation occurred relatively quickly during a period of tens of minutes.
6. Hot tip dilution appears to minimise PM losses in terms of mass and number.
7. Aspects of the operation of VPR systems have been demonstrated; results indicate that the VPR configuration in terms of temperatures and dilution ratio is significant. It can therefore be concluded that commercial versions of these devices must be carefully evaluated prior to selection and deployment in future PM sampling processes.
8. For the engine test, in agreement with the HES test campaign, where dilution was added at 7m downstream of the sampling probe, it was observed that a dilution ratio of greater than 10:1 promoted significantly lower number counts (above the expected losses of an additional diluter stage), suggesting that the volatile particles are not fully removed at low dilution ratios.
9. When operating eductor-type dilution systems, it is difficult to achieve a specified dilution ratio. This has been attributed to the balances of pressures between the inlet, outlet and diluent flow. Hence in the case of this test, and in agreement with trends witnessed during HES testing, the 25m downstream dilutor produced lower than expected dilution ratios.
10. Modelling of the HES experiment has shown good agreement with experimental data. As such this has shown that volatile PM losses are significant at sample line conditions below 160°C. A difference in the volatile particle concentrations can be observed with varying the sample line length, which can be attributed to diffusion losses and coagulation losses due to increased residence time.
11. A departure between CO_2 and smoke emissions from engine data has been shown, but more experimentation would be required to determine how common this event is. In any case there is a real need for more engine testing in order to build in the findings of this report.

12. Whilst a number of carbon burn-off and optical methods exist, there is a lack of agreement between them.
13. Cooling the sampling probe results in small losses of NO_x and Hydrocarbons and impacts the loss of smoke particulates.
14. In-situ Lidar measurement techniques are strongly dependent on metrological factors.

References

Agrawal, H., et al. (2008), In-use gaseous and particulate matter emissions from a modern ocean going container vessel, *Atmospheric Environment*, *42*(21), 5504-5510.

Aiken, A. C., et al. (2008), O/C and OM/OC Ratios of Primary, Secondary, and Ambient Organic Aerosols with High-Resolution Time-of-Flight Aerosol Mass Spectrometry, *Environ. Sci. Technol.*, *42*(12), 4478-4485.

Baron, P. A., and K. Willeke (2001), *Aerosol measurement: Principles, techniques and applications*, 2nd ed., John Wiley and Sons, New York.

Berry, M. V., and I. C. Percival (1986), Optics of fractal clusters such as smoke, Optica Acta, 33(5), 577-591.

Bennett M., Christie S., Graham A. and Raper D. (2010) 'Lidar observations of aircraft exhaust plumes', *J. Atmospheric and Oceanic Technology*, **10,** 1638-1651.

Birch, M. E., and R. A. Cary (1996), Elemental carbon-based method for monitoring occupational exposures to particulate diesel exhaust, Aerosol Science and Technology, 25(3), 221-241.

Bohren, C. F., and D. R. Huffman (1983), Absorption and Scattering of Light by Small Particles., 544 pp., John Wiley & Sons, Inc, New York.

Bond, T. C., et al. (1999), Calibration and Intercomparison of Filter-Based Measurements of Visible Light Absorption by Aerosols, Aerosol Sci. Technol., 30(6), 582-600.

Bond, T. C., and R. W. Bergstrom (2006), Light Absorption by Carbonaceous Particles: An Investigative Review, Aerosol Sci. Technol., 40(1), 27-67.

CAEP (2008), FOA Guidance Manual for Use By MODTF, *CAEP Working Paper*, CAEP8-WG3-WP09.

Chow, J.C., J.G. Watson, D. Crow, D.H. Lowenthal, and T. Merrifield "Comparison of IMPROVE and NIOSH Carbon Measurements" Aerosol Sci. Technol. 34: 23-34 (2001).

EASA Study - Petzold, A., and R. Marsh (2009), Study on Sampling and Measurement of Aircraft Particulate Emissions SAMPLE – Final Report.

Eberhard W.L., Brewer W.A and R. L. Wayson R.L. (2005), 'Lidar observation of jet engine exhaust for air quality', *Proc. 85th AMS Annual Meeting, 2nd Symposium on Lidar Atmospheric Applications*, San Diego, CA.

Glassmann, I, Combustion, 3rd Ed., Academic Press, San Diego, California, 1996

Helsper, C., et al. (1993), Investigations of a new aerosol generator for the production of carbon aggregate particles, Atmospheric Environment Part A-General Topics, 27(8), 1271-1275)

Hess, M., et al. (1998), Optical Properties of Aerosols and Clouds: The Software Package OPAC, Bull. Am. Met. Soc., 79(5), 831-844.

Hinds, W. C. (1999), *Aerosol Technology: Properties, Behaviour and Measurement of Airborne Particles.*, 483 pp., John Wiley & Sons, Inc., New York.

International Civil Aviation Organisation. *International standards and recommended practices, Environmental Protection, Annex 16, Volume 11,* Aircraft Engine Emissions 2nd edition 1993.

Kärcher B, A trajectory box model for aircraft exhaust plumes. J. Geophys. Res. 100 (1995), 18835-18844.

Liu, B. Y. H., and D. Y. H. Pui (1974), Submicron aerosol standard and primary, absolute calibration of condensation nuclei counter, Journal of Colloid and Interface Science, 47(1), 155-171

Moosmüller, H., et al. (2009), Aerosol light absorption and its measurement: A review, Journal of Quantitative Spectroscopy and Radiative Transfer, 110(11), 844-878.

Ouimette, J. R., and R. C. Flagan (1982), The extinction coefficient of multicomponent aerosols, Atmosph. Env., 16(10), 2405-2419.

EASA Study - Petzold, A., and R. Marsh (2009), Study on Sampling and Measurement of Aircraft Particulate Emissions SAMPLE – Final Report.

Petzold A. and Niessner R. (1995) Method comparison study on soot-selective techniques. Mikrochim. Acta 117, 215-237

Petzold, A., and F. Schröder (1998), Jet engine exhaust aerosol characterisation, *Aerosol Sci. Technol., 28*, 62-76.

Petzold, A., et al. (1999), In situ observations and model calculations of black carbon emission by aircraft at cruise altitude, J. Geophys. Res.-Atmos., 104(D18), 22171-22181.

Petzold, A., and M. Schönlinner (2004), Multi-angle absorption photometry - A new method for the measurement of aerosol light absorption and atmospheric black carbon, *J. Aerosol Sci., 35*(4), 421-441.

Petzold, A., et al. (2005a), Particle emissions from aircraft engines – a survey of the European project PartEmis, *Meteorologische Zeitschrift, 14*, 465-476.

Petzold, A., et al. (2005b), Evaluation of multiangle absorption photometry for measuring aerosol light absorption, *Aerosol Sci. Technol., 39*, 40-51.

SAE (1997), ARP 1179: Aircraft gas turbine smoke measurement, *SAE Aerospace Recommended Practice*.

SAE E-31 *Position paper on particulate measurements*, SAE E-31 committee, 3 April 2002.
SAE (2004), AIR 5892: Nonvolatile Exhaust Particle Measurement Techniques, *SAE Aerospace Information Report*.

SAE (2009), AIR 6037: Aircraft Exhaust Nonvolatile Particle Matter Measurement Method Development, *SAE Aerospace Information Report*.

Scheibel, H. G., and J. Porstendörfer (1983), Generation of monodisperse Ag- and NaCl-aerosols with particle diameters between 2 and 300 nm, Journal of Aerosol Science, 14(2), 113-126

Schmid, H., et al. (2001), Results of the carbon conference international aerosol carbon round robin test stage I, *Atmos. Environ., 35*, 2111-2121.

Schnaiter, M., et al. (2006), Strong spectral dependence of light absorption by organic carbon particles formed by propane combustion, Atmos. Chem. Phys., 6(10), 2981-2990.

Seinfeld, J. H., and S. N. Pandis (1998), Atmospheric Chemistry and Physics: From Air Pollution to Climate Change., 1326 pp., John Wiley & Sons, Inc, New York.

Snelling, D. R., et al. (2005), A calibration-independent LII technique for soot measurement by detecting absolute light intensity, *Applied Optics*, *44*, 6773-6785.

Slowik, J.G., Cross, E.S., Han, J.-H., Davidovits, P., Onasch, T.B., Jayne, J.T., W., L.R., Canagaratna, M.R., Worsnop, D.R., Chakrabarty, R.K., Moosmüller, H., Arnott, W.P., Schwarz, J.P., Gao, R.-S., Fahey, D.W., Kok, G.L., Petzold, A., 2007: An Inter-Comparison of Instruments Measuring Black Carbon Content of Soot Particles, *Aerosol Sci. Technol.*, 41, 295-314.

Sorokin A., X. Vancassel, P. Mirabel, On volatile particle formation in aircraft exhaust plumes, Phys. Chem. Earth (C) 26 (2001) 557-561.

Symonds, J. P. R., et al. (2007), Diesel soot mass calculation in real-time with a differential mobility spectrometer, *Journal of Aerosol Science*, *38*(1), 52-68.
Vancassel X., A. Sorokin, P. Mirabel, A. Petzold, C. Wilson, Volatile particles formation during PartEmis: a modelling study. Atmos. Chem. Phys. 4 (2004), 439-447.

Wahl, C, Kapernaum, M, Zornek, T, Rindlisbacher, T, DLR / FOCA Line Loss Study, 2010, available from FOCA.

Wilson C.W., A. Petzold, S. Nyeki, U. Schumann, R. Zellner, Measurement and prediction of emissions of aerosols and gaseous precursors from gas turbine engines (PartEmis): an overview, Aerosp. Sci. Tech. 8 (2004), 131-143

Yu F., R. P. Turco, The formation and evolution of aerosols in stratospheric aircraft plumes : Numerical simulations and comparisons with observations. J. Geophys. Res. 103 (1998), 25915-2593

Yu F., R.P. Turco, B. Kärcher, The possible role of organics in the formation and evolution of ultrafine aircraft particles. J. Geophys. Res. 104 (1999), 4079-4088.

Appendix A – Fuel specification

FAO: Mike Miller
QinetiQ Gas Turbine Technologies

QinetiQ

Report Summary			
Report No.	F201006969	**Material**	AVTUR F-35
Overall Status	n/a	**Specification**	DEF STAN 91-91/6
Received From	QinetiQ GTT	**Senders Ref.**	Email Mike Miller
Date Received	28/APR/2010	**QinetiQ Ref.**	FST/FLC/12/7/11
Sample Description		**System Information**	
2 x 500ml plastic bottles (treated as one sample)		2010006969 - Sample 2	
Reason For Test			
Request from Mike Miller.			
Comments			

Sample Results				
Sample Number	**Status**	**Test**	**Results**	**Method**
2010006969	n/a	Density at 15 ℃	798.2 kg/m3	IP 365 (FLM 42)
		Sulphur By XRF	0.07 % Mass	FLM183
		Distillation, IBP	150.1 ℃	IP 123 (FLM 39)
		10% Recovered at	169.7 ℃	IP 123 (FLM 39)
		50% Recovered at	197.2 ℃	IP 123 (FLM 39)
		90% Recovered at	240.0 ℃	IP 123 (FLM 39)
		FBP	263.7 ℃	IP 123 (FLM 39)
		Residue	1.3 % v/v	IP 123 (FLM 39)
		Loss	0.9 % v/v	IP 123 (FLM 39)
		Net heat of combustion	43.287 MJ/kg	ASTM D3338-05
		Total Aromatics by HPLC	17.7 % v/v	IP 436
		Smoke Point	23.1 mm	IP 57
		Naphthalenes	1.13 % Vol	ASTM D 1840
		Kinematic Viscosity at -20℃	3.86 mm²/s	IP 71/ASTM D445
		Hydrogen	14.19 % Mass	ASTM D5291

Name: J Amero

Authorised By: J.A.AMERO

Date: 10/MAY/2010

From: Fuels & Lubricants Centre
Cody Technology Park,
Building A7, Room 1068,
Farnborough, Hampshire.
GU14 0LX

Tel : 01252 39 7449
Fax : 01252 39 7182
Email: jaamero@QinetiQ.com

EUROPEAN AVIATION SAFETY AGENCY
AGENCE EUROPÉENNE DE LA SÉCURITÉ AÉRIENNE
EUROPÄISCHE AGENTUR FÜR FLUGSICHERHEIT

Postal address
Postfach 101253
50452 Cologne
Germany

Visiting address
Ottoplatz 1
50679 Cologne
Germany

Tel +49_221_89990-000
Fax +49_221_89990-999
Mail info@easa.europa.eu
Web easa.europa.eu